Metallic Nanostructures for Enhanced Sensing and Spectroscopy

by

Aftab Ahmed
B.Eng., NED University, 2002
M.Sc., King Fahd University of Petroleum and Minerals, 2008

A Dissertation Submitted in Partial Fulfillment
of the Requirements for the Degree of

DOCTOR OF PHILOSOPHY

in the Department of Electrical and Computer Engineering

Supervisory Committee

Metallic Nanostructures for Enhanced Sensing and Spectroscopy

by

Aftab Ahmed
B.Eng., NED University, 2002
M.Sc., King Fahd University of Petroleum and Minerals, 2008

Supervisory Committee

Dr. Reuven Gordon, (Department of Electrical and Computer Engineering)
Supervisor

Dr. Thomas E. Darcie, (Department of Electrical and Computer Engineering)
Departmental Member

Dr. Rustom Bhiladvala, (Department of Mechanical Engineering)
Outside Member

Abstract

Supervisory Committee

Dr. Reuven Gordon, (Department of Electrical and Computer Engineering)
Supervisor

Dr. Thomas E. Darcie, (Department of Electrical and Computer Engineering)
Departmental Member

Dr. Rustom Bhiladvala, (Department of Mechanical Engineering)
Outside Member

The interaction of light and matter at nanoscale is the subject of study of this dissertation. Particularly, the coupling of light to surface plasmons and their applications in the fields of spectroscopy and sensing is the focus of this work. In terms of spectroscopy, the simple reason of using light to study the chemical structures of different materials is the fact that the energy of light lies in the range of vibrational and electronic transitions of matter. Further, the ability to squeeze light to subwavelength dimensions opens up new possibilities of designing nano-optical devices. In this work we explore surface plasmons for two major applications: (i) Directivity enhanced Raman spectroscopy and (ii) Chemical/biological sensing.

Here a new enhancement phenomenon has been demonstrated experimentally in regards to Raman spectroscopy. Typically, Raman enhancement is considered in terms of local fields only. Here we show the use of directive nanoantennas to provide additional enhancement of two orders of magnitude. The nanoantenna design is optimal in the sense that almost all of the scattered light is coupled into the numerical aperture of the collecting lens. It is shown that the additional enhancement from directivity pushes the sensitivity to single molecule regime. Further, the out of plane radiation and simplicity of the design makes it an ideal candidate for use with typical commercial microscope setups.

Extra ordinary transmission through nanohole arrays in metallic films is studied for refractive index sensing. Bulk resolution of 6×10^{-7} is demonstrated by optimizing array dimensions, wavelength of operation, noise reduction and consideration of sensitivity of the detecting CCD camera.

Self-assembled nanostructures are investigated for spectroscopic applications. Time dependent studies of nanorods assembled in end-to-end and side-by-side configurations are conducted. The end-to-end configuration results in higher local field enhancements whereas; the side-by-side configuration shows a reduction in local fields because of the cancellation of radial field components between the neighbouring nanorods. It should be noted that higher fields are desirable for Raman spectroscopy.

Grating structures have been analysed using reduced coupled mode theory. In most cases, only three lowest order modes prove to be sufficient for accurate description of the system response. Here we present design guidelines for broadband operation and optimization of high quality factor resonators.

Finally the complex reflection coefficient from arbitrary terminated nanorods has been investigated. Phase of reflection plays an important role in the determination of resonance wavelength of nanoantennas. It is shown that the localized surface plasmon resonance of nanoparticles can be considered in terms of propagating surface plasmons along a nanorod of similar geometry where the length of the nanorod approaches zero accompanied with π degrees of phase of reflection.

The contributions made in this work can prove useful in the fields of analytical chemistry and biomedical sensing. The directive nanoantenna can find applications in a number of areas such as light emitting devices, photovoltaics, single photon sources and high resolution microscopy. Our work related to EOT based sensing is already approaching the resolution of commercially available refractive index sensors with the added advantage of multiplexed detection.

Table of Contents

List of Figures

Acknowledgments

I would like to begin by expressing my gratitude to my supervisor Dr. Reuven Gordon. I was fortunate to work under his supervision and had the opportunity to benefit from his insight and expertise in the field of photonics and plasmonics. I am also grateful to Dr. Gordon for his contentious guidance and support throughout my program of study.

I would like to thank Dr. M. A. Al-Sunaidi for introducing me to the research in the field of electromagnetics and for his guidance during my MS program in electrical engineering.

I gratefully acknowledge the critical contributions made by my collaborators throughout this work: Y. Pang, G. Hajisalem, G. A. C . Tellez, A. Lee, S. B. Hasan, G. Andrade, and M. Souza.

I am grateful for the financial support provided by NSERC Strategic Network for Bioplasmonic Systems (BiopSys), Canada.

I was lucky to be surrounded by a great group of friends and an excellent team of coworkers and would like to thank them all for their support.

Dedication

To my family.

Glossary

List of symbols:

ε_d	Permittivity of dielectric materila
ε_m	Frequency dependent permittivity of metal
ε'_m	Real part of the frequency dependent permittivity of metal
ε''_m	Imaginary part of the frequency dependent permittivity of metal
ω	Angular frequency
ω_p	Plasma frequency
ω_{sp}	Surface plasmon frequency
n	Refractive index
E	Electric field strength
H	Magnetic field strength
k_{spp}	Wavenumber of surface plasmon polariton
k_g	Reciprocal wavenumber of a periodic structure
β	Propagation constant
Λ	Period of array or grating structures
ϕ_r	Phase of reflection
$\lvert r \rvert$	Magnitude of reflection coefficient
T	Optical tranmission

Abbreviations:

ABC	Absorbing boundary conditions
DERS	Directivity enhanced Raman spectroscopy
EF	Enhancement factor
EOT	Extraordinary optical transmission
FDTD	Finite difference time domain
FIB	Focused ion beam
LSP	Localized surface plasmon
NA	Numerical aperture
NSOM	Near-field scanning optical microscopy
PCA	Principal component analysis
PML	Perfectly matched layer
RIU	Refractive index unit
SEM	Scanning electron microscopy
SP	Surface plasmon
SPP	Surface plasmon polariton
SPR	Surface plasmon resonance
SERS	Surface enhanced Raman spectroscopy
SM-SERS	Single molecule surface enhanced Raman spectroscopy
TFSF	Total field scattered field

Chapter 1

1 Introduction

1.1 Motivation

Optics is one of the oldest disciplines in physics. During the past few decades optics has undergone rapid progress with regard to understanding of the interaction of light with very small structures, particularly metallic nanostructures. Classical laws from ray optics can no longer be applied to analyze structures much smaller than the wavelength of light. The study of light matter interaction at nanoscale has evolved into a multidisciplinary field of nanophotonics with applications in physics, chemistry, applied sciences and biology. Nanophotonics can be broadly divided into two parts: (i) Confinement of light to nanoscale dimensions; an exciting application is the near-field scanning optical microscopy (NSOM) which provides a significantly better resolution of less than 100 nm as compared to far-field microscopy. (ii) Confinement of matter to nanoscale dimensions; this involves different methods to confine the dimensions of matter to synthesize nanostructures, for example nanoparticles, which exhibit interesting properties and have been extensively used to enhance Raman scattering as will be discussed later.

Recent developments in the fabrication capabilities have enabled us to design and develop exciting new devices. Structures much smaller than the wavelength of light allow for the confinement of light below diffraction limit. This made possible the design and development of a variety of new devices for a number of applications such as spectroscopy [1-7], sensing [8-11], microscopy [5, 12], solar cells [13-15], single photon sources [16, 17] and negative index materials or metamaterials [18, 19].

Metallic nanostructures are the main focus of this work. The reason for that is the negative permittivity of metal, which makes these structures special within the wavelength range of interest (visible – near-IR). The interaction of light (photon) with the free electrons in the metal gives rise to a propagating surface wave, surface plasmon polariton (SPP), or a localized excitation, localized surface plasmon (LSP). These are mixed photon-plasma modes. These mixed modes exhibit very interesting properties due to resonance effects. For instance, extremely large propagation constants, and field localization to subwavelength dimensions.

Another interesting effect of plasmonics is the extraordinary optical transmission (EOT) [9]. Study of metallic subwavelength hole arrays has shown the surprising result of very high optical transmission, which is contradictory to what is expected from Bethe's aperture theory. EOT has been extensively used for the design of ultra sensitive refractive index sensors and is expected to play an important role in the design of photonic circuits.

These nanostructures have been investigated extensively in the past decade and at present the study of these structures is receiving considerable attention. Originally this trend of smaller and smaller dimensions was motivated by the integration of electronic circuitry, but as we move towards smaller dimensions new physical effects become evident, which may be explored in the future.

1.2 Outline of This Work

The main objective of this work is the design and development of improved sensors for spectroscopic and bio-sensing applications. The central contributions of this work include the design and development of a new type of nanoantenna for spectroscopic applications and EOT based refractive index sensor with a resolution of 6×10^{-7}.

This work investigates the method of reduced coupled mode theory (CMT) as a potential analytical approach for the design of nanostructures. It is observed that certain non-resonant nanostructures can be analysed efficiently and accurately using this method, but the method fails to produce converged results when applied to resonant structures.

We also studied different configurations of self-assembled nanorods (NRs) for enhanced Raman spectroscopy.

This work follows the article-style dissertation format and is organized as follows: The remaining part of Chapter 1 discusses briefly the contributions of this dissertation. Chapter 2 presents a brief introduction to CMT, FDTD, surface plasmons, surface enhanced Raman spectroscopy (SERS), and EOT. Chapter 3 summarizes the problems investigated in this dissertation that are outlined in detail in the article manuscripts presented in the Appendices. Figure 1-1 shows a graphical outline of the new contributions of this work.

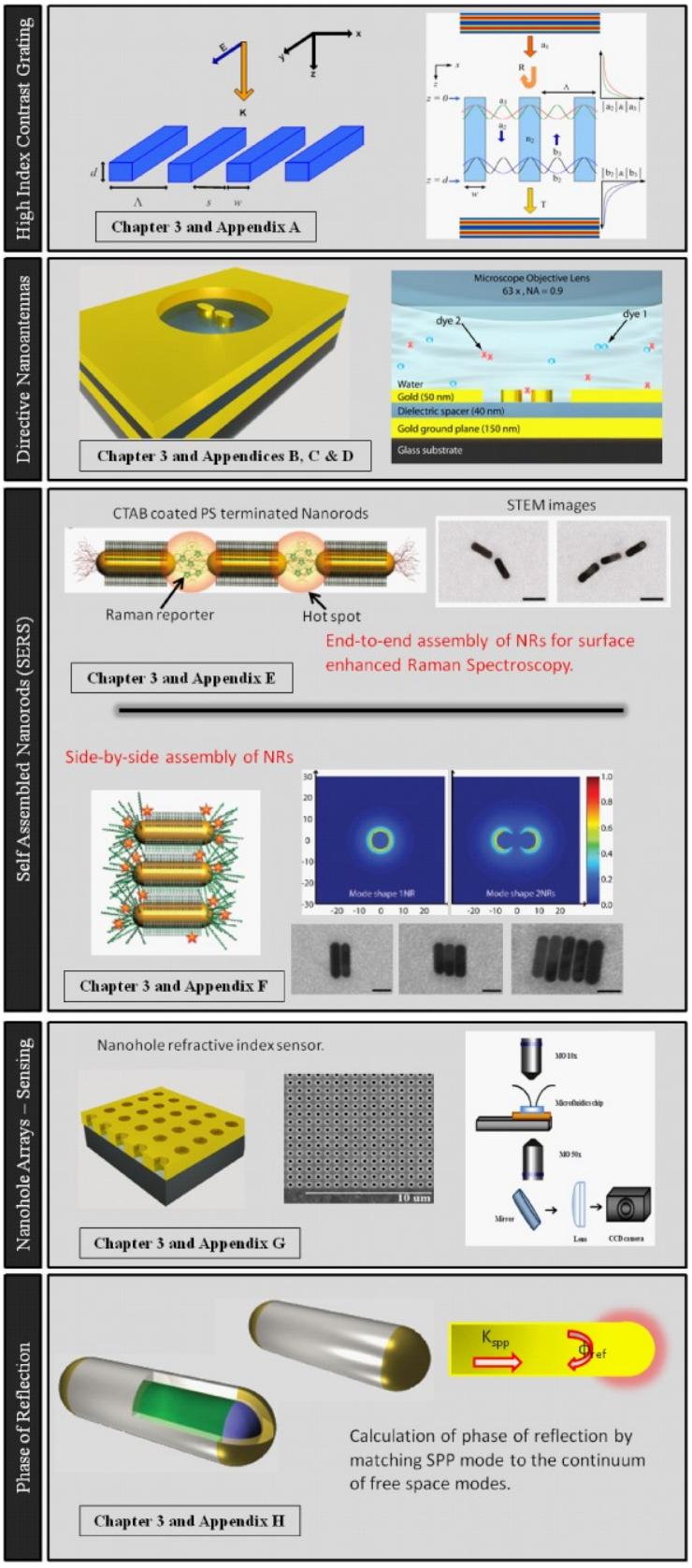

Figure 1-1: Thesis outline, problems considered in this thesis.

The first part of this work focuses on the application of reduced CMT for the design and analysis of high index contrast gratings. It is shown that in most cases, only the first two higher order modes are sufficient to characterize the response of the gratings. Reduced CMT provides physical insight into the design problem. Specifically, we present design guidelines for broadband reflectance and transmittance. These gratings can also be used as a high Q cavity with resonant wavelength strongly dependent on surrounding index.

Another problem considered here is the translation of microwave antenna design concepts to the visible/NIR regime. Microwave antennas provided solution to communication problems, whereas optical antennas prove to be useful typically for spectroscopy and microscopy applications. We present a nanoantenna design with near optimal directivity. Improved sensitivity of the design is demonstrated by detecting the vibrational (Raman) spectrum of single molecule. Enhancement factor in SERS is normally attributed to the local field effects. Here we demonstrate a new type of enhancement factor resulting from the directional radiation of the nanoantenna. It is shown that directivity enhanced Raman scattering (DERS) provides an additional two orders of magnitude enhancement factor. Another desirable feature of the design is its ability to radiate out of plane making it an ideal candidate for use in typical commercial microscopes.

Raman spectroscopy is a powerful technique for the detection and identification of materials. The weak Raman cross-section is enhanced with the help of surface plasmons that generate extremely high local fields, leading to the widely used technique of SERS. In this work we have investigated the self assembly of gold NRs for the enhancement of Raman signal. It is shown that not all configurations result in enhanced Raman signal.

Surface plasmon assisted EOT through subwavelength hole arrays in metal films offer extremely sensitive refractive index sensing. A slight change in the refractive index of the surrounding medium can produce a huge change in the transmission through the array. In this work, we have investigated nanohole arrays for improved sensitivity. A resolution of 6×10^{-7} refractive index units (RIU) is demonstrated using thick metal films. It should be noted that the observed resolution is comparable to that of state of the art commercial sensors available. Further, the design allows for multiplexed detection.

Finally, the complex reflection coefficient associated with arbitrary terminated NRs is investigated. NRs are modeled as Fabry Perot resonators in which the two ends of the NR act as mirrors with complex reflection coefficients.

1.3 Authors' Contributions

This thesis is based on projects which have either been published or submitted to peer-reviewed scientific journals. The contributions of all authors are provided in detail below:

1.3.1 High Index Contrast Gratings using CMT

A. Ahmed wrote the manuscript, performed FDTD simulations of the designed structures, performed the reduced CMT analysis and developed the design guideline for broadband reflectance and transmittance under the supervision of Dr. R. Gordon. M. Liscidini performed the analysis of the gratings using rigorous coupled wave analysis (RCWA).

1.3.2 Antenna Design for Directivity Enhanced Raman Spectroscopy

A. Ahmed contributed to this project by designing different nanoantennas, performing FDTD simulations, Raman measurements and article writing. Nanoantenna design was inspired by the microwave antenna theory, with the objective of a direction antenna radiating out of the plane. A. Ahmed studied different nanoantenna designs theoretically as well as using numerical simulations. Y. Pang carried out FDTD simulations and experiments for the parabolic reflector nanoantenna and G. Hajisalem synthesized nanoprisms used in the parabolic reflector design. This work was done under the supervision of R. Gordon.

1.3.3 Directivity Enhanced Raman Spectroscopy using Nanoantennas

This work was carried out by A. Ahmed and R. Gordon. A. Ahmed designed the circular waveguide nanoantenna, carried out all Raman scattering experiments, analysed data, performed FDTD simulations and wrote the manuscript with critical comments and technical guidance from R. Gordon.

1.3.4 Single Molecule Directivity Enhanced Raman Scattering using Nanoantennas

Detection of the vibrational spectrum of single molecule is highly desirable for chemical and biomedical applications. In this work we demonstrated single molecule

detection using fabricated nanoantenna. This project was carried out by A. Ahmed and R. Gordon. All the Raman scattering experiments, FDTD simulations, design of nanoantenna, data analysis and article writing were done by A. Ahmed under the supervision of R. Gordon.

1.3.5 End-to-End Assembly of NRs for SERS

A. Ahmed carried out all FDTD simulations, related data analysis and physical interpretation of observed results. A. Ahmed and R. Gordon worked towards the analytical interpretation of the observed experimental results, explained the generation of high local fields in the gaps between neighbouring NRs and also studied the effects of non collinear configurations. A. Lee contributed to the project by designing and carrying out all experiments, data analysis, interpretation and article writing. G. F. S. Andrade carried out initial SERS experiments with A. Lee. M. L. Souza carried out the SERS measurements with A. Lee on the optimized system. N. Coombs developed and carried out experiments on correlating the structure and SERS with A. Lee. E. Tumarkin did statistical analysis on nanorod chain populations with A. Lee. K. Liu took a number of extinction measurements and prepared samples for TEM analysis at the beginning of the project. R. Gordon, A. G. Brolo and E. Kumacheva provided critical guidance and suggestions on data analysis, interpretation, and article writing.

1.3.6 Side-by-side Assembly of NRs for SERS

A. Ahmed carried out all FDTD simulations, related data analysis and physical interpretation of observed results. A. Ahmed also performed modal analysis to demonstrate the cancellation of the radial electric field resulting in lower intensity Raman signal. A. Lee contributed to the project by designing and carrying out all experiments, data analysis, interpretation and article writing. D. P. dos Santos carried out initial SERS experiments with A. Lee. A. Lee carried out the final SERS measurements. N. Coombs carried out TEM imaging. J. I. Park did statistical analysis on nanorod populations. R. Gordon, A. G. Brolo and E. Kumacheva provided critical guidance and suggestions on data analysis, interpretation and article writing.

1.3.7 EOT based Refractive Index Sensing

A. Ahmed helped G. A. C. Tellez in FDTD simulations, related data analysis, nanohole arrays fabrication, experiments and article writing. R. Gordon provided critical guidance and suggestions on optical setup, data analysis, interpretation and article writing. G. A. C. Tellez designed and developed the microfluidic chip. A. Ahmed also worked towards the theoretical calculations for estimation of design parameters such as nanohole periodicity, hole dimensions and metal film thickness. A. Ahmed also investigated the effect of the fundamental HE11 mode cutoff on the performance of the nanoarrays.

1.3.8 Phase of Reflection from the Terminations of NRs

A. Ahmed along with R. Gordon worked towards the analytical solution for the complex phase of reflection using the idea of power conservation. Analytical predictions showed similar trends as compared to results of numerical simulations but were not in good quantitative agreement especially towards the shorter wavelengths.

S. B. Hasan along with R. Filter, R. Vogelgesang, C. Rockstuhl and F. Lederer performed the numerical simulations using COMSOL MULTIPHYSICS platform, wrote the manuscript and performed related data analysis. R. Gordon provided technical suggestions regarding the complex reflection coefficient.

Chapter 2

2 Methods and Review

This chapter briefly describes the methods of reduced CMT and FDTD that have been used in this work to analyze the nanostructures. A brief introduction to surface plasmons and their excitation is also provided.

Reduced CMT, where only a few lowest order modes are considered, proves useful for the analysis of broadband structures, but is unable to provide converged results for resonant structures. Fully converged results can be obtained using FDTD. The strength of FDTD is the determination of frequency response of the system using just one simulation run (impulse response). In this work we have employed a commercial FDTD package from Lumerical Inc.

2.1. Coupled Mode Theory

CMT has been widely used for the analysis of guiding structures in the optical regime and predicting the effects of periodic perturbations (periodic in the longitudinal/transverse directions) in an otherwise perfect guide. The method is rigorous if all modes are included, nevertheless, CMT can yield extremely accurate results even if a small subset of the modes is retained; however, CMT can be more efficient than other methods, such as RCWA and FDTD, by selecting the appropriate modal expansion.

Optical diffraction gratings have been studied for years for their applications in filtering, spectroscopy [20, 21], lasers and other optoelectronic devices [22], bio-sensing [23], light emitting diodes [24], and ultra broadband mirrors [25]. High-index-contrast gratings (HCGs) differ from the conventional sub-wavelength gratings by the fact that the grating structure is surrounded by a low index material. In the past, numerical methods such as RCWA and FDTD method have been used to analyze such structures; however, those methods can be computationally taxing and do not provide the physical insight offered by CMT.

CMT formalism is based on the expansion of the total field in a perturbed waveguide as a superposition of confined modes. The perturbation results in the coupling between co-directional and contra-directional modes as shown below. The coupled mode equations governing the mode amplitudes are given as (from [26])

$$N_m\left(\frac{da_m}{dz}+j\beta_m a_m\right)=-j\sum_{n=1}^{M}\kappa_{mn}a_n-j\sum_{n=1}^{M}\chi_{mn}b_n, \tag{2.1}$$

$$N_m\left(\frac{db_m}{dz}-j\beta_m b_m\right)=j\sum_{n=1}^{M}\chi_{mn}a_n+j\sum_{n=1}^{M}\kappa_{mn}b_n; \tag{2.2}$$

where a_m and b_m are the mode amplitudes of forward and backward travelling modes respectively, β_m is the propagation constant, N_m is the normalization constant, κ_{mn} and χ_{mn} are the coupling coefficients between co-directional and contra-directional propagating waves, respectively. The coupling coefficients are defined as

$$\kappa_{mn}=\frac{\omega\varepsilon_0}{4}\iint(\bar{n}^2-n^2)(e_{tm}e_{tn}-\frac{n^2}{\bar{n}^2}e_{zm}e_{zn})dxdy, \tag{2.3}$$

$$\chi_{mn}=\frac{\omega\varepsilon_0}{4}\iint(\bar{n}^2-n^2)(e_{tm}e_{tn}+\frac{n^2}{\bar{n}^2}e_{zm}e_{zn})dxdy; \tag{2.4}$$

where ε_0 is the permittivity of free space, n and $\bar{n}$ are the refractive indices of the unperturbed and perturbed structures respectively, e_{tm} and e_{zm} are the transverse and longitudinal components of the m^{th} mode respectively. Considering only two higher order modes result in a system of six coupled first order differential equations. Which can be solved using the boundary conditions, for further details the reader is referred to Appendix A and Ref. [26].

2.2. Finite Difference Time Domain Method

The FDTD method solves Maxwell's curl equations in a leap frog manner using Yee's cell as will be shown in this section [27]. Numerical dispersion, numerical phase velocity and the stability of the FDTD method will also be presented here. It is important to note that FDTD, being a time domain method, allows for the determination of frequency response of the system by running just one simulation (impulse response).

Yee's algorithm solves for both the electric and magnetic fields in time and space, using the coupled Maxwell's curl equations. Thus both the electric and magnetic material properties can be modeled. The Yee's cell is show in Figure 2-1.

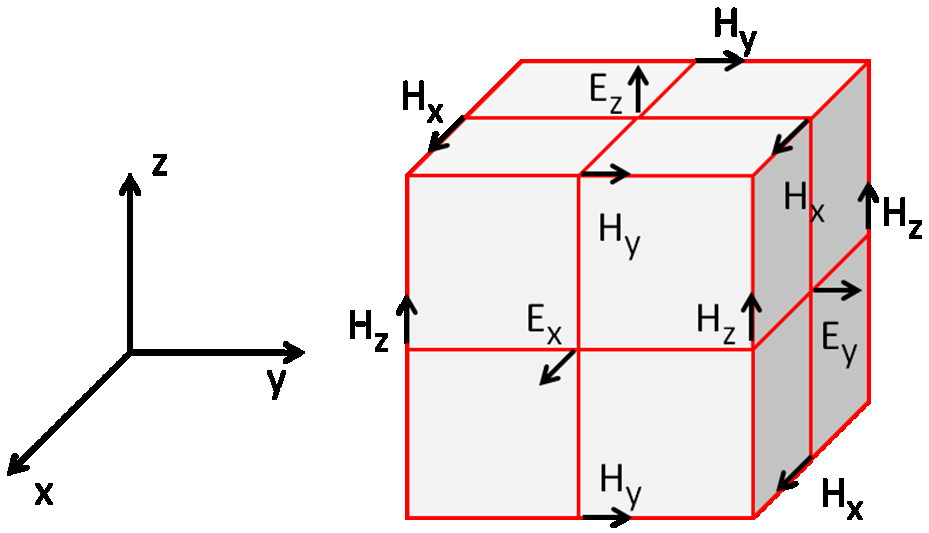

Figure 2-1: Yee's mesh for solving Maxwell's curl equations [28].

Every E component is surrounded by four circulating H components and vice versa. Yee's mesh thus creates interlinked arrays of Faraday's law and Ampere's law contours in a three dimensional space. At the beginning of the problem we specify the permittivity and permeability of the material at each field component location. The E and H components are updated using a leapfrog time-stepping algorithm. All of the E field components are calculated and stored in memory for a particular time step using the previously stored H field data. Then all of the H field components are calculated using the previously computed E data so on.

2.2.1. Spatial Grid and Time Steps

While defining an FDTD model for a given problem, one has to choose proper grid parameters. There are two rules that restrict this choice: (i) the spatial increment must be small enough to resolve the shortest wavelength. A rule-of-thumb is that the shortest wavelength must correspond to at least five unit cells. Special care must be taken while dealing with plasmonic structures where very large propagation constants give rise to much smaller wavelengths. (ii) any geometrical detail must be represented well enough by FDTD cells. Another rule-of-thumb is that the smallest geometrical dimension should be divided into at least two or three cells. Typically the second choice of the grid parameter is the more restrictive. Once spatial increments are chosen, the time step is bounded via a stability condition given as [28]

$$\Delta t \le \left(c\sqrt{\frac{1}{\Delta x^2}+\frac{1}{\Delta y^2}+\frac{1}{\Delta z^2}} \right)^{-1}; \tag{2.5}$$

where c is the largest wave propagation velocity in the problem; usually the speed of light in vacuum, $\Delta x, \Delta y$ and Δz are the grid steps in *x, y* and *z* directions respectively. Since a shorter time step does not improve accuracy, one usually chooses a value for Δt that is close to the stability limit (the Courant-number).

2.2.2. Excitation

Application of update equations makes sense only if either some initial conditions are given, or if an energy source is applied. There are many case-dependent source models available. The simplest one is the so-called hard source: some field components at some locations are given pre-defined values in the time-domain, while the other field values are updated normally. The problem of the hard source is that any reflected wave returning back to the source will be perfectly re-reflected. To make the source transparent for the reflected waves, the system can be excited using an additive source term. Since the source is totally separated from the field interactions, it can be placed inside a structure yet not forming part of it.

Such point sources are sometimes useful in theoretical considerations, but most practical problems involve more complicated source fields. One frequently used source model is a plane wave source. In the simplest case, one can produce a plane wave by choosing field locations along a line parallel to a coordinate direction, and apply the added source technique. This can be generalized easily to diagonal directions as well.

2.2.3. Boundary Conditions

Boundary conditions are imposed to terminate the simulation domain. In most cases it is one of the following: (i) perfect electric conductor (PEC) or electric wall, (ii) perfect magnetic conductor (PMC) or magnetic wall, (iii) absorbing boundary condition (ABC/PML) and (iv) periodic boundary condition (PBC). PEC is used to represent ideal conductors. PMC may be applied on symmetry planes to reduce the size of the computational volume. ABC is used to absorb outgoing waves to minimize reflections from boundaries.

ABC is needed to simulate an infinite open space, to prevent outward going waves from reflecting back to the simulation domain. There is a multitude of ABC's for FDTD algorithm available. Two common ABCs are the Mur absorbing boundaries and Berenger's Perfectly Matched Layer (PML). In short, Mur ABC is extremely simple to implement while still providing satisfactory absorption for a great variety of problems. Berenger's PML requires considerable enlargement of the computational volume, but is essentially frequency independent and superior to most ABCs. Unlike PML, which is actually an absorbing region, Mur ABC is a boundary condition which is used to calculate the field values at the terminus mesh points in a FDTD simulation. For a 1D simulation, the time stepping for these points is carried out using $\left(\frac{\partial}{\partial z}-\frac{\partial}{c\partial t}\right)E_i=0$, where z is the propagation direction.

2.2.4. Numerical Dispersion

For a fixed cell size, different frequency components of a wave propagate at slightly different velocities. This phenomenon is called numerical dispersion, and it is inherently present in the FDTD algorithm. Furthermore, velocity depends also on the angle of propagation with respect to the coordinate axis. The latter is sometimes called numerical anisotropy, but usually these two effects are combined in the single term "numerical dispersion". In fact waves propagate in the numerical grid always at a velocity less than the physical velocity. The basic effect of numerical dispersion is that it produces a cumulative phase error that is in general difficult to predict, even though bounds can be calculated. For a detailed discussion of the topic the reader is referred to [28]. In order to keep the numerical dispersion small, one has to choose small enough grid parameters, with respect to smallest wavelength considered. Resolution of $\lambda=20\Delta x$ assures that the maximum dispersion error is less than 0.28 %.

2.2.5. Modeling Dispersive Materials

There are three different methods used for simulating dispersive materials, these are: (i) Fourier transform method, (ii) Auxiliary differential equation method and (iii) Z-transform method.

In time domain, the relation between the electric field density D and electric field strength E is given by a convolution involving permittivity and E. The convolution becomes a product after applying Fourier transform. Permittivity is then introduced using any of the dispersive models, for instance Drude or Lorentz. The resulting expression is transformed back to time domain, which results in an explicit expression for time stepping of D, from which E can be computed for the next time step.

It should be mentioned here that we have used the commercial FDTD solver which can model dispersive material using different models with user specified parameters as well as fits to the experimental data of different metals.

2.3. Surface Plasmon Polaritons

In 1957, Ritchie predicted a special kind of surface wave that can exist at the interface between a metal and dielectric [29]. These waves were called surface plasmon polaritons (SPPs). The energy in this type of wave is shared between the electron charge density of the metal (plasmon) and the electromagnetic wave (photon) and is well confined to the surface. The electromagnetic fields decay exponentially in the transverse direction. The specific mode shape and decay rate is dependent on the material involved and geometry of the structures. The reason for the existence of such wave is the opposite sign of the dielectric constants of the two media involved i.e., metal and dielectric.

2.3.1. Single interface

Let us consider a metal dielectric interface as shown in Figure 2-2. The structure is invariant with respect to the *y* direction. By using Maxwell's equations and applying the necessary boundary conditions, we can derive the dispersion relation for the structure and the corresponding field profile. A typical surface plasmon wave on a single interface is shown in Figure 2-2 below.

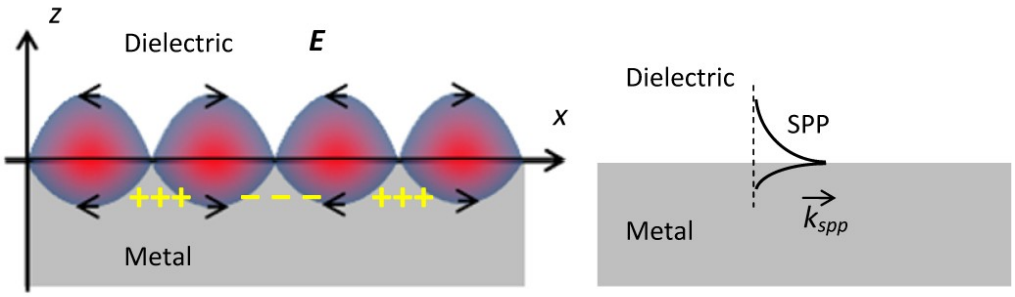

Figure 2-2: Electric field lines of a SPP wave on a single interface, the structure is invariant w.r.t *y* axis. A typical representation of SPP wave indicating field decay in the transverse direction.

Only transverse magnetic (TM) modes can exist due to the boundary conditions. The dispersion relation for a single interface is given as [30]

$$k_x = k_0 \sqrt{\frac{\varepsilon_m \varepsilon_d}{\varepsilon_m + \varepsilon_d}}; \tag{2.6}$$

where k_0 is the free space wave vector, ε_m and ε_d are the dielectric constants of metal and dielectric respectively. It can be seen that the propagation constant k_x tends to infinity as ε_m approached $-\varepsilon_d$ in case of negligible damping. This results in very large imaginary transverse wave vectors and the resulting wave is confined to the surface, decaying exponentially on both sides of the interface. Using a Drude fit for the dielectric constant of metal results in surface plasmon frequency where the propagation constant approaches infinity at

$$\omega_{sp} = \frac{\omega_p}{\sqrt{1+\varepsilon_m}}; \tag{2.7}$$

where ω_p is the bulk plasmon frequency of the metal. The dispersion relation of Eq. 2.5 is shown in Figure 2-3 for an interface between silver and two different dielectric media. For the case of real metal with complex dielectric constant, the denominator in Eq. 2.5 does not cancel out completely resulting in bending of the dispersion curve as shown below.

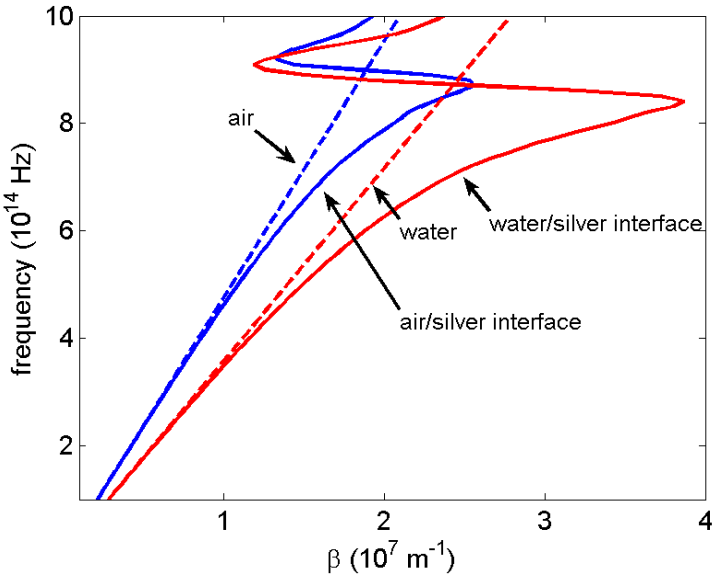

Figure 2-3: Dispersion relation for two different interfaces. Silver was modeled using the experimental data of Palik [31].

It is interesting to note that the dispersion curve is sensitive to the refractive index of the surrounding medium and it is exactly this property that is being exploited for the design of sensors.

2.3.2. Multiple Interfaces

More interesting is the case of two interfaces in close proximity such that the SPP waves on the two interfaces couple. This geometry can be further subdivided into two categories (a) metal insulator metal (MIM) structures and (b) insulator metal insulator (IMI) structures. Here we will only consider the case of symmetric structures where the superstrate and substrate have the same dielectric coefficient. For non-symmetric structures the reader is referred to [32].

Let us consider the case of IMI, two separate dispersion relations can be obtained that describe the symmetric and asymmetric modes [30]. Figure 2-4 shows the two modes and the corresponding dispersion curves. It is interesting to note that the confinement of the odd modes to the interface reduces as the metal film thickness is reduced, thus forming a long range surface plasmon (LRSP), whereas even modes exhibit the opposite behaviour. Their confinement increases to the interface as the thickness of the metal film is reduced and thus the propagation length is drastically reduced. These waves are referred to as short range surface plasmons (SRSP).

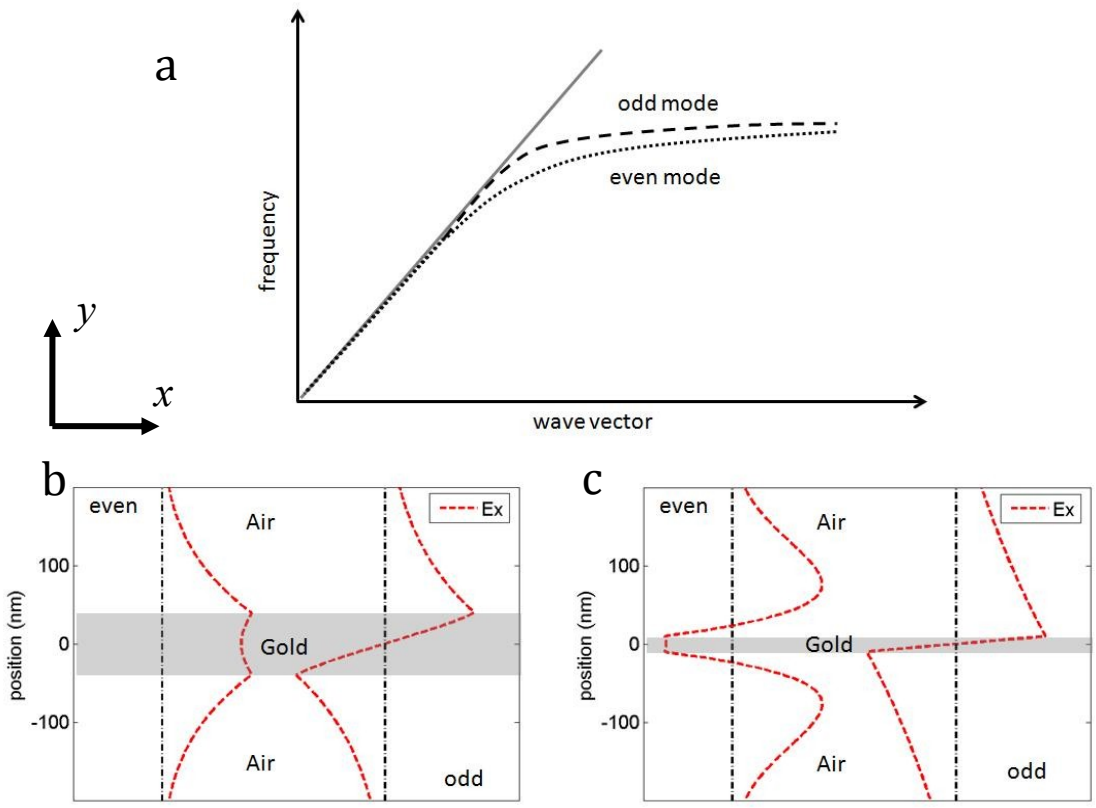

Figure 2-4: Dispersion curves for the odd and even modes supported by IMI structure along with the y-directed E field for metal film thickness of 80 nm and 20 nm. Gold was modeled by a fit to the experimental data of Johnson and Christy.

Considering MIM geometry, the most interesting mode is the fundamental odd mode which does not show cutoff as thickness of dielectric layer is reduced [32]. Further, very large wavenumbers can be produced even well below ω_{sp}, resulting in small penetration lengths into the metal. Figure 2-5 shows even and odd modes for dielectric slab thickness of 80 nm and 20 nm. The gold was modeled by a fit to the experimental data of Johnson and Christy [33].

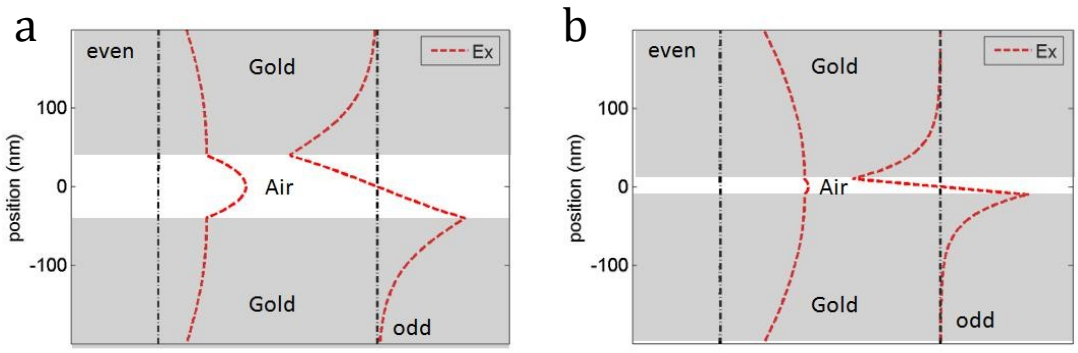

Figure 2-5: Even and odd modes supported by MIM structure for metal film thickness of 80 nm and 20 nm. Gold was modeled by a fit to the experimental data of Johnson and Christy.

2.3.3. SPP wave on a cylindrical nanorod

Cylindrical nanorods have been used in this work to serve as the dipole feed element of the nanoantenna, it is thus beneficial to discuss the SPP wave and the corresponding field configurations on a cylindrical nanostructure. Further, our work related to the self-assembly of NRs also deals with cylindrical structures. Field profile of the SPP wave in this geometry explains the reason for the poor performance of the side-by-side configuration as shown in Appendix F.

Consider a cylindrical NR of radius r as shown in Figure 2-6. It can be shown that the fields inside and outside of the metal core are represented by modified Bessel functions of first and second kind respectively. Matching the tangential field components at the boundary between metal and surrounding medium results in the following dispersion relation

$$\frac{K_0(p_d r)}{I_0(p_m r)} - \frac{\varepsilon_d p_m K_0'(p_d r)}{\varepsilon_m p_d I_0'(p_m r)} = 0; \tag{2.7}$$

where K_0 and I_0 are the modified Bessel functions $p_i^2 = k_{spp}^2 - \omega^2 \mu_0 \varepsilon_i$. For very small radius, the dispersion curve is very similar to that of IMI structure and there is no low frequency cut-off. It should be noted that resonance is determined by the length of the nanorod forming a Fabry Perot resonator.

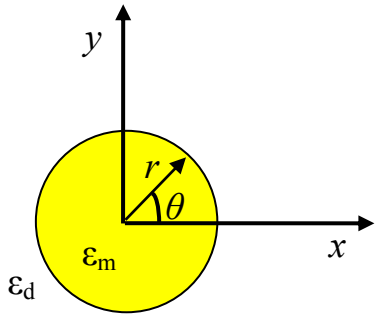

Figure 2-6: Cylindrical nanorod geometry.

2.4. Excitation of SPPs

It can be seen from the dispersion curves of Figures (2-3, 2-4), that the wavevector of the SPP is always larger in magnitude than that of the surrounding medium. This represents a mismatch of momentum; excitation of SPP at a planner interface thus requires special arrangements. Further, only TM waves can excite SPP considering the invariance of the planer geometry in the transverse direction. Several techniques have been devised for this purpose including total internal reflection coupling and grating coupling to account for the missing momentum.

2.4.1. Total Internal Reflection Coupling

The first method for the excitation of SPP is based on the total internal reflection of an incident wave on an interface between two different dielectric media. This method was introduced by Kretschmann and a schematic of this process is shown in Figure 2-7.

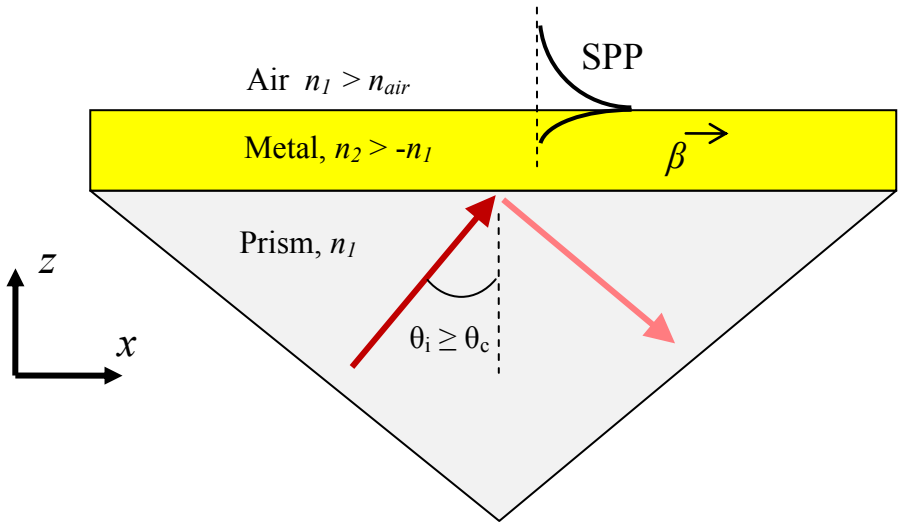

Figure 2-7: Kretschmann geometry for the excitation of SPP using total internal reflection.

Let us assume that the wave is incident on the interface from a medium of higher refractive index n_1, and let n_{air} be the index of the second medium (air) with $n_1 > n_{air}$. From Snell's law there exist a critical angle above which there is no transmitted wave in medium 2. At the critical angle the transmitted wave travels along the interface and thus represents the maximum possible in-plane propagation constant that could be achieved $(k_z = 0)$. For incident angles larger than the critical angle, k_z becomes evanescent, which results in $\beta > k_0$, thus making it possible to excite SPP.

2.4.2. Grating Coupling

The second method for the compensation of in-plane momentum is based on breaking the translational invariance by patterning a surface grating. It is important that the introduced perturbation (i.e. grating) must be small so that it does not change the SPP mode significantly. In other words, the grating thickness must be small as compared to its period Λ. This type of periodic perturbation does not completely breaks the translational symmetry but it allows for the addition and subtraction of integer multiple of $k_g = 2\pi / \Lambda$ to the original in-plane wave vector k_x. A schematic representation of this method is shown in Figure 2-8 below along with the application related to the EOT based sensing, where a change in the surrounding index causes a shift in the resonance wavelength.

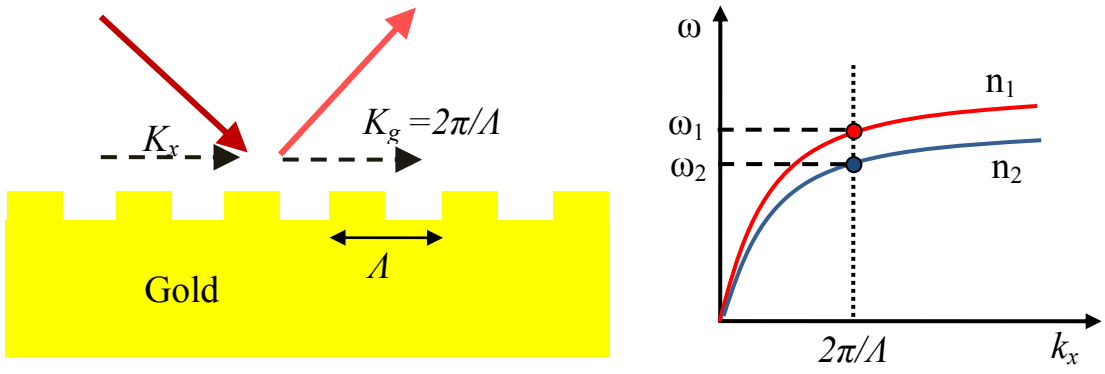

Figure 2-8: (a) SPP excitation using grating coupling. (b) Excitation using normal incidence and the shift in resonance due to index change.

2.5. Localized Surface Plasmons

For very small metallic particles the concept of translational invariance no longer applies and the modes cannot be described in terms of wave vectors as we did for the SPP. For particles of dimension smaller than the wavelength of the incident light the modes only exist for discrete frequency values. These modes are known as localized surface plasmon (LSP). The curved surface of the nanoparticle makes the excitation of LSP directly possible without the need for special phase matching techniques. Let us consider a spherical metallic nanoparticle as shown in Figure 2-9.

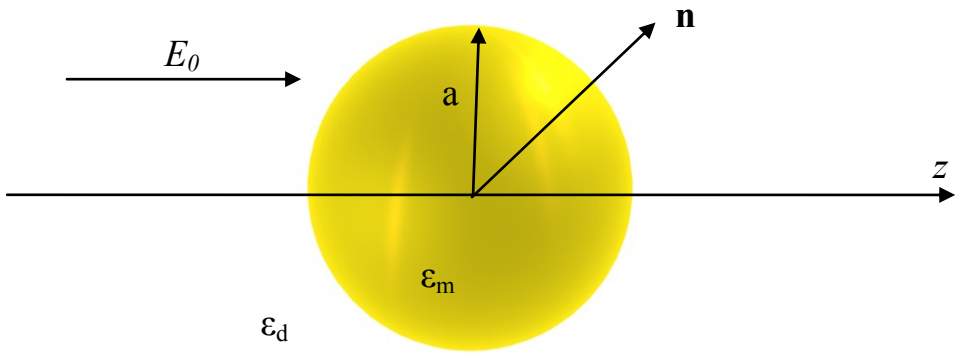

Figure 2-9: A spherical metallic nanoparticle of radius a placed in a constant electric field of magnitude E_0 and dielectric constant of the surrounding medium ε_d.

In the electrostatic approximation the fields can be derived using the Laplace equation, $\nabla^2\Phi = 0$, where Φ is the electric potential. The electric field can then be obtained from the gradient of potential as $E = -\nabla V$. This results in the following relations for the field inside and out of the sphere.

$$\mathbf{E_{in}} = \frac{3\varepsilon_d}{\varepsilon_m + 2\varepsilon_d}\mathbf{E_0}, \tag{2.8}$$

$$\mathbf{E_{out}} = \mathbf{E_0} + \frac{3\mathbf{n}(\mathbf{n}.\mathbf{p}) - \mathbf{p}}{4\pi\varepsilon_0\varepsilon_d r^3}; \tag{2.9}$$

where r is the radial distance of the point of observation from the center of the particle, E_0 is the magnitude of incident field, $\mathbf{n}$ is a unit vector in the direction of observation point, and $\mathbf{p}$ is the dipole moment given by

$$\mathbf{p} = 4\pi\varepsilon_0\varepsilon_d a^3 \frac{\varepsilon_m - \varepsilon_d}{\varepsilon_m + 2\varepsilon_d}\mathbf{E_0}; \quad (2.10)$$

where a is the radius of the nanoparticle [30]. From Eq. 2.10 we can see a resonant enhancement in the dipolar moment for the wavelength range where ε_m approaches $-2\varepsilon_d$. This resonant enhancement in turn enhances the fields both inside and out of the particle. In fact it is this field enhancement at the plasmon resonance on which a number of applications of optical devices rely.

2.6. Surface Enhanced Raman Spectroscopy

It is necessary to first introduce the Raman effect before SERS can be discussed. The Raman effect was discovered by Chandrasekhara Venkata Raman in 1921 [34]. What Raman observed was scattered radiation with higher energy as compared with the incident light. This process is now called anti-Stokes Raman scattering. The change in frequency is determined by the energy levels of the degrees of freedom of the molecule under investigation. Thus each type of molecule has a unique Raman spectrum and therefore Raman spectrum serves as a fingerprint of the molecule. Raman, unlike Rayleigh, is an inelastic process where the frequency of scattered light is either higher than the incident light (anti-Stokes) or lower than the incident light (Stokes). Scattering without change of frequency is called Rayleigh scattering.

The interaction of light with molecules is predominantly determined by the energy levels of the degrees of freedom of the molecule. These are either electronic (movement of electrons) or vibrational/rotational (movement of atoms in the molecule). The number of atoms in a molecule determines the degrees of freedom. An energy level diagram can be used to visualize these energy levels and serve as a convenient aid to understand the physical phenomena resulting in Raman effect, as shown in Figure 2-10 below. Raman scattering, unlike fluorescence, is an instantaneous process, whereas fluorescence on the other hand involves the absorption of a photon followed by the emission after a finite lifetime delay. Raman scattering can thus be viewed as simultaneous absorption and scattering. The absorption excites the molecule to a virtual state, which is followed by relaxation of the molecule to the ground state without any lifetime delay. It is not necessary for the incident photon to have the same energy as the transition energy from

ground to excited state. The concept of virtual state has no physical meaning; it is a convenient visualization tool to understand the scattering process especially when the incident photon has energy less then that required for the first possible transition. As the energy of incident photon approaches the transition energy we observe an increase in Raman cross-section. This phenomena is referred to as resonant Raman scattering. For further details the reader is referred to [35].

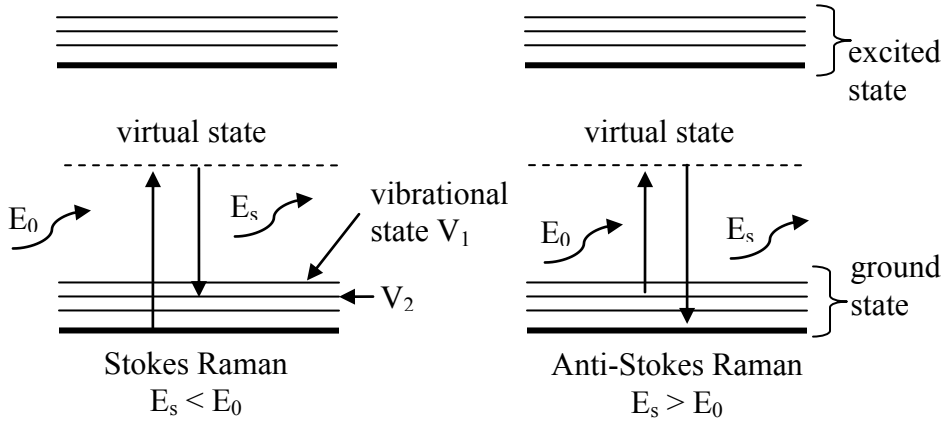

Figure 2-10: Energy diagram illustrating Stokes and anti-Stokes Raman scattering. The concept of virtual state has no physical meaning but it serves as a mathematical construction of perturbation theory.

The Raman spectrum contains considerably more information as compared to fluorescence. However, it suffers from extremely low efficiency with typical cross sections from 10^{-28} to 10^{-24} cm^2 per molecule as compared to 10^{-16} cm^2 for fluorescence.

It is thus necessary to enhance the inherently weak Raman signal. Surface plasmons provide the solution to this problem and the effect is commonly known as surface enhanced Raman Scattering (SERS). Since its discovery [36, 37], SERS has been used widely for enhancing the weak Raman cross section. SERS benefits from the high electric fields at the surface or in the gaps between closely spaced metallic nanoparticles. Assuming a broad spectral enhancement (approximately same enhancement at the excitation and stokes shifted wavelengths), the enhancement factor (EF) is commonly estimated as proportional to the fourth power of the ratio of the local electric field to the incident electric field. Initial experiments on single molecule SERS reported an EF of 10^{14} using colloidal silver nanoparticles [38, 39]. Different methods and substrates have

been devised to generate regions of high local electric fields, usually by confinement of light to sub-wavelength dimensions. These regions are referred to as hotspots [2, 40-42].

2.7. Extraordinary Optical Transmission

Subwavelength nanohole arrays have attracted considerable attention since the discovery of EOT [9]. Contrary to the prediction of Bethe's aperture theory, significantly higher transmission was observed through nanohole arrays in a metal film. According to Bethe's theory, the transmission through a single sub-wavelength hole scales as $(r/\lambda)^4$, where r is the radius of the hole. T. W. Ebbesen et. al. [9], demonstrated transmission efficiencies exceeding unity through sub-wavelength holes, when normalized to the surface area of the holes. It should be noted that Bethe's theory predicts an efficiency of approximately 10^{-3}.

It has been suggested that the observed high transmission is a consequence of SPPs excited by the periodic hole array [43] and the wavelength of transmission peak for the case of a square array can be estimated as

$$\lambda_{\max}(i,j) = \Lambda(i^2 + j^2)^{-1/2} \sqrt{\frac{\varepsilon_m \varepsilon_d}{\varepsilon_m + \varepsilon_d}}; \tag{2.11}$$

where Λ is the array period and i and j are integer numbers corresponding to different SPP modes. This relation has been derived using Eq. 2.5 and the in-plane wavenumber of grating coupling. It should be noted that this expression is only an approximation since it does not take into account scattering losses.

Recent studies have pointed out the possibility of localized waveguide modes playing important role in the high transmission through nanohole arrays [44, 45]. The illuminating light couples to the LSP and the nanohole forms a Fabry-Perot resonator, with a large electromagnetic field localized in each hole. This results in resonantly enhanced transmission through the hole. It should be noted that the transmission peak is mainly determined by the aperture geometry and is almost independent of the array periodicity.

As an illustration of EOT, Figure (2-11) shows the simulated transmission spectra of circular nanohole arrays in gold film over a glass substrate. The periodicity of the square array is 570 nm and the medium above the array is water. The vertical blue dashed line

shows the resonance peak predicted by Eq. 2.11 for the top interface (gold-water). It can be seen that the observed peak in transmission is slightly shifted to the red when compared to the prediction of Eq. 2.11. It should be noted that the hole radius of 130 nm is much smaller than the resonance peak wavelength of 850 nm.

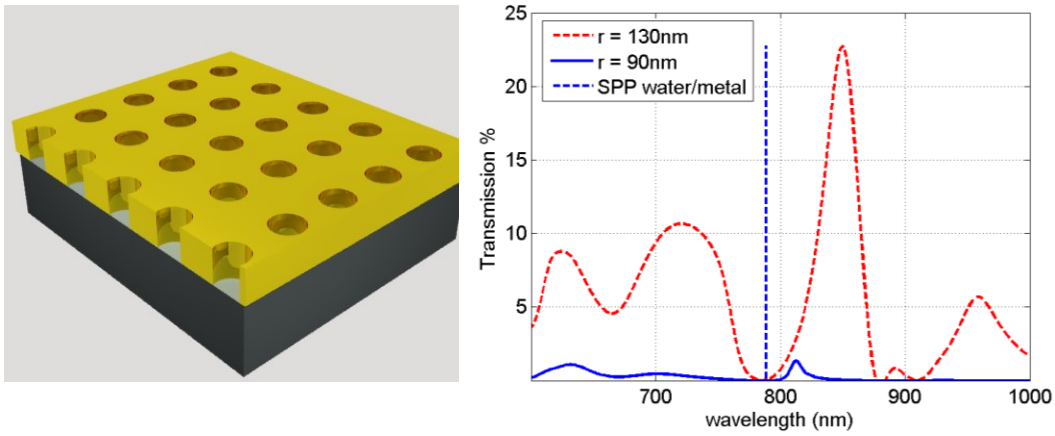

Figure 2-11: Transmission spectra of circular nanohole arrays in 300 nm thick gold film over a glass substrate. The periodicity of the square array is 570 nm and index of top medium is 1.33.

Eq. 2.11 indicates the dependence of resonance peak on the refractive index of the surrounding medium. We have exploited this property for the development of improved refractive index sensors.

Chapter 3

3 Contributions

This dissertation presents the results of eight studies organized under subsections from 3.1 to 3.8. These studies are described in detail in the manuscripts included as Appendices A through H. The projects considered here can be categorized as follows: (i) Design of top-down (focused ion beam milling) fabricated nanoantennas for spectroscopic applications. (ii) Study of self-assembled nanostructures for spectroscopic applications. (iii) EOT and improved sensing. (iv) Design of high index contrast gratings using CMT. (v) Determination of complex reflection coefficient from NRs terminations.

3.1. Design and Analysis of high index contrast gratings using Coupled Mode Theory (Appendix A)

Optical diffraction gratings have been used widely for applications including filtering, spectroscopy, lasers and biosensing. These gratings can function as a broadband mirror, filters or high quality cavity resonators. The HCG structure studied in this work is shown in Figure xxx along with the two higher order evanescent modes. HCG of refractive index n_2, thickness d and period Λ is surrounded by a low index medium. Forward and propagating modes are represented by amplitudes a_i and b_i respectively. The choice of a cosine wave expansion is motivated by the symmetry within the periodic structure.

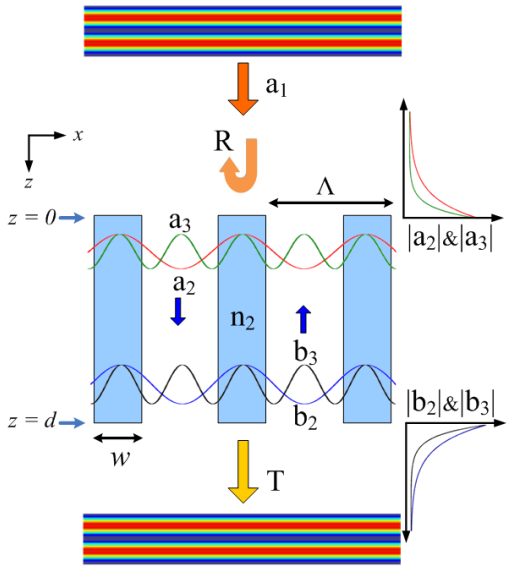

Figure 3-1: HCG geometry and the first two higher order evanescent modes.

The first objective of this study was to show that the behaviour of the gratings can be predicted using truncated coupled mode theory keeping only the first two higher order modes. This huge reduction in number of modes considerably simplifies the problem and provides further insight into the role each mode plays in the overall response of the structure. The second objective was to explore the possibility of using grating structures for refractive index sensors when they are operated as a very narrow band reflector. A slight change in the refractive index of the surrounding medium can affect the resonance and thus the transmission through the grating.

HCG differs from the conventional sub-wavelength gratings by the fact that the index of the grating structure is considerably higher than the surrounding material. The HCG was first proposed in 2004 [25], in the context of broadband mirrors, and since then has attracted considerable attention for the development of broadband high reflectivity mirrors to replace bulky Bragg reflectors.

In this work we have shown that in most cases retaining only the first two higher order modes predicts the response of the grating with high degree of accuracy. The results obtained by truncated CMT were in good agreement with the fully converged results obtained from RCWA and FDTD. Using CMT we were able to derive the following relationship for broadband operation

$$\beta_2^2 = \frac{-q}{(1+q)}\beta_1^2\left(1+\operatorname{sinc}\left(\frac{2\pi w}{\Lambda}\right)\right), \tag{3.1}$$

where β_1 and β_2 are the propagation constants of the first two modes, w and Λ are the width and period of the grating respectively, $q = \frac{(n_2^2 - n_1^2)w}{2\Lambda}$, n_1 and n_2 are the refractive indices of the surrounding medium and grating structure respectively.

HCG can also be used as a high Q resonator. Precise adjustment of the dimensions can lead to the condition that the average energy in the forward propagating modes is completely coupled into the backward propagating modes at the opposite interface of structure, over a very narrow band of frequencies. Such coupling mechanism prevents the leakage of electromagnetic energy from the grating structure, further the low loss material of the grating makes it a high Q resonator. It was observed that such high Q resonators require a larger number of modes for convergence (18 modes). Although

reduced CMT can predict the resonance wavelength but the quality factor cannot be accurately determined. The idea of using such structures as refractive index sensors was not followed any further mainly because of its limitations in terms of convergence. Detailed discussion can be found in Appendix A.

3.2. Antenna Design for DERS (Appendix B)

Here we describe the different designs considered for directive out of plane radiation. The different nanoantenna designs considered in this work lead to the development of the circular waveguide nanoantenna or cantenna. Cantenna design is described in detail in the next section and in Appendix C. In this work we present the details of the design steps leading to the cantenna design as well as a comparison of the different nanoantennas including the parabolic reflector nanoantenna.

Typically SERS substrates comprise of nanoparticles over a glass substrate. The high local fields on the surface of the nanoparticles results in enhanced Raman scattering. In terms of directivity, this is not an efficient design as most of the scattered light is radiated into the glass substrate due to its high refractive index. Efficiency of such design can be considerably improved by the introduction of a ground plane to coherently reflect the scattered light from a nanoparticle. The idea of ground plane was adopted from our previous work [46]. Over 50× enhancement in the observed Raman signal was reported. It is critical to place the feed element at a specific distance from the ground plane for in-phase reflections; this distance was found to be $\lambda/8$ where λ is the wavelength in the dielectric spacer.

Radiation patterns of different designs were investigated using far-field projections with FDTD simulations. Designs were compared by their corresponding beam efficiencies (BE)

$$BE = \frac{\int_0^{2\pi}\int_0^{\theta_0} p(\theta,\phi)\sin(\theta)d\theta d\phi}{P_{rad}}, \tag{3.2}$$

where P_{rad} is total radiated power given as

$$P_{rad} = \int_0^{2\pi}\int_0^{\pi} p(\theta,\phi)\sin(\theta)d\theta d\phi, \tag{3.3}$$

and $p(\theta,\phi)$ is the radiation pattern of the antenna obtained from the numerical simulations.

Parasitic elements are known to reflect or direct the radiation from a feed element as shown by the Yagi-Uda design. Therefore, two reflectors were introduced to reduce the beam width of the nanoantenna in one plane, resulting in improved BE. To restrict the beam width in the perpendicular plane another set of reflectors was introduced, forming a square waveguide like structure and simulation results showed even better BE. This motivated the design of a circular reflector and it was found that the circular reflector results in the best BE, producing a symmetrical beam out of the plane of substrate with half power beam width (HPBW) of 85 degrees in both planes.

The cantenna design produced 125× stronger Raman signal as compared to the signal obtained from nanoparticle over a glass substrate. In general, this design is very similar to the amateur radio cantenna design shown in Figure 3-2.

Figure 3-2: The cantenna used for boosting the range of wireless networks.

Another design considered in this work is that of a parabolic reflector nanoantenna. Raman experiments were carried out and it was shown that such an antenna can enhance the Raman signal by three orders of magnitude as compared to nanoprisms over glass substrate. The cantenna design was preferred for the single molecule Raman experiments due to the fact that the fabrication of parabolic reflector nanoantenna is more challenging. Further details are provided in Appendix B.

3.3. Directivity Enhanced Raman Spectroscopy using Nanoantennas (Appendix C)

Here we present the design of a top-down fabricated nanoantenna with the objective of obtaining directional radiation out of the plane and into the numerical aperture of the collecting lens. Improved directivity at optical wavelengths can have tremendous impact in areas such as optical microscopy, spectroscopy, sensing and applications involving single photon sources, where efficient collection and emission is critical. The motivation for this work was to extend the concept of directivity to the visible/NIR regime of the spectrum.

Although Yagi-Uda equivalent nanoantenna designs have been demonstrated recently [47-49], these designs suffered from the fact that the main beam was directed into the substrate and thus could not be used readily with a typical microscope setup.

It should be noted that the nanoantenna design is affected by the plasmonic properties of the metal and thus microwave designs cannot be simply scaled down to operate in the visible regime. As an example, the dipole feed element of our design, having a total length of 130 nm, radiates resonantly at a free space wavelength of 840 nm. This length is considerably shorter in comparison to its microwave counterpart (the half-wavelength dipole).

The proposed design uses a center fed dipole element as the main feed element and a ground plane reflector to prevent loss of scattered light into the substrate and also reinforce the local fields at the feed which is desirable for SERS experiments. The use of a ground plane has also been adopted from microwave antenna design.

The use of ground plane ensures out of plane radiation but with a very broad beam in the lateral plane (along the surface of the substrate). A circular in-plane reflector was introduced to reshape the beam and thus allows for the collection of almost all of the scattered light. The ring-reflector acts to create a lateral standing wave that reflects light back towards the central dipole antenna structure. It is interesting to note that the optimized directivity is observed when the radius of the ring reflector is equal to 250 nm for the nanoantenna designed to operate at a wavelength of 840 nm. This is most similar to a circular waveguide, which has a lateral resonance when the wavelength is 3.4 times the radius of the circular waveguide (i.e., at the lowest order mode cut-off). This

corresponds to a resonance at 250 nm, which is precisely the radius value that was found to give the greatest DERS in the experiments.

The circular reflector is an important feature of the nanoantenna design because it allows for an additional 5.5× enhanced Raman as compared to just using the ground plane alone. This enhancement is almost entirely attributed to directivity effects with only a small contribution from local field enhancement. Further details are provided in Appendix C.

3.4. Single Molecule Directivity Enhanced Raman Scattering using Nanoantennas (Appendix D)

This work demonstrates the detection of single molecules using the cantenna design presented in Sections 3.2 and 3.3. In this work we have used the technique of bi-analyte [50] to verify the single molecule nature of the observed Raman signal.

The Raman process is inherently extremely inefficient, with typical cross sections from 10^{-28} to 10^{-24} cm^2 per molecule [51, 52], as compared to 10^{-16} cm^2 for fluorescence [53]. To observe the vibration spectrum of single molecules, it is thus necessary to generate an enhancement factor of 10^8 (for resonant Raman) to 10^{12} for ordinary Raman.

The single molecule limit is the ultimate sensitivity desired for many scientific and applied areas, such as sensing, analytical chemistry and biomedicine [54, 55]. It is shown for the first time that the huge enhancement required for detecting the vibrational spectrum of single molecules is achievable from a top-down fabricated structure. Previously reported fabricated structures resulted in enhancement factors that were smaller than the required enhancement factor by two orders of magnitude [56, 57]. The directivity of the nanoantenna provides the additional enhancement and allows for the detection of Raman spectrum of single molecules. In past either colloidal solutions or random structures were used for the detection of single molecule using SERS [39, 41]. Less than 1% of the total sites in those structures provide enough enhancements required for single molecule detection.

The single hotspot (feed gap) of our design prevents the problem of spatial averaging. Previously used approaches for detecting single molecules suffer from the presence of a number of hotspots in the probed volume. Thus it is difficult to say that the observed signal is indeed from a single molecule or a number of molecules in different hotspots.

A fundamental challenge regarding single molecule experiments is the differentiation of single molecule signal (Raman spectrum) from that of multiple molecules. K. Kneipp et al., [38] proposed a quantification method depending on the Raman signal strength. Recent studies have questioned this approach and have argued that temporal fluctuations in Raman signal are not sufficient evidence of single molecule sensitivity; as Raman signal is not quantized [58].

Here we have used two different Raman dyes (i) Nile Blue A (NBA) and (ii) Rhodamine 6G (R6G) to statistically prove the single molecule nature of the observed signal. The bi-analyte method requires the collection of sufficiently large number of spectra from the sample. Each spectrum represents an event and each event can be characterized as NBA event, R6G event, mixed event or a null event. The resulting probability distribution shows a transition from majority mixed events to single molecule events, as the dye concentration is gradually reduced. When the dye concentration is low, it is very unlikely that two or more molecules will be present in the hotspot. This is also verified by the probability distribution where very few mixed events are registered. Thus it can be claimed that a vast majority of the single dye events are indeed single molecule events with a few events of more than one molecule of same type.

FDTD simulations and Raman experiments verified the single molecule sensitivity. Also, we were able to show the Raman intensity distribution of single molecules and it was verified that the distribution follows a long tail nature (truncated Pareto) [59, 60]. Our results indicated the adsorption of the dye molecule to gold surface lasting for typically a few seconds indicating that the process is reversible. For more details please see Appendix D.

3.5. End-to-End Self-Assembled Nanorods for SERS (Appendix E)

The main objective of this study was to design and develop an improved platform based on self-assembly of NRs for spectroscopic applications. We also studied the hotspots (high electric field regions) created between the tips of adjacent nanorods as a function of time, while the nanorods are allowed to assemble in an end-to-end manner forming a chain.

The extinction spectrum of an isolated NR exhibits two resonant peaks, longitudinal and transverse. The length of the rod determines the longitudinal resonance. Considering

the end-to-end assembly, we are mainly interested in the longitudinal resonance. NRs can be modeled as Fabry Perot resonators and the hemispherical termination serves as a mirror with complex phase of reflection. Resonance is observed when the length of the nanorod equals half a SPP wavelength, assuming a weak wavelength dependence of the phase of reflection.

When gold NRs are assembled into an end-to-end formation, coupling of alternating dipoles along the chain occurs resulting in a red shift of the longitudinal resonance. This results in the formation of a periodic array of hotspots in the spaces between adjacent NR ends. The shift in resonance affects the Raman enhancement factor which goes as the forth power of the local electric field at excitation and Stokes shifted wavelengths. The self-organization of gold NRs offers a tool for the generation of controlled hotspots for enhanced Raman spectroscopy. Possible applications include spectroscopy and sensing [61-63].

Constructive coupling between adjacent NRs is expected to produce stronger hotspots. It is interesting to note that the electric field strength in the hotspot increased as the chain grew from one (monomer) to three rods (trimer) per chain. Further increase in chain length showed reduction in field strength. This effect originated from the trade-off between the local field enhancement and optical absorption (that is, loss) in the NR chains. A figure of merit that compares the local field enhancement to the loss is the ratio between the real and imaginary parts of the relative permittivity of the NRs. For gold, this figure of merit is at its maximum at ~770 nm, which was close to the resonance wavelength of the trimer.

We also studied angled configurations of NRs. A significant reduction in field intensity and extinction cross section was observed for non-collinear configurations. Therefore the greatest contribution in extinction and SERS arose from co-linear chains, with a minor influence on E field intensity from off-axis NRs. Details of this work are presented in Appendix E.

3.6. Side-by-Side Self-Assembled Nanorods for SERS (Appendix F)

This work presents the study of gold NRs assembled in side-by-side assembly. The main observation of this work is that not all geometries of nanoparticles result in field enhancement. In the side-by-side configuration, the dominant radial electric field

component of the SP mode undergoes significant reduction in magnitude due to destructive interference.

We show numerically using mode solutions that as the number of NRs increases the effective index (n_{eff}) of the system decreases thus reducing the propagation constant. Reduction in n_{eff} had to be compensated by a proportional amount of reduction in the resonant wavelength. Therefore, a blue shift is expected to occur as the number of NRs aligned in side-by-side manner increases. We also investigated the 3D stacks of NRs arranged in a side-by-side manner and observed a similar trend of reduction of the electric field. SERS experiments were performed and a good agreement with the numerical results was demonstrated. For further details see Appendix F.

3.7. Optimizing the Resolution of Nanohole Arrays in Metal Films for Refractive Index Sensing (Appendix G)

In this work the concept of EOT has been exploited for the development of refractive index sensors. For improved resolution we focused on the optimization of the following factors that play an important role in determining the sensitivity of the sensor; (i) Nanohole array parameters such as metal film thickness, periodicity and hole diameter, (ii) Noise in the system, (iii) Laser excitation wavelength and (iv) Efficiency of the detecting camera.

Resolution is defined as the smallest change in refractive index that the sensor can detect and is limited mainly by the noise of the system. A bulk resolution of 6×10^{-7} RIU was demonstrated which is comparable to the state of the art commercial SPR sensor with resolution of 1×10^{-7} RIU [64]. The design presented here is much simpler and allows for multiplexed detection. These results are encouraging for biosensing applications [65, 66].

Nanohole arrays were fabricated using focused ion beam (FIB) milling in gold layers of different thicknesses (100 nm, 300 nm and 500 nm) over a glass substrate. For measuring change in intensity due a change in the index of refraction we used a microfluidic flow channel which consisted of a polydimethylsiloxane (PDMS) microchip made by rapid prototyping lithography [67].

Comprehensive FDTD simulations were carried out to optimize the required periodicity, thickness and nanohole size; keeping in view the optimal sensitivity of the CCD camera used in this experiment (~600 nm). Such an optimization allows for higher

photon collection efficiency, and therefore low signal-to-shot-noise ratio. Metal film thickness was also studied and it was observed that thicker films (300-500 nm) result in better sensitivity. In practice, however, we are limited by the ability to make high-aspect nanoholes in thick films and the duration of milling. Therefore, we did not attempt films thicker than 500 nm. Details of this work are presented in Appendix G.

3.8. Relating Localized Nanoparticle Resonances to an Associated Antenna Problem (Appendix H)

The objective of this work was to study the complex reflection coefficient from arbitrary terminations of NRs, specially the simplest case of a circular rod with a hemispherical termination. This work was carried out in collaboration with Dr. S. B. Hasan from the institute for condensed matter theory and solid state optics in Jena, Germany.

The phase of reflection from the ends of NRs has been a subject of study for some time, and recently the phase of reflection from flat ended NRs was calculated [68]. Only numerical solutions for the phase of reflection from hemispherical terminations are available to date. It was the intention of this work to study the phase of reflection and its effect on the resonance of nanowire antennas. Further, an attempt was made to derive a simple analytical relation for the phase of reflection from such terminations, using the law of power conservation.

Silver nanorods with radius smaller than 10 nm were considered. Numerically calculated reflection coefficient from a hemispherical termination shows almost complete reflection of the incident energy with nearly zero phase of reflection at longer wavelengths. As wavelength approaches the surface plasmon wavelength the magnitude of reflection falls drastically along with a gradual increase in the phase. Knowledge of the phase of reflection can aid in the determination of resonance wavelength of a nanoparticle. It is thus proposed that the localized surface plasmon resonance occurs at frequencies where the phase of reflection of propagating surface wave approaches π. Excellent agreement has been demonstrated regarding the resonant wavelength of different nanoparticles and the ones predicted by the SPP model. Details are provided in Appendix H.

For the derivation of an analytical solution, we begin by calculating the fundamental mode of the NR. The resulting field is then used for the calculation of absorption and scattering from a sphere of same radius as the NR. The law of power conservation is then invoked which requires $P_{inc} = P_{abs} + P_{scat} + P_{ref}$ where $P_{inc}, P_{abs}, P_{scat}$ and P_{ref} are the incident, absorbed, scattered and reflected powers respectively. Our analytical solutions produced similar trends as the numerical simulations but failed to provide a good quantitative agreement, especially towards the longer wavelengths where the analytical results showed a unity reflection coefficient. Therefore, these analytical results were not included in the final manuscript. The disagreement is attributed to the fact that the scattering and absorption of a hemisphere are approximated by half of that of a full sphere.

Chapter 4

4 Summary, Conclusions and Future Work

4.1. Summary and Conclusions

The work presented in this dissertation focuses on the design of nanometer scale structures for enhanced spectroscopic and sensing applications. Plasmonic properties of metallic nanostructures have been explored for different applications presented in this work.

One of the achievements of this work is the demonstration of single molecule Raman sensitivity from top-down fabricated nanoantenna design. This design can prove very useful in applications involving sensing and biomedicine. We introduced the idea of DERS which is different from the traditional Raman enhancement resulting from local field effects. DERS provides an additional two orders of magnitude enhancement and thus pushes the limit of sensitivity to the single molecule regime. The DERS design presented has the main radiation lobe out of the plane and therefore it is well suited for typical microscope setups. For single molecule sensing our design has the important advantage of minimized spectral averaging effect as compared to the previously used method of colloidal solutions or random structures. Our results indicated the adsorption of the dye lasting for typically a few seconds indicating that the process is reversible.

The self-assembled geometries considered in this work shed light on the optical properties of ensemble of nanorods and their possible applications regarding spectroscopy. It is shown that end-to-end assembly of NRs results in higher local fields thus proving a desirable configuration for SERS. Side-by-side configuration of NRs suffers from the destructive interference of the radial component of the SPP mode, resulting in poor performance. Considering end-to-end assembly, our results show an intensity enhancement of 4000× due to the very small gaps between neighbouring NRs. This means an enhancement of 10^7 which is approaching the required enhancement for single molecule resonant Raman detection.

Another achievement of this work is the demonstration of an extremely sensitive nanohole array sensor. The observed resolution of 6×10^{-7} is comparable to the state of the art commercial sensor available today. Furthermore, our substrate based design allows for

multiplexed detection. Resolution was improved by optimizing the operation wavelength, array dimensions, system noise and consideration of the detector sensitivity. Our experimental and simulation results indicated an improved resolution for thicker films (300 nm, 500 nm) as compared to 100 nm thick gold films. This might be attributed to the exponential decay of waveguide mode inside the nanohole.

We also presented a simple and insightful method of reduced coupled mode theory for the design and analysis of grating structures. It is shown that in most non-resonant cases only three modes are sufficient to predict the response of the structure with high accuracy. This led to the derivation of design guidelines for broadband operations. In case of resonant operation, more modes need to be considered for convergence. It was also shown that even for the case of resonant grating structures, reduced CMT can be used for optimization purposes.

Finally the phase of reflection from arbitrary terminated NRs has been investigated. The calculated phase of reflection has been verified by comparison with the LSP resonance of different nanoparticles. Knowledge of the phase of reflection can prove to be useful for the design of nanoantennas.

4.2. Future Work

Regarding the directive radiation from nanoantennas, an interesting project for future work would be the investigation of antenna arrays. Translation of antenna array concepts from microwave antenna theory can lead to improved sensing at optical wavelengths. Our work of single molecule detection using a single nanoantenna required slightly higher analyte concentration comparing to the previous works on SM detection. For situations where lower analyte concentrations are unavoidable, the antenna arrays can provide a possible solution. We demonstrated the nanoantenna design for Raman experiments. Future work can be directed towards the practical application of this design in the field of biosensing.

Our work related to the self assembly of nanorods indicated sufficiently large Raman enhancement factors to consider the detection of single molecules via resonant Raman scattering. Future work could explore other geometries for higher local field enhancements and can also explore hybrid metal-insulator structures for the said purpose.

Sensing based of EOT through subwavelength arrays is a promising area for future research. The influence of hole shape needs further investigation. Our preliminary results on elliptical nanoholes indicated the possibility of improved sensing.

Another possible theoretical project would be the calculation of phase of reflection from nanorod terminations. The method of single mode match can be used for this purpose. In this method the nanorod termination is divided into a number of very short segments of constant cross section. The method of mode matching (using only one mode) is then applied at the intersection between two neighbouring segments for the determination of the complex reflection coefficient.

Bibliography

[1] P. Bharadwaj, *et al.*, "Nanoscale spectroscopy with optical antennas," *Chemical Science,* vol. 2, pp. 136-140, 2011.

[2] A. Ahmed and R. Gordon, "Directivity Enhanced Raman Spectroscopy Using Nanoantennas," *Nano Letters,* vol. 11, pp. 1800-1803, Apr 2011.

[3] K. Kneipp, *et al.*, *Surface-enhanced Raman scattering physics and applications*. New York: Springer, 2006.

[4] M. G. Banaee and K. B. Crozier, "Mixed Dimer Double-Resonance Substrates for Surface-Enhanced Raman Spectroscopy," *ACS Nano,* vol. 5, pp. 307-314, 2011/01/25 2010.

[5] E. Betzig and R. J. Chichester, "Single Molecules Observed by Near-Field Scanning Optical Microscopy," *Science,* vol. 262, pp. 1422-1425, November 26, 1993 1993.

[6] M. Futamata, *et al.*, "Microscopic morphology and SERS activity of Ag colloidal particles," *Vibrational Spectroscopy,* vol. 30, pp. 17-23, 2002.

[7] S. Kuhn, *et al.*, "Enhancement of single-molecule fluorescence using a gold nanoparticle as an optical nanoantenna," *Physical Review Letters,* vol. 97, Jul 7 2006.

[8] M. Vala, *et al.*, "High-performance compact SPR sensor for multi-analyte sensing," *Sensors and Actuators B: Chemical,* vol. 148, pp. 544-549, 2010.

[9] T. W. Ebbesen, *et al.*, "Extraordinary optical transmission through sub-wavelength hole arrays," *Nature,* vol. 391, pp. 667-669, 1998.

[10] J. Homola, *Surface Plasmon Resonance Based Sensors*. New York: Springer, 2006.

[11] A. Ahmed and R. Gordon, "Single Molecule Directivity Enhanced Raman Scattering using Nanoantennas," *Nano Lett.,* vol. 12, pp. 2625-2630, 2012.

[12] H. G. Frey, *et al.*, "High-Resolution Imaging of Single Fluorescent Molecules with the Optical Near-Field of a Metal Tip," *Physical Review Letters,* vol. 93, p. 200801, 2004.

[13] H. A. Atwater and A. Polman, "Plasmonics for improved photovoltaic devices," *Nature Materials,* vol. 9, pp. 205-213, 2010.

[14] K. Nakayama, *et al.*, "Plasmonic nanoparticle enhanced light absorption in GaAs solar cells," *Applied Physics Letters,* vol. 93, pp. 121904-3, 2008.

[15] R. Corkish, *et al.*, "Solar energy collection by antennas," *Solar Energy,* vol. 73, pp. 395-401, 2002.

[16] J. Kim, *et al.*, "A single-photon turnstile device," *Nature,* vol. 397, pp. 500-503, Feb 11 1999.

[17] B. Lounis and W. E. Moerner, "Single photons on demand from a single molecule at room temperature," *Nature,* vol. 407, pp. 491-493, Sep 28 2000.

[18] R. A. Shelby, *et al.*, "Experimental Verification of a Negative Index of Refraction," *Science,* vol. 292, pp. 77-79, April 6, 2001 2001.

[19] V. G. Veselago and E. E. Narimanov, "The left hand of brightness: past, present and future of negative index materials," *Nature Materials,* vol. 5, pp. 759-762, 2006.

[20] F. Kneubühl, "Diffraction Grating Spectroscopy," *Appl. Opt.,* vol. 8, pp. 505-519, 1969.
[21] G. A. De Biase*, et al.*, "Spectroscopy by Grating Synthesis," *Appl. Opt.,* vol. 11, pp. 1163-1168, 1972.
[22] K. T. V. Grattan and B. T. Meggitt, *Optical fiber sensor technology, advanced applications, Bragg gratings and distributed sensors*. Boston: Kluwer academic, 2000.
[23] C.-L. Chang*, et al.*, "In situ assembled diffraction grating for biomolecular detection," *Applied Physics Letters,* vol. 90, pp. 233901-3, 2007.
[24] Y. Kanamori*, et al.*, "High efficient light-emitting diodes with antireflection subwavelength gratings," vol. 14, pp. 1064-1066, 2002.
[25] C. F. R. Mateus*, et al.*, "Ultrabroadband mirror using low-index cladded subwavelength grating," vol. 16, pp. 518-520, 2004.
[26] W.-P. Huang and J. Mu, "Complex coupled-mode theory for optical waveguides," *Opt. Express,* vol. 17, pp. 19134-19152, 2009.
[27] K. S. Yee, "Numerical solutions of initial boundary value problems involving Maxwell's equations in isotropic media," *IEEE Trans. Antennas and Propagation,* vol. 14, pp. 302-307, 1966.
[28] A. Taflove, *Computational Electrodynamics*. Norwood, MA: Artech House, 1995.
[29] R. H. Ritchie, "Plasma Losses by Fast Electrons in Thin Films," *Physical Review,* vol. 106, pp. 874-881, 1957.
[30] S. A. Maier, *Plasmonics fundamentals and applications*. New York: Springer, 2007.
[31] E. D. Palik, *Handbook of Optical Constants of Solids*. San Diego: Academic Press, 1998.
[32] B. Prade*, et al.*, "Guided optical waves in planar heterostructures with negative dielectric constant," *Physical Review B,* vol. 44, pp. 556-572, 1991.
[33] P. B. Johnson and R. W. Christy, "Optical Constants of the Noble Metals," *Physical Review B,* vol. 6, pp. 4370-4379, 1972.
[34] C. V. Raman and K. S. Krishnan, "A new type of secondary radiation," *Nature,* vol. 121, pp. 501-502, 1921.
[35] D. A. Long, *The Raman effect*. Chichester: John Wiley and sons, 2002.
[36] M. G. Albrecht and J. A. Creighton, "Anomalously intense Raman spectra of pyridine at a silver electrode," *J. Am. Chem. Soc.,* vol. 99, pp. 5215-5217, 1977/06/01 1977.
[37] D. L. Jeanmaire and R. P. Vanduyne, "Surface Raman Spectroelectrochemistry .1. Heterocyclic, Aromatic, and Aliphatic-Amines Adsorbed on Anodized Silver Electrode," *J. Electroanal. Chem.,* vol. 84, pp. 1-20, 1977.
[38] K. Kneipp*, et al.*, "Single molecule detection using surface-enhanced Raman scattering (SERS)," *Phys. Rev. Lett.,* vol. 78, pp. 1667-1670, 1997.
[39] S. Nie and S. R. Emory, "Probing Single Molecules and Single Nanoparticles by Surface-Enhanced Raman Scattering," *Science,* vol. 275, pp. 1102-6, Feb 21 1997.
[40] M. Moskovits, "Surface-Roughness and Enhanced Intensity of Raman-Scattering by Molecules Adsorbed on Metals," *J. Chem. Phys.,* vol. 69, pp. 4159-4161, 1978.

[41] H. W. Liu, *et al.*, "Single molecule detection from a large-scale SERS-active Au(79)Ag(21) substrate," *Sci. Rep.,* vol. 1, 2011.
[42] Y. Fang, "Measurement of the distribution of site enhancements in surface-enhanced Raman scattering (vol 321, pg 388, 2008)," *Science,* vol. 322, pp. 1790-1790, Dec 19 2008.
[43] J. A. Porto, *et al.*, "Transmission resonances on metallic gratings with very narrow slits," *Physical Review Letters,* vol. 83, 1999.
[44] K. J. K. Koerkamp, *et al.*, "Strong Influence of Hole Shape on Extraordinary Transmission through Periodic Arrays of Subwavelength Holes," *Physical Review Letters,* vol. 92, p. 183901, 2004.
[45] K. L. van der Molen, *et al.*, "Role of shape and localized resonances in extraordinary transmission through periodic arrays of subwavelength holes: Experiment and theory," *Physical Review B,* vol. 72, p. 045421, 2005.
[46] Q. A. Min, *et al.*, "Substrate-based platform for boosting the surface-enhanced Raman of plasmonic nanoparticles," *Optics Express,* vol. 19, pp. 1648-1655, Jan 17 2011.
[47] A. G. Curto, *et al.*, "Unidirectional Emission of a Quantum Dot Coupled to a Nanoantenna," *Science,* vol. 329, pp. 930-933, Aug 20 2010.
[48] T. Pakizeh and M. Kall, "Unidirectional Ultracompact Optical Nanoantennas," *Nano Letters,* vol. 9, pp. 2343-2349, Jun 2009.
[49] T. H. Taminiau, *et al.*, "Enhanced directional excitation and emission of single emitters by a nano-optical Yagi-Uda antenna," *Opt. Express,* vol. 16, pp. 10858-10866, Jul 7 2008.
[50] P. G. Etchegoin, *et al.*, "Statistics of single-molecule surface enhanced Raman scattering signals: Fluctuation analysis with multiple analyte techniques," *Anal. Chem.,* vol. 79, pp. 8411-8415, Nov 1 2007.
[51] S. M. Nie and S. R. Emery, "Probing single molecules and single nanoparticles by surface-enhanced Raman scattering," *Science,* vol. 275, pp. 1102-1106, Feb 21 1997.
[52] S. Shim and R. A. Mathies, "Development of a tunable femtosecond stimulated Raman apparatus and its application to beta-carotene," *J. Phys. Chem. B,* vol. 112, pp. 4826-4832, Apr 17 2008.
[53] N. P. W. Pieczonka and R. F. Aroca, "Single molecule analysis by surfaced-enhanced Raman scattering," *Chem. Soc. Rev.,* vol. 37, pp. 946-954, 2008.
[54] J. K. T. X. S. Xie, "Optical studies of single molecules at room temperature," *Annu. Rev. Phys. Chem.,* vol. 49, 1998.
[55] F. Kulzer and M. Orrit, "Single-molecule optics," *Annu. Rev. Phys. Chem.,* vol. 55, pp. 585-611, 2004.
[56] F. Hao, *et al.*, "Plasmon resonances of a gold nanostar," *Nano Lett.,* vol. 7, pp. 729-732, Mar 2007.
[57] C. L. Nehl, *et al.*, "Optical properties of star-shaped gold nanoparticles," *Nano Lett.,* vol. 6, pp. 683-688, Apr 2006.
[58] P. G. Etchegoin, *et al.*, "Statistics of single molecule SERS signals: is there a Poisson distribution of intensities?," *Phys. Chem. Chem. Phys.,* vol. 9, pp. 3006-3010, 2007.

[59] L. Zaninetti and M. Ferraro, "On the truncated Pareto distribution with applications," *Cent. Eur. J. Phys.,* vol. 6, pp. 1-6, Mar 2008.
[60] E. C. Le Ru*, et al.*, "Surface Enhanced Raman Scattering Enhancement Factors: A Comprehensive Study," *The Journal of Physical Chemistry C,* vol. 111, pp. 13794-13803, 2007/09/01 2007.
[61] L. V. Brown*, et al.*, "Heterodimers: Plasmonic Properties of Mismatched Nanoparticle Pairs," *Acs Nano,* vol. 4, pp. 819-832, 2010.
[62] S. H. Sun and C. B. Murray, "Synthesis of monodisperse cobalt nanocrystals and their assembly into magnetic superlattices (invited)," *Journal of Applied Physics,* vol. 85, pp. 4325-4330, Apr 1999.
[63] J. W. Liu and Y. Lu, "A colorimetric lead biosensor using DNAzyme-directed assembly of gold nanoparticles," *Journal of the American Chemical Society,* vol. 125, pp. 6642-6643, 2003.
[64] *Biacore, www.biacore.com*.
[65] C. Escobedo*, et al.*, "Flow-through vs flow over: Analysis of transport and binding in nanohole array plasmonic biosensors," *Anal. Chem.,* vol. 82, 2010.
[66] W. L. Barnes*, et al.*, "Surface plasmon subwavelength optics," *Nature,* vol. 424, pp. 824-830, 2003.
[67] D. C. Duffy*, et al.*, "Rapid prototyping of microfluidic systems in poly(dimethylsiloxane)," *Anal. Chem.,* vol. 70, 1998.
[68] R. Gordon, "Reflection of Cylindrical Surface Waves," *Opt. Express,* vol. 17, 2009.

Appendix A: Design and Analysis of High Index Contrast Gratings Using Coupled Mode Theory

(2010, IEEE Photonics Journal, volume 2, pp 884-893)

Design and Analysis of High Index Contrast Gratings Using Coupled Mode Theory

Aftab Ahmed, Marco Liscidini and Reuven Gordon, *Senior Member, IEEE*

[1,3]*Department of Electrical and Computer Engineering, University of Victoria, Victoria, BC V8W 3P6, Canada*

[2]*Department of Physics "A. Volta", University of Pavia via Bassi, 6, 27100 Pavia, Italy*

Abstract: We analyze high refractive index contrast sub-wavelength grating structures using truncated coupled mode theory (CMT). CMT not only provides physical insight into the role of each mode in the overall response, but also allows for improved design. An analytic expression is derived for the design of broadband reflectors, providing a near-optimal design, within 0.08% of the maximum broadband reflectivity calculated by the finite difference time domain method. Furthermore, the CMT is used to design a high-quality narrowband reflector with 28% improved quality factor over previously reported results, as quantified by rigorous coupled wave analysis.

Index Terms: Photonic materials and Engineered photonic structures, Theory and design, Engineered photonic nanostructures, Subwavelength structures.

Introduction

Coupled mode theory (CMT) has been widely used for analysis of guiding structures in the optical regime for predicting the effects of periodic perturbations (periodic in the longitudinal/transverse directions) in an otherwise perfect guide [1]. Since its first introduction in early 1950s for microwave devices [2], CMT has experienced a long series of developments and by the early seventies it was applied to optical devices [3-4]. The method is rigorous if all modes are included and CMT can yield extremely accurate results even if a small subset of the modes is retained; however, CMT can be more efficient than other methods, such as rigorous coupled wave analysis (RCWA) or finite difference time domain (FDTD), by selecting the appropriate modal expansion. Furthermore, CMT is not limited to periodic boundaries, and can be applied quite generally; for example, recently, perfectly matched layer (PML) has been introduced into

the formalism of CMT to simulate an unbounded geometry by discretizing continuous radiation modes while having negligible effect on the bound guided modes [5].

Optical diffraction gratings have been studied for years for their applications in filtering, spectroscopy [6-8], lasers and other optoelectronic devices [9-10]. Recently, these structures were employed for bio-sensing applications as well [11]. Gratings with period smaller then the incident wavelength are referred to as sub-wavelength gratings, as a result all higher order modes are evanescently bound, which leads to interesting effects. Typical applications include reflectors for vertical cavity surface emitting lasers (VCSELs) [12-14], high efficiency light emitting diodes [15], and ultra broadband mirrors [16]. High-index-contrast gratings (HCGs), also known as suspended gratings, differ from the conventional sub-wavelength gratings by the fact that the grating structure is surrounded by a low index material. The HCG was first proposed in 2004 [16-17] and since then has attracted attention for the development of broadband high reflectivity mirrors due to the high index contrast in the in-plane direction. In the past, numerical methods such as RCWA [18] and FDTD method [19] have been used to analyze such structures; however, those methods can be computationally taxing and do not provide the physical insight of CMT.

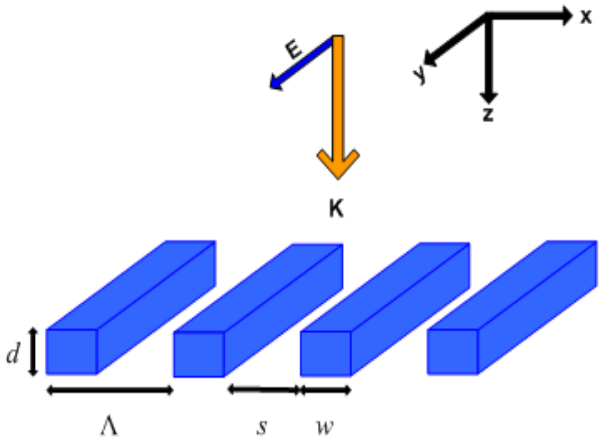

Figure A-1: High-Index Contrast Grating (HCG) with period Λ, width w thickness d and spacing s. Incident electric field is parallel to the grating (TE).

In this paper, we present a CMT approach for the design and analysis of HCGs to achieve close to optimal dimensions for a specific application and to understand the underlying physics as it relates to the coupling between optical modes. For the HCG problem, while CMT mode selection provides only a modest reduction in expansion order over RCWA, the CMT method allows for clear insight into the physics of the HCG operation in different parameter regimes, as well as efficient design of near optimal structures. For the HCG examples considered here, CMT provides accurate results for as few as 3 modes, showing that these modes indeed have a dominant role in the response of the system. In Section II, we present the HCG structure and describe the CMT method. Section III presents the results and discussions. First, the constraint on coupling coefficients to yield broadband response is derived, and the results obtained are compared with FDTD and RCWA simulations. Secondly, high quality (Q) resonators are considered in order to maximize the Q-factor by the adjustment of parameters and the results are compared with RCWA.

CMT Formulation

Figure A-1 shows the HCG structure to be analyzed, the structure is periodic in the x-direction, and the three parameters that dictate the reflectivity of the grating are period (Λ), width (w) and thickness (d). The ratio of width (w) to period (Λ) is defined as the duty cycle (η). The periodic structure is assumed to be surrounded by a homogeneous low index material with refractive index (n_1), whereas the refractive index of the grating is (n_2). The polarization of incident excitation is taken to be transverse electric (TE) with respect to the *xz*-plane.

The coupled mode equations governing the mode amplitudes are given as (from [5])

$$N_m\left(\frac{da_m}{dz}+j\beta_m a_m\right)=-j\sum_{n=1}^{M}\kappa_{mn}a_n-j\sum_{n=1}^{M}\chi_{mn}b_n \tag{A.1.a}$$

$$N_m\left(\frac{db_m}{dz}-j\beta_m b_m\right)=j\sum_{n=1}^{M}\chi_{mn}a_n+j\sum_{n=1}^{M}\kappa_{mn}b_n \tag{A.1.b}$$

where a_m and b_m are the mode amplitudes of forward and backward travelling modes respectively, β_m is the propagation constant, κ_{mn} and χ_{mn} are the coupling coefficients

between co-directional and contra-directional propagating waves, respectively. These are defined as

$$\kappa_{mn} = \frac{\omega\varepsilon_o}{4}\iint(\bar{n}^2 - n^2)(e_{tm}e_{tn} - \frac{n^2}{\bar{n}^2}e_{zm}e_{zn})dxdy \quad \text{(A.2.a)}$$

$$\chi_{mn} = \frac{\omega\varepsilon_o}{4}\iint(\bar{n}^2 - n^2)(e_{tm}e_{tn} + \frac{n^2}{\bar{n}^2}e_{zm}e_{zn})dxdy \quad \text{(A.2.b)}$$

$$\kappa_{mn} = \kappa_{nm} \quad \text{(A.3)}$$

In the case of TE polarization

$$\kappa_{mn} = \chi_{mn} \quad \text{(A.4)}$$

Finally, the normalization constants N_m are defined as

$$N_m = \frac{1}{2}\iint(e_{tm} \times e_{tn})dxdy \quad \text{(A.5)}$$

where ω is the angular frequency of the incident excitation, ε_o is the permittivity of free space, n and $\bar{n}$ are the refractive indices of the unperturbed and perturbed structures under investigation respectively, e_{tm} and e_{zm} are the transverse and longitudinal components of the m^{th} mode respectively.

Due to the periodic nature of the problem, the chosen modes bare close resemblance to the Fourier modes found in RCWA. The choice of a cosine wave expansion (motivated by the symmetry within the period) does not provide significant reduction in the modes used. Therefore, in this case, as a pure computational method CMT is not better than RCWA for the HCG problem; however, as we will show in the following analysis, CMT provides additional physical insight into the HCG operation in terms of mode coupling and analytic design criteria can be advised with this approach.

In the following analysis we consider only three modes $(M = 3)$: the fundamental excitation (plane wave with amplitude a_1) and the first two evanescent higher order modes (cosine waves with amplitudes a_2 and a_3). The coupling equations are given as

$$[X]' = [A] \times [X] \quad \text{(A.6.a)}$$

where $'$ signifies differentiation with respect to z and

$$[X] = [a_1 \quad a_2 \quad a_3 \quad b_1 \quad b_2 \quad b_3]^T \quad \text{(A.6.b)}$$

$$[A] = j\begin{bmatrix} -K_{11}-\beta_1 & -K_{12} & -K_{13} & -\Psi_{11} & -\Psi_{12} & -\Psi_{13} \\ -K_{21} & -K_{22}-\beta_2 & -K_{23} & -\Psi_{21} & -\Psi_{22} & -\Psi_{23} \\ -K_{31} & -K_{32} & -K_{33}-\beta_3 & -\Psi_{31} & -\Psi_{32} & -\Psi_{33} \\ \Psi_{11} & \Psi_{12} & \Psi_{13} & K_{11}+\beta_1 & K_{12} & K_{13} \\ \Psi_{21} & \Psi_{22} & \Psi_{23} & K_{21} & K_{22}+\beta_2 & K_{23} \\ \Psi_{31} & \Psi_{32} & \Psi_{33} & K_{31} & K_{32} & K_{33}+\beta_3 \end{bmatrix} \quad \text{(A.6.c)}$$

where $K_{mn} = \kappa_{mn} / N_m$ and $\Psi_{mn} = \chi_{mn} / N_m$. We define all these variables in terms of the dimensions of grating and the incident wavelength, after performing the required integrations we obtain

$$K_{11} = \beta_1 q \quad \text{(A.7.a)}$$

$$K_{12} = K_{11}\text{sinc}(\pi w / \Lambda) \quad \text{(A.7.b)}$$

$$K_{13} = K_{11}\text{sinc}(2\pi w / \Lambda) \quad \text{(A.7.c)}$$

$$K_{21} = 2\frac{\beta_1}{\beta_2} K_{11}\text{sinc}(\pi w / \Lambda) \quad \text{(A.7.d)}$$

$$K_{22} = \frac{\beta_1}{\beta_2} K_{11}(1+\text{sinc}(2\pi w / \Lambda)) \quad \text{(A.7.e)}$$

$$K_{23} = \frac{\beta_1}{\beta_2} K_{11}(\text{sinc}(\pi w / \Lambda) + \text{sinc}(3\pi w / \Lambda)) \quad \text{(A.7.f)}$$

$$K_{31} = 2\frac{\beta_1}{\beta_3} K_{11}\text{sinc}(2\pi w / \Lambda) \quad \text{(A.7.g)}$$

$$K_{32} = \frac{\beta_1}{\beta_3} K_{11}(\text{sinc}(\pi w / \Lambda) + \text{sinc}(3\pi w / \Lambda)) \quad \text{(A.7.h)}$$

$$K_{33} = \frac{\beta_1}{\beta_3} K_{11}(1 + \text{sinc}(4\pi w / \Lambda)) \quad \text{(A.7.i)}$$

where q and propagation constants are defined as

$$q = \frac{(n_2^2 - n_1^2)w}{2\Lambda} \quad \text{(A.8.a)}$$

$$\beta_1 = \frac{2\pi}{\lambda_o} \quad \text{(A.8.b)}$$

$$\beta_2 = \beta_1\sqrt{1-\left(\frac{\lambda_o}{\Lambda}\right)^2} \quad \text{(A.8.c)}$$

$$\beta_3 = \beta_1 \sqrt{1 - \left(\frac{2\lambda_o}{\Lambda}\right)^2} \tag{A.8.d}$$

Eq. A.6. is a system of coupled first order differential equations, it merely represents an eigenvalue problem, the solution is given as

$$[X] = \left[e^{\lambda_a z} V_a \quad e^{\lambda_b z} V_b \quad e^{\lambda_c z} V_c \quad e^{\lambda_d z} V_d \quad e^{\lambda_e z} V_e \quad e^{\lambda_f z} V_f \right] \times [C] \tag{A.9.a}$$

$$[C] = [c_1 \quad c_2 \quad c_3 \quad c_4 \quad c_5 \quad c_6]^T \tag{A.9.b}$$

where elements of C are the unknown coefficients that need to be determined from the boundary conditions, λ_i are eigenvalues and V_i are the corresponding eigenvectors. We need six boundary conditions to solve the system of Eq. A.9. The structure is excited with a forward propagating plane wave only, with amplitude $a_1 = 1$ at $z = 0$, thus the backward propagating plane wave b_1 has an amplitude of 0 at $z = d$. The remaining boundary conditions are dictated by the possibility of existence of the evanescent waves. Evanescent waves a_2 and a_3 are exponentially increasing with respect to z, therefore these must have zero amplitudes at $z = d$ and similar constraints apply to b_2 and b_3 at the $z = 0$ boundary. Application of these boundary conditions results in

$$[C] = F^{-1} \times [1 \quad 0 \quad 0 \quad 0 \quad 0 \quad 0]^T \tag{A.10.a}$$

where

$$[F] = \begin{bmatrix} V_{a1} & V_{b1} & V_{c1} & V_{d1} & V_{e1} & V_{f1} \\ e^{\lambda_a d} V_{a2} & e^{\lambda_b d} V_{b2} & e^{\lambda_c d} V_{c2} & e^{\lambda_d d} V_{d2} & e^{\lambda_e d} V_{e2} & e^{\lambda_f d} V_{f2} \\ e^{\lambda_a d} V_{a3} & e^{\lambda_b d} V_{b3} & e^{\lambda_c d} V_{c3} & e^{\lambda_d d} V_{d3} & e^{\lambda_e d} V_{e3} & e^{\lambda_f d} V_{f3} \\ e^{\lambda_a d} V_{a4} & e^{\lambda_b d} V_{b4} & e^{\lambda_c d} V_{c4} & e^{\lambda_d d} V_{d4} & e^{\lambda_e d} V_{e4} & e^{\lambda_f d} V_{f4} \\ V_{a5} & V_{b5} & V_{c5} & V_{d5} & V_{e5} & V_{f5} \\ V_{a6} & V_{b6} & V_{c6} & V_{d6} & V_{e6} & V_{f6} \end{bmatrix} \tag{A.10.b}$$

where V_{jn} is the n^{th} element of j^{th} eigenvector.

It is interesting to note that at a specific wavelength and dimensions of the gratings, F is nearly singular, this is the condition that results in exponential rise of C and thus we observe huge field enhancement of the higher order modes, as will be shown in the results.

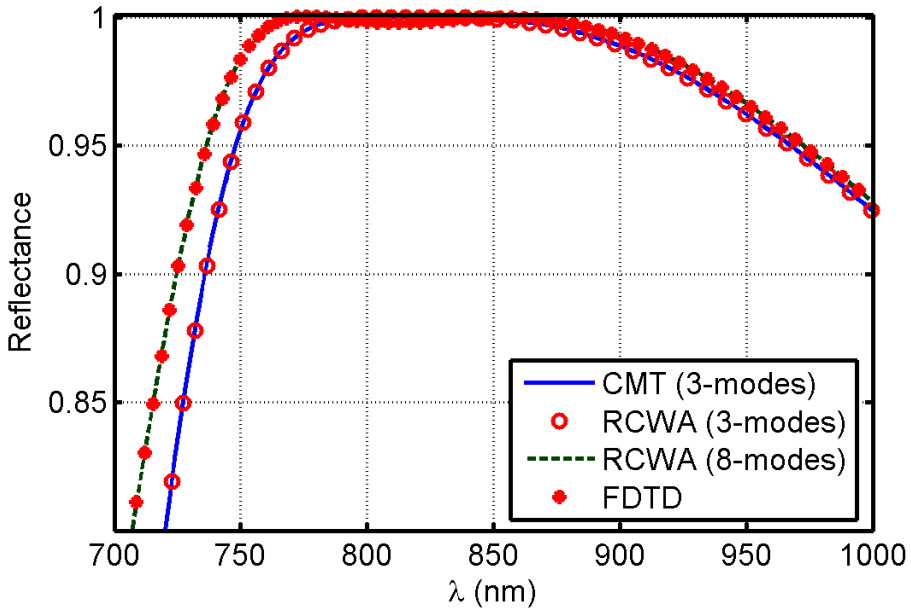

Figure A-2: HCG designed to operate as surface-normal broadband mirror at wavelength of 850 nm, period $\Lambda = 620\,\text{nm}$, width $w = 220\,\text{nm}$ and thickness $d = 140\,\text{nm}$. Reflectivity using the CMT and RCWA with only three lowest order modes, along with fully converged RCWA (8-modes) and FDTD.

Results and Discussions

We analyzed HCG for two different applications, namely (a) broadband mirrors and (b) high-Q resonators. Comparisons with RCWA [20] and FDTD verify that this approach produces accurate and insightful results.

HCG for Surface-Normal Broadband Mirrors

We first demonstrate the accuracy of the results obtained by using CMT with only three lowest order modes. Figure A-2 shows the reflectivity of HCG designed to operate at a wavelength of 850 nm at normal incidence. The grating is comprised of rectangular strips of AlGaAs with refractive index of 3.2 surrounded by air. The dimensions of the grating are, period $\Lambda = 620\,\text{nm}$, width $w = 220\,\text{nm}$, and thickness $d = 140\,\text{nm}$. The reflectivity spectra obtained using RCWA and FDTD are also plotted in Figure A-2 for comparison. It should be noted that CMT and RCWA give exactly the same results when equal number of modes are used, therefore the results presented using RCWA are equivalent to that of CMT results (fully converged for 8 modes). The advantages of using CMT with few modes are the ability to visualize the mode amplitudes as a function of distance along the propagation direction and the understanding of their interaction with

each other. While RCWA matches FDTD, the CMT response is slightly shifted towards longer wavelengths. Nevertheless, it should be noted that though the result is obtained using only three modes, it is in good agreement with those of RCWA and FDTD.

One of the advantages of a CMT approach is the possibility of an analytic design for broadband applications. To derive the necessary conditions for broadband response we rewrite matrix A of Eq. A.6c, but for the case of $M = 2$ as

$$A = j\begin{bmatrix} D & E \\ -E & -D \end{bmatrix} \tag{A.11}$$

where D and E are 2×2 matrices representing the coupling between co-directional and contra-directional propagating modes respectively. For broadband response we look for the condition when the absolute difference between co-directional coupling and contra-directional coupling changes slightly over the band of operation, therefore the required condition is $|D| = |E|$. Since the off-diagonal elements cancel:

$$(K_{11} + \beta_1)(K_{22} + \beta_2) = K_{11}K_{22} \tag{A.12}$$

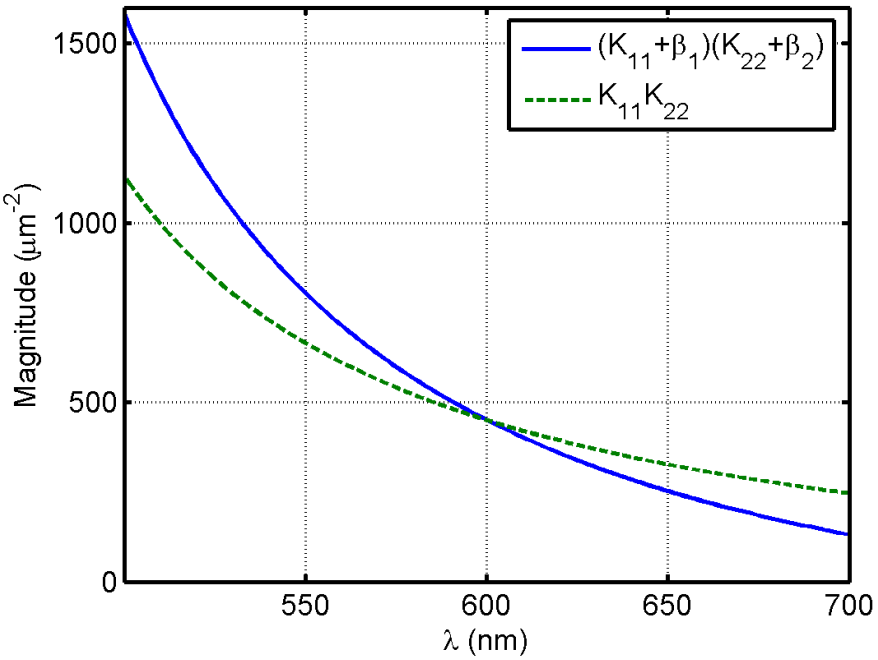

Figure A-3: Same mode co-directional (blue solid line) and contra-directional (green dashed line) coupling as a function of wavelength for the determination of broadband response. Parameters are $\Lambda = 443\,\text{nm}$, $w = 160.8\,\text{nm}$, $d = 99\,\text{nm}$ and $n_2 = 3.2$.

Therefore when the product of self-coupling approaches the product of coupling coefficients of same but contra-directional propagating modes then broadband response is observed. Figure A-3 shows a plot of Eq. A.12 designed to operate at wavelength of $600\,\text{nm}$, it is this small difference around the center wavelength that causes the broadband response. Eq. A.12 leads us to the following condition for broadband operation

$$\beta_2^2 = \frac{-q}{(1+q)}\beta_1^2\left(1+\text{sinc}\left(\frac{2\pi w}{\Lambda}\right)\right) \tag{A.13}$$

For a specific grating index and wavelength of interest, Eq. A.13 can provide the required period Λ and duty cycle η. Figure A-4a shows the points satisfying Eq. A.13 for a grating index of 3.2 designed to operate at a wavelength of 600 nm. Once the period and width are determined from Eq. A.13, the next step is the determination of grating thickness d. It should be noted that the design rule of Eq. A.13 is not just for broadband high reflectivity, it can also be used for the design of broadband high transmittance structures, depending on the thickness d. With the dimensions obtained from Figure A-4a we can calculate the required grating thickness resulting in a minimum transmitted power through the grating, which corresponds to the zeros of the fundamental mode a_1 at $z = d$. Figure A-4b shows the mode amplitude of the forward propagating mode a_1 at $z = d$ as a function of thickness, dictating the thickness to be 99 nm ($d = 138\,\text{nm}$ will result in broadband high transmittance). Our proposed design guideline provides following dimensions for design A with center wavelength of $\lambda = 600\,\text{nm}$, $\Lambda = 443\,\text{nm}$, $w = 160.8\,\text{nm}$ and $d = 99\,\text{nm}$. Figure A-4d shows mode amplitudes as a function of distance along the propagation direction z of the incident excitation.

To investigate the accuracy of the design procedure, comprehensive numerical simulations using FDTD method were carried out. (FDTD was used here because it is efficient for broadband calculations; however, a few calculations were selected and showed agreement with RCWA). A comparison of the results obtained using CMT and FDTD methods is shown in Figure A-4c. FDTD verifies the broadband characteristic of the design. For design criteria of reflectivity higher than 99% over the entire band of operation, FDTD results show that the width w can range from 153 nm to 178 nm. It is noted that the value of 160.8 nm predicted by the proposed design rule falls within this

range. Furthermore, it is also observed from FDTD results that the minimum ripple in reflectance is achieved for $w = 167\,\text{nm}$, resulting in reflectance value of higher than 99.48%, whereas Design A gives a reflectance higher than 99.4% over the entire bandwidth. This confirms that, in this case this design approach provides near optimal results in terms of ripple. Achieving a large reflection over the band of operation is desired for many applications, such as VCSELs [12-14].

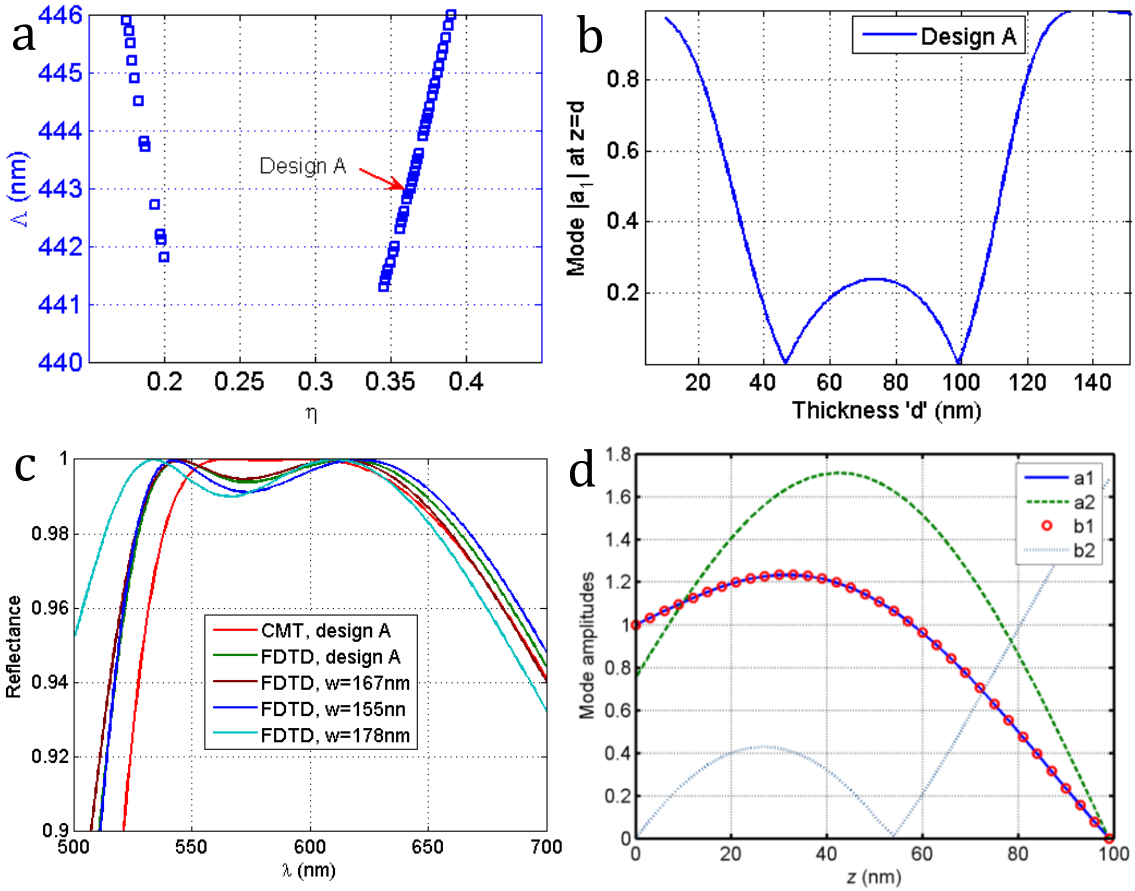

Figure A-4: (a) Design of broadband reflector for center wavelength of 600 nm, with grating index of 3.2. (b) Forward propagating fundamental mode amplitude at $z = d$ for the determination of the optimal thickness. (c) Reflectivity obtained using CMT and FDTD for design A and for slight variations in width. Dimensions for design A are $\Lambda = 443\,\text{nm}$, $w = 160.8\,\text{nm}$ and $d = 99\,\text{nm}$. (d) Mode amplitudes as a function of distance along the propagation direction z of the incident excitation.

HCG for High-Q Resonators

Another interesting application of HCG is its use as a very narrow band reflector or high-Q resonator. Precise adjustment of the dimensions can lead to the condition that the

average energy in the forward going mode is completely coupled into the backward propagating modes at the opposite interface of structure over a very narrow band of frequencies. This condition is achieved when the matrix F given by Eq. A.10b becomes nearly singular, which is approached when any two rows of F become linearly dependent [21].This results in very large values of the coefficients C of Eq. A.9 with strong coupling to higher order modes.

To calculate the quality factor of such a resonator we compare the response to a Fano-resonance [23], which is given by:

$$R = \frac{r^2(\omega-\omega_o)^2 + t^2(1/\tau)^2 - 2rt(\omega-\omega_o)(1/\tau)}{(\omega-\omega_o)^2 + (1/\tau)^2} \qquad \text{(A.14.a)}$$

where ω_o is the resonant frequency, τ is the resonance lifetime, r and t are reflectivity and transmittance of a slab of the same thickness as the grating structure being studied. Fano-resonance occurs due to the interference between a narrowband and broadband scattering phenomenon, which in the case of HCG comes from the transverse higher order harmonic interference with the zero order mode. The quality factor of the resonator is given as

$$Q = \omega_o \tau \qquad \text{(A.14.b)}$$

The stronger the interaction of the incident normal mode with the in-plane higher order harmonics, the narrower the resonance. It should be mentioned here that these narrow band resonator structures are extremely sensitive to dimensions, and the numerical calculations can require a large number of modes to be accurate.

Figure A-5a shows the points of maximum field strength for the first higher order mode, a_2, as a function of period and duty cycle of the gratings with a slab thickness of $d = 625\,\text{nm}$ and grating index $n_2 = 3.078$, using the proposed method. Two designs are pointed out for comparison and to demonstrate the strength of the method in finding an improved configuration. Design C with period of 812 nm was proposed previously [22]. Design D results in a Q-factor of 46 times higher than Design C. It should be noted that these values were obtained using only three modes. To obtain full convergence, however, RCWA requires at least 18 modes, as shown in Figure A-5c. (In this case, RCWA is better suited for the high-quality simulations, which require long simulation times with FDTD; however, close agreement was found with FDTD simulations with a long

integration time). The Fano-fit is also plotted in Figure A-5c. Q-factor values obtained from the fit are 66×10^3 for Design C and 85×10^3 for Design D.

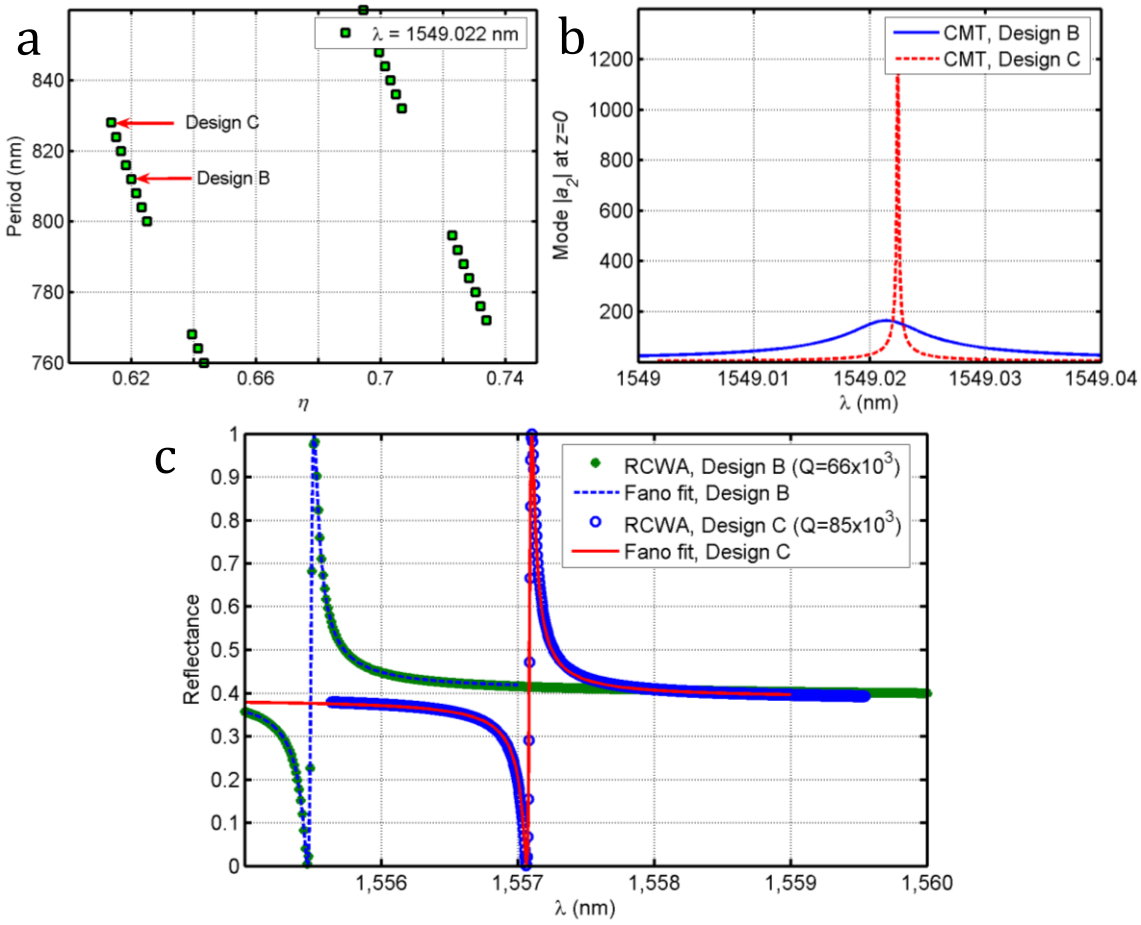

Figure A-5: (a) Maximum field strength of the first higher order mode a_2 versus period Λ and duty cycle η with thickness $d=625\,\text{nm}$ and grating refractive index of 3.078 using CMT. (b) Comparison of the two designs regarding the strength of interaction between the incident and the evanescent higher order modes. (c) Reflectivity, using RCWA with 18 modes. For Design C $w=519.68\,\text{nm}$, $\Lambda=812\,\text{nm}$ and for design D $w=519.27$, $\Lambda=828\,\text{nm}$. Q values obtained from the fit are 66×10^3 and 85×10^3 for design C and D respectively.

There is a significant reduction in the actual Q factor in the fully converged case; however, the trend of increase in Q is maintained for the RCWA (as with the CMT method): going from Design C to D shows an increase of 28% in the Q value. Therefore, the CMT method improves the performance of these high-Q resonators, as well as providing suitable parameters for strong coupling to the first higher order mode.

Conclusion

We presented a CMT method to explore the characteristics of high-index-contrast gratings over a wide range of design parameters such as period, duty cycle, thickness and wavelength of operation. A design procedure was presented for broadband high reflectivity applications that showed near optimal performance in terms of broadband reflection with minimal ripple. Such broadband reflectors are of interest for numerous applications, including tunable VCSELs. The method was also used to search for higher Q resonators, with a 28% improvement over past results demonstrated. These high-Q resonators are of particular interest for sensor applications. Other desirable features of the CMT method are its efficiency, simplicity and ability to provide physical insight. It should be mentioned that the method provides estimates for an optimal design and, once the dimensions are estimated for desired operation, RCWA/FDTD or any other rigorous method (including higher order CMT) can be used to accurately describe the optical properties of these structures.

References

[1] W. Snyder and J. D. Love, "Optical waveguide theory," *Chapman and Hall, New York,* 1983.

[2] J. R. Pierce, "Coupling of modes of propagation," *Journal of Applied Physics*, vol. 25, no.2, pp. 179-183, 1954.

[3] Yariv, "Coupled-mode theory for guided-wave optics," *IEEE Journal of Quantum Electronics,* vol. 9, no. 9, pp. 919- 933, 1973.

[4] R. A. Waldron, "The theory of coupled modes," *Quart. Journal Mech. and Applied Mathematics,* vol. 18, pp. 385-404, 1964.

[5] W. Huang and J. Mu, "Complex coupled-mode theory for optical waveguides," *Optics Express,* vol.17, no.21, pp. 19134-19152, 2009.

[6] S. P. Davis, "Diffraction grating spectrographs," *New York, Holt, Rinehart, and Winston,* 1970.

[7] F. Kneubuhl, "Diffraction grating spectroscopy," *Applied Optics*, vol. 8, no. 3, pp. 505-519, 1969.

[8] G. A. De Biase, F. Sacchetti, and D. Trevese "Spectroscopy by grating synthesis," *Applied Optics*, vol. 11, no. 5, pp. 1163-1168, 1972.

[9] K.T.V. Grattan and B. T. Meggitt, "Optical fiber sensor technology, advanced applications, Bragg gratings and distributed sensors," *Boston, Dordrecht, Kluwer academic,* 2000.

[10] E. G. Loewen and E. Popov, "Diffraction gratings and applications," *New York, Marcel Dekker,* 1997.

[11] J. Chang-Hasnain, Chun-Li, G. Savran and A. Cagri, "In situ assembled diffraction grating for biomolecular detection," *Applied Physics Letters,* vol. 90, no. 23, 2007.

[12] A. Haglund, J.S. Gustavsson, J. Bengtsson and P. Jedrasik, "Design and evaluation of fundamental-mode and polarization-stabilized VCSELs with a sub-wavelength surface grating," *IEEE Journal of Quantum Electronics*, vol. 42, no. 3, pp. 231-240, 2006.

[13] S. Goeman, S. Boons, B. Dhoedt, K. Vandeputte, K. Caekebeke, P. V. Daele, and R. Baets, "First demonstration of highly reflective and highly polarization selective diffraction gratings (GIRO-gratings) for longwavelength VCSELs," *IEEE Photonics Technology Letters*, vol. 10, no. 9, pp. 1205–1207, 1998.

[14] M. Ortsiefer, M. Gorblich, Yan Xu, E. Ronneberg, J. Rosskopf, R. Shau and M. C. Amann, "Polarization control in buried tunnel junction VCSELs using a birefringent semiconductor/dielectric sub-wavelength grating," *IEEE Photonics Technology Letters,* vol.22, no. 1, pp. 15-17, 2010.

[15] Y. Kanamori, M. Ishimori and K. Hane, "High efficient light-emitting diodes with antireflection subwavelength gratings," *IEEE Photonics Technology Letters*, vol. 14, no. 8, pp. 1064-1066, 2002.

[16] F. R. Mateus, M. C. Y. Huang, D. Yunfei, A. R. Neureuther, and C. J. Chang-Hasnain, "Ultrabroadband mirror using low-index cladded subwavelength grating," *IEEE Photonics Technology Letters*, vol. 16, no. 2, pp. 518–520, 2004.

[17] F. R. Mateus, M. C. Y. Huang, C. Lu, C. J. Chang-Hasnain, and Y. Suzuki, "Broad-band mirror (1.12–1.62 um) using a subwavelength grating," *IEEE Photonics Technology Letters,* vol. 16, no. 7, pp. 1676–1678, 2004.

[18] M. G. Moharam and T. K. Gaylord, "Rigorous coupled-wave analysis of metallic surface-relief gratings," *Journal of Optical Society America A*, vol. 3, no. 11, pp. 1780-1787, 1986.

[19] K. Hwan, L. Chrostowski, E. Bisaillon and D. Plant "DBR, Sub-wavelength grating and photonic crystal slab Fabry-Perot cavity design using phase analysis by FDTD," *Optics Express*, vol. 15, no. 16, pp. 10330-10339, 2007.

[20] M. Whittaker and I. S. Culshaw, "Scattering-matrix treatment of patterned multilayer photonic structures," *Physical Review B*, vol. 60, pp. 2610-2618, 1999.

[21] C. D. Meyer "Matrix analysis and applied linear algebra," S*ociety of Industrial and Applied Mathematics*, *Philadelphia,* 2000.

[22] Y. Zhou, C. Y. Huang, C. Chase, V. Karagodsky, M. Moewe, B. Pasala, G. Sedgwick and C. J. Chang-Hasnain, "High-Index-Contrast grating (HCG) and its Applications in optoelectronic devices," *IEEE Journal of Selected Topics in Quantum Electronics,* vol. 15, no. 5, pp.1-15*,* 2009.

[23] S. Fan, W. Suh, and J. D. Joannopoulos, "Temporal coupled-mode theory for the Fano resonance in optical resonators," *Journal of Optical Society of America A*, vol. 20, pp. 569–572, 2003.

[24] S. Mani Tripathi, A. Kumar, E. Marin and J.-P. Meunier "Bragg grating based biochemical sensor using submicron Si/SiO2 waveguides for lab-on-a-chip applications: a novel design," A*pplied Optics* vol.48, no.23, pp. 4562-4567, 2009.

Appendix B: Antenna Design for Directivity Enhanced Raman Spectroscopy

(2012, International Journal of Optics, volume 2012, 729138)

Antenna Design for Directivity Enhanced Raman Spectroscopy

*Aftab Ahmed, Yuanjie Pang, Ghazal Hajisalem and Reuven Gordon**

Department of Electrical and Computer Engineering, University of Victoria, Victoria, BC V8W 3P6, Canada

ABSTRACT: Antenna performance can be described by two fundamental parameters: directivity and radiation efficiency (RE). Here we demonstrate nanoantenna designs in terms of improved directivity. Performance of the antennas is demonstrated in Raman scattering experiments. The radiated beam is directed out of the plane by using a ground plane reflector for easy integration with commercial microscopes. Parasitic elements, parabolic and waveguide nanoantennas with a ground plane are explored. The nanoantennas were fabricated by a series of electron beam evaporation steps and focused ion beam milling. As we have shown previously, the circular waveguide nanoantenna boosts the measured Raman signal by 5.5× with respect to a dipole antenna over a ground plane; here we present the design process that led to the development of that circular waveguide nanoantenna. This work also shows that the parabolic nanoantenna produces a further four-fold improvement in the measured Raman signal with respect to a circular waveguide nanoantenna. The present designs are nearly optimal in the sense that almost all the beam power is coupled into the numerical aperture of the microscope. These designs can find applications in microscopy, spectroscopy, light emitting devices, photovoltaics, single photon sources and sensing.

KEYWORDS: Plasmonics, optical antennas, nanoantennas, directivity, Raman scattering.

Introduction

Antennas have been widely used in radio communications for more than a century for efficient transmission of information over long distances. Since its discovery in 1895, enormous progress has been made with better control of antenna parameters (for a brief history see [1] and references therein). For example, directional emission was demonstrated by Yagi-Uda in the microwave regime [2] where the radiation from the feed element is directed with the assistance of reflector and director parasitic elements.

The directivity of antennas has played a vital role in microwave communication systems, specifically in satellite communication for the realization of high gain antennas.

Radio antennas provide solutions to communication problems, whereas recent developments for realization of optical antennas were mainly dictated by microscopy and spectroscopy applications [3, 4]. Typically antennas have dimensions of the order of the operating wavelength, requiring antenna dimensions in nanometers for operation in the visible regime. In the visible-IR regime, the metal cannot be taken as a perfect conductor and the nanoantenna design must be modified due to plasmonic properties [5-8]. Recent developments in the nanotechnology have made the fabrication of such small structures possible, leading to the development of optical single element and Yagi-Uda equivalent nanoantennas [9-20]. Directing the emission from optical emitters is highly desired for efficient detection, and by reciprocity, efficient excitation as well. Typical applications include light emitting devices [21, 22], photovoltaics [23-27] sensing [28, 29], spectroscopy [30-32], single photon sources [33, 34] and microscopy [3, 35, 36].

In a recent work, our group has shown that the scattered radiation from nanoparticles can be directed out of the plane of substrate and into the collection microscope using a ground plane reflector [37]. Enhancement of over 50× was observed in the measured Raman signal as compared to nanoprisms over a glass substrate. We also demonstrated recently an experimental work on waveguide nanoantenna to boost the Raman signal by beam forming in the lateral plane [38]. A further 5.5× enhancement was observed with a circular waveguide nanoantenna as compared to a dipole nanoantenna over a gound plane.

The main objective of this work is to present the design of planner nanoantennas for optimal performance in directivity-enhanced Raman scattering (DERS). Here we present the details of the design process that led to the development of circular waveguide nanoantenna, the different designs considered for beam forming in the lateral plane and the possibility of higher local fields for further Raman enhancement. We also show experimentally that the parabolic reflector can enhance the Raman signal by 4× as compared to the circular waveguide nanoantenna owing to its improved directivity and enhanced local fields, however, it is challenging to fabricate.

Antenna Design Parameters

The total power radiated by an antenna can be given as

$$P_{rad} = \int_0^{2\pi} \int_0^{\pi} p(\theta,\phi)\sin(\theta)d\theta d\phi \tag{B.1}$$

where $p(\theta,\phi)$ is the normalized angular power density also know as radiation pattern of an antenna. Directivity is defined as the antennas ability to radiate in a specific direction more efficiently as compared to a hypothetical isotropic radiator [39]

$$D = \frac{4\pi}{P_{rad}} p(\theta,\phi) \tag{B.2}$$

Considering the numerical aperture (NA) of the microscope objective, a more suitable parameter for describing the beam forming ability of an antenna is the beam efficiency (BE).

$$BE = \frac{\int_0^{2\pi} \int_0^{\theta_0} p(\theta,\phi)\sin(\theta)d\theta d\phi}{P_{rad}} \tag{B.3}$$

where θ_0 is the cone half angle. Cone angle of 30 degrees was calculated from the measured spot size $'d'$ of approximately 1.5 μm, using: $\theta_0 = \sin^{-1}(\lambda/2d)$. This corresponds to a NA of 0.28.

Radiation patterns of single element nanoantennas are typically dipolar in nature resulting in poor directivity $(D_{\max} = 1.5)$. Directive emission at optical wavelengths has been achieved using multi-element nanoantennas [11, 13, 40]. Radiation patterns of those antennas reveal that the main beam is directed in the plane of the substrate thus cannot be readily used in an ordinary microscope setup. Further, vertical Yagi-Uda nanoantenna has been realized using top-down approach [15]. Improved directivity at optical wavelengths can have tremendous impact in areas such as optical microscopy, spectroscopy, sensing and applications involving single photon sources, where efficient collection and emission is critical.

Another important factor in the context of Raman measurements is the local field strength. It has been recently shown that maximum field enhancement results when power radiated by the antenna is equal to the power loss in the antenna [41-43]. This is

commonly referred to as impedance matching in microwave antenna theory [39]. Even higher local field can be achieved by reducing the mode volume of the antenna by reducing the feedgap between the two elements of the dipole antenna [43].

Design and Fabrication

In this paper we investigate different nanoantenna designs for DERS with the desired features of out of plane radiation and enhanced local fields. The introduction of ground plane prevents loss of scattered radiation into the substrate and proper adjustment of antenna distance from the ground plane can result in radiation enhancement out of the plane. Further improvement of directivity is demonstrated by beam shaping in the lateral plane using different designs including parasitic elements, waveguide antennas and parabolic reflectors. The multilayer substrate is fabricated by electron beam evaporation and the different designs are milled using focused ion beam (FIB).

Figure B-1 illustrates the multilayer substrate used for the fabrication of nanoantennas studied in this work. The antennas were designed to be tested under Raman microscope. The dimensions of different layers and the dipole antenna were calculated to achieve best performance at wavelength of 840 nm (mean of excitation and Raman scattered wavelengths). The antenna consists of a 130 nm long and 50 nm wide dipole. Traditionally, dipole antenna characteristic lengths were of the order of wavelength of operation $(\lambda/2)$, but the real metal response requires that shorter effective wavelengths are introduced for the determination of dipole length in infrared and optical regions [7]. A 150 nm thick gold layer was used as ground plane to ensure that it was optically thick.

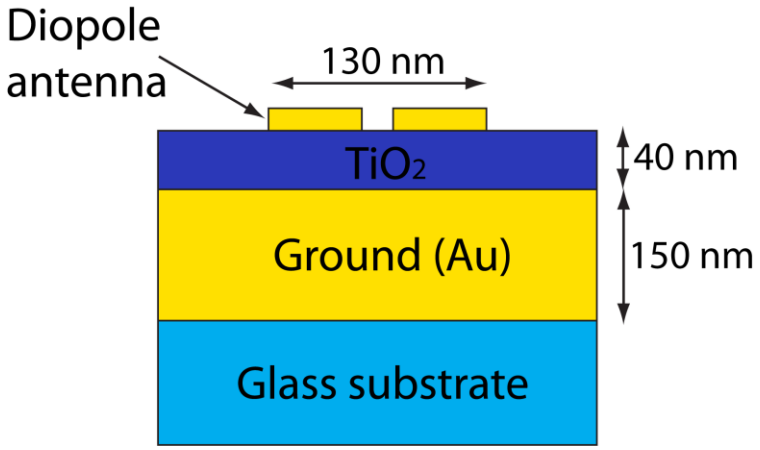

Figure B-1: Multilayer substrate to control the radiation pattern of a dipole antenna. Thicknesses of ground plane, dielectric (TiO2) spacer and top gold layer

are 150 nm, 40 nm and 50 nm respectively. Dipole antenna length of 130 nm with a 20 nm feedgap was used to operate at wavelength of 840 nm.

The optimal thickness of dielectric spacer (TiO_2) was calculated numerically to be 40 nm using finite-difference time-domain (FDTD) simulations. It should be noted that this is smaller than the typical quarter wavelength value due to penetration into the metal, as well as impedance matching effects [43].

The multilayer substrate was fabricated by evaporation of gold and TiO_2 onto glass substrate by means of electron beam evaporation under a pressure of 2×10^{-6} Torr. The proposed nanoantenna structures were milled on the top 50 nm thick gold layer using FIB. Figure B-2 shows the different nanoantennas investigated in this work for normal emission. Relative efficiencies of these structures are discussed in the simulation section below, where it is shown that the circular waveguide nanoantenna shown in Figure B-2c, results in best performance in terms of directivity.

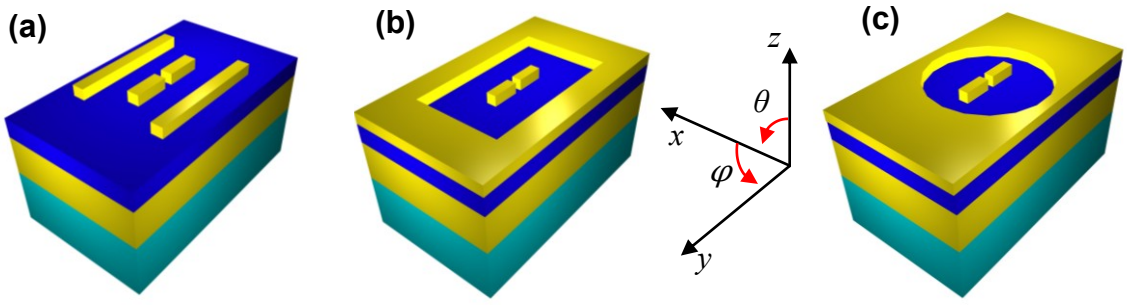

Figure B-2: (a) Dipole antenna over ground with two parasitic reflectors 150 nm long and 100nm from the feed element. (b) Dipole antenna over ground plane with a square reflector of length 500 nm (square waveguide antenna). (c) Dipole antenna over ground plane with a circular reflector of radius 250 nm (circular waveguide antenna).

Another promising design translated from the microwave antenna theory is that of the parabolic reflector antenna. We demonstrate DERS from the beam forming abilities of a parabolic reflector nanoantenna. Figure B-3 shows the schematic of the parabolic nanoantenna. A paraboloid shaped trench was milled into a silicon wafer using FIB. As shown in the figure, the focal length of this paraboloid was designed to be 500 nm, and the diameter of the top circle is 2 μm. A layer of 100 nm thick gold (optically thick) was evaporated onto the silicon wafer by means of electron beam evaporation under a pressure of 2×10^{-6} Torr.

The conformity of the evaporated layer to the hole on silicon creates a parabolic reflector antenna on Au layer. PMMA was then spin-coated on top of the Au layer as a spacing dielectric layer. We chose PMMA and the spin-coating technique to make the spacer layer for reasons of simplicity and repeatable thickness control. Finally, Ag nanoprisms, synthesized in water by white-light assisted conversion of spherical nanoparticles [44], were mixed with 3μMol rhodamine 6G dye and drop-coated onto the PMMA surface. The nanoprisms serve as the feed of the parabolic reflector nanoantenna.

The experiments of [37] are first repeated using PMMA for the determination of optimal thickness of the PMMA layer. As a result (not shown), the first and second order coherent SERS enhancement peaks are found at 120 nm and 420 nm PMMA thickness. We choose to spin-coat 420 nm PMMA (corresponding to the second order SERS enhancement) onto our parabolic reflector, since this thickness is more compatible with the focal length of our parabolic reflector, bringing the feed Ag nanoprism near the paraboloid focal point.

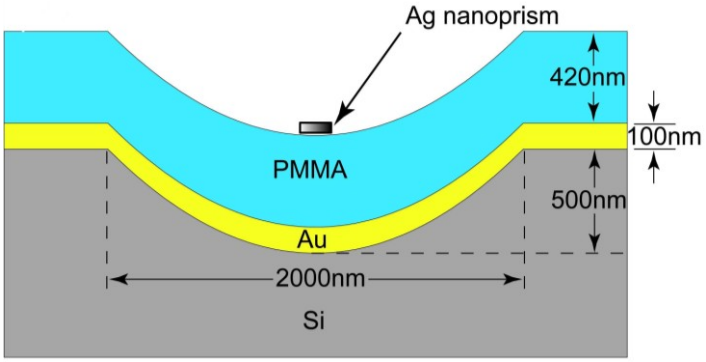

Figure B-3: The schematic drawing of the proposed parabolic reflector nanoantenna.

Simulation Results

The proposed structures were simulated using FDTD method. The simulation domain was terminated by perfectly matched layers (PMLs) for minimal reflections. The antenna structure was enclosed by a set of 2D field monitors forming a box to perform far-field projections and for the determination of field patterns. For the antenna structures shown in Figure B-2, an electric dipole source located at the feed-gap of the dipole antenna was used to excite the nanoantenna.

FDTD simulations indicate the following parameters for best performance for each type of antenna. Two 150 nm long parasitic reflectors, 100 nm away from the feed element resulted in a half power beam width (HPBW) of 110 degrees in the *xz-plane*. Radiation patterns of this structure show a very broad HPBW in the *yz-plane*. To further improve the directivity in both planes we introduced reflectors parallel to the *x-axis* as well. It was demonstrated numerically that a square reflector with length of 500 nm resulted in best performance. The corresponding HPBWs are 85 degrees and 90 degrees in the *xz* and *yz-planes* respectively. Even better performance is observed by using a circular waveguide antenna as shown in Figure B-2c, producing a symmetrical beam out of the plane of substrate with HPBW of 85 degrees in both planes. Figure B-4a, b shows the radiation pattern in the *xz* and *yz* planes respectively at the wavelength of 840 nm. It can be seen that in the absence of ground reflector, most of the scattered power is directed into the substrate and away from the microscope objective.

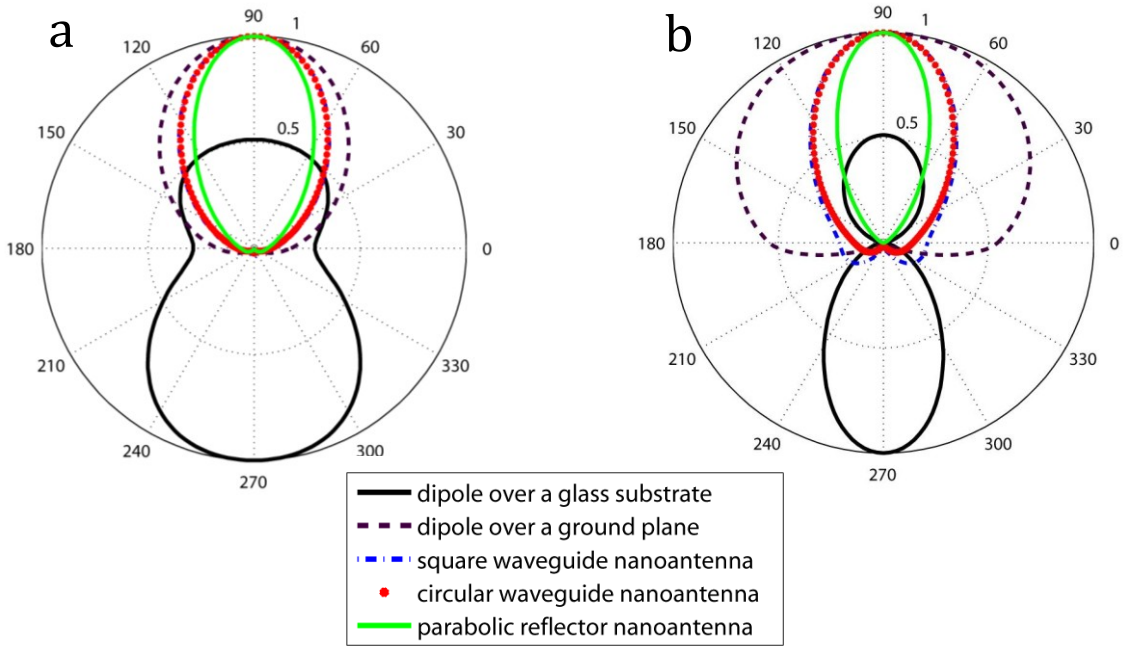

Figure B-4: Radiation patterns of a dipole antenna on a glass substrate, dipole over ground plane, square waveguide nanoantenna (side length = 500 nm), circular waveguide nanoantenna (radius = 250 nm) and parabolic reflector nanoantenna. Calculated using far field projections of 3D FDTD simulations (a) *xz* plane (b) *yz* plane.

The circular waveguide nanoantenna gives a nearly optimal radiation pattern resulting in the collection of almost all of the scattered light by a numerical aperture of 0.75. The

radiation patterns of the parabolic reflector is also plotted in Figure B-4 for comparison. It can be seen that the parabolic reflector nanoantenna results in an even better directivity as compared to the circular waveguide nanoantenna.

The ring-reflector acts to create a lateral standing wave that reflects light back towards the central dipole antenna structure. This is most similar to the waveguide antenna, which has a lateral resonance when the wavelength is 3.4× the radius of the circular waveguide (i.e., at the lowest order mode cut-off) [39, 45]. Larger and smaller radii do not provide this resonance at the desired wavelength of 840 nm and thus give in smaller directivities. The radiation patterns of circular waveguide nanoantenna with slightly smaller and larger radii (not shown) show splitting of the main beam into two lobes, thus lowering the directivity in the normal direction.

Since the present design is optimized to work at around 840 nm, this corresponds to a radius of 250 nm, which is precisely the radius value that was found to give the greatest DERS in the experiment. The beam forming for this antenna design allows for directive emission into a numerical aperture of approximately 0.75; therefore, it is well suited for microscope setups.

Another parameter dictating the intensity of Raman signal is the local field enhancement that arises from plasmonic resonances, tapers, gaps and high-curvature in the antenna design [46, 47]. Impedance matching and reduction of mode volume of the antenna provides maximum local field enhancement [43]. Figure B-5 a, b shows the local field intensity in the antenna gap for gap sizes of 20 and 5 nm respectively at the design wavelength of 840 nm (log scale).

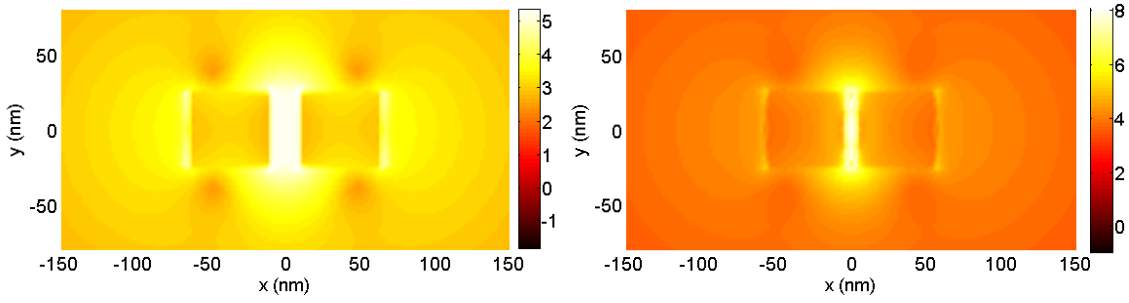

(a) feedgap = 20nm (b) feedgap = 5nm

Figure B-5. E field intensity $(|E|/|E_0|)^2$ at the design wavelength of 840 nm for (a) gap size of 20 nm (b) gap size of 5 nm (log scale).

By reducing the gap size from 20 nm to 5 nm, the normalized E field intensity $(|E|/|E_0|)^2$ increases by approximately 1000×. Intensity of Raman signal is proportional to the square of E field intensity thus we expect an enhancement of 10^6. The feedgap of the fabricated circular waveguide nanoantenna was 20 nm. Thus it is clear that the Raman signal can be considerably enhanced by reducing the feedgap, which is a challenging task.

Now we present the simulation results of the parabolic reflector nanoantenna. Figure B-6 shows the electric field intensity profile at a vertical segment of the structures at the design wavelength of 840 nm. It can be seen that the local field intensity at the Ag prism over a parabolic reflector is much larger than that over a planar reflector. From the field intensity profiles in the PMMA layer, it can be seen that the Ag nanoprism is placed at the second anti-node of the parabolic reflector at 840 nm wavelength, the same as in the planar reflector case; it is also at the focal point of the paraboloid. Therefore, the two effects, constructive interference and focusing, combine to give the enhanced Raman signal. Our parabolic reflector is able to collect more power from the incoming Gaussian wave to the Ag nanoprism feed element, indicating a better coupling between the far- and the near-field, or in an conventional antenna concept, a higher directivity.

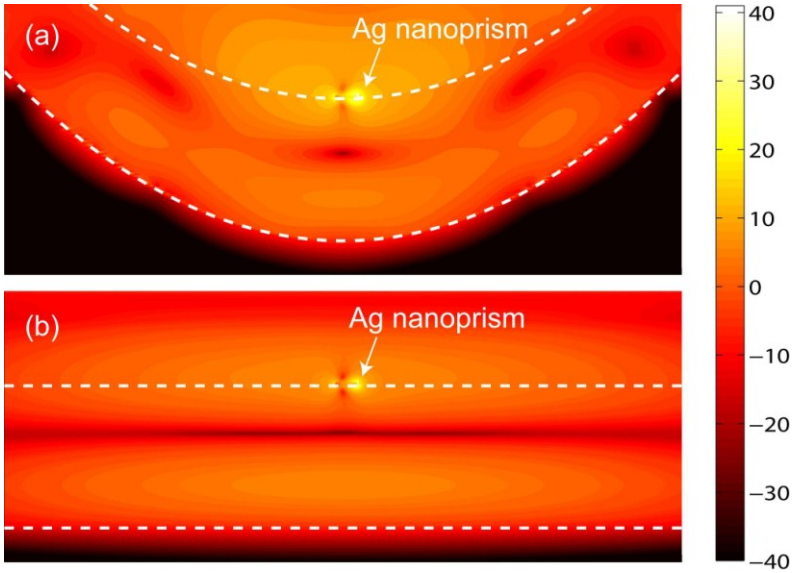

Figure B-6: FDTD simulation results comparing the vertical segment electric field intensity profiles of an Ag nanoprism above (a) a parabolic reflector and (b) a planar reflector. The white dotted lines show the Au ground plane and the PMMA layer surfaces. The color map is in dB scale.

In terms of Raman enhancement at the Ag nanoprism feed element, the relative Raman signal enhancement is proportional to the product of the excitation field intensity $|E_{exc}|^2$ and the emitted Raman field intensity $|E_{raman}|^2$. The Raman enhancement factor was computed at the near-field of the Ag prism (within a rectangular box 10 nm away from the Ag prism). It was found from the local field enhancement that the Raman enhancement near an Ag prism in a parabolic reflector arrangement is $40\times$ larger than in a planar reflector arrangement. It is due to this high local field effect that the parabolic reflector nanoantenna results in a stronger Raman signal as compared to the circular waveguide nanoantenna (of Figure B-2c) which produces only $1.2\times$ enhancement of the local field by the introduction of the circular ring around the dipole over a ground plane.

Raman Scattering Experiments

Raman scattering experiments were carried out for the fabricated circular waveguide and parabolic antennas using Rhodamine 6G as the Raman dye excited by a 785 nm laser. For this CW excitation, there is negligible two-photon fluorescence, which would show up as background in the Raman spectrum. The emitted wavelength at 1509 cm^{-1} Stoke's line (λ=890 nm) was measured using a Renishaw inVia Raman microscope with a $100\times$ objective and a spot size 'd' of approximately 1.5 μm (as determined by mapping experiments). Raman dye, Rhodamine 6G (400 μM in ethanol) was drop coated and the sample was allowed to dry for 6 hours.

Figure B-7a shows the measured Raman signal intensity as a function of Raman shift using the circular waveguide nanoantenna. The circular reflector with radius of 250 nm resulted in the strongest DERS signal as is predicted by the numerical results of Figure B-4.

For comparison, detected intensities from dipole over ground and from the un-milled regions of the top gold surface (without any dipole antenna) are also shown. A dipole antenna of same dimensions and on the same substrate was fabricated by removing a ring of diameter 10 μm, to approximate the absence of the ring structure. This dipole over ground is used as the reference for the calculation of EF. The measured spot size of 1.5 μm results in illumination of an area of 1.76 $(\mu m)^2$, which is much larger than the area of the antenna gap. From the results of Figure B-7a, it can be seen that the contribution

from the gold surface alone (i.e., without the antenna) is small when compared to that from the antenna. It should be noted that the Raman scattering intensity is boosted about 5.5× as compared to dipole over ground and about 13× with respect to the top Au surface. Note that this 5.5× increase is in addition to the 50× signal increase by use of the ground plane [37], and this additional enhancement is attributed to the improved directivity of the ring structure. Thus the total enhancement from the circular waveguide nanoantenna can be estimated to be 275× as compared to nanoparticles on a glass substrate. Figure B-7b shows an SEM image of the fabricated circular waveguide nanoantenna.

To demonstrate that the observed increase in Raman intensity is mainly from antenna directivity and with only a small contribution from local field enhancement, we calculated the enhancement factor arising from local electric field (EF_{loc}) in the antenna feedgap. $EF_{loc} = |E_{exc}|^2 \, |E_{scat}|^2$, where $|E_{exc}|^2$ and $|E_{scat}|^2$ are the electric field intensities at the excitation wavelength of 785 nm and Stokes shifted scattered radiation at wavelength of 890 nm, respectively. We observe maximum $EF_{loc} = 1.2$. The measured 5.5× increase in Raman intensity is thus predominantly from improved directivity of the antenna. Numerically calculated EF using beam efficiency and radiation patterns of Figure B-4 with cone angle of 30 degrees is in excellent agreement with the experimental results.

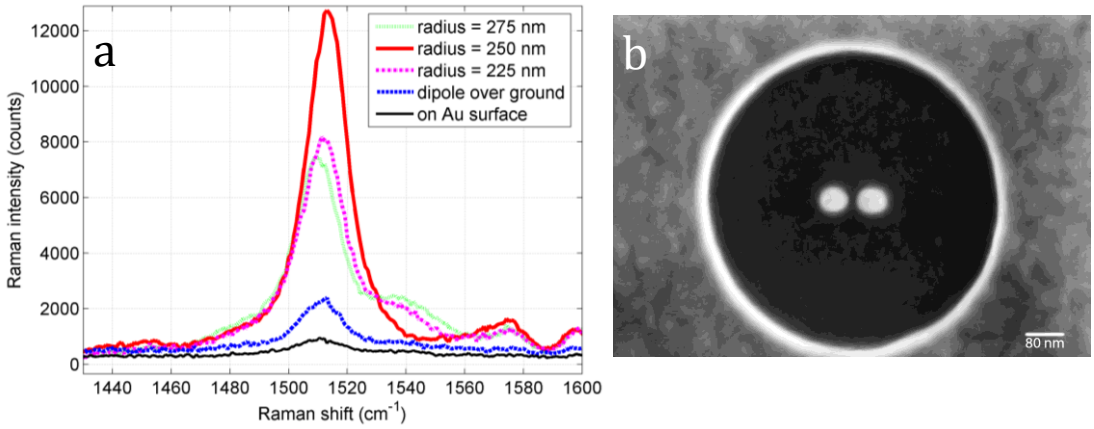

Figure B-7. (a) Raman spectra from the nanoantenna structure for various radii of circular reflector, dipole over a ground plane and the top unmilled Au surface. (b) Scanning electron microscopy image of the fabricated circular waveguide nanoantenna.

Figure B-8 shows an SEM of an Ag nanoprism (a), the scanning ion microscopy image of the fabricated structure (b) and a 6×6 μm^2 map of the Raman signal of the 1509 cm^{-1}

Stokes line around a parabolic reflector nanoantenna (c). A clear enhancement to the Raman signal is obtained from the parabolic reflector nanoantenna as compared to the surrounding area, where it is equivalent to a planar reflector nanoantenna. By comparing the maximum Raman signal from a parabolic reflector nanoantenna to the average surrounding signal, a 22× enhancement is obtained.

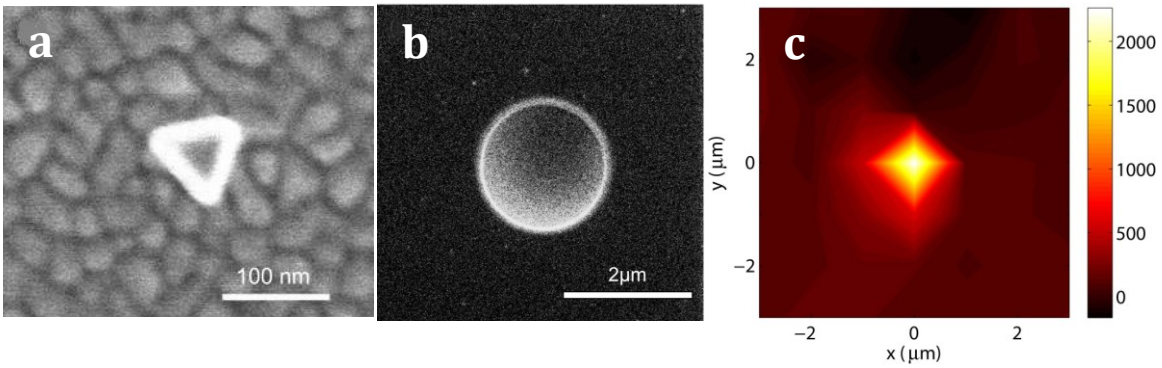

Figure B-8: (a) Scanning electron microscopy image of Ag nanoprism. (b) A scanning ion microscope image of the paraboloid drilled on silicon taken directly from the FIB. (c) A 6×6 μm^2 map of the Raman signal around a parabolic reflector nanoantenna.

Our previous experiments on Ag nanoprism over planar reflector experiments have already shown a 50× Raman enhancement as compared to Ag nanoprisms on glass (without any reflector) [37]. Combining the result of this work and Ref. [37], we estimate that our designed parabolic reflector structure can enhance the SERS signal from metallic nanoprisms by 1100×. In other words, by directivity engineering, we have boosted the SERS signal from isolated metallic nanoprisms by 3 orders of magnitude.

We confirm that this high signal is not from an aggregation of nanoprisms by taking an SEM image of the antenna. We explain the Raman enhancement with respect to only nanoprisms on glass substrate by the high directivity from the parabolic antenna and enhanced local fields. In a SERS experiment where the nanoprisms are deposited directly onto glass, the light emission is in favor of the direction into the glass substrate due to higher refractive index of the glass. In comparison, the parabolic antenna gives an emission pattern with a tightly focused lobe into the air, with nearly all emitted light directed into the collecting microscope objective. In other words, we have improved the near- and far-field coupling from a poor efficiency to a nearly perfect efficiency by the

parabolic antenna. Therefore, the 1100× enhancement between the two cases is not surprising.

The 22× SERS enhancement over the planar reflector from our experiment is very encouraging, but is still an underestimate of the parabolic reflector nanoantenna's DERS enhancement potential – still lower than our theoretical prediction of 40× enhancement. This may be due to the misalignment between the Ag nanoprism feed element and the Au parabolic reflector in the nanoantenna. The drop-coating technique is convenient to deposit the Ag nanoprisms; however, exactly controlling the nanoprism position is difficult. In future steps, we plan to build the metal feed element using lithographical methods such as FIB lithography. In that way, the position of the feed element can be precisely controlled, and an even higher SERS enhancement is hypothesized.

Conclusions

We have demonstrated directivity-enhanced Raman scattering (DERS) using directive nanoantennas including parasitic elements, parabolic and waveguide designs. The circular waveguide nanoantenna with a feedgap of 20 nm produces an enhancement factor of 275× as compared to nanopartilces over a glass substrate. This enhancement factor can be further increased by reducing the feedgap. Parabolic reflector results in an overall enhancement factor of 1100× as compared to nanoprisms over a glass substrate; however, as demonstrated in this work, the fabrication of the parabolic structure is more challenging. The enhancement in these waveguide designs is specifically attributed to directivity effects; i.e., beam-shaping the antenna cone to fall within the numerical aperture of the imaging optics. Therefore, DERS is separate from other near-field enhancements that arise, for example, from plasmonic effects. Considering the numerical aperture of our microscope Raman system, the nanoantenna presented has near-perfect excitation and collection of the electromagnetic energy. This work is also exciting for related applications, for example, photovoltaics, light emitting applications, microscopy, sensing and single molecule detection [29, 31, 36].

The authors acknowledge support from NSERC Strategic Network for Bioplasmonic Systems (BiopSys), Canada.

References

[1] P. Bharadwaj, et al., "Optical Antennas," Advances in Optics and Photonics, vol. 1, pp. 438-483, 2009.

[2] H. Yagi, Proc. IRE, vol. 16, pp. 715-741, 1928.

[3] A. Hartschuh, et al., "Tip-enhanced near-field optical microscopy of carbon nanotubes," Analytical and Bioanalytical Chemistry, vol. 394, pp. 1787-1795, Aug 2009.

[4] S. Kawata and Y. Inouye, "Scanning Probe Optical Microscopy Using a Metallic Probe Tip," Ultramicroscopy, vol. 57, pp. 313-317, Feb 1995.

[5] C. Fumeaux, et al., "Measurement of the resonant lengths of infrared dipole antennas," Infrared Physics & Technology, vol. 41, pp. 271-281, Oct 2000.

[6] F. Neubrech, et al., "Resonances of individual metal nanowires in the infrared," Applied Physics Letters, vol. 89, Dec 18 2006.

[7] L. Novotny, "Effective wavelength scaling for optical antennas," Physical Review Letters, vol. 98, Jun 29 2007.

[8] S. B. Hasan, et al., " Relating localized nanoparticle resonances to an associated antenna problem," Physical Review B (in press), 2011.

[9] J. N. Farahani, et al., "Single quantum dot coupled to a scanning optical antenna: A tunable superemitter," Physical Review Letters, vol. 95, Jul 1 2005.

[10] S. Kuhn, et al., "Enhancement of single-molecule fluorescence using a gold nanoparticle as an optical nanoantenna," Physical Review Letters, vol. 97, Jul 7 2006.

[11] T. H. Taminiau, et al., "Optical antennas direct single-molecule emission," Nature Photonics, vol. 2, pp. 234-237, Apr 2008.

[12] A. Sundaramurthy, et al., "Toward nanometer-scale optical photolithography: Utilizing the near-field of bowtie optical nanoantennas," Nano Letters, vol. 6, pp. 355-360, Mar 2006.

[13] A. G. Curto, et al., "Unidirectional Emission of a Quantum Dot Coupled to a Nanoantenna," Science, vol. 329, pp. 930-933, Aug 20 2010.

[14] H. Wang, et al., "Nanorice: A hybrid plasmonic nanostructure," Nano Letters, vol. 6, pp. 827-832, Apr 2006.

[15] D. Dregely, et al., "3D optical Yagi-Uda nanoantenna array," Nature Communications, vol. 2, Apr 2011.

[16] P. Muhlschlegel, et al., "Resonant optical antennas," Science, vol. 308, pp. 1607-1609, Jun 10 2005.

[17] P. J. Schuck, et al., "Improving the mismatch between light and nanoscale objects with gold bowtie nanoantennas," Physical Review Letters, vol. 94, p. 017402, Jan 14 2005.

[18] P. Anger, et al., "Enhancement and quenching of single-molecule fluorescence," Physical Review Letters, vol. 96, Mar 24 2006.

[19] T. Kosako, et al., "Directional control of light by a nano-optical Yagi-Uda antenna," Nature Photonics, vol. 4, pp. 312-315, May 2010.

[20] S. Graells, et al., "Direct Growth of Optical Antennas Using E-Beam-Induced Gold Deposition," Plasmonics, vol. 5, pp. 135-139, Jun 2010.

[21] E. Ozbay, "Plasmonics: Merging photonics and electronics at nanoscale dimensions," Science, vol. 311, pp. 189-193, Jan 13 2006.

[22] S. Wedge, et al., "Coupled surface plasmon-polariton mediated photoluminescence from a top-emitting organic light-emitting structure," Applied Physics Letters, vol. 85, pp. 182-184, Jul 12 2004.

[23] R. Corkish, et al., "Solar energy collection by antennas," Solar Energy, vol. 73, pp. 395-401, 2002.

[24] S. Pillai, et al., "Surface plasmon enhanced silicon solar cells," Journal of Applied Physics, vol. 101, May 1 2007.

[25] H. R. Stuart and D. G. Hall, "Absorption enhancement in silicon-on-insulator waveguides using metal island films," Applied Physics Letters, vol. 69, pp. 2327-2329, Oct 14 1996.

[26] L. Tang, et al., "Nanometre-scale germanium photodetector enhanced by a near-infrared dipole antenna," Nature Photonics, vol. 2, pp. 226-229, Apr 2008.

[27] A. M. Marks, "Device for conversion of light to electric power," U.S. Patent 4,445,050, 1984.

[28] C. C. Neacsu, et al., "Scanning-probe Raman spectroscopy with single-molecule sensitivity," Physical Review B, vol. 73, May 2006.

[29] N. Liu, et al., "Nanoantenna-enhanced gas sensing in a single tailored nanofocus," Nature Materials, vol. 10, pp. 631-636, Aug 2011.

[30] S. A. Maier, "Plasmonic field enhancement and SERS in the effective mode volume picture," Optics Express, vol. 14, pp. 1957-64, Mar 6 2006.

[31] S. Nie and S. R. Emory, "Probing Single Molecules and Single Nanoparticles by Surface-Enhanced Raman Scattering," Science, vol. 275, pp. 1102-6, Feb 21 1997.

[32] H. X. Xu, et al., "Spectroscopy of single hemoglobin molecules by surface enhanced Raman scattering," Physical Review Letters, vol. 83, pp. 4357-4360, Nov 22 1999.

[33] J. Kim, et al., "A single-photon turnstile device," Nature, vol. 397, pp. 500-503, Feb 11 1999.

[34] B. Lounis and W. E. Moerner, "Single photons on demand from a single molecule at room temperature," Nature, vol. 407, pp. 491-493, Sep 28 2000.

[35] T. Kalkbrenner, et al., "Optical microscopy via spectral modifications of a nanoantenna," Physical Review Letters, vol. 95, Nov 11 2005.

[36] C. Hoppener and L. Novotny, "Antenna-based optical imaging of single Ca2+ transmembrane proteins in liquids," Nano Letters, vol. 8, pp. 642-646, Feb 2008.

[37] Q. A. Min, et al., "Substrate-based platform for boosting the surface-enhanced Raman of plasmonic nanoparticles," Optics Express, vol. 19, pp. 1648-1655, Jan 17 2011.

[38] A. Ahmed and R. Gordon, "Directivity Enhanced Raman Spectroscopy Using Nanoantennas," Nano Letters, vol. 11, pp. 1800-1803, Apr 2011.

[39] C. A. Balanis, Antenna theory analysis and design, Third ed. New Jersey: John Wiley and Sons, 2005.

[40] T. Pakizeh and M. Kall, "Unidirectional Ultracompact Optical Nanoantennas," Nano Letters, vol. 9, pp. 2343-2349, Jun 2009.

[41] A. Alu and S. Maslovski, "Power Relations and a Consistent Analytical Model for Receiving Wire Antennas," Ieee Transactions on Antennas and Propagation, vol. 58, pp. 1436-1448, May 2010.

[42] A. Alu and N. Engheta, "Tuning the scattering response of optical nanoantennas with nanocircuit loads," Nature Photonics, vol. 2, pp. 307-310, May 2008.

[43] T. J. Seok, et al., "Radiation Engineering of Optical Antennas for Maximum Field Enhancement," Nano Letters, vol. 11, pp. 2606-2610, Jul 2011.

[44] R. C. Jin, et al., "Photoinduced conversion of silver nanospheres to nanoprisms," Science, vol. 294, pp. 1901-1903, Nov 30 2001.

[45] D. M. Pozar, Microwave Engineering. New York: John Wiley and Sons, 1998.

[46] D. R. Ward, et al., "Electromigrated nanoscale gaps for surface-enhanced Raman spectroscopy," Nano Letters, vol. 7, pp. 1396-1400, May 2007.

[47] J. Theiss, et al., "Plasmonic Nanoparticle Arrays with Nanometer Separation for High-Performance SERS Substrates," Nano Letters, vol. 10, pp. 2749-2754, Aug 2010.

Appendix C: Directivity Enhanced Raman Spectroscopy Using Nanoantennas

(2011, Nano Letters, volume 11, pp 1800-1803)

Directivity Enhanced Raman Spectroscopy Using Nanoantennas

Aftab Ahmed and Reuven Gordon

Department of Electrical and Computer Engineering, University of Victoria, Victoria, British Columbia V8W 3P6, Canada

ABSTRACT: Directing the emission from optical emitters is highly desired for efficient detection and, by reciprocity, efficient excitation as well. As a scattering process, Raman benefits from directivity enhancements in both excitation and emission. Here we demonstrate directivity enhanced Raman scattering (DERS) using a nanoantenna fabricated by focused ion beam milling. The nanoantenna uses a resonant ring-reflector to shape the emitted beam and achieve DERS – this configuration is most similar to a waveguide antenna. The ring reflector boosts the measured Raman signal by a factor of 5.5 (as compared to the ground plane alone), and these findings are in quantitative agreement with comprehensive numerical simulations. The present design is nearly optimal in the sense that almost all the beam power is coupled into the numerical aperture of the microscope. Furthermore, the emission is directed out of the plane, so that this design can be used to achieve DERS using conventional Raman microscopes, which has yet to be achieved with Yagi – Uda and traveling wave antenna designs.

KEYWORDS: Plasmonics, optical antennas, nanoantennas, directivity, Raman scattering

Directed emission and reception of electromagnetic energy has played a vital role in radio and microwave communications, for example, with the Yagi – Uda antenna.[1,2]. In the visible – IR regime, nanoantenna design is modified by plasmonic properties [3-5]. Several works have demonstrated efficient near-field coupling of single emitters to free space radiation using single element optical antennas [6-12]. Radiation patterns of those nanoantennas are typically dipolar in nature resulting in poor directivity, where the maximum radiation intensity in a certain direction is 1.5× that of an isotropic radiator [13]. Improved directivity at optical wavelengths can have tremendous impact in areas such as optical microscopy [14,15], spectroscopy [16-19], sensing [20,21], and applications involving single photon sources [22,23], where efficient collection and

emission is critical. For example, directive emission from quantum dots at optical wavelengths was achieved with the optical equivalent of a Yagi – Uda antenna.[24]. Polarization of the emitted light from single molecules using nanoparticles was studied recently and it was shown that by breaking the dipolar symmetry the polarization of the radiated light can be strongly modulated [25].

Even though directive emission at optical wavelengths has been achieved using multielement nanoantennas [25-30], the radiation patterns of those antennas reveal that the main beam is directed into the substrate; thus they cannot be readily used in an ordinary microscope setup and they require special optical arrangements for excitation of the molecules and collection of the scattered light. To achieve a vertical (i.e., out-of-plane) coupling, the Yagi – Uda design will require stacking of nanorods in direction normal to the substrate, which is challenging. Here we demonstrate a simple single element nanoantenna design with a ground plane and a ring reflector. The resonant beam forming for this antenna design allows for surface-normal directive emission into a numerical aperture comparable to typical microscope configurations; therefore, it is well-suited for microscope setups.

The electromagnetic enhancement of Raman intensity is normally considered in terms of local field enhancement and effects of directivity are typically not taken into account explicitly [31,32]. By using a directive antenna, however, it is possible to increase the coupling to the "feed-gap", thereby allowing of directivity enhanced Raman scattering (DERS). In other words, the goal here is to improve the coupling between the radiative and near-field zones, whereas past approaches have focused on the enhancement of near-field arising from plasmonic resonances, tapers, gaps, and high curvature in the antenna design [32,33]. We calculated enhancement factors arising from local field enhancement (EF_{loc}) and total enhancement taking into account the directional characteristics of the antenna (EF_{tot}) as well. It is established that the observed 5.5× increase in DERS is mainly due to the beam forming capabilities of the antenna and $EF_{loc} = 1.2$.

The main contribution of this work is to demonstrate DERS by means of a directive optical antenna that is well-suited for conventional Raman microscopes (i.e., it is directive to within the numerical aperture of the microscope). We optimize the ring-reflector element to maximize the DERS, and the experimental findings are supported

quantitatively by 3D finite difference time domain (FDTD) simulations, as well as waveguide-antenna theory.

Figure C-1 illustrates the antenna design and its realization. The antenna was designed to be tested under Raman microscopy with excitation laser of $\lambda = 785$ nm. Stokes shifted scattered radiation from Rhodamine 6G dye at $\lambda = 880$ nm was collected using a commercial Raman microscope. The dimensions of different layers and the dipole antenna were calculated to achieve best performance at the mean wavelength of 840 nm. The antenna consists of 130 nm long and 45 nm wide dipole with a 20 nm (measured) feed gap.

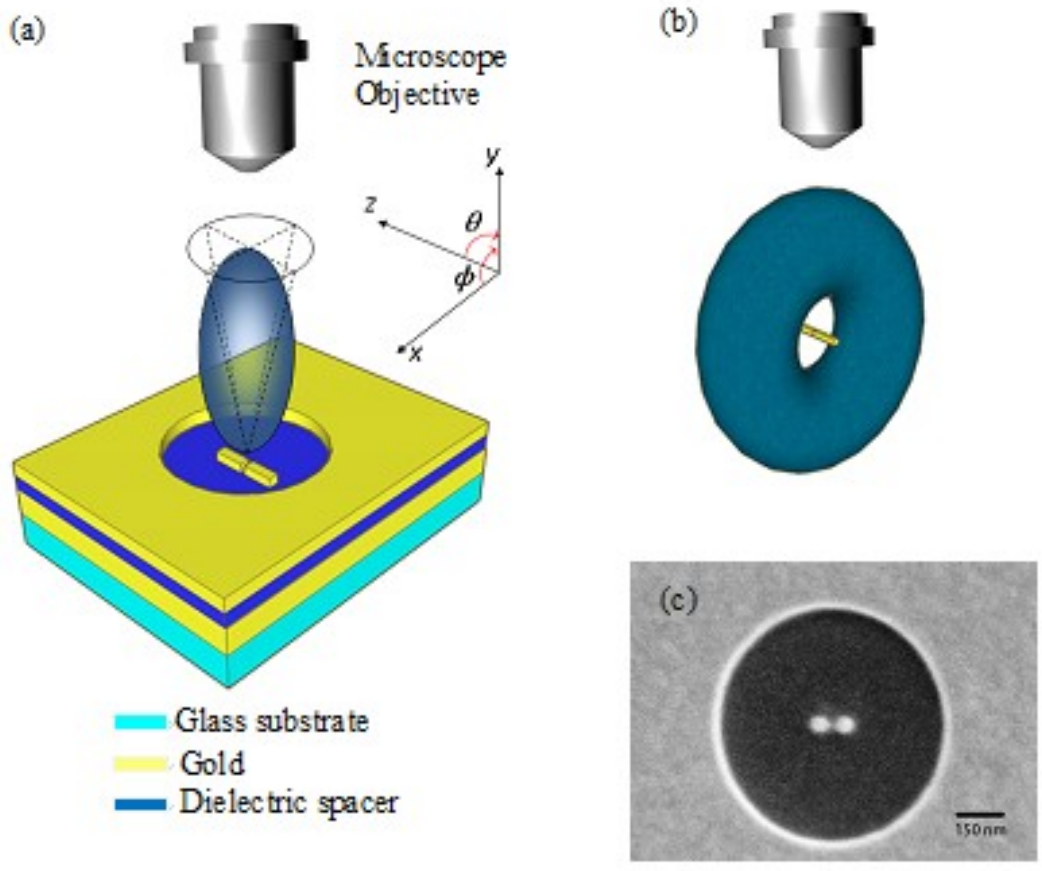

Figure C-1: (a) Multilayer substrate to control the radiation pattern of a dipole antenna, thicknesses of ground plane, dielectric (TiO2) spacer, and top gold layer are 150, 40, and 50 nm, respectively. Dipole antenna length of 130 nm and width 45 nm with a 20 nm feed-gap was used to operate at wavelength of 840 nm; radius of circular reflector for maximum directivity, was found to be 250 nm. (b) Radiation pattern of a dipole antenna. (c) Scanning electron microscopy (SEM) image of the fabricated structure (top view).

Traditionally, dipole antenna characteristic lengths were of the order of wavelength of operation (λ/2), but the real metal response requires that shorter effective wavelengths are introduced for the determination of dipole length in infrared and optical regions [3-5]. A 150 nm thick gold layer was used as ground plane to ensure that it was optically thick. The optimal thickness of dielectric spacer (TiO2) was calculated numerically to be 40 nm using FDTD [34]. The proposed structure was milled in the top 50 nm thick gold layer using focused ion beam (FIB). Further details of the experiment and numerical calculations are found in the Supporting Information.

Figure C-2a shows DERS intensity as a function of Raman shift. The circular reflector with radius of 250 nm resulted in the strongest DERS signal. For comparison detected intensities from dipole over ground and from the unmilled regions of the top gold surface (without any dipole antenna) are also shown. The measured spot size of the microscope of 1.5 μm results in illumination of an area of 1.76 μm^2, which is much larger than the area of the antenna gap. From the results of Figure C-2a, it can be seen that the contribution from the gold surface alone (i.e., without the antenna) is small when compared to that from the antenna. It should be pointed out that the Raman spectra of Figure C-2a show features around 1575 cm^{-1} for the case when there is ring reflector. These features are present in all spectra, but are too weak to be visible in the absence of the ring reflector.

Figure C-2b shows the detected DERS intensity at 1364 cm^{-1} for varying radii of the ring reflector (red triangles) and that from top gold layer without any antenna (dashed black line), normalized to DERS intensity at the same wavenumber from a dipole over ground plane. The dipole over ground plane was fabricated by milling a dipole antenna of the same dimensions and on the same substrate and by removing a ring of diameter 10 μm, to approximate the absence of the ring structure.

The nanoantennas' radiation patterns were investigated numerically using the FDTD method. Field intensities were projected into the far field for the determination of radiation patterns at the mean wavelength of 840 nm. Panels a and b of Figure C-3 show these patterns in the *yz* and *xy* planes, respectively. It can be seen that the radiated power is more directive as compared to a dipole over ground plane and single dipole in free space. From the simulations results, we calculated EF_{tot} of 5.2 and 12.7 for a cone angle

of 30 degrees from the nanoantenna with respect to a dipole over ground and a dipole antenna in free space, respectively. This was found for the nanoantenna with 250 nm radius.

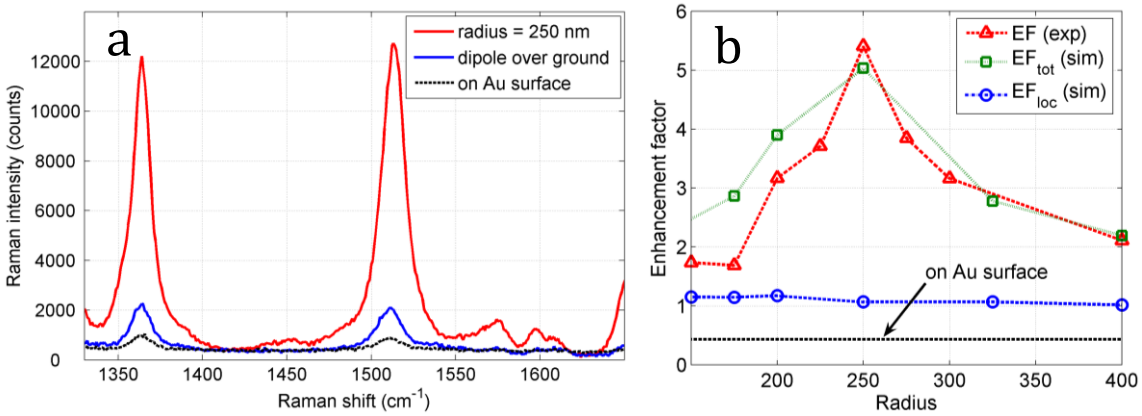

Figure C-2. (a) Rhodamine 6G Raman spectra from the nanoantenna structure with 250 nm radius of circular reflector in comparison with spectra from a dipole over ground plane and from the top gold surface without any antenna. Dye molecules were excited using a laser beam of λ = 785 nm. (b) Enhancement factors obtained from the antenna for various radii of circular reflector with 130 nm long dipole. Experimentally observed EF from peak Raman intensity at 1364 cm_1 (red triangles), EFtot due to directional properties of the antenna and local field effects numerically calculated by FDTD using beam efficiency with cone angle of 30_ (green squares) and EFloc due to local field enhancement only (blue circles). All EFs are normalized to dipole over ground plane. The dashed black line gives the Raman intensity obtained from the top Au surface without any antenna normalized to dipole over ground.

Considering the spot size of the Raman microscope used in the experiment, the numerical aperture was estimated to be 0.26, which corresponds well to that cone angle. Therefore, these enhancement results appear to be in quantitative agreement with the experimental DERS results as shown in Figure C-2b.

EF_{tot} of Figure C-2b was calculated from radiation patterns of Figure C-3 using the beam efficiency (BE)

$$BE = \int_0^{2\pi}\int_0^{\theta} U\sin(\theta)d\theta d\phi \Big/ \int_0^{2\pi}\int_0^{\pi} U\sin(\theta)d\theta d\phi \qquad \text{(C.1)}$$

where U is the radiation intensity per unit solid angle (obtained from Figure C-3) and θ is cone half angle of the collection microscope [13]. A dipole source at the feed gap of the nanoantenna was used to excite the structure, and radiation patterns at the mean wavelength of 840 nm were obtained using far-field projections. It should be noted that

by reciprocity, this captures the enhancement of the excitation as well, thus $EF_{tot} = BE^2$. The numerically calculated enhancement factors of Figure C-2b for varying ring-reflector radius are also in good agreement with those obtained from the DERS experiments.

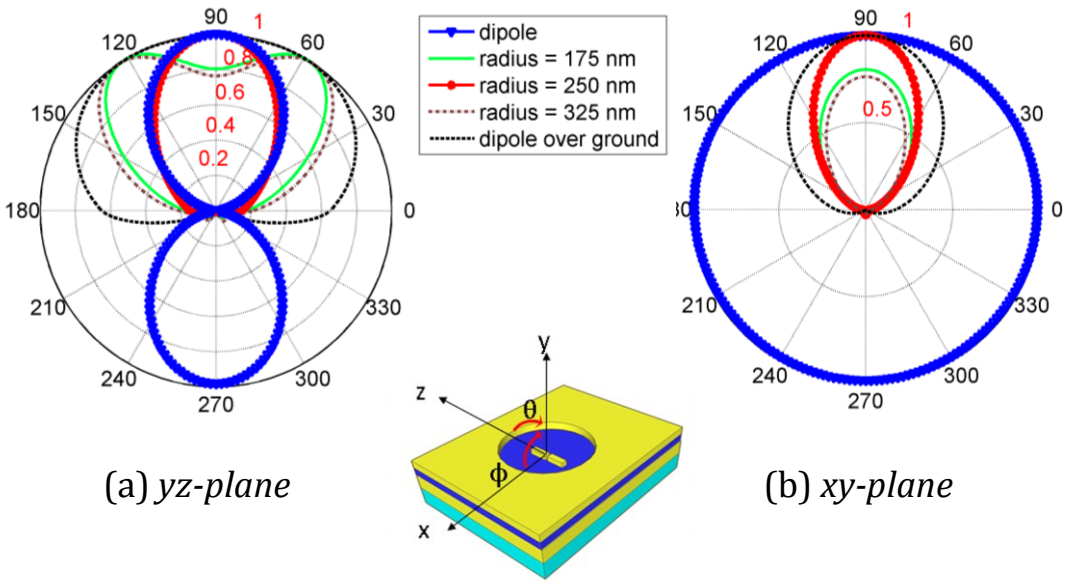

Figure C-3: Radiation patterns of a simple dipole antenna, dipole over ground plane, and the nanoantenna structure for various radii of circular reflector as calculated using far field projections of 3D FDTD simulations. The patterns are normalized to the maximum of *yz* plane: (a) *yz* plane; (b) *xy* plane.

To demonstrate that the observed increase in Raman intensity is mainly from antenna directivity and with only a small contribution from local field enhancement, we calculated the local electric field in the antenna gap. $EF_{loc} = |Eexc|^2 |Escat|^2$, where $|Eexc|^2$ and $|Escat|^2$ are the electric field intensities at the excitation wavelength of 785 nm and Stokes shifted scattered radiation at wavelength of 880 nm, respectively (see Supporting Information). We observe a slight increase in the local fields as compared to a dipole over ground, resulting in $EF_{loc} = 1.2$. The measured 5.5× increase in Raman intensity is thus predominantly from improved directivity of the antenna, as shown in Figure C-3.

The directivity achieved by the ring reflector warrants further discussion, since this is not a typical antenna configuration. The ring reflector acts to create a lateral standing wave that reflects light back toward the central dipole antenna structure. This is most similar to the waveguide antenna, which has a lateral resonance when the wavelength is 3.4 times the radius of the circular waveguide (i.e., at the lowest order mode cutoff) [35,36]. Since the present design is optimized to work at around 840 nm, this corresponds

to a resonance at 250 nm, which is precisely the radius value that was found to give the greatest DERS in the experiment.

The Yagi – Uda design is more directive than our circular lateral reflector design, with emission cones demonstrated of ~15 degrees [24]. We do not view this as a particular shortcoming for DERS, since the primary concern is to effectively couple to within the numerical aperture of the Raman microscope, and for this, the directivity achieved with our design appears to be sufficient. Furthermore, the nanoantenna studied here is readily fabricated to achieve emission out of the plane and into the microscope objective. Past works on Yagi – Uda structures were confined to within the plane, and the emission was only at high angles to the surface normal; therefore, that in-plane design is not practical for Raman microscope use. Similarly, traveling wave antenna structures with broad band unidirectional emission have also been demonstrated recently, but these also emit into the substrate [37]. It is foreseeable that future vertically oriented Yagi – Uda and traveling wave designs may be demonstrated; however, that represents a significant challenge.

In conclusion, we have demonstrated directivity enhanced Raman scattering (DERS) using a directive antenna structure with a ground plane reflector and circular lateral reflector. The circular reflector is an important feature of the nanoantenna design because it allows for 5.5× enhanced Raman as compared to just using the ground plane alone. This enhancement is almost entirely attributed to directivity effects with only a small contribution from local field enhancement, i.e., beam shaping the antenna cone to fall within the numerical aperture of the imaging optics. Therefore, DERS is separate from other near-field enhancements that arise, for example, from plasmonic effects. Considering the numerical aperture of our microscope Raman system, the nanoantenna presented has near-perfect excitation and collection of the electromagnetic energy. This work is also exciting for related light scattering applications, for example, emission/absorption using single molecules and quantum dots [14,15,23].

The authors acknowledge support from the NSERC Strategic Network for Bioplasmonic Systems (BiopSys), Canada.

References

[1] Uda, S. J. Inst. Electr. Eng. Jpn. 273–282, 1926.

[2] Yagi, H. Proc. Inst. Radio Eng. 16, 715–741, 1928.

[3] C. Fumeaux*, et al.*, "Measurement of the resonant lengths of infrared dipole antennas," *Infrared Physics & Technology,* vol. 41, pp. 271-281, 2000.

[4] F. Neubrech*, et al.*, "Resonances of individual metal nanowires in the infrared," *Applied Physics Letters,* vol. 89, 2006

[5] L. Novotny, "Effective wavelength scaling for optical antennas," *Physical Review Letters,* vol. 98, 2007.

[6] J. N. Farahani*, et al.*, "Single quantum dot coupled to a scanning optical antenna: A tunable superemitter," *Physical Review Letters,* vol. 95, 2005.

[7] S. Kuhn, et al., "Enhancement of single-molecule fluorescence using a gold nanoparticle as an optical nanoantenna," Physical Review Letters, vol. 97, 2006

[8] A. Sundaramurthy*, et al.*, "Toward nanometer-scale optical photolithography: Utilizing the near-field of bowtie optical nanoantennas," *Nano Letters,* vol. 6, pp. 355-360, 2006.

[9] D. P. Fromm*, et al.*, "Exploring the chemical enhancement for surface-enhanced Raman scattering with Au bowtie nanoantennas," *Journal of Chemical Physics,* vol. 124, 2006

[10] O. L. Muskens*, et al.*, "Strong enhancement of the radiative decay rate of emitters by single plasmonic nanoantennas," *Nano Letters,* vol. 7, pp. 2871-2875, 2007

[11] R. M. Bakker*, et al.*, "Enhanced localized fluorescence in plasmonic nanoantennae," *Applied Physics Letters,* vol. 92, 2008.

[12] H. Wang*, et al.*, "Nanorice: A hybrid plasmonic nanostructure," *Nano Letters,* vol. 6, pp. 827-832, 2006

[13] C. A. Balanis, Antenna theory analysis and design, Third ed. New Jersey: John Wiley and Sons, 2005

[14] E. Betzig and R. J. Chichester, "Single Molecules Observed by near-Field Scanning Optical Microscopy," Science, vol. 262, pp. 1422-1425, 1993

[15] H. G. Frey, et al., "High-resolution imaging of single fluorescent molecules with the optical near-field of a metal tip," Physical Review Letters, vol. 93, 2004

[16] P. Bharadwaj, et al., "Nanoplasmonic enhancement of single-molecule fluorescence," Nanotechnology, vol. 18, 2007

[17] T. H. Taminiau, et al., "lambda/4 Resonance of an optical monopole antenna probed by single molecule fluorescence," Nano Letters, vol. 7, pp. 28-33, 2007

[18] A. Hartschuh, et al., "High-resolution near-field Raman microscopy of single-walled carbon nanotubes," Physical Review Letters, vol. 90, 2003

[19] S. Nie and S. R. Emory, "Probing Single Molecules and Single Nanoparticles by Surface-Enhanced Raman Scattering," *Science,* vol. 275, pp. 1102-6, 1997.

[20] P. J. Schuck*, et al.*, "Improving the mismatch between light and nanoscale objects with gold bowtie nanoantennas," *Physical Review Letters,* vol. 94, p. 017402, 2005

[21] P. Muhlschlegel*, et al.*, "Resonant optical antennas," *Science,* vol. 308, pp. 1607-1609, 2005

[22] J. Kim*, et al.*, "A single-photon turnstile device," *Nature,* vol. 397, pp. 500-503, 1999.

[23] B. Lounis and W. E. Moerner, "Single photons on demand from a single molecule at room temperature," *Nature,* vol. 407, pp. 491-493, 2000.

[24] A. G. Curto*, et al.*, "Unidirectional Emission of a Quantum Dot Coupled to a Nanoantenna," *Science,* vol. 329, pp. 930-933, 2010

[25] T. Shegai*, et al.*, "Managing light polarization via plasmon-molecule interactions within an asymmetric metal nanoparticle trimer," *P. Natl. Acad. Sci. USA,* vol. 105, pp. 16448-16453, 2008

[26] T. Pakizeh and M. Kall, "Unidirectional Ultracompact Optical Nanoantennas," *Nano Letters,* vol. 9, pp. 2343-2349, 2009.

[27] T. H. Taminiau*, et al.*, "Optical antennas direct single-molecule emission," *Nature Photonics,* vol. 2, pp. 234-237, 2008

[28] T. Kosako*, et al.*, "Directional control of light by a nano-optical Yagi-Uda antenna," *Nature Photonics,* vol. 4, pp. 312-315, 2010

[29] T. H. Taminiau*, et al.*, "Enhanced directional excitation and emission of single emitters by a nano-optical Yagi-Uda antenna," *Opt. Express,* vol. 16, pp. 10858-10866, 2008

[30] D. X. Wang, et al., "Optical antennas integrated with concentric ring gratings: electric field enhancement and directional radiation," Optics Express, vol. 19, pp. 2148-2157, 2011

[31] D. R. Ward*, et al.*, "Electromigrated nanoscale gaps for surface-enhanced Raman spectroscopy," *Nano Letters,* vol. 7, pp. 1396-1400, 2007.

[32] J. Theiss*, et al.*, "Plasmonic Nanoparticle Arrays with Nanometer Separation for High-Performance SERS Substrates," *Nano Letters,* vol. 10, pp. 2749-2754, 2010.

[33] Y. M. Hou*, et al.*, "Surface-enhanced Raman spectroscopy on coupled two-layer nanorings," *Applied Physics Letters,* vol. 96, 2010

[34] Q. A. Min*, et al.*, "Substrate-based platform for boosting the surface-enhanced Raman of plasmonic nanoparticles," *Optics Express,* vol. 19, pp. 1648-1655, 2011

[35] D. M. Pozar, *Microwave Engineering*. New York: John Wiley and Sons, 1998

[36] C. A. Balanis, *Advanced Engineering Electromagnetics*. John Wiley and Sons: New York, 1989.

[37] T. Shegai*, et al.*, "Unidirectional Broadband Light Emission from Supported Plasmonic Nanowires," *Nano Letters,* vol. 11, pp. 706-711, 2011

Supporting Information for Appendix C

Details of fabrication:

The multilayer substrate was prepared by a 7.5 kV electron beam evaporator in an Angstrom Engineering physical vapor deposition system. A 150 nm thick gold layer (ground plane) was coated on a glass substrate. This was then coated with a TiO_2 spacing layer and finally 50 nm thick gold layer was coated on top of the spacer layer. The multilayer substrate was then milled using Hitachi FB-2100 focused ion beam system. The structure was fabricated with a low power beam and a 30-0-30 setting (i.e., 30 kV accelerating voltage, condenser lens mode and beam diameter), at a magnification of $180\text{k}\times$. To cut the top 50 nm thick gold layer, the number of passes set to 5 with a dwell time of 0.5 microseconds (as determined by calibration runs and EDX imaging). The milled structure was then imaged using Hitachi S-4800 scanning electron microscopy system.

Details of Raman measurement:

Raman scattering measurements were carried out using a RENISHAW inVia Raman microscope system. Excitation laser at $\lambda = 785\,\text{nm}$ was used with a $100\times$ objective with a spot size $'d'$ of approximately 1.5 μm (as determined by mapping experiments). Rhodamine 6G (400 μM in ethanol) was drop coated and the sample was allowed to dry for 6 hours. Each spectrum was collected with a total integration time of 42 seconds. Cone angle of 30 degrees was calculated from the spot size using: $\theta = \sin^{-1}(\lambda/2d)$.

Details of simulation:

The proposed structure was simulated using FDTD solutions software by Lumerical Inc. For accurate modeling of the structure, a mesh size of $2\,\text{nm}$ was used. The simulation domain was terminated by perfectly matched layer (PML) for minimal reflections. Gold was modeled by a fit to the experimental data [1] and the refractive index of the TiO_2 was found experimentally.

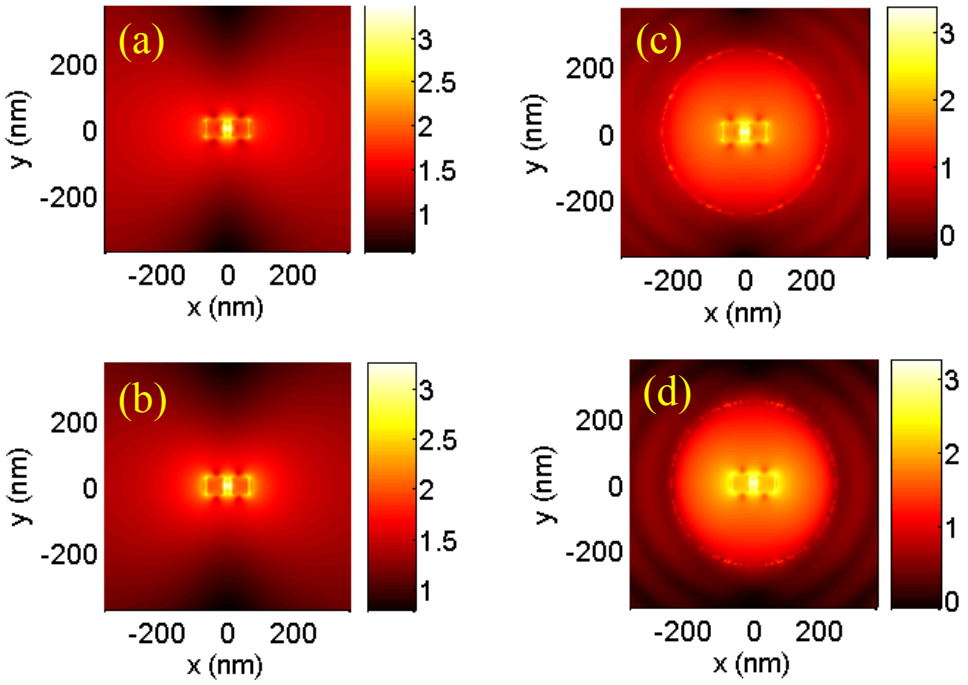

Figure C-S1. (a, b) Electric field intensity profiles at excitation wavelength of 785 nm and at Stokes shifted scattered radiation at wavelength of 880 nm respectively, in the feed gap of the dipole antenna over ground plane without circular ring (log scale). (c, d) Electric field intensity profiles at excitation and scattered wavelength respectively, in the feed gap of the antenna with circular ring of radius 250 nm (log scale).

The antenna structure was enclosed by a set of 2D field monitors to perform far-field projections and for the determination of field patterns. The nanoantenna was excited by an electric dipole source located at the feed-gap of the dipole antenna. To calculate the enhancement factor due to local field effects, the sum of electric field intensity over the 2D monitor of Figure C-S1 was used.

[1] P. B. Johnson and R. W. Christy, "Optical Constants of the Noble Metals," *Physical Review B,* vol. 6, pp. 4370-4379, 1972.

Appendix D: Single Molecule Directivity Enhanced Raman Scattering using Nanoantennas

(2012, Nano Letters, volume 12, pp 2625-2630)

Single Molecule Directivity Enhanced Raman Scattering using Nanoantennas

Aftab Ahmed and Reuven Gordon

Department of Electrical and Computer Engineering, University of Victoria, Victoria, British Columbia V8W 3P6, Canada

ABSTRACT: Single molecule detection by directivity enhanced Raman scattering is demonstrated using nanoantennas. Bi-analyte Raman scattering is used to confirm the detection of single molecules of Rhodamine 6G and Nile Blue A in aqueous solution. Calculations show that Raman enhancement factors of 10^{13} can be achieved by combined optimization of the local field enhancement (hotspot with 10^{11} enhancement) and antenna directionality, (with 10^{2} enhancement).

KEY WORDS: Nanoantenna, SERS, Single molecule detection, directivity.

The single molecule limit is the ultimate sensitivity desired for many scientific and applied areas, such as sensing, analytical chemistry and biomedicine [1, 2]. While fluorescence spectroscopy has long allowed for single molecule detection [3], limited information can be extracted from fluorescence spectra at room temperature. Raman spectroscopy provides more structural information than fluorescence, as well as allowing for a distinct spectrum to provide multiplexed detection within a small spectral window [4, 5]. Raman scattering, however, suffers from extremely low efficiency with typical cross sections from 10^{-28} to 10^{-24} cm^2 per molecule [6, 7], as compared to 10^{-16} cm^2 for fluorescence [8]. To observe the vibration spectra of single molecules, it is necessary to generate an enhancement factor (EF) of 10^{8} (for resonant Raman) to 10^{12}, assuming the same spectral sensitivity.

Since its discovery [9, 10], surface-enhanced Raman scattering (SERS) has been used-widely for enhancing the weak Raman cross section [11]. SERS benefits from the high electric fields at the surface or in the gaps between closely spaced metallic nanoparticles. Assuming a broad spectral enhancement, the EF is commonly estimated as proportional

to the fourth power of the local electric field as compared to the incident electric field. Initial experiments on single molecule SERS reported an enhancement factor of 10^{14} using colloidal silver nanoparticles [6, 12].

Single metal nanoparticles typically do not provide enough EF to achieve SM-SERS and the active SM-SERS sites are the gaps between metallic nanoparticles (i.e., the hotspots) [13], although in some cases their EF can reach 4×10^{9} [14, 15]. Different methods and substrates have been devised for the generation of hotspots [16-31]; however, the best results still come from random structures that have multiple hotspots and suffer from poor reproducibility and uniformity. Few examples exist of top-down fabricated structures that demonstrated EF approaching 10^{8} and 10^{11} that are reproducible [25, 32]. By adding a near-field probe, progress has been made towards single molecule detection using tip enhanced resonance Raman scattering [33, 34].

Recently, we have demonstrated directivity enhanced Raman scattering (DERS), which augments the usual hotspot EF by an additional contribution from the directivity of the nanoantenna [35]. This directivity provides an additional two orders of magnitude EF to the Raman signal because it boosts the coupling of both the incident and scattered photons. Therefore, we claimed previously that DERS is a promising candidate for single molecule Raman detection.

Here we demonstrate single molecules DERS. The single molecule nature of the observed Raman spectra is verified by the bi-analyte technique and the statistical data is analyzed using peak finding algorithm and modified principal component analyses (MPCA) [36, 37]. Comprehensive numerical simulations confirm that the combined directivity and hotspot enhancement factors are sufficiently large to provide reproducible single molecule detection from a top-down fabricated structure with a single (and localized) dominant hotspot.

In our recent works, we have demonstrated the design of a nanoantennas for directional out of the plane coupling [35, 38]. It was shown there that an EF of 50× can be achieved by the introduction of ground plane as compared to a simple nanoparticle over a glass substrate and a further 5× enhancement is observed by the introduction of the circular reflector as compared to a dipole over ground plane. Thus DERS from the “cantenna” (waveguide antenna) design showed an additional EF of 10^{2} from the directivity effect

alone (over and above hotspot enhancements) [35]. Here we demonstrate SM-DERS from the "cantenna" structure, with parameters tuned to operate in solution. The Raman cross section is enhanced by two different factors. First, the small feed-gap between the dipole elements results in high local fields, providing a contribution to the EF of ~10^{11}. This hotspot contribution includes the optimized radiation efficiency of the antenna by appropriate location of the ground-plane, allowing for a factor of 10 enhancement (accounting for both incident and scattered light) [39]. Second, the optimum directional properties of the nanoantenna provide efficient excitation and collection of scattered radiation with the aforementioned 10^2 EF. Thus, an effective EF of 10^{13} is expected from our simulation results, which is sufficient for observing the vibrational spectrum of single molecule.

The fixed single hotspot in the feed-gap of our nanoantenna eliminates the problem of spatial averaging. Colloidal solutions of silver nanoparticles suffer from the averaging effect of many hotspots present in the solution depending on the colloid concentration [12, 36]. Thus the observed spectrum at any given time can be arriving from many dye molecules located in different hotspots in the probed volume. The focused-ion beam (FIB) milled nanoantenna is a reliable SM-SERS substrate with precise control over the dimensions, whereas aggregated colloids are very heterogeneous in nature and show less than 1% SM-SERS active sites [13, 40].

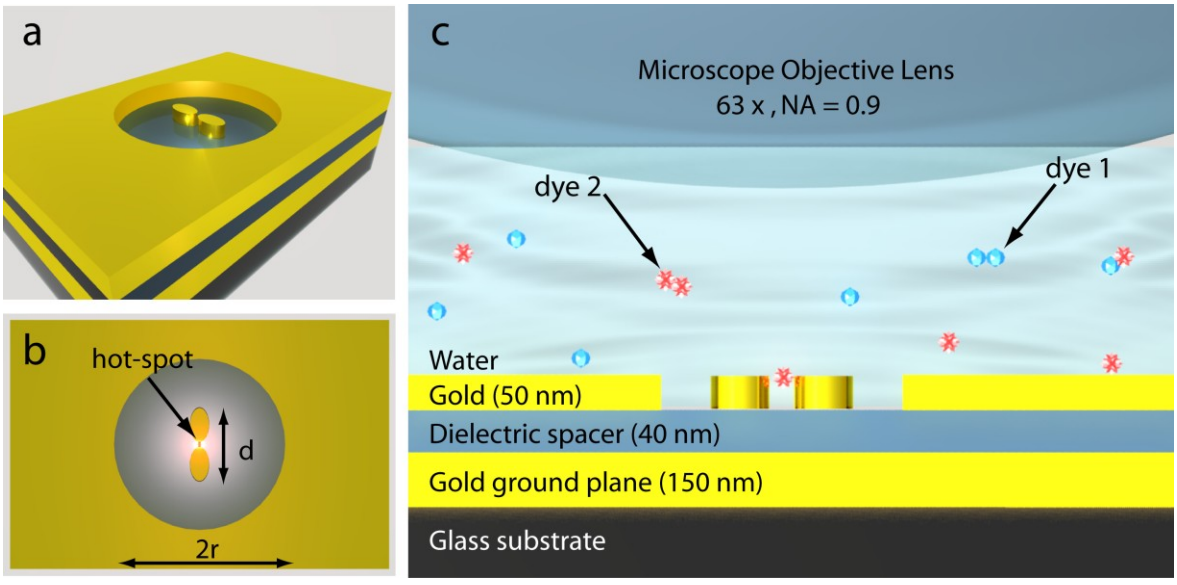

Figure D-1: (a) Schematic of the directional nanoantenna operating at wavelength of 800 nm, total dipole length '*d*' of 80 nm, radius of circular ring, r,

190 nm and a feed-gap of ~6 nm. (b) Top view showing the hotspot. (c) The experimental setup showing two different dyes of same concentration in aqueous solution (not to scale).

A number of design guidelines from classical antenna theory have been translated into the visible/IR regime [38, 39, 41-48]. Figure D-1 shows a schematic of the "cantenna" used in this work. The nanoantenna uses a ground plane reflector to prevent loss of scattered radiation into the substrate. It is critical to place the feed element at the correct height from the ground plane for coherent normal emission and improved radiation efficiency [35, 39]. Furthermore, to shape the radiated beam in the lateral plane, we used a ring reflector around the dipole feed element, as shown in Figure D-1. This design is nearly optimal in the sense that almost all the beam power is coupled into the numerical aperture of the microscope.

Previous works have suggested that temporal fluctuations in SERS intensity are not sufficient evidence for single molecule detection because peak intensities are not quantized for SERS, due to variations in the hotspot [49, 50]. Statistical verification of single molecule sensitivity can be achieved by using two different analytes in solution [36, 51]. Here, Rhodamine 6G (R6G) and Nile Blue A (NBA) dyes were chosen due the close proximity of their Stokes peaks at 610 cm^{-1} and 590 cm^{-1}, and due to their comparable cross-sections [36]. A 200 nM aqueous solution of these dyes was excited by a continuous wave laser of wavelength 785 nm with 6 mW at the sample, well away from resonant excitation. It should be noted that dye concentration of 200 nM revealed the single molecule regime in contrast to the much lower 2 nM concentration of a previous work [36]. This higher concentration does not mean that our approach is not as sensitive since here there is only one hotspot in the excited volume, as compared to many hotspots in past works. In other words, we are limited by the diffusion of molecules into the single hotspot. For the purposes of clear demonstration, this has the benefit of avoiding the inherent inaccuracies associated with extremely low concentrations, such as surface adsorption, contamination and dilution errors [51, 52].

The nanoantenna is designed to operate in an aqueous solution at a wavelength of 800 nm (between the excitation and Stokes wavelengths) and thus the design is modified from our previous work to account for the higher refractive index of water [35]. The dimension scaling is not linear, due to plasmonic effects [41], which requires a more drastic

reduction in dipole length as compared to the value obtained from index division alone. The resulting design parameters calculated by finite difference time domain (FDTD) simulations show best performance with a dipole length of 80 nm (61% of free space design) and a ring reflector radius of 190 nm.

Raman scattering experiments were carried out using a commercial Raman microscope (Renishaw inVia Raman Microscope). Each spectrum was collected with an integration time of 300 ms to minimize temporal averaging effects. A dwell time of one second between consecutive measurements was used to ensure statistical independence. A 63× water immersion microscope objective with numerical aperture (NA) of 0.9 was used. Figure D-2a shows a total of 2000 collected Raman spectra from the aqueous solution of R6G and NBA. This number is sufficiently large for reliable statistical analysis [49, 51]. The Stokes-shifted peaks of R6G and NBA at wavenumbers of 610 cm^{-1} and 590 cm^{-1} can be clearly seen. The intensities at those wavenumbers are plotted in Figure D-2b for clearer presentation. We observe a shift in the peak position, which is typical of the single molecule regime [36].

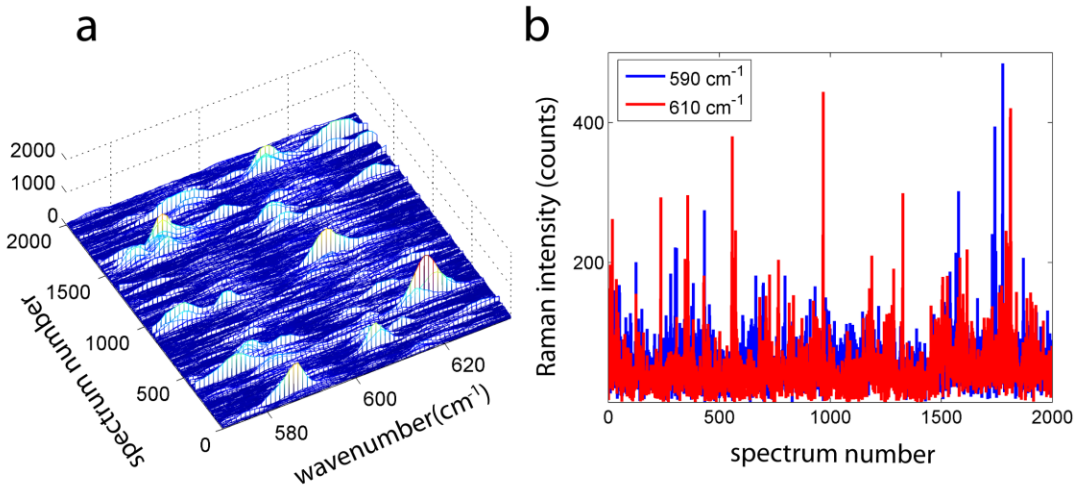

Figure D-2: (a) Raman spectra collected from a 200 nM aqueous solution of Rhodamine 6G and Nile blue A with an integration time of 300 ms and 1 second dwell time between each spectrum. (b) Intensity of Stockes shifted radiation at wavenumbers of 592 cm^{-1} and 610 cm^{-1} as a function of spectra number. Events of single analyte can be clearly seen.

R6G is known to stick to metal surfaces and a number of previous studies have relied on adsorption of the dye molecule [6,12]. Our Raman studies produced signal from R6G lasting for a few seconds typically, indicating that the process of adsorption is reversible.

In recent years, a number of single molecule SERS studies have reported similar fluctuations in R6G spectra attributed to desorption of R6G [53-55]. It has also been suggested that desorption of R6G molecule might be light assisted [56].

We used a peak search algorithm to capture the Raman events. Here each spectrum is divided into two parts by defining a boundary at 600cm^{-1} wavenumber. The spectral region below and above the boundary corresponds to NBA and R6G events. Peak Raman intensity values and their corresponding spectrum number are then computed (I_i^n , $i = 1, 2$ represents the dye and $n = 1 - 2000$ is the spectrum number). The threshold level is defined as double the sum of signal mean and the standard deviation. Events below this threshold level are discarded. Contribution of dye-1 to the total signal can be calculated as $I_1^j / (I_1^j + I_2^j)$ for a given spectrum. If the two dyes have comparable intrinsic SERS cross sections then this ratio also represents the probability of dye-1 p_{dye1} [36]. This procedure is repeated for all the spectra and a histogram for p_{dye1} is generated as shown in Figure D-3a. Single dye events ($p_{dye1} = 1$, $p_{dye1} = 0$) imply that the signal is arriving from either a single molecule or few identical molecules. The very small number of mixed signal events in the histogram of Figure D-3a, suggests that majority of the single dye events are indeed single molecule events with negligible number of events belonging to few identical molecule events. At a higher concentration of 2μM the distribution is predominantly mixed, showing that this is not in the single molecule regime (see Supporting Information).

We also attempted a modified principle component analysis (MPCA) [36, 37]. MPCA typically uses two principal components corresponding to the two largest eigenvalues to represent the dataset. It should be pointed out that spectral shift of Raman peak position causes slightly larger third and fourth eigenvalues as compared to the ideal case without spectral variation [36]. Our calculations show that although only two principal components (i.e., eigenvectors) can capture most events with the result similar to that of Figure D-3a, a significant number of events are missed (see Supporting Information for details).

The observed Raman spectra consist of four different cases. (i) Dye-1 (NBA) events, only Raman peak corresponding to dye-1 is present. (ii) Dye-2 (R6G) events, only

Raman peak corresponding to dye-2 is present. (iii) Mixed events, both Raman peaks are present. (iv) Null events, neither Raman peak is observed.

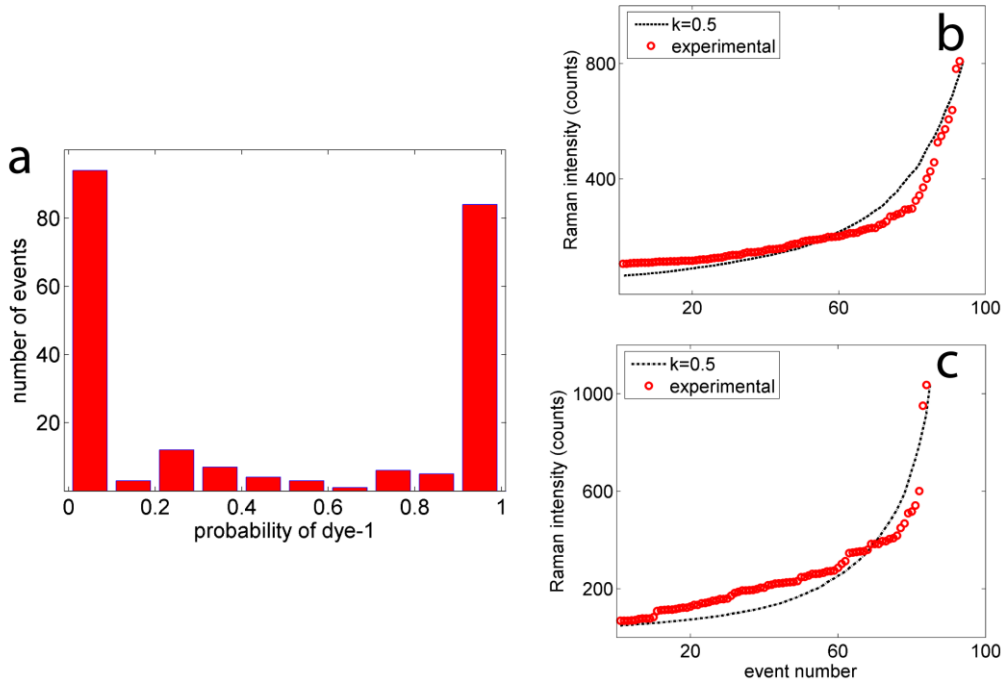

Figure D-3: (a) Probability of dye1 as calculated by peak search algorithm. The large number of single dye events confirms single molecule regime. A total of 219 events are retained from 2000 spectra. (b) Comparison of single molecule (probability of dye-1 < 0.05) Raman intensity distribution to truncated Pareto distribution. (c) Probability of dye-1 > 0.95. The long tail intensity distribution is evident and is comparable to a truncated Pareto distribution with k = 0.5.

The intensity distribution of SM-SERS has been questioned in recent years, the presence of Poisson's or truncated Pareto distribution has been argued [12, 49, 57]. The use of Poisson's distribution in single molecule Raman experiments has been criticized since the SM-SERS intensities are not quantized [49]. SM-SERS exhibits a long tail intensity distribution and thus can be modeled by a truncated Pareto distribution [36, 51, 58]. A random variable X with truncated Pareto distribution can be generated as follows [58]:

$$X = F_{\min}\left(1 - U\left(1 - (F_{\min}/F_{\max})^{k}\right)\right)^{-1/k} \qquad \text{(D.1)}$$

where U is a uniformly distributed random variable over [0,1], $F_{\min}$ and $F_{\max}$ are the minimum and maximum values of the truncated Pareto distribution respectively and k is a positive parameter. In Figure D-3(b, c) we have plotted the observed Raman intensity of

SM-SERS events (probability of dye-1 < 0.05, and probability of dye-1 > 0.95), it can be seen that the observed intensities have a long tail distribution. This distribution is best fit by the Pareto distribution with k = 0.5, but as described elsewhere, the Pareto fit is not exact [21, 36]. Recent experiment on SM-SERS reported a value of k = 1 [36]. The larger k in that experiment was attributed to the heterogeneous nature of the colloidal solution, where enhancements vary significantly from one hotspot to another (spatial averaging effects). The smaller value of observed k here thus supports our claim of minimizing the spatial averaging effect by having a single hotspot.

To experimentally estimate the EF, we have collected ordinary Raman signal from a 200 μM solutions of R6G and NBA with a total integration time of 10 minutes. Scaling appropriately by the collection times and the number of molecules (based on a probed volume of 250 μm^3), these measurements suggest an EF of 3.6×10^{13} for the 610 cm^{-1} mode of R6G and 1.2×10^{13} for the 590 cm^{-1} mode of NBA. The higher EF for R6G is attributed to sticking as discussed above.

Comprehensive FDTD simulations were carried out to estimate the enhancement due to local fields (EF_{loc}) and due to directivity of the nanoantenna (EF_{dir}). The nanoantenna is designed to operate at the wavelength of 800 nm, between the 785 nm laser excitation and the Stokes-shifted radiation at 825 nm. EF_{loc} is proportional to the square of electric field intensity and thus can be estimated as $|E|^4 / |E_0|^4$. It is noted once again that EF_{loc} of 10^{11} is achieved due to the combined effect of small feed-gap and the interaction with the ground plane reflector as shown in Figure D-4a (dot-dashed blue). The optimized distance of 40 nm $\left(\lambda/_{n8}\right)$ where n is the refractive index of the medium, between the dipole feed element and the ground plane results in an optimized radiation efficient design, which is the key for higher local electric fields as demonstrated in the past [39].

The total enhancement factor (EF_{tot}) is the product of EF_{dir} and EF_{loc} and is also shown in Figure D-4a (solid black). The design is optimized to operate at 800 nm and the maximum EF_{tot} is 4.2×10^{13}. It is important to note that directionality will certainly influence the local fields as a consequence of reciprocity theorem if plane wave excitation is used. However our electric dipole source, located at the feed-gap of the nanoantenna and representing a dye molecule, allows for the separation of EF_{dir} from

EF_{loc}. EF_{dir} is calculated by determining the total power emitted from the dipole and the power emitted into the numerical aperture of microscope for two cases: (i) with the full cantenna and (ii) with the dipole antenna on the glass substrate alone (i.e without the ground reflector and ring director elements).

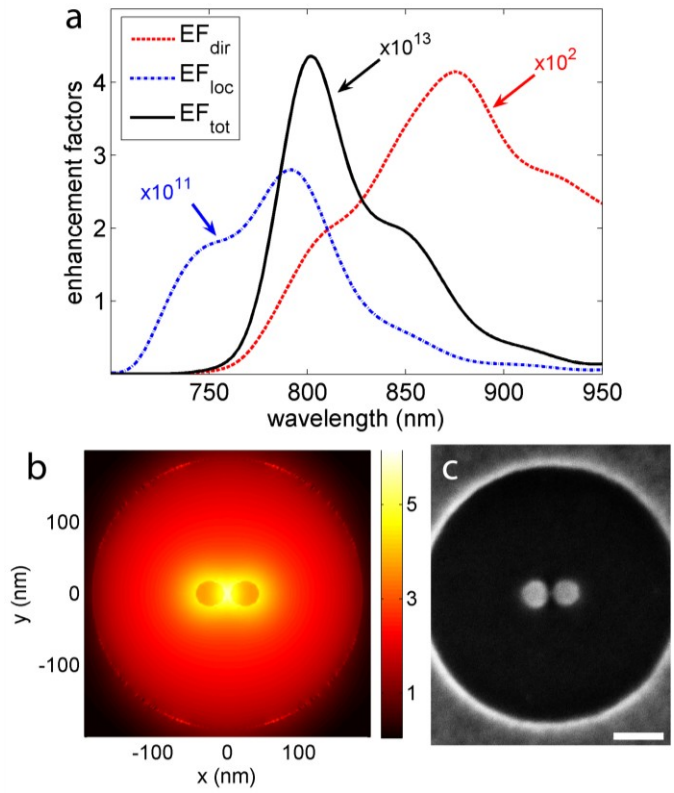

Figure D-4: (a) Enhancement factor directional (dashed red), is the power radiated by the nanoantenna out of the plane of the substrate normalized to that of a dipole over glass substrate. Enhancement factor local (dot-dashed blue) is the normalized electric field intensity square $|E|^4 / |E_0|^4$, it goes as high as 10^{11} due to small feed-gap and ground reflector. Total enhancement (solid black) is the product of directional and local EFs. It is seen that at the design wavelength of 800 nm the total EF of 4.2×10^{13} is estimated. (b) Normalized electric field intensity $|E|^2 / |E_0|^2$ profile (log scale) at the design wavelength of 800 nm to influence both the excitation laser at 785 nm and the Stokes shifted radiation at 825nm. (b) Scanning electron microscopy image of the fabricated nanoantenna with feed-gap of ~6 nm, dipole length and width of 80 nm and 35 nm respectively. The scale bar is 90 nm.

Figure D-4b shows the normalized electric field intensity $|E|^2 / |E_0|^2$ profile over the cross section of the nanoantenna at wavelength of 800 nm. A scanning electron microscopy (SEM) image of the fabricated nanoantenna is shown in Figure D-4c.

In conclusion, we have demonstrated single molecule directivity enhanced Raman scattering using nanoantenna fabricated by a top-down approach, taking advantage of high local field and directional characteristics of the nanoantenna. The single antenna hotspot (feed-gap) avoids the issue of spatial averaging effects found in past single molecule approaches. This work is promising for ultra-sensitive Raman substrates fabricated by top-down means. For situations where lower concentrations are desired, additional antennas may be added to increase the number of hot-spots, which suggests an opportunity to use antenna array concepts in future designs. It is interesting to note that resonant Raman studies may achieve single molecule sensitivity for larger lithographically defined gaps by using directivity since EFs of only $10^8 – 10^9$ are required [8].

The authors acknowledge support from the NSERC Strategic Network for Bioplasmonic Systems (BiopSys), Canada.

References:

[1] J. K. T. X. S. Xie, "Optical studies of single molecules at room temperature," Annu. Rev. Phys. Chem., vol. 49, 1998.

[2] F. Kulzer and M. Orrit, "Single-molecule optics," Annu. Rev. Phys. Chem., vol. 55, pp. 585-611, 2004.

[3] R. A. Keller, et al., "Single molecule fluorescence analysis in solution," Appl. Spectroscopy, vol. 50, pp. A12-A32, Jul 1996.

[4] Y. C. Cao, et al., "Raman dye-labeled nanoparticle probes for proteins," J. Am. Chem. Soc., vol. 125, pp. 14676-14677, Dec 3 2003.

[5] L. Sun, et al., "Surface-enhanced raman scattering based nonfluorescent probe for multiplex DNA detection," J. Anal. Chem., vol. 79, pp. 3981-3988, Jun 1 2007.

[6] S. M. Nie and S. R. Emery, "Probing single molecules and single nanoparticles by surface-enhanced Raman scattering," Science, vol. 275, pp. 1102-1106, 1997.

[7] S. Shim and R. A. Mathies, "Development of a tunable femtosecond stimulated Raman apparatus and its application to beta-carotene," J. Phys. Chem. B, vol. 112, pp. 4826-4832, Apr 17 2008.

[8] N. P. W. Pieczonka and R. F. Aroca, "Single molecule analysis by surfaced-enhanced Raman scattering," Chem. Soc. Rev., vol. 37, pp. 946-954, 2008.

[9] M. G. Albrecht and J. A. Creighton, "Anomalously intense Raman spectra of pyridine at a silver electrode," J. Am. Chem. Soc., vol. 99, pp. 5215-5217, 1977/06/01 1977.

[10] D. L. Jeanmaire and R. P. Vanduyne, "Surface Raman Spectroelectrochemistry .1. Heterocyclic, Aromatic, and Aliphatic-Amines Adsorbed on Anodized Silver Electrode," J. Electroanal. Chem., vol. 84, pp. 1-20, 1977.

[11] K. Kneipp, et al., Surface-enhanced Raman scattering physics and applications. New York: Springer, 2006.

[12] K. Kneipp, et al., "Single molecule detection using surface-enhanced Raman scattering (SERS)," Phys. Rev. Lett., vol. 78, pp. 1667-1670, 1997.

[13] J. P. Camden, et al., "Probing the structure of single-molecule surface-enhanced Raman scattering hot spots," J. Am. Chem. Soc., vol. 130, pp. 12616-+, Sep 24 2008.

[14] F. Hao, et al., "Plasmon resonances of a gold nanostar," Nano Lett., vol. 7, pp. 729-732, Mar 2007.

[15] C. L. Nehl, et al., "Optical properties of star-shaped gold nanoparticles," Nano Lett., vol. 6, pp. 683-688, Apr 2006.

[16] M. Moskovits, "Surface-Roughness and Enhanced Intensity of Raman-Scattering by Molecules Adsorbed on Metals," J. Chem. Phys., vol. 69, pp. 4159-4161, 1978.

[17] H. W. Liu, et al., "Single molecule detection from a large-scale SERS-active Au(79)Ag(21) substrate," Sci. Rep., vol. 1, 2011.

[18] J. F. Li, et al., "Shell-isolated nanoparticle-enhanced Raman spectroscopy," Nature, vol. 464, pp. 392-395, Mar 18 2010.

[19] Y. Fang, "Measurement of the distribution of site enhancements in surface-enhanced Raman scattering (vol 321, pg 388, 2008)," Science, vol. 322, pp. 1790-1790, Dec 19 2008.

[20] P. Johansson, et al., "Surface-enhanced Raman scattering and fluorescence near metal nanoparticles," Phys. Rev. B, vol. 72, Jul 2005.

[21] E. C. Le Ru, et al., "Enhancement factor distribution around a single surface-enhanced Raman scattering hot spot and its relation to single molecule detection," J. Chem. Phys., vol. 125, Nov 28 2006.

[22] D.-K. Lim, et al., "Nanogap-engineerable Raman-active nanodumbbells for single-molecule detection," Nat. Mater., vol. 9, pp. 60-67, 2010.

[23] H. Wang, et al., "Nanosphere arrays with controlled sub-10-nm gaps as surface-enhanced Raman spectroscopy substrates," J. Am. Chem. Soc., vol. 127, pp. 14992-14993, Nov 2 2005.

[24] S. Lal, et al., "Profiling the near field of a plasmonic nanoparticle with Raman-based molecular rulers," Nano. Lett., vol. 6, pp. 2338-2343, Oct 11 2006.

[25] D. R. Ward, et al., "Electromigrated nanoscale gaps for surface-enhanced Raman spectroscopy," Nano Lett., vol. 7, pp. 1396-1400, May 2007.

[26] L. L. Tay, Towards Near-field Single Molecule Surface Enhanced Raman Scattering Detection [microform]: University of Toronto, 2001.

[27] M. Moskovits, et al., SERS and the single molecule. Berlin: Springer, 2002.

[28] S. Balint, et al., "Simple Route for Preparing Optically Trappable Probes for Surface-Enhanced Raman Scattering," Journal of Physical Chemistry C, vol. 113, pp. 17724-17729, Oct 15 2009.

[29] M. G. Banaee and K. B. Crozier, "Mixed Dimer Double-Resonance Substrates for Surface-Enhanced Raman Spectroscopy," ACS Nano, vol. 5, pp. 307-314, 2011/01/25 2010.

[30] A. Lesuffleur, et al., "Periodic nanohole arrays with shape-enhanced plasmon resonance as real-time biosensors," Applied Physics Letters, vol. 90, pp. 243110-3, 2007.

[31] A. Lee, et al., "Probing Dynamic Generation of Hot-Spots in Self-Assembled Chains of Gold Nanorods by Surface-Enhanced Raman Scattering," Journal of the American Chemical Society, vol. 133, pp. 7563-7570, 2011/05/18 2011.

[32] N. A. Hatab, et al., "Free-Standing Optical Gold Bowtie Nanoantenna with Variable Gap Size for Enhanced Raman Spectroscopy," Nano Letters, vol. 10, pp. 4952-4955, 2010.

[33] K. F. Domke, et al., "Toward Raman fingerprints of single dye molecules at atomically smooth Au(111)," J. Am. Chem. Soc., vol. 128, pp. 14721-14727, Nov 15 2006.

[34] A. Weber-Bargioni, et al., "Hyperspectral Nanoscale Imaging on Dielectric Substrates with Coaxial Optical Antenna Scan Probes.," Nano Letters, vol. 11, pp. 1201-1207, Mar 2011.

[35] A. Ahmed and R. Gordon, "Directivity Enhanced Raman Spectroscopy Using Nanoantennas," Nano Lett., vol. 11, pp. 1800-1803, Apr 2011.

[36] P. G. Etchegoin, et al., "Statistics of single-molecule surface enhanced Raman scattering signals: Fluctuation analysis with multiple analyte techniques," Anal. Chem., vol. 79, pp. 8411-8415, Nov 1 2007.

[37] I. T. Jolliffe, Principal component analysis, 2nd ed. New York: Springer, 2002.

[38] Q. A. Min, et al., "Substrate-based platform for boosting the surface-enhanced Raman of plasmonic nanoparticles," Opt. Express, vol. 19, pp. 1648-1655, Jan 17 2011.

[39] T. J. Seok, et al., "Radiation Engineering of Optical Antennas for Maximum Field Enhancement," Nano Lett., vol. 11, pp. 2606-2610, Jul 2011.

[40] K. A. Bosnick, et al., "Fluctuations and local symmetry in single-molecule rhodamine 6G Raman scattering on silver nanocrystal aggregates," J. Phys. Chem. B, vol. 106, pp. 8096-8099, Aug 22 2002.

[41] L. Novotny, "Effective wavelength scaling for optical antennas," Phys. Rev. Lett., vol. 98, Jun 29 2007.

[42] P. J. Schuck, et al., "Improving the mismatch between light and nanoscale objects with gold bowtie nanoantennas," Phys. Rev. Lett., vol. 94, Jan 14 2005.

[43] A. G. Curto, et al., "Unidirectional Emission of a Quantum Dot Coupled to a Nanoantenna," Science, vol. 329, pp. 930-933, Aug 20 2010.

[44] D. Dregely, et al., "3D optical Yagi-Uda nanoantenna array," Nat. Communications, vol. 2, Apr 2011.

[45] T. H. Taminiau, et al., "Enhanced directional excitation and emission of single emitters by a nano-optical Yagi-Uda antenna," Opt. Express, vol. 16, pp. 10858-10866, Jul 7 2008.

[46] T. Shegai, et al., "Managing light polarization via plasmon-molecule interactions within an asymmetric metal nanoparticle trimer," P. Natl. Acad. Sci. USA, vol. 105, pp. 16448-16453, Oct 28 2008.

[47] Y. Chu, et al., "Beamed Raman: directional excitation and emission enhancement in a plasmonic crystal double resonance SERS substrate," Opt. Express, vol. 19, pp. 20054-20068, 2011.

[48] R. U. Tok, et al., "Unidirectional broadband radiation of honeycomb plasmonic antenna array with broken symmetry," Optics Express, vol. 19, pp. 22731-22742, Nov 7 2011.

[49] P. G. Etchegoin, et al., "Statistics of single molecule SERS signals: is there a Poisson distribution of intensities?," Phys. Chem. Chem. Phys., vol. 9, pp. 3006-3010, 2007.

[50] P. C. Andersen, et al., "Flashy silver nanoparticles," J. Phys. Chem. B, vol. 108, pp. 2148-2153, Feb 19 2004.

[51] E. C. Le Ru, et al., "Proof of single-mokeule sensitivity in surface enhanced Raman scattering (SERS) by means of a two-analyte technique," J. Phys. Chem. B, vol. 110, pp. 1944-1948, 2006.

[52] P. Hildebrandt and M. Stockburger, "Surface-enhanced resonance Raman spectroscopy of Rhodamine 6G adsorbed on colloidal silver," The Journal of Physical Chemistry, vol. 88, pp. 5935-5944, 1984/11/01 1984.

[53] L. Zeiri, et al., "Silver Nanoparticles Deposited on Porous Silicon as a Surface-Enhanced Raman Scattering (SERS) Active Substrate," Appl. Spectrosc., vol. 66, pp. 294-299, 2012.

[54] A. Weiss and G. Haran, "Time-Dependent Single-Molecule Raman Scattering as a Probe of Surface Dynamics," The Journal of Physical Chemistry B, vol. 105, pp. 12348-12354, 2001/12/01 2001.

[55] M. Futamata, et al., "Microscopic morphology and SERS activity of Ag colloidal particles," Vibrational Spectroscopy, vol. 30, pp. 17-23, 2002.

[56] J. C. Tully, "Chemical dynamics at metal surfaces," Annu. Rev. Phys. Chem., vol. 51, p. 153, 2000.

[57] K. Kneipp and H. Kneipp, "Two-photon excited surface-enhanced Raman scattering," Surface-Enhanced Raman Scattering: Physics and Applications, vol. 103, pp. 183-196, 2006.

[58] L. Zaninetti and M. Ferraro, "On the truncated Pareto distribution with applications," Cent. Eur. J. Phys., vol. 6, pp. 1-6, Mar 2008.

Supporting Information for Appendix D

Details of fabrication:

Electron beam evaporator (Angstrom Engineering) was used for the evaporation of the multilayer substrate. A 150 nm thick gold layer (ground plane) was coated on a glass substrate. This was then coated with a 40 nm TiO_2 spacer layer and finally 50 nm thick gold layer was coated on top of the spacer layer. The top gold layer was then milled using Hitachi FB-2100 focused ion beam system. The structure was fabricated with a low power beam to mill a very small feed-gap (30-0-30 setting - kV accelerating voltage - condenser lens mode - beam diameter), at a magnification of $180\text{k}\times$. To cut the top 50 nm thick gold layer, the number of passes set to 5 with a dwell time of 0.5 microseconds (as determined by calibration runs and EDX imaging). The milled structure was then imaged using Hitachi S-4800 scanning electron microscopy system.

Details of Raman measurement:

Raman scattering measurements were carried out using a Renishaw inVia Raman Microscope system. Excitation laser at $\lambda = 785$ nm was used with a $63\times$ water immersion objective and a numerical aperture of 0.9. The nanoantenna was immersed in a 200 nM aqueous solution of Nile blue A and Rhodamine 6G. Each spectrum was collected with a total integration time of 300 ms to minimize the effects of temporal averaging and 1sec interval between consecutive spectra to ensure statistical independence of the spectra.

Data analysis using modified principal component analysis (MPCA):

It is not the purpose of this supporting information to explain the details of modified principal component analysis (MPCA), instead here we will briefly describe the steps taken to analyze the data. For details of MPCA the reader should see [1].

A rectangular matrix of size $(T \times N)$ is formed from the collected spectra, where T is the number of spectra and N is the number of wavelengths. Following the steps of MPCA we calculate the eigenvalues and eigenvectors. Figure D-S1(a) shows the eigenvalues of the collected data. It should be noted that spectral variations in the observed Raman peaks gives rise to slightly higher values for third and fourth eigenvalues. As mentioned in the main text, this requires the inclusion of at least the first four eigenvectors to represent the entire dataset accurately. Figure D-S1(b-d) shows

events of NBA and R6G where it is demonstrated that in some cases two eigenvector are sufficient but they fail to represent accurately the entire data.

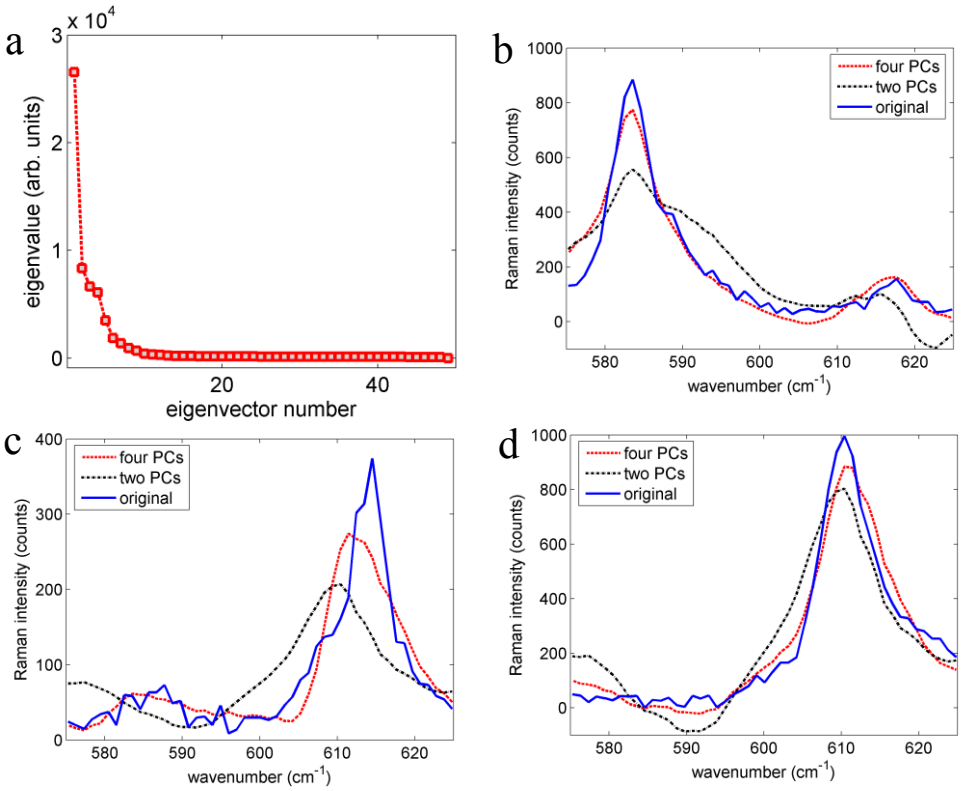

Figure D-S1: (a) Eigenvalues of the collected 2000 spectra with 49 wavenumbers, the first two eigenvalues dominates the response, slightly higher values for 3rd and 4th eigenvalues due to spectral variations of Raman peaks. (b-d) Reconstruction of a Nile Blue A and Rhodamine 6G events using only first two and first four eigenvectors. (b) and (c) shows the events that cannot be accurately reconstructed using only the first two eigenvectors whereas (d) demonstrates the case where two eigenvectors are enough for the reconstruction of original spectrum.

Probability of dye-1 was calculated using the magnitude ratio of the two independent components as given in Ref. 1. A total of 91 events were retained as shown in Figure D-S2 in comparison to 219 events obtained from the peak search algorithm.

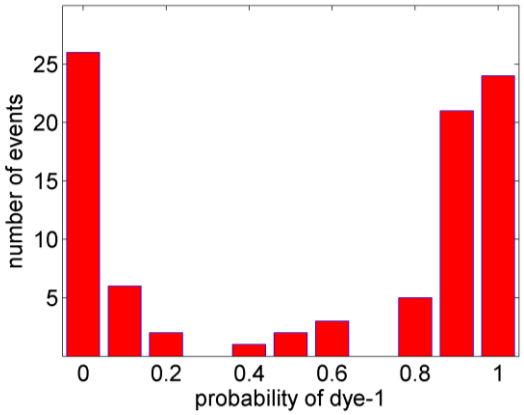

Figure D-S2: Probability of dye-1 calculated by MPCA from a 200 nM aqueous solution of Nile blue A and Rhodamine 6G. A total of 91 events were retained from 2000 spectra.

Mixed events regime (higher concentration of dyes):

Statistical analysis of the observed Raman signal shows that an increase in the analyte concentration results in a shift from single molecule regime to mixed events regime. Figure D-S3 shows the probability of Nile blue A from a 2 μM solution using peak search algorithm. In this case, most events show contribution from both of the dyes with negligible number of single dye events.

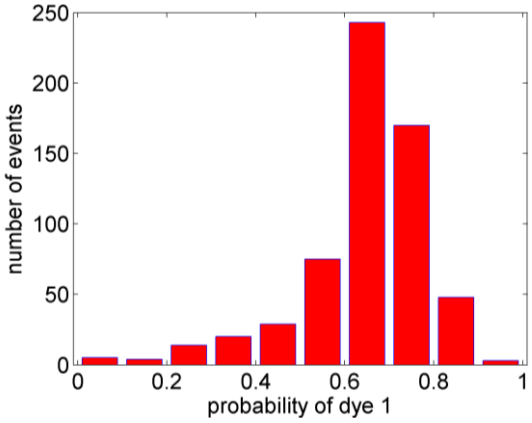

Figure D-S3: Probability of dye-1 calculated by peak search algorithm from a 2 uM aqueous solution of Nile blue A and Rhodamine 6G. A total of 161 events were retained from 2250 spectra.

Experimental enhancement factor:

The ordinary Raman signal I_{OR} was collected from a 200 μM aqueous solution of R6G and NBA for the determination of enhancement factor. A total integration time of 10 minutes was used to collect an observable Raman signal. I_{OR} was normalized to the signal

obtained from a water solution without the dyes to remove the huge fluorescence background. Figure D-S4 shows a comparison of the observed Raman intensities with and without the nanoantenna. I_{DERS} was collected from a 200 nM sample with 300 ms integration time and it is normalized to the average background level for comparison with the normalized $I_{OR.}$ We estimate an EF of approximately 10^{10} from these values.

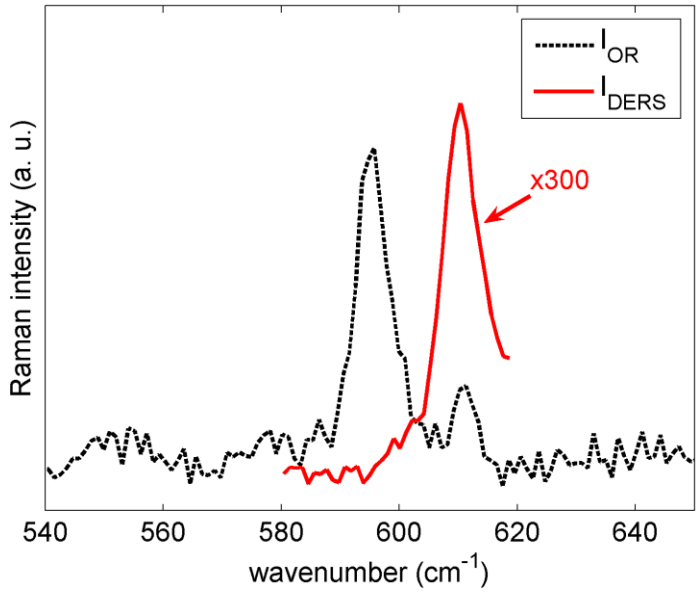

Figure D-S4: Comparison of Raman intensities with and without the nanoantenna for the calculation of EF. I_{DERS} was collected from a 200 nM sample with 300 ms integration and it is normalized to the average background level for comparison with the normalized $I_{OR.}$ I_{OR} is obtained from a 200 μM solution with total integration time of 10 minutes.

Details of simulation:

The proposed structure was simulated using FDTD solutions software by Lumerical Solutions Inc. For accurate modeling of the structure, a mesh size of 1.3 nm was used. The simulation domain was terminated by perfectly matched layer (PML) for minimal reflections. Gold was modeled by a fit to experimental data [2]. The nanoantenna was excited by an electric dipole source located at the feed-gap of the dipole antenna. To calculate the enhancement factor due to local field effects, a 2D electric field intensity monitor was used.

[1] P. G. Etchegoin*, et al.*, "Statistics of single-molecule surface enhanced Raman scattering signals: Fluctuation analysis with multiple analyte techniques," *Anal. Chem.,* vol. 79, pp. 8411-8415, Nov 1 2007.

[2] P. B. Johnson and R. W. Christy, "Optical Constants of the Noble Metals," *Physical Review B,* vol. 6, pp. 4370-4379, 1972.

Appendix E: Probing Dynamic Generation of Hot-Spots in Self-Assembled Chains of Gold Nanorods by Surface-Enhanced Raman Scattering

(2011, Journal of the American Chemical Society, volume 133, pp 7563-7570)

Probing Dynamic Generation of Hot-Spots in Self-Assembled Chains of Gold Nanorods by Surface-Enhanced Raman Scattering

Anna Lee,† Gustavo F. S. Andrade,‡ Aftab Ahmed,§ Michele L. Souza,‡ Neil Coombs,† Ethan Tumarkin,† Kun Liu,† Reuven Gordon,*,§ Alexandre G. Brolo,*,‡ and Eugenia Kumacheva*,†

†Department of Chemistry, University of Toronto, 80 Saint George Street, Toronto, Ontario M5S 3H6, Canada

‡Department of Chemistry, University of Victoria, P.O. Box 3065, Victoria, British Columbia V8W 3V6, Canada

§Department of Electrical and Computer Engineering, University of Victoria, Victoria, British Columbia V8W 3P6, Canada

ABSTRACT: Further progress in the applications of self-assembled nanostructures critically depends on developing a fundamental understanding of the relation between the properties of nanoparticle ensembles and their time-dependent structural characteristics. Following dynamic generation of hot-spots in the self-assembled chains of gold nanorods, we established a direct correlation between ensemble-averaged surface-enhanced Raman scattering and extinction properties of the chains. Experimental results were supported with comprehensive finite-difference time-domain simulations. The established relationship between the structure of nanorod ensembles and their optical properties provides the basis for creating dynamic, solution-based, plasmonic platforms that can be utilized in applications ranging from sensing to nanoelectronics.

Introduction

Organization of individual nanoparticles (NPs) into hierarchical nanostructures—superlattices or small clusters—constitutes a frontier area of research in nanoscience. While NPs alone offer many scientific challenges and applications, ensembles of NPs show unique coupled properties that potentially can be exploited in functional nanoscale devices [1-6]. Self-assembly of NPs offers a simple, cost-efficient, solutionbased method for producing ensembles of NPs, as well as the ability to fabricate nanostructures on nonplanar substrates [7-12]. Currently, self-assembled nanostructures composed of metal,

semiconductor, and magnetic NPs have shown applications in the areas of data storage, imaging, and sensing of chemical and biochemical species [13-21]. The utilization of self-assembled nanostructures in other applications, in comparison with those produced by nanofabrication techniques, is limited by the difficulty in generating defect-free structures with precisely controlled geometry and distance between the NPs. Furthermore, fundamental understanding has to be developed on the relationship between the properties of self-assembled NP clusters and their dynamic structural characteristics such as aggregation number, mutual NP orientation, and interparticle distance. With this framework in place, it would be possible to predict the properties of self-assembled structures, both theoretically and practically, in a reproducible fashion.

In the particular case of metal nanocrystals, gold NPs with various shapes have been organized in a broad range of nanostructures including chains, two-dimensional sheets, and superlattices [22-26]. In comparison with isotropic, shape-symmetric NPs, the self-assembly of gold nanorods (NRs) leads to more interesting, and potentially more useful applications, as it provides the ability to exploit vectorial properties of the resulting nanostructures [27-29]. Typically, optical properties of ensembles of gold NRs are characterized by measurements of extinction in the visible and near-infrared (NIR) spectral ranges. Individual gold NRs show two types of localized surface plasmon resonances (LSPRs), due to the coherent oscillations of the conduction band electrons in directions that are parallel and perpendicular to the long NR axis [30, 31]. End-to-end assembly of gold NRs in chains leads to the coupling of alternating dipoles along the chain, which results in a red shift of the longitudinal LSPR. Side-by-side assembly of NRs results in a blue shift of longitudinal LSPR and a red shift of the transverse LSPR [30, 32, 33].

Coupling of LSPRs in chains of gold NRs results in the formation of a periodic array of enhanced electric fields (hotspots) in the spaces between the NR ends. Thus, self-organization of gold NRs offers a tool for studies of optical properties of ordered NR ensembles by surface-enhanced Raman scattering (SERS). Furthermore, the dynamic self-assembly of NRs in welldefined, one-dimensional nanostructures provides the ability to explore the role of order in NR ensembles on their SERS properties. Currently, the majority of studies of hot-spots have been carried out for NP assemblies with a limited

degree of order [34-36], which led to the insufficient understanding of the effect of structural characteristics of the aggregates on their SERS properties. In addition, research has been focused on isolated NP aggregates ("single particle" SERS), and an understanding of the properties of the system comprised of many NP assemblies remains elusive. In an attempt to achieve greater control over hot-spot generation in NP clusters, recent studies have focused on SERS of self-assembled dimers and trimers of spherical gold NPs in single-aggregate and ensemble-averaged systems [37-39]. However, currently, only a single report exists on the generation of hot-spots in self-assembled chains of gold NRs. This report is focused on the reorientation of analyte molecules in the gaps between NR ends [40].

Here we report the results of experimental and theoretical studies of the relationship between the dynamic structural characteristics of self-assembled clusters of gold NRs and their ensemble-averaged SERS properties resulting from the controlled generation of plasmonic electromagnetic hot-spots. We took advantage of the geometrical and chemical anisotropy of NRs to induce their assembly in chains in an end-to-end fashion. In the course of assembly, the dielectric environment and the spacing between adjacent NRs remained constant. The process was monitored by correlating the average aggregation number of NRs in the chains with their extinction and ensemble-averaged SERS signals (presently, such a correlation has been demonstrated only for nanostructures fabricated by the top-down method) [41, 42]. The experimental findings were supported by the results of finite-difference time-domain simulations of the optical properties of NR assemblies. Our work establishes a strong link between experiment and theory, and it provides an important insight into the properties of hot-spots in ordered, solution-based nanostructures. In addition to the fundamental importance of these results, the established relationship between the structure of NR assemblies and their optical properties provides the basis for the development of new design rules for the generation of nanostructures with applications spanning from biomedicine to nanoelectronics.

Experimental Section

Synthesis of Gold NRs.

Gold NRs were prepared by the "seedmediated growth method" devised by El-Sayed et al. [43]. Briefly, seed NPs were obtained by the reduction of $HAuCl_4$, dissolved in an

aqueous solution of cetyltrimethylammonium bromide (CTAB), with cold sodium borohydride ($NaBH_4$). The growth solution was prepared by dropwise addition of ascorbic acid in an aqueous solution of $HAuCl_4$, CTAB, and $AgNO_3$. A seed solution aged for 5 min was added to the growth solution, and the NR growth was initiated. The color of the solution mixture changed from clear to deep purple after incubation for 10 h at 27^o C. The resultant CTAB-coated gold NRs were purified by two centrifugation cycles (8500 rpm for 30 min). In the next step, we conducted exchange of CTAB ligands attached to the ends of NRs with thiol-terminated polystyrene (SH-PS, Polymer Source Inc.) with a molecular weight of 12000 g/mol [28] and polydispersity index of 1.09. Approximately 0.5 mL of the concentrated aqueous solution of CTAB coated NRs (~1.0 mg/mL) was rapidly injected under sonication into 10 g of THF solution containing 5 mg of SH-PS (~0.05 wt %). The mixture was sonicated for 30 min at 42 kHz (±0.6%) and incubated at room temperature for 24 h. The resultant NRs were further purified by seven centrifugation cycles at 8500 rpm for 30 min. A concentrated solution of PS-functionalized NRs was collected and redispersed in THF to form a stock solution.

End-to-End Self-Assembly of NRs.

Prior to the self-assembly experiments, 760 μL of tetrahydrofuran (THF) was evaporated from the stock NR solution. The dried NRs were redissolved in 2.45 mL of dimethylformamide (DMF). A solution of the Raman reporter molecule Oxazine 720 (OX) in DMF (4 μM) was added dropwise under shaking to the NR solution in DMF. Following 30 min of agitation under gentle vortex conditions, the mixture was incubated for 1 h. End-to-End self-assembly of the NRs was triggered by dropwise addition of the DMF/ water mixture, containing 20 vol% of water. As soon as NR self-assembly began we carried out, at regular time intervals, parallel extinction and SERS measurements, as well as the preparation of samples for electron microscopy experiments.

Characterization of Self-Assembled NR Structures

Scanning transmission electron microscopy (STEM) images of individual NRs and self-assembled NR chains were obtained using a Hitachi S-5200 field emission SEM equipped with a transmitted electron detector operating at 30 kV. Extinction measurements were carried out using a Varian Cary 5000 UV-visible-NIR spectrometer.

In SERS measurements, 1.5 mL of the solution of self-assembled NRs was placed in a vial. Raman spectra excited with a 785 nm laser line were acquired with a Renishaw InVia System spectrometer coupled to a Leica microscope. The laser power was set to 1% of the full power (approximately 80 μW). The laser beam was focused on the sample by a 5× objective lens (NA = 0.12). The calculated interrogated volume was 6.46 nL. The spectra were measured with a 4 cm^{-1} resolution, using a 1 s exposure and 25 scans.

Control SERS experiments were conducted using a roughened gold substrate. A solid gold electrode with surface area of 0.3 cm^2 was roughened with 20 successive oxidation – reduction cycles from -0.3 to +1.25 V at 100 mV/s in an aqueous 0.1 M KCl working solution. The electrode was then isolated from the electrochemical cell and exposed to a 4 μM solution of OX in water, in pure DMF, or in the DMF/water mixture (20 vol % of water). After 15 min exposure, the surface was rinsed with an appropriate solvent, that is, with water, DMF, or the DMF/water mixture, and dried under nitrogen flux. The SERS spectra of OX adsorbed to the gold substrate were acquired using excitation at 785 nm (laser power 1%, four accumulations, and 5 s exposure time).

Simulations

The assembly of NRchains was simulated by the finite difference time domain (FDTD) method [44]. Polarization of the incident field was parallel to the long NR axis. The simulation domain was terminated with perfectly matched layer (PML). The complex permittivity of gold was modeled using the experimental data of Johnson and Christy [45]. To calculate the absorption and scattering cross sections of NR chains, we employed the formalism of the total field scattered field (TFSF). We introduced a set of two-dimensional power monitors, which formed two surfaces enclosing the NRs, one inside the TF region (power monitor 1, or PM1) and the other one in the SF region (power monitor 2, or PM2). We calculated the absorption cross section of the nanostructures by evaluating the net power flow into PM1, which represented the power loss in the NRs. The total power exiting PM2 was used for the calculation of the scattering cross section as $\sigma_{scat} = P_{scat}/ I_s$, where P_{scat} is the scattered power obtained from PM2 and I_s is the intensity of the light source. The extinction cross section was determined by the summation of scattering and absorption cross sections.

Results and Discussion

Figure E-1 illustrates site-specific functionalization of gold NRs and dynamic generation of hot-spots via end-to-end NR assembly. The NRs with a mean length of 37.6±4.4 nm and a mean diameter of 11.4±1.0 nm were used as the building blocks of the chains. In the ligand-exchange step, SH-PS replaced CTAB at the ends of NRs, transforming them into amphiphilic species [28]. These NRs were well-dispersed in DMF, a good solvent for both the CTAB molecules coating the long sides of the NRs and the SH-PS molecules attached to the NR ends [28]. End-to-end assembly of the NRs was triggered by introducing 20 vol% of water to the solution of amphiphilic NRs in DMF in the presence of the Raman reporter, OX. With the addition of water, the mixture became a poor solvent for the PS ligands localized at NR ends but remained a good solvent for the hydrophilic CTAB ligands coating the long side of the NRs. In order to avoid unfavorable contact of PS molecules with the DMF/water solution and to reduce the surface energy of the system, the NRs associated in the end-to-end manner.

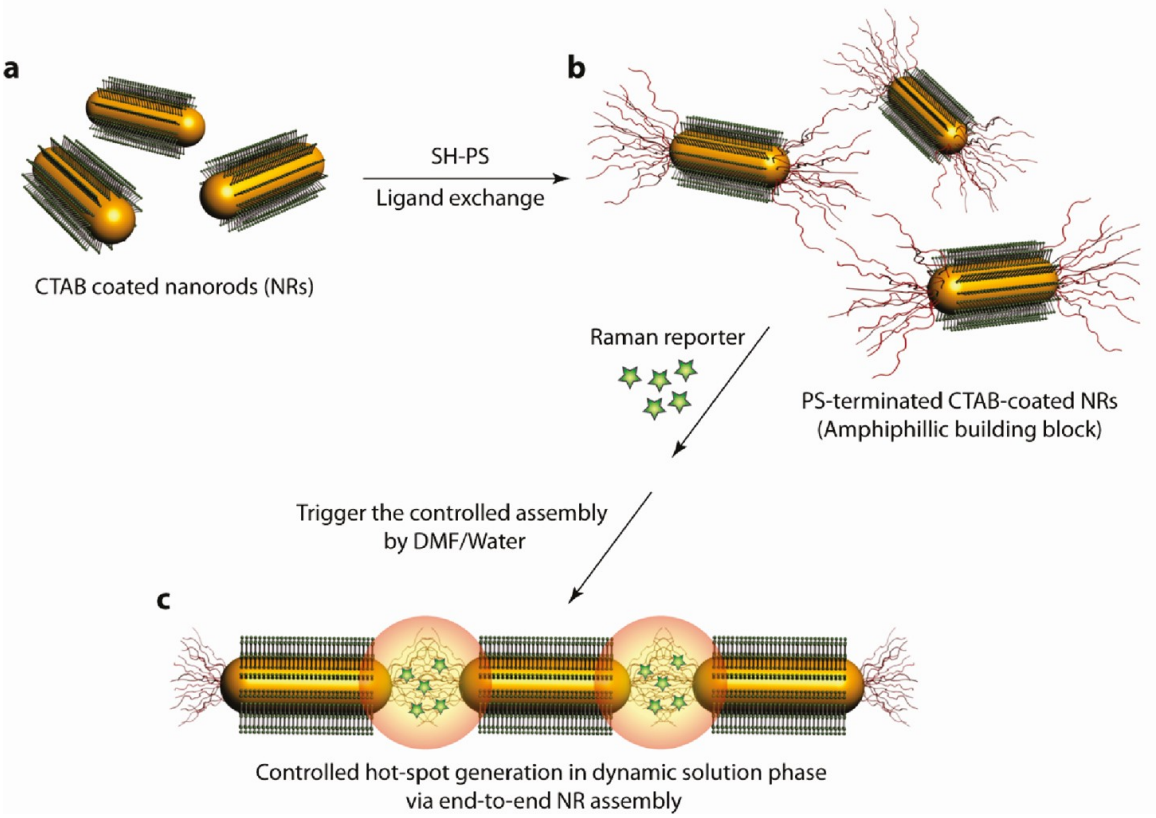

Figure E-1: Schematic of the generation of hot-spots via end-to-end self-assembly of gold NRs in chains. (a) Gold NRs stabilized with CTAB. (b) Ligand exchange of CTAB with SH-PS at the edges of the NRs. (c) End-to-end assembly

of NRs triggered by adding water to the solution of NRs in DMF, in the presence of Raman reporter OX. The volume fraction of water in the DMF/water mixture is 20 vol %. Hot-spots are generated between the ends of adjacent NRs. The distance between the adjacent NRs in the chain is maintained constant. Schematic is not drawn to scale.

Figure E-2a shows representative STEM images of the NR assemblies in various stages of chain growth. STEM imaging was carried out at low voltage (30 kV), which is suitable for imaging organic macromolecules. All the images were acquired without staining. The diffuse gray regions between the ends of adjacent NRs in the chains correspond to the globules of SH-PS molecules that formed in the poor DMF/water solvent. Using image analysis, we determined that the average distance between the ends of adjacent NRs throughout the self-assembly process remained 8.9 ± 1.5 nm. We note that, while STEM images are valuable in determining the average aggregation number of NRs in the chain and inter-NR spacing, the conformation of the chain may be influenced by the drying process. Therefore, the precise conformation of the chains in solution cannot be directly inferred from the micrographs presented in Figure E-2a.

The evolution of NR chains in the course of self-assembly was characterized by the change in their average aggregation number $\bar{X}_n$ as

$$\bar{X}_n = \frac{N_0}{N_{tot}} = \frac{\sum n_x x}{\sum n_x} \tag{E.1}$$

where N_0 and N_{tot} are the number of NR chains and the total number of NRs in the system, respectively, and n_x is the number of chains containing x NRs. The values of $\bar{X}_n$ were calculated by analyzing STEM images of the nanochains formed in the course of self-assembly experiments. The kinetics of growth of the NR chains resembled the evolution of polymer chains in reaction-controlled step-growth polymerization, as reported in our earlier work [46]; however, the self-assembly of the NRs in the presence of OX occurred at a greatly increased rate in comparison with the OX-free system.

The extinction and SERS measurements were carried out within the time of self-assembly t from ~5 min to 18 h, concurrent with the collection of samples for STEM imaging. Figure E-2b shows the evolution of the extinction spectra of the system undergoing self-assembly. In the course of chain growth, the longitudinal LSPR peak

shifted from 754 to 812 nm, due to the coupling of alternating dipoles along the NR chain. The end-to- end arrangement led to the reduction in resonance energy with respect to individual NRs [30, 32, 33, 47-49]. In the course of self-assembly, the width of the longitudinal LSPR peak broadened by ~12% when the aggregation number increased from 1 to 8, which was significantly narrower than for solution-based aggregates of gold NPs reported to date. The absorption peak at 659 nm corresponded to OX molecules. This peak was not noticeably shifted or reduced in intensity for a period of at least 18 h, which suggested good structural and temporal stability of OX during NR self-assembly.

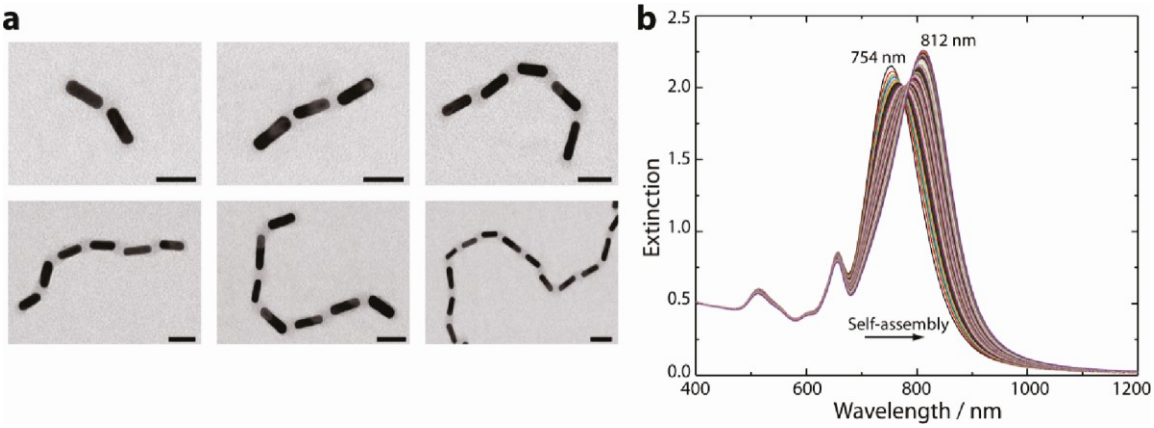

Figure E-2: (a) Representative STEM images of the self-assembled chains of NRs. Diffuse gray regions between adjacent NRs indicate the presence of SH-PS globules forming in a poor solvent. Scale bar is 40 nm. (b) Variation in extinction properties of NRs in the course of their self-assembly in chains. The spectral position of LSPR shifts from 754 to 812 nm, with the aggregation number of the NR chains changing from 1 at $t < 5$ min to 8 at $t = 18$ h. Transverse LSPR is located at 514 nm. The peak at 660 nm corresponds to OX.

Figure E-3a illustrates the evolution of the ensemble-averaged SERS spectra of OX in the course of the self-assembly experiments. The most enhanced bands at 563 and 604 cm^{-1} (assigned to vibrational modes of the phenoxazine ring of the dye) [50, 51] were consistent with the Raman spectrum of the solution of OX in DMF (Supporting Information). The same values of vibrational frequencies for OX adsorbed on the surface of NRs and for the solution of OX in DMF suggested that the reported molecule was physisorbed onto the gold surface [52].

By exploiting the sensitivity of SERS spectra to changes in their local environment, we determined the location of OX with respect to the CTAB-coated long NR sides and SH-PS-capped NR edges. In principle, OX could be localized within the CTAB layer and/or

could be associated with SH-PS molecules at the NR ends. In the first instance, the localization of OX could be dominated by the hydrophobic interactions with hydrocarbon chains of CTAB, since the localization of positively charged OX molecules in the vicinity of the cationic groups of CTAB was less likely. Alternatively, OX could be associated with the SH-PS ligands, so that the nonpolar component of the dye would interact with hydrophobic PS molecules, and its polar head would be in the solvent environment.

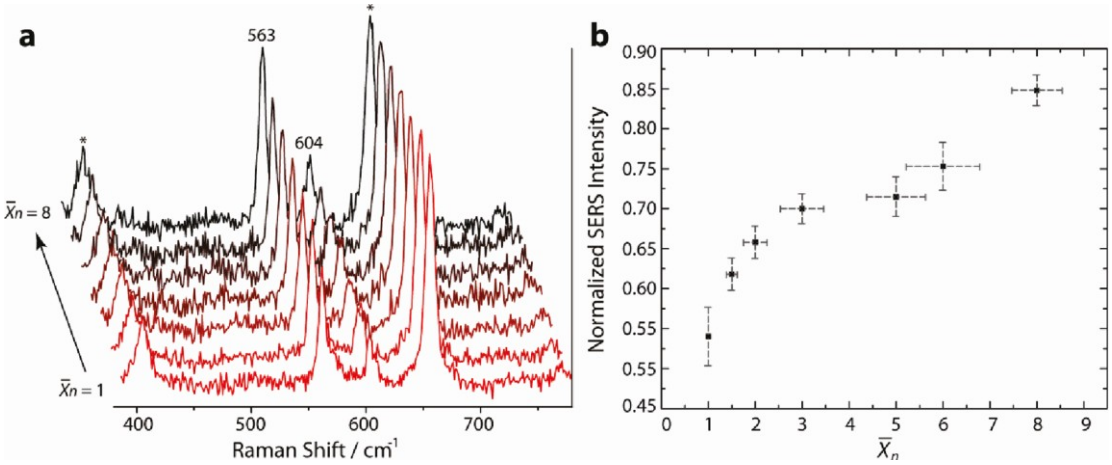

Figure E-3: (a) Evolution of normalized ensemble-averaged SERS spectra in self-assembled NR chains. The average aggregation number of NR assemblies changes from $\bar{X}_n$ = 1 at t < 5 min (bright-red spectrum) to 8 at t = 18 h (black spectrum). The SERS peaks at 563 and 604 cm^{-1} are normalized against the SERS peak of DMF at 659 cm^{-1} (indicated with asterisks). (b) Variation in the normalized SERS peak intensity measured at 563 cm^{-1} plotted as a function of the average aggregation number of the NR chains. SERS variation (y error) is based on three measurements taken within 15 min. Approximately 1000 NRs (including individual species) were used in the calculations of number of NRs (x error). Laser excitation wavelength was 785 nm.

To address the question of the predominant localization of the dye in the NR chains, we carried out a series of control SERS experiments with OX dissolved in several solvents, namely, water, DMF, and the DMF/water mixture at a water content of 20 vol %. The experiments were conducted using a roughened gold substrate. The SERS frequency of the strongest OX band in the 500-600 cm^{-1} region depended on the type of solvent: In water, the SERS band was centered at 595 cm^{-1}, similar to previously reported results [50, 51]. In DMF, the spectral position of the peak was 567 cm^{-1} (Supporting Information). In the DMF/water mixture, the SERS spectrum of OX featured two peaks located at 595 and 567 cm^{-1} (See Supporting Information).

For the self-assembled NR chains, the main SERS peak of OX was measured at 563 cm^{-1}, very close to 567 cm^{-1}, suggesting that OX was located in a DMF environment. The absence of a shoulder at 595 cm^{-1} suggested that no appreciable interactions existed between OX and water. Therefore, it was reasonable to conjecture that OX was predominately localized within the hot-spot region between the ends of the NRs from which water is largely excluded. We note that this did not rule out the possibility of OX molecules being located in the hydrophobic environment in the CTAB layer; however, the species outside the hot-spots did not significantly contribute to the overall SERS signal. Furthermore, the fact that the vibrational frequency of OX at 563 cm^{-1} did not change in the course of assembly indicated that the location of physisorbed OX remained unaltered. The relative intensities of the bands of OX at 563 and 604 cm^{-1} also remained constant throughout the process of self-assembly, suggesting that OX retained its orientation and geometry with respect to the NR surface without any appreciable molecular reorientation [53, 54].

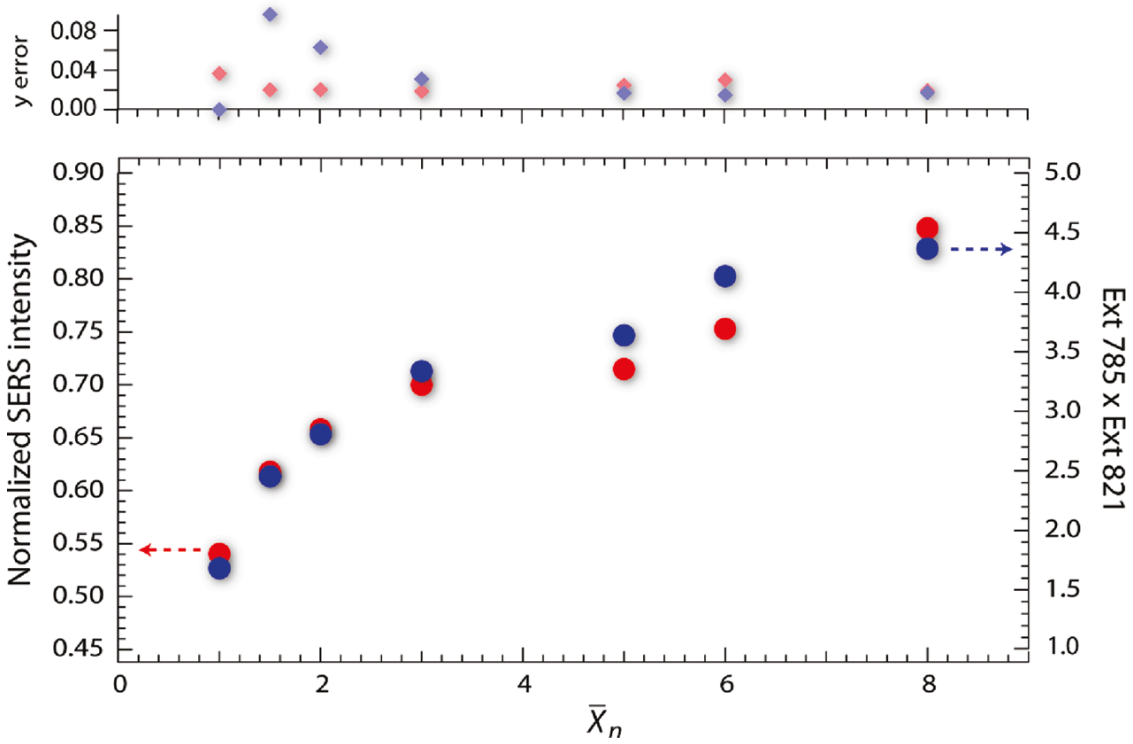

Figure E-4: Correlation of the normalized intensity of SERS peak at 563 cm^{-1} (red circles) and the product of extinctions measured at 785 and 821 nm (blue circles), plotted as a function of the average aggregation number $\bar{X}_n$ of the NR chains. Top: *y* errors of the intensity of SERS peak (red squares) and the product of extinctions (blue squares) were calculated on the basis of three measurements.

The change in the SERS intensity was determined over the course of NR self-assembly by using the intensity of the peak corresponding to DMF vibration at 659 cm^{-1} as an internal standard. Figure E-3b shows the variation in the ratio of intensities of the peak at 563 cm^{-1} of OX to the intensity of the peak at 659 cm^{-1}, plotted as a function of $\bar{X}_n$. Importantly, the change in ensemble-averaged normalized SERS intensity was not monotonic: it increased for $1 \le \bar{X}_n \le 3$, leveled off for $3 \le \bar{X}_n \le 5$, and increased again for $5 \le \bar{X}_n \le 8$.

To understand this nonlinear behavior, we considered only SERS arising from the electromagnetic effect. Under resonance conditions, the incident light absorbed by the nanostructure generates localized surface plasmons, thereby creating a strong local electromagnetic field, $E_{loc}(\omega_{exc})$, close to the surface of the NRs. This effect leads to the enhancement in intensity of the Raman scattered light by the OX molecule, which is assumed to be a point dipole. The scattered light also excites localized surface plasmons and generates an enhanced field, $E_{loc}(\omega_{RS})$, at the Raman Stokes frequency. The field enhancement GSERS is proportional to the square of the product of the local field at the incident frequency and the local field at the scattered Raman Stokes frequency [42, 55_58], that is,

$$G_{SERS} = \left| E_{loc}(\omega_{exc}) E_{loc}(\omega_{RS}) \right|^2 \qquad \text{(E.2)}$$

As discussed above, light extinction (absorption + scattering) at wavelengths matching the resonances of the nanostructure generates LSPR that leads to field localization. Therefore, a correlation between the SERS efficiency and the product of extinctions at ω_{exc} and ω_{RS} should be expected.

We plotted the variations in the normalized SERS intensity and the product of the extinctions measured at the excitation wavelength of 785 nm (ω_{exc}) and at the wavelength of the Stokes-shifted radiation of 821 nm (ω_{RS}) versus the average aggregation number, $\bar{X}_n$, of the NR chains (Figure E-4). In the course of NR self-assembly, the product of extinctions varied, since the spectral position of the longitudinal LSPR gradually red-shifted (see Figure E-2). Figure E-4 shows a strong correlation between the variation in SERS intensity and the product of extinctions, both plotted as a function of $\bar{X}_n$. Such correlation indicated that the variation in SERS properties with NR assembly indeed

originated from the inherent electromagnetic properties of the self-assembled nanostructure, rather than from chemical effects. In addition, the results shown in Figure E-4 suggested a narrow distribution of hot-spots, confirming the high level of organization of the dynamic self-assembled system in solution. We note that a direct correlation between extinction and SERS is qualitatively followed in simple nanostructures such as individual gold spheres [59] and organized arrays, but it falls apart dramatically in strongly coupled random systems with a large distribution of spatially localized resonances [60].

In order to further highlight the relationship between SERS enhancement and the dynamic evolution of hot-spots, we conducted comprehensive FDTD simulations by numerically solving Maxwell's curl equations by iteration over time [44]. Figure E-5 shows examples of electric field (E field) profiles corresponding to different wavelengths for the chains of collinearly assembled NRs. The field inside individual NRs rapidly decayed, while hotspots between adjacent NRs exhibited a maximum E field intensity 4000-fold greater than the intensity of the incident field.

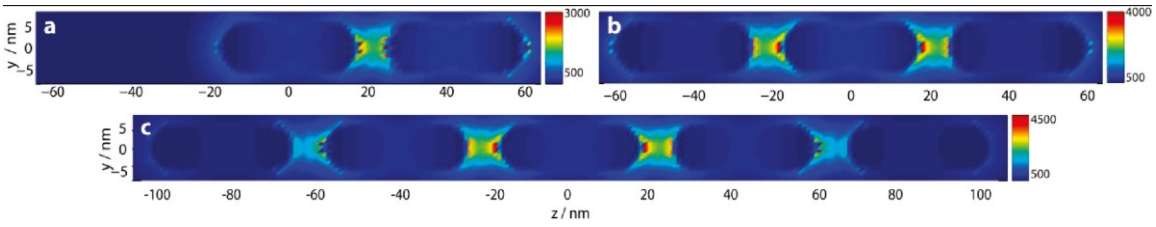

Figure E-5: Three-dimensional finite-difference time-domain (3D-FDTD) simulation of the end-to-end assembly of gold NRs. Electric field profile was calculated at the resonance wavelength of the collinear NR chain at (a) 760, (b) 782, and (c) 802 nm. Polarization of the incident light is parallel to the long axes of the NRs (i.e., to the z-coordinate). Hot-spots between adjacent NRs show a maximum electric field intensity 4000 times greater than the incident field.

In our work, the self-assembled NR chains were characterized by the distribution of their aggregation numbers and the variation in the angle between adjacent NRs within the chain. In order to examine the role of the distribution in $\bar{X}_n$ of the NR chains, we performed FDTD simulations for chains with different lengths and then used experimentally determined aggregation statistics to calculate the electric field intensities (see Supporting Information). For $\bar{X}_n$ = 8, the E field intensity squared had the largest value when normalized with respect to the aggregation number of the chain, which was

consistent with experimental results shown in Figure E-3. While the longer chains had a lower maximum intensity, they also had a weaker variation in their maximum intensity wavelength compared to the shorter chains. This spectral purity provided greater enhancement in the E field when statistically averaged.

When the distribution in the aggregation numbers was not taken into account, the field intensity was highest for chains containing three NRs, when normalized by the number of NRs in the chain (Supporting Information). This effect originated from the trade-off between the local field enhancement and optical absorption (that is, loss) in the NR chains. A figure of merit that compares the local field enhancement to the loss is the ratio between the real and imaginary parts of the relative permittivity of the NRs. For gold, this figure of merit is at a maximum at ~760 nm, close to the resonance wavelength of the trimer structure.

Since the SERS and LSPR properties of the NR assemblies depend on the collinearity of the NRs with respect to the long axis of the chain [32, 33, 48], we have performed FDTD calculations for dimers and trimers of NRs with varying orientations with respect to each other (Supporting Information). The deviation from collinearity at the angles between the long axes of the NRs of 20, 40, 60, and 90 degrees, resulted in a significant reduction of extinction and, thus, decreasing E field intensity (Supporting Information). This result implied that in ensemble measurements, the greatest contribution to extinction and SERS arose from the chains with a collinear NR arrangement, with a minor influence on E field intensity from “off-axis” NRs.

The persistence length of the chains formed by the 40-nmlong NRs in the DMF/water mixture with 20 vol% of water was 230 nm, corresponding to $\bar{X}_n \approx 6$ [28a]. We admit that chain conformations determined from the TEM images of dried samples or from the AFM images of the chains on the solid substrate under solution may not accurately reflect the configuration of chains in solution. Therefore, extensive cryo-TEM experiments followed by the deliberate analysis of the statistical distribution of angles along the chains with different aggregation numbers will provide more insight into the relationship between the SERS properties and the chain flexibility.

For the calculation of scattering and absorption cross sections, we employed the total field/scattered field method for the separation of the scattered field from the incident

radiation. Our calculations showed that the extinction cross-section mainly originated from NR absorption, whereas the contribution from scattering was minor (Supporting Information). Experimental and calculated results obtained for the extinction and variations in the spectral position of the longitudinal LSPR (Figure E-6a) were in good agreement when NR number distribution was considered. Figure E-6b shows the change in the calculated extinctions (a product of those measured at 785 and 821 nm) and E field intensity squared as a function of $\bar{X}_n$. A strong correlation between the two trends was consistent with the relationship expressed in Eq 2. Significantly, the experimental results (Figure E-4) and theoretical results shown in Figure E-6b are in good qualitative agreement.

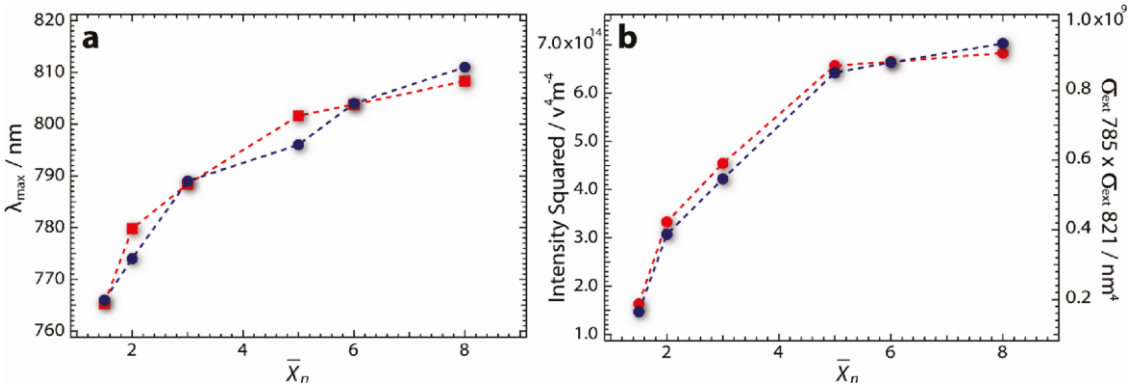

Figure E-6: (a) Variation in experimentally measured (blue circles) and calculated (red squares) spectral position of the longitudinal LSPR, plotted as a function of the average aggregation number, $\bar{X}_n$, of the NR chains. (b) Variation in the calculated product of the squares of the electric field (intensity) at 785 and 821 nm (red circles) and the product of the extinction cross sections at 785 and 821 nm (blue circles), plotted vs $\bar{X}_n$.

Conclusions

Following dynamic generation of hot-spots via controlled, solution-based self-assembly of gold NR chains, we have established a direct relationship between extinction and SERS properties of the chains. An important aspect of our experiments included the formation of ensembles with a well-defined, invariant distance between adjacent NRs. Our work opens the way for studies of optical properties of other geometry-dependent dynamic plasmonic systems, e.g., ensembles of side-by-side gold NRs and compartmentalization of molecules or particles in hotspots. Building from the correlation between SERS and extinction, practical applications of self-assembled structures ranging

from chemical and biological sensing to nanoelectronics, e.g., plasmonic circuits, become a step closer.

A.L. and E.K. thank Shun Lo, Christina McLaughlin, James Li, and Prof. Gilbert Walker (University of Toronto). G.F.S.A. and M.L.S. thank the Canadian Bureau for International Education, Department of Foreign Affairs and International Trade (CBIEDFAIT) for fellowships for postdoctoral research and an Emerging Leaders of Americas Partnership (ELAP) program. All authors thank NSERC Canada for financial support of the Strategic Network for Bioplasmonic Systems (Biopsys) and thank Lumerical, Inc.

References

[1] S. A. Claridge, et al., "Cluster-Assembled Materials," Acs Nano, vol. 3, pp. 244-255, 2009.

[2] S. C. Glotzer and M. J. Solomon, "Anisotropy of building blocks and their assembly into complex structures," Nature Materials, vol. 6, pp. 557-562, 2007.

[3] M. Grzelczak, et al., "Directed Self-Assembly of Nanoparticles," Acs Nano, vol. 4, pp. 3591-3605, 2010.

[4] S. Mann, "Self-assembly and transformation of hybrid nano-objects and nanostructures under equilibrium and non-equilibrium conditions," Nature Materials, vol. 8, pp. 781-792, 2009.

[5] Z. H. Nie, et al., "Properties and emerging applications of self-assembled structures made from inorganic nanoparticles," Nature Nanotechnology, vol. 5, pp. 15-25, 2010.

[6] S. Srivastava and N. A. Kotov, "Nanoparticle assembly for 1D and 2D ordered structures," Soft Matter, vol. 5, pp. 1146-1156, 2009.

[7] A. Lee, et al., "Lamellar Envelopes of Semiconductor Nanocrystals," Journal of the American Chemical Society, vol. 131, pp. 10182-10188, 2009.

[8] Z. Y. Tang, et al., "Self-assembly of CdTe nanocrystals into free-floating sheets," Science, vol. 314, pp. 274-278, 2006.

[9] E. V. Shevchenko, et al., "Structural diversity in binary nanoparticle superlattices," Nature, vol. 439, pp. 55-59, 2006.

[10] S. Z. Zhang, et al., "Nanonecklaces assembled from gold rods, spheres, and bipyramids," Chemical Communications, pp. 1816-1818, 2007.

[11] J. Q. Zhuang*, et al.*, "Supercrystalline colloidal particles from artificial atoms," *Journal of the American Chemical Society,* vol. 129, pp. 14166, 2007.

[12] M. R. Jones*, et al.*, "DNA-nanoparticle superlattices formed from anisotropic building blocks," *Nature Materials,* vol. 9, pp. 913-917, 2010.

[13] Z. L. Wang, "Nanobelts, nanowires, and nanodiskettes of semiconducting oxides - From materials to nanodevices," *Advanced Materials,* vol. 15, pp. 432-436, 2003.

[14] R. J. Tseng*, et al.*, "Digital memory device based on tobacco mosaic virus conjugated with nanoparticles," *Nature Nanotechnology,* vol. 1, pp. 72-77, 2006.

[15] J. Lee*, et al.*, "Exciton-plasmon interactions inmolecular spring assemblies of nanowires and wavelength-based protein detection," *Nature Materials,* vol. 6, pp. 291-295, 2007.

[16] C. Desvaux*, et al.*, "Multimillimetre-large superlattices of air-stable iron-cobalt nanoparticles," *Nature Materials,* vol. 4, pp. 750-753, 2005.

[17] C. Sonnichsen*, et al.*, "A molecular ruler based on plasmon coupling of single gold and silver nanoparticles," *Nature Biotechnology,* vol. 23, pp. 741-745, 2005.

[18] S. H. Sun and C. B. Murray, "Synthesis of monodisperse cobalt nanocrystals and their assembly into magnetic superlattices (invited)," *Journal of Applied Physics,* vol. 85, pp. 4325-4330, 1999.

[19] L. V. Brown*, et al.*, "Heterodimers: Plasmonic Properties of Mismatched Nanoparticle Pairs," *Acs Nano,* vol. 4, pp. 819-832, 2010.

[20] J. W. Liu and Y. Lu, "A colorimetric lead biosensor using DNAzyme-directed assembly of gold nanoparticles," *Journal of the American Chemical Society,* vol. 125, pp. 6642-6643, 2003.

[21] A. I. Denisyuk*, et al.*, "Transmitting Hertzian Optical Nanoantenna with Free-Electron Feed," *Nano Letters,* vol. 10, pp. 3250-3252, 2010.

[22] A. P. Alivisatos*, et al.*, "Organization of 'nanocrystal molecules' using DNA," *Nature,* vol. 382, pp. 609-611, 1996.

[23] C. L. Chen*, et al.*, "A new peptide-based method for the design and synthesis of nanoparticle superstructures: Construction of highly ordered gold nanoparticle

double helices," *Journal of the American Chemical Society,* vol. 130, pp. 13555, 2008.

[24] C. A. Mirkin*, et al.*, "A DNA-based method for rationally assembling nanoparticles into macroscopic materials," *Nature,* vol. 382, pp. 607-609, 1996.

[25] C. L. Chen and N. L. Rosi, "Preparation of Unique 1-D Nanoparticle Superstructures and Tailoring their Structural Features," *Journal of the American Chemical Society,* vol. 132, pp. 6902, 2010.

[26] E. R. Zubarev*, et al.*, "Amphiphilicity-driven organization of nanoparticles into discrete assemblies," *Journal of the American Chemical Society,* vol. 128, pp. 15098-15099, 2006.

[27] K. K. Caswell*, et al.*, "Preferential end-to-end assembly of gold nanorods by biotin-streptavidin connectors," *Journal of the American Chemical Society,* vol. 125, pp. 13914-13915, 2003.

[28] (a) Z. H. Nie*, et al.*, "Self-assembly of metal-polymer analogues of amphiphilic triblock copolymers," *Nature Materials,* vol. 6, pp. 609-614, 2007. (b) Z. H. Nie*, et al.*, "Supramolecular" assembly of gold nanorods end-terminated with polymer "Pom-Poms": Effect of pom-pom structure on the association modes," *Journal of the American Chemical Society,* vol. 130, pp. 3683-3689, 2008. (c) D. Fava*, et al.*, "Evolution of Self-Assembled Structures of Polymer-Terminated Gold Nanorods in Selective Solvents," *Advanced Materials,* vol. 20, pp. 4318-4322, 2008.

[29] S. T. S. Joseph*, et al.*, "Gold nanorods to nanochains: Mechanistic investigations on their longitudinal assembly using alpha,omega-alkanedithiols and interplasmon coupling," *Journal of Physical Chemistry B,* vol. 110, pp. 150-157, 2006.

[30] P. K. Jain*, et al.*, "Plasmon coupling in nanorod assemblies: Optical absorption, discrete dipole approximation simulation, and exciton-coupling model," *Journal of Physical Chemistry B,* vol. 110, pp. 18243-18253, 2006.

[31] S. Link*, et al.*, "Simulation of the optical absorption spectra of gold nanorods as a function of their aspect ratio and the effect of the medium dielectric constant," *Journal of Physical Chemistry B,* vol. 103, pp. 3073-3077, Apr 1999.

[32] L. S. Slaughter, *et al.*, "Effects of Symmetry Breaking and Conductive Contact on the Plasmon Coupling in Gold Nanorod Dimers," *Acs Nano,* vol. 4, pp. 4657-4666, 2010.

[33] A. M. Funston, *et al.*, "Plasmon Coupling of Gold Nanorods at Short Distances and in Different Geometries," *Nano Letters,* vol. 9, pp. 1651-1658, 2009.

[34] C. J. Addison and A. G. Brolo, "Nanoparticle-containing structures as a substrate for surface-enhanced Raman scattering," *Langmuir,* vol. 22, pp. 8696-8702, Oct 2006.

[35] Hu X, *et al.*, "nr sers," *Journal of Physical Chemistry B,* vol. 109, p. 19385, 2005.

[36] B. Nikoobakht and M. A. El-Sayed, "Surface-enhanced Raman scattering studies on aggregated gold nanorods," *Journal of Physical Chemistry A,* vol. 107, pp. 3372-3378, 2003.

[37] G. Chen, *et al.*, "High-Purity Separation of Gold Nanoparticle Dimers and Trimers," *Journal of the American Chemical Society,* vol. 131, pp. 4218, 2009.

[38] G. Goddard, *et al.*, "High-Resolution Spectral Analysis of Individual SERS-Active Nanoparticles in Flow," *Journal of the American Chemical Society,* vol. 132, pp. 6081-6090, 2010.

[39] T. A. Laurence, *et al.*, "Rapid, Solution-Based Characterization of Optimized SERS Nanoparticle Substrates," *Journal of the American Chemical Society,* vol. 131, pp. 162-169, 2009.

[40] T. Chen, *et al.*, "Hotspot-Induced Transformation of Surface-Enhanced Raman Scattering Fingerprints," *Acs Nano,* vol. 4, pp. 3087-3094, 2010.

[41] N. Felidj, *et al.*, "Optimized surface-enhanced Raman scattering on gold nanoparticle arrays," *Applied Physics Letters,* vol. 82, pp. 3095-3097, 2003.

[42] N. Felidj, *et al.*, "Controlling the optical response of regular arrays of gold particles for surface-enhanced Raman scattering," *Physical Review B,* vol. 65, 2002.

[43] B. Nikoobakht and M. A. El-Sayed, "Preparation and growth mechanism of gold nanorods (NRs) using seed-mediated growth method," *Chemistry of Materials,* vol. 15, pp. 1957-1962, 2003.

[44] Taflove A and H. S. C, *Computational Electrodynamics: The Finite-Difference Time Domain Method*, 2nd ed. Boston: Artech House, 2000.

[45] P. B. Johnson and R. W. Christy, "Optical constants of noble metals," *Physical Review B,* vol. 6, pp. 4370-4379, 1972.

[46] K. Liu*, et al.*, "Step-Growth Polymerization of Inorganic Nanoparticles," *Science,* vol. 329, pp. 197-200, 2010.

[47] E. Prodan and P. Nordlander, "Plasmon hybridization in spherical nanoparticles," *Journal of Chemical Physics,* vol. 120, pp. 5444-5454, 2004.

[48] C. Tabor*, et al.*, "Effect of Orientation on Plasmonic Coupling between Gold Nanorods," *Acs Nano,* vol. 3, pp. 3670-3678, 2009.

[49] L. Shao*, et al.*, "Angle- and Energy-Resolved Plasmon Coupling in Gold Nanorod Dimers," *Acs Nano,* vol. 4, pp. 3053-3062, 2010.

[50] A. G. Brolo and A. C. Sanderson, "Surface-enhanced Raman scattering (SERS) from a silver electrode modified with oxazine 720," *Canadian Journal of Chemistry-Revue Canadienne De Chimie,* vol. 82, pp. 1474-1480, 2004.

[51] A. G. Brolo*, et al.*, "Ratio of the surface-enhanced anti-Stokes scattering to the surface-enhanced Stokes-Raman scattering for molecules adsorbed on a silver electrode," *Physical Review B,* vol. 69, p. 045424, 2004.

[52] R. Aroca, "Surface-Enhanced Vibrational Spectroscopy," ed. New York: John Wiley & Sons, 2006.

[53] M. Moskovits, "Surface Selection-Rules," *Journal of Chemical Physics,* vol. 77, pp. 4408-4416, 1982.

[54] M. Moskovits and J. S. Suh, "Surface selection-rules for surface-enhanced Raman-spectroscopy - calculations and application to the surface-enhanced Raman-spectrum of phthalazine on silver," *Journal of Physical Chemistry,* vol. 88, pp. 5526-5530, 1984.

[55] K. Kneipp*, et al.*, "Ultrasensitive chemical analysis by Raman spectroscopy," *Chemical Reviews,* vol. 99, pp. 2957-2975, 1999.

[56] M. Moskovits, "Surface-Enhanced Spectroscopy," *Reviews of Modern Physics,* vol. 57, pp. 783-826, 1985.

[57] G. C. Schatz*, et al.*, "Electromagnetic mechanism of SERS," in *Surface-Enhanced Raman Scattering: Physics and Applications*. vol. 103, ed, pp. 19-45, 2006.

[58] D. A. Weitz*, et al.*, "The enhancement of Raman-scattering, resonance Raman-scattering, and fluorescence from molecules adsorbed on a rough silver surface," *Journal of Chemical Physics,* vol. 78, pp. 5324-5338, 1983.

[59] K. L. Kelly*, et al.*, "The optical properties of metal nanoparticles: The influence of size, shape, and dielectric environment," *Journal of Physical Chemistry B,* vol. 107, pp. 668-677, 2003.

[60] E. C. Le Ru*, et al.*, "On the connection between optical absorption/extinction and SERS enhancements," *Physical Chemistry Chemical Physics,* vol. 8, pp. 3083-3087, 2006.

Supporting Information for Appendix E

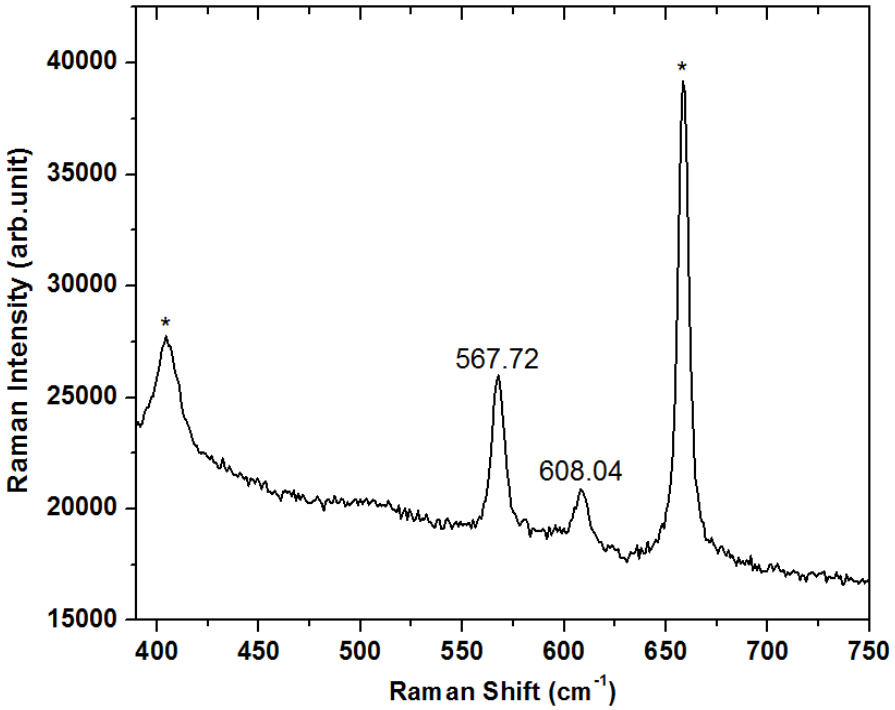

Figure E-S1: Raman spectrum of 400 µM of Oxazine 720 (OX) dissolved in DMF (indicated with asterisk).785 nm laser excitation was used.

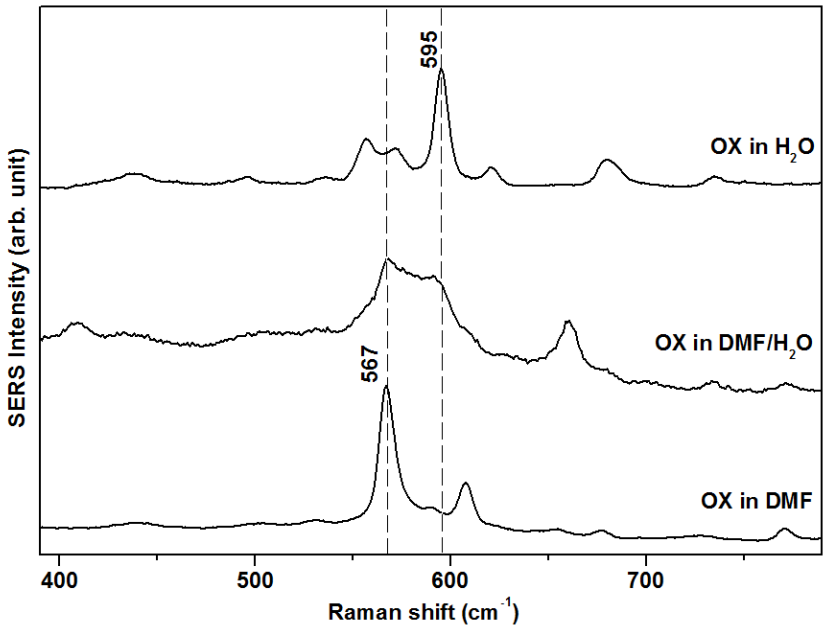

Figure E-S2: SER spectra of oxazine 4 µM adsorbed on roughened gold substrate as a function of solvent environment (a) H_2O, (b) DMF and (c) DMF/ H_2O mixture containing 20 vol. % of H_2O.

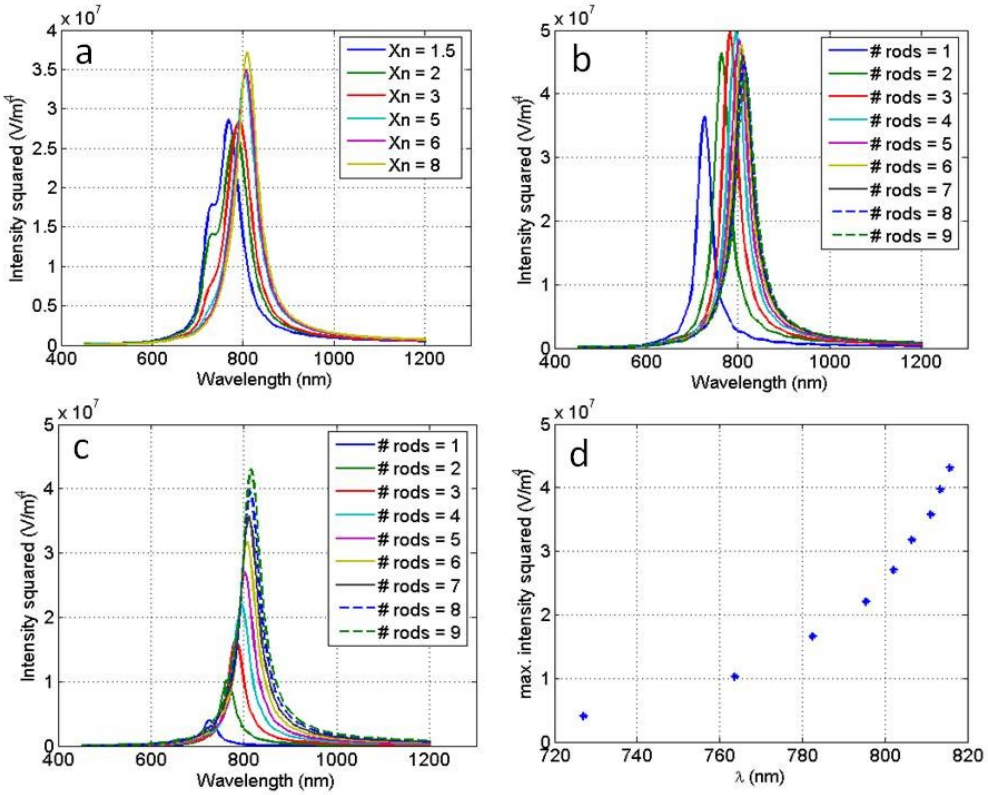

Figure E-S3: FDTD simulation showing (a) Electric field intensity squared obtained from incorporating average NR aggregation number, as a function of wavelength (factoring in experimentally determined statistical data) (b) Normalized sum of electric field intensity squared over a small volume enclosing the NR chain, for ideal NR chain lengths (Standard deviation is equal to zero) ranging from 1 to 9 NRs as a function of wavelength. (c) Sum of electric field intensity squared over a small volume enclosing NRs, chain lengths (number of NRs ranging from 1 to 9) as a function of wavelength (not normalized). (d) Peak electric field intensity squared values plotted against their corresponding resonant wavelengths. Number of NRs increases from 1 to 9 (left to right)

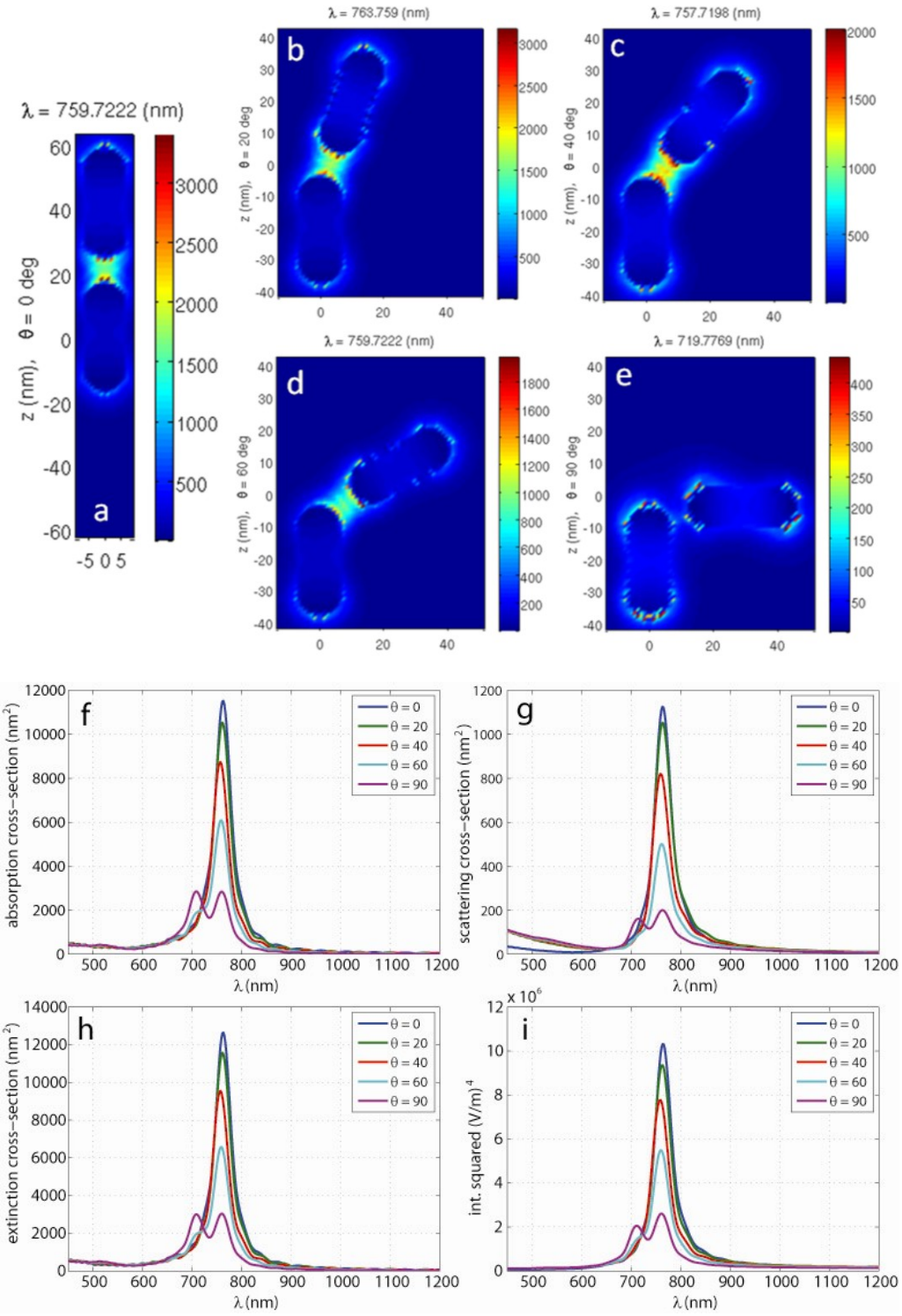
λ = 759.7222 (nm)
z (nm), θ = 0 deg
a
λ = 763.759 (nm)
b
z (nm), θ = 20 deg
λ = 757.7198 (nm)
c
z (nm), θ = 40 deg
λ = 759.7222 (nm)
d
z (nm), θ = 60 deg
λ = 719.7769 (nm)
e
z (nm), θ = 90 deg
f
absorption cross−section (nm²)
λ (nm)
g
scattering cross−section (nm²)
λ (nm)
h
extinction cross−section (nm²)
λ (nm)
i
x 10⁶
int. squared (V/m)⁴
λ (nm)
θ = 0
θ = 20
θ = 40
θ = 60
θ = 90

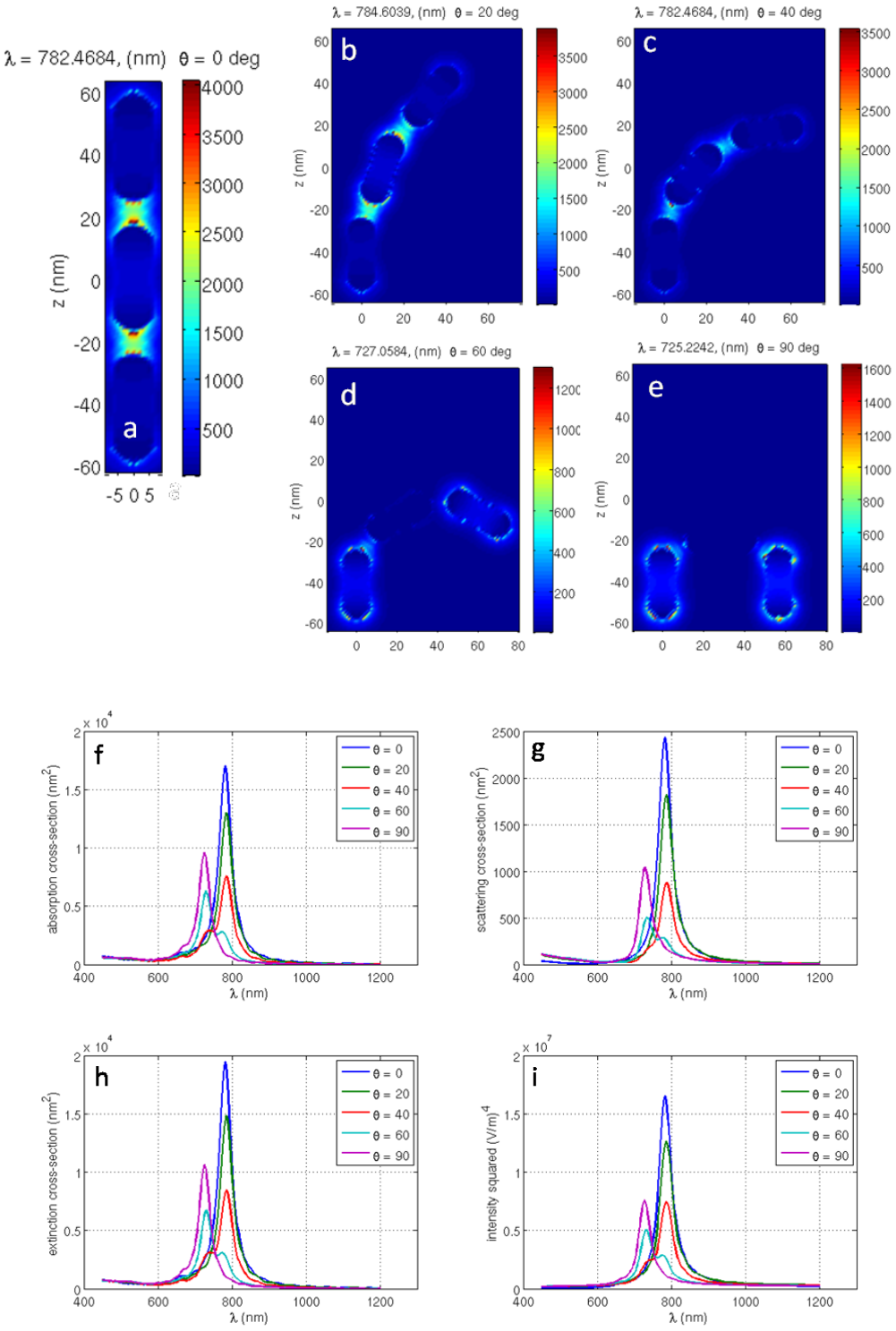

Figure E-S4: Three-dimensional finite-difference time-domain (3D-FDTD) simulation showing examples of electric field profiles for end-to-end assembled gold NR dimmers and trimers. Polarization of the incident light is parallel to z-coordinate. Angular variance of (a) 0 degrees (b) 20 degrees (c) 40 degrees (d) 60

degrees (e) 90 degrees (f - i) Calculated absorption, scattering, extinction cross sections and electric field intensity squared respectively of various angled NR dimmers and trimers as a function of wavelength. Electric field strength between adjacent NRs decreases as angle between adjacent NRs increases.

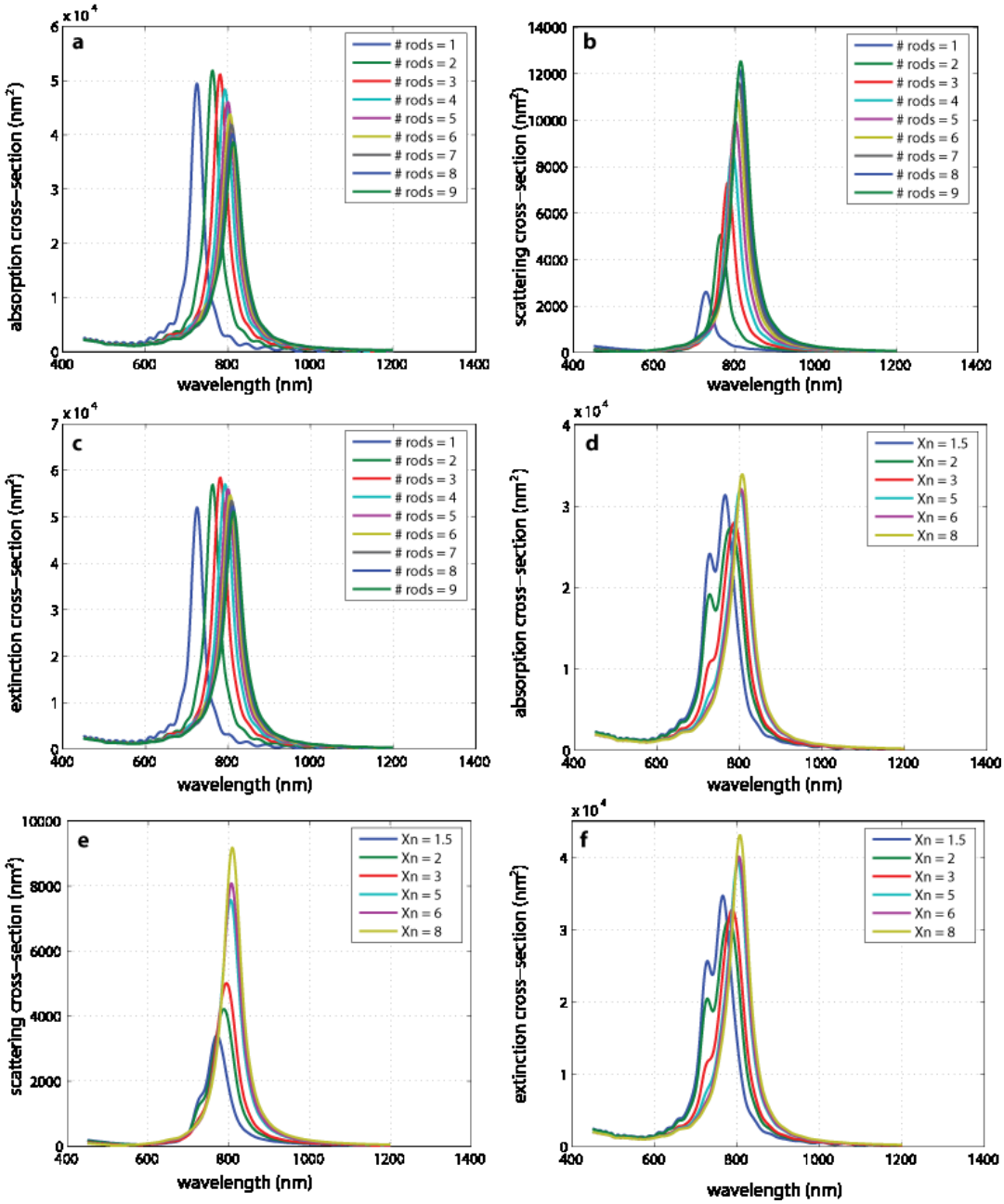

Figure E-S5: Calculated absorption, scattering and extinction cross sections as a function of wavelength for various NR chain lengths ((a) to (c) respectively) and average NR aggregation number ((d) to (f) respectively). A total-field scattered field (TFSF) source is utilized for calculating the scattering and absorption cross-sections. Incident field polarization is parallel to the major rod axis (i.e. z), the bandwidth of source is from 600 nm to 1000 nm. Simulation domain is

terminated with perfectly matched layer (PML). A mesh override region of (1 nm x 1nm x 1nm) mesh size is defined for better modeling of the circular rods in Cartesian coordinates. A 3-D time domain monitor is utilized for recording the field strengths as a function of time and a Fourier transform provides the frequency domain results. Extinction cross-section was calculated for different NR chain lengths and a certain factor (see main text) from each curve was added according to the experimental statistical data to lead figure (f). The heterogeneity of NR chain size at each stage of the assembly is one of the contributing factors to variations in the observed amplitude.

Appendix F: Side-by-Side Assembly of Gold Nanorods Reduces Ensemble-Averaged SERS Intensity

(2012, The Journal of Physical Chemistry C, volume 116, pp 5538-5545)

Side-by-Side Assembly of Gold Nanorods Reduces Ensemble-Averaged SERS Intensity

Anna Lee[†], Aftab Ahmed[‡], Diego P. dos Santos[‡], Neil Coombs[†], Jai Il Park[†], Reuven Gordon[*‡], Alexandre G. Brolo[*§], and Eugenia Kumacheva[*†]

[†]*Department of Chemistry, University of Toronto, 80 Saint George Street, Toronto, Ontario M5S 3H6, Canada*

[§]*Department of Chemistry, University of Victoria, P.O. Box 3065, Victoria, British Columbia, V8W 3 V6, Canada*

[‡]*Department of Electrical and Computer Engineering, University of Victoria, Victoria, British Columbia, V8W 3P6, Canada*

ABSTRACT: It is generally expected that aggregates of metal nanoparticles are more efficient surface-enhanced Raman scattering (SERS) probes than individual nanoparticles, due to the enhancement of the electric field in the interparticle gaps. We show that, for asymmetric nanoparticles, such as gold nanorods (NRs), this is not always the case: the plasmonic behavior of NRs depends on the mutual orientation of the NRs in the ensemble. We report the results of experimental studies and theoretical analysis of the optical properties of clusters of side-by-side assembled gold NRs. Ensembleaveraged SERS spectroscopy showed a reduction in SERS intensity. Comprehensive finite-difference time-domain simulations showed a reduction of electric field intensity as the number of NRs per cluster increased. This is due to destructive interference as the radial component of the surface plasmon modes of the NRs in the cluster interact with each other. The present work expands our understanding of the configuration-specific optical behavior of asymmetric gold nanoparticles. Furthermore, it offers guidance toward the "design rules" for the development of colloidal NR systems for sensing applications.

Introduction

The utilization of light−metal interactions at the nanoscale shows promising applications in nanoantennas [1−5], extraordinary transmission [6, 7], and plasmonic waveguides [8−10] all of which can be realized through precise control of the architecture, dimensions, and composition of metallic nanostructures. In parallel to "top-

down" nanofabrication, "bottomup" methods utilizing colloidal metallic nanoparticles (MNPs) as the building blocks are receiving increasing attention, because of the low cost of the fabrication and their potential use in vivo [11−14].

One of the important applications of the plasmonic properties of MNPs is their utilization in surface-enhanced Raman scattering (SERS), which provides structural information about analytes adsorbed on the surface of MNPs and offers exceptionally high sensitivity as compared with ordinary Raman scattering [15−19]. The amplification of Raman intensity arises from local electromagnetic field enhancement due to the surface plasmon resonance (SPR) of MNPs. The magnitude of the Raman scattering from analytes in close proximity to the surface of MNPs is approximately proportional to the fourth power of the local field at the excitation frequency, when the electromagnetic mechanism of SERS is considered [15, 20, 21].

The spectral position of the SPR of MNPs can be tuned by varying the dimensions and shapes of MNPs, as well as the nature of the surrounding medium. There is also significant interest in ensembles of MNPs, owing to the coupling of plasmons of adjacent particles [9, 22]. Structural, configuration dependent, plasmonic behavior of ensembles of MNPs can affect both the intensity and the spectral position of the SPR wavelength, thereby providing greater insight into the utilization of the plasmon coupling phenomena.

Currently, the majority of experimental studies of SERS properties of clusters of MNPs have been carried out for irregular, aggregated systems. These structures exhibited a significant variability in their optical properties. As a result, there remains an insufficient understanding of the influence of the architecture of aggregates of MNPs on their SERS properties, particularly, in a solution state.

Gold nanorods (NRs) are of particular interest because of their intrinsic shape-anisotropy. They exhibit transverse and longitudinal SPR, which correspond to the coherent electron oscillations perpendicular and parallel to the long NR axis, respectively [23]. The shape-dependent properties of NRs enable spectral tunability of the longitudinal SPR in the near-IR region. In addition, in their ensembles, gold NRs can exhibit a welldefined mutual alignment in a side-by-side or end-to-end manner [24−27]. The surface plasmon coupling between gold NRs in their ensembles depends not only on the interparticle distance but also on the mutual orientation of the NRs with respect to each

other. Therefore, gold NRs are well suited for the fundamental studies of the optical properties of aggregated NP systems [18, 19, 22, 24, 25, 27].

Thus far, many researchers have focused on the "single-particle" scattering measurements of isolated dimers of NRs in a dry state, in which the NRs were arranged in the end-to-end, side-by-side, L-shaped, or T-shaped manner [24, 25]. Experimental results showed that the scattering intensity of dimers depends on the polarization direction of the incident light. The maximum intensity was reached, when the polarization was parallel to the long axis of the NRs. These experimental findings were in agreement with plasmon hybridization calculations and finite-difference time-domain (FDTD) simulations [24]. A study of the effect of angular orientations of NRs in dimers fabricated by electron beam lithography showed the dependence of plasmon coupling on NR orientation, separation, induced dipole strength, and the dielectric constant of the medium [28]. "Single-particle" measurements of scattering, extinction, and SERS of NR dimers and a theoretical explanation of geometry-specific NR assembly [26] have provided a deeper insight into the optical behavior of isolated NP aggregates [29]. Yet, currently, a comprehensive understanding of the optical properties of ensemble-averaged system behavior, factoring in aggregate populations, SPR shift, and electric field (E field) distribution in a dynamic solution-based assembly remains challenging. A small piece of this puzzle has been addressed by our previous work, in which the optical properties of chains of NRs assembled in the end-to-end manner were reported [30]. Specifically, we studied the localized E-field intensity regions ("hot spots") that were generated between the ends of adjacent NRs [31, 32] and showed a direct correlation between extinction and ensemble-averaged SERS, as a function of the average aggregation number of NR chains during their assembly [30]. The calculated E-field intensity showed a decrease as the average length of NR chains increased beyond trimers, due to a "trade-off" between losses and local field enhancement. For the end-to-end NR alignment, the E field is oriented along the NR axis, and the near E fields couple constructively, thereby leading to a red shift of the longitudinal SPR [24, 25].

With respect to side-by-side assembly of gold NRs, a number of methods have been demonstrated [33], including the use of chelating agents [34], an antibody to a toxin molecule (microcystin-LR) [35] and the addition of anions via electrostatic interactions

(citrate) [36]. However, to date, only a single experimental study exists that reports on the solution-state SERS properties of side-by-side assembled NRs. This study showed a 10-fold increase in intensity of the SERS signal of the resonant dye, as compared with the SERS of the individual NRs [36]. While we note that 3D multilayered stacks and 2D superstructures are highly SERS-active [34, 37, 38], these structures have a distinct E field distribution and, consequently, different SERS properties, in comparison with small solution-based side-by-side assembled NR clusters. For this reason, the results of our work cannot be directly compared with those of superstructures.

Here, we report experimental and theoretical analyses of the optical properties of side-by-side assembled gold NR clusters. Experimentally, we examined the extinction and ensembleaveraged SERS properties of the NR clusters following their assembly in the solution state. Our results showed a blue shift of SPR wavelength, as expected, but surprisingly, a reduction of SERS intensity. Finite-difference time-domain (FDTD) simulations [39] confirmed the reduction in E-field intensity, as the number of NRs per cluster increases, due to destructive interference between the E-field radial components.

Materials and Methods

Synthesis of Gold Nanorods

All chemicals were purchased from Sigma Aldrich (Canada) and used without further purification. Cetyltrimethylammonium bromide (CTAB)-coated gold NRs were synthesized by the "seedmediated growth method" devised by El-Sayed et al [40]. Briefly, seed solution was prepared by the reduction of $HAuCl_4$, dissolved in an aqueous solution of CTAB, with cold sodium borohydride ($NaBH_4$). The growth solution was prepared by dropwise addition of ascorbic acid into an aqueous solution of $HAuCl_4$, CTAB, and $AgNO_3$. To initiate NR growth, a 5 min-aged seed solution was injected into the growth solution and incubated for 10 h at 27 °C. The resultant CTAB-coated gold NRs were purified by two centrifugation cycles at 8500 rpm for 30 min (*Eppendorf* centrifuge 5417R).

Side-by-Side Assembly of Gold Nanorods

The site-specific ligand exchange of CTAB was carried out at the NR ends with thiol-terminated polystyrene (SH-PS), purchased from Polymer Science Inc.) with a molecular

weight of 12000 g/mol and a polydispersity index of 1.09 [33]. Approximately 0.5 mL of the concentrated aqueous solution of CTAB-coated NRs (~1.0 mg/mL) was rapidly injected under sonication (42 kHz ± 0.6%) into 10 g of tetrahydrofuran (THF) solution containing 5 mg of SH-PS (~0.05 wt %) [30]. The solution mixture was sonicated for 30 min and incubated at room temperature for ~24 h. Purification of the sample from free polymer was carried out by eight centrifugation cycles at 8500 rpm for 30 min, and THF was used as a solvent. This purified sample was used as a stock NR solution. Next, 3 μM of a Raman reporter, cresyl violet (CV), was introduced into 990 μL of the stock solution under shaking. Following a 30 min agitation under gentle vortex conditions, the mixture was incubated for 1 h. To trigger side-by-side NR assembly, we added dropwise a THF-water mixture containing 10 vol % of water. All subsequent physical measurements were carried out on the same batch of NRs. As soon as NR self-assembly began, we carried out all subsequent physical measurements in parallel.

Characterization

The evolution of the side-by-side NR assemblies was monitored by using a Cary 500 UV/Vis/NIR spectrophotometer. Extinction spectra were recorded in the spectral range from 400 to 1200 nm at room temperature by using a 1 cm path length cell. Scanning transmission electron microscopy (STEM) images were recorded with a Hitachi S- 5200 field emission SEM equipped with a transmitted electron detector. The surface-enhanced Raman scattering (SERS) measurements were carried out by using a compact Raman system (Advantage Raman Series, DeltaNu) (785 nm laser line, the laser beam diameter of 35 μm at the focal point). The intensity of SERS was calibrated and normalized to the Raman spectra of cyclohexane and polystyrene, in order to correct for variations in optical alignment and instrument response. The spectra were acquired with a 5 cm^{-1} resolution. Control SERS measurements of CV adsorbed from either THF or water on a roughened gold substrate were conducted by using a Renishaw InVia System spectrometer coupled to a Leica microscope. The laser excitation and power were 785 nm (Renishaw solid-state laser model HPNIR785) and ~8 mW, respectively. The spectra were measured using a 20× objective (NA = 0.4) with an exposure time of 10 s and 5 scans. A solid gold electrode was roughened with 25 successive oxidation and reduction cycles from 0.3 to 1.2 V in an aqueous 0.1 M KCl working solution. A platinum wire was

used as a counter electrode, and the reference electrode was Ag|AgCl|KCl(sat). The roughened gold electrode was then isolated from the electrochemical cell, and CV in THF or water was introduced for the SERS measurements.

Finite-Difference Time-Domain (FDTD) Simulations.

To model the complex permittivity of gold, we used the experimental data of Johnson and Christy [41]. The simulation domain was terminated by a perfectly matched layer to ensure minimum reflections from the boundaries of the simulation domain. The total field scattered field (TFSF) source was used for the determination of absorption, scattering, and extinction cross sections of assembled NRs, which divided the simulation domain into two regions. In one region, only scattered fields were present, while the other region contains both the incident and the scattered fields. The scattering cross section was determined by calculating the Poynting vector over a closed surface surrounding the NRs in the scattered field region. The absorption cross section was calculated by determining the net flow of power into a closed surface surrounding the NRs in the total field region. The incident plane wave was polarized at 45° to the long axis of the NRs, and as such, this polarization probes both the transverse and the longitudinal SPR. The mesh override region was defined with a mesh size of 1 nm for accurate modeling of the cylindrical structure in a Cartesian coordinate system.

Results and Discussion

By exploiting the anisotropy of the NRs in shape and surface energy [42-44], we carried out site-specific exchange of CTAB at the NR ends with thiol-terminated polystyrene SH-PS [33]. The SH-PS tethered to the NR ends rendered the NRs analogous to an “amphiphilic” molecular species with a hydrophilic long side and hydrophobic end groups. Later in the text, we refer to the PS-functionalized NRs as the “NRs”, unless otherwise stated. We triggered the self-assembly of the NRs in a side-by-side manner by changing the quality of solvent for the ligands. We note that THF is a poor solvent for CTAB, and the stability of the NRs in THF was attributed to the polystyrene ligands (the values of the second virial coefficient, A2, is 9.0×10^{-4} mol cm^3 g^{-2}, equivalent to Flory-Huggins interaction parameter equal to 0.4) [33]. We added water to the THF solution of

the NRs to a total concentration of water of 10 wt %, thereby reducing the solubility of the PS ligands. As a result, the NRs assembled in the side-by-side manner (Figure F-1).

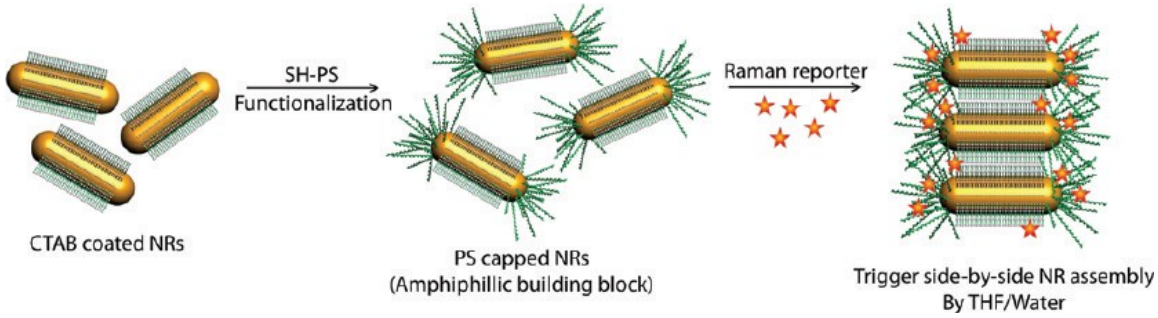

Figure F-1: Schematic illustration of the side-by-side NR assembly. A SH-PS is attached to the ends of CTAB-coated gold NRs in THF via site-specific ligand exchange. After the addition of the Raman reporter, the side-by-side assembly was triggered by the addition of water (10 vol %).

Figure F-2a shows photographs of the solutions of NRs following their self-assembly over time. The typical color of the solutions changed from reddish-purple to blue. We did not observe any apparent "precipitation" throughout the acquisition of all measurements. The NR ensembles showed colloidal and temporal stability for at least 3 months. Figure F-2b shows the evolution of extinction spectra of NR solutions, plotted over the course of assembly. The consistent blue shift of the longitudinal SPR peak from 770 to 715 nm indicated that the NRs were assembled in a side-by-side configuration [26]. The blue shift occurred due to the parallel alignment of dipole modes of individual NRs (this result will be addressed below by numerical simulations) [24]. We did not observe SPR peak broadening, which could be characteristic for the formation of large, irregular NR aggregates. The transverse SPR showed a relatively small red shift from 510 to 519 nm, due to attractive interaction between NRs.

Representative scanning transmission electron microscopy (STEM) images of the NR clusters in various stages of their self-assembly are shown in Figure F-2a (low-magnification STEM images of the NR assemblies are presented in the Supporting Information). Using image analysis, we determined that, throughout the self-assembly process, the average distance between the long sides of adjacent NRs remained at 1.97 ± 0.48 nm. This inter-NR spacing was smaller than would be expected for four layers of CTAB ligands (~4 nm, assuming capping of the NR sides with a CTAB bilayer) [45, 46],

presumably, due to the interdigitation of CTAB molecules in the gaps between the NRs [47, 48].

We did not calculate the average aggregation number of the NR ensembles, because it is well established that, upon evaporation of the solvent on a carbon-coated TEM grid, gold NRs form stacks, in which they are aligned in the parallel manner [47]. The alignment occurs due to the van der Waals forces acting between the NRs: on the basis of Hamaker integral approximation, for small NR separation distance, the side-by-side configuration is preferred [49]. Nevertheless, inspection of the TEM images showed that the number of individual NRs decreased through the course of self-assembly. For example, 24 h after triggering the self-assembly, we observed ~57% of individual NRs, 28% of dimers, 10% of trimers, and 3% of tetramers, whereas for 216 h long assembly, the fractions of these species were 30, 44, 18, and 8%, respectively.

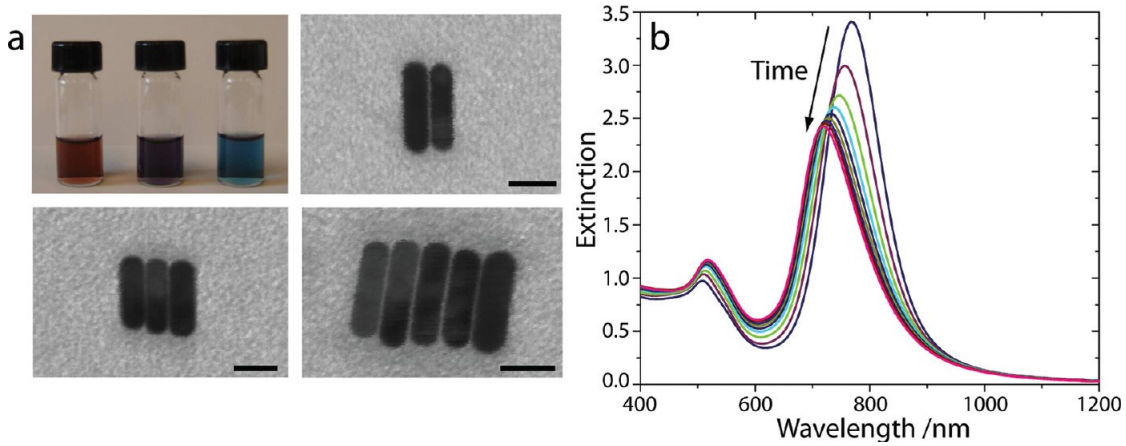

Figure F-2: (a) A photograph showing a typical change in color of the solution of self-assembling NRs as a function of time from reddish-purple to blue (top left). Representative scanning transmission electron microscopy (STEM) images of NRs in various stages of self-assembly. The scale bar is 15 nm. (b) Variation in extinction properties of NR ensembles over time.

Concurrently, with extinction measurements over the course of side-by-side assembly of the NRs, we monitored ensembleaveraged SERS of cresyl violet (CV) (Figure F-3a). The most enhanced SERS bands of CV appeared at 535 and 595 cm^{-1} and were caused by in plane vibrational ring modes of CV [50]. The band at 900 cm^{-1} corresponded to the ring "breathing" mode of THF [51] and was used as an internal standard. The position of the bands shown in the SERS spectrum were in accordance with the ordinary Raman spectrum of CV, which suggested that CV was physically adsorbed on the surface of the

NRs. Figure F-3b shows the variation in the normalized SERS peak intensity of CV at 535 and 595 cm^{-1}, plotted as a function of self-assembly time, *t*. We observed a gradual reduction in normalized SERS intensities of both peaks of CV for *t* increasing from 5 min to 216 h. In the control experiment, the spectrum of the solution containing the same amount of CV and individual (not assembled) NRs showed relatively constant intensities of the SERS peak at 595 cm^{-1} for the duration up to 216 h.

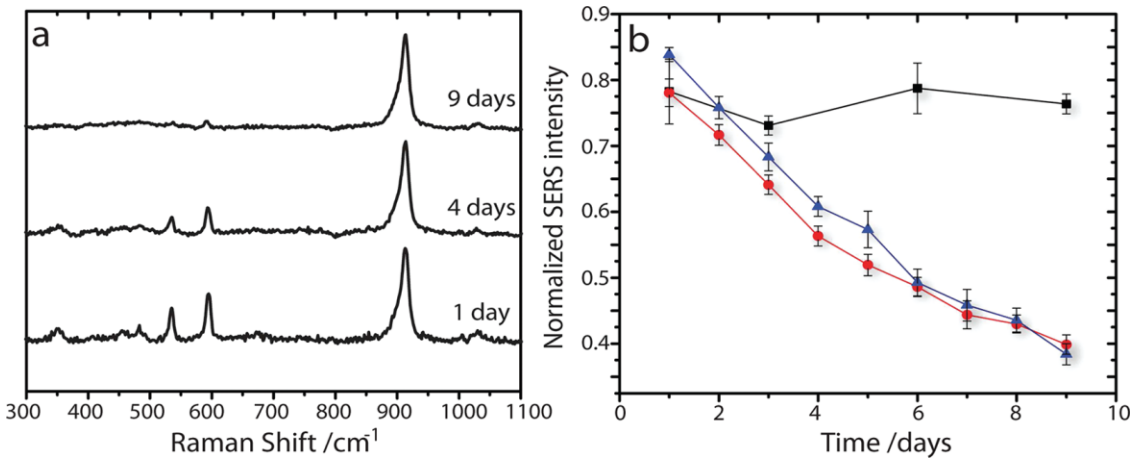

Figure F-3. (a) Representative ensemble-averaged SERS spectra of cresyl violet (CV), measured in the course of side-by-side assembly of the NRs as a function of time. The band at 900 cm^{-1} corresponds to THF and was used as an internal standard to normalize the intensity of SERS of CV at 535 and 595 cm^{-1}. (b) Normalized SERS intensity at 535 cm^{-1} (red circle), 595 cm^{-1} (blue triangle), and in control experiments conducted without the assembly of the NRs (black square, for SERS of CV at 595 cm^{-1}) as a function of time.

To further investigate the experimental findings, we conducted comprehensive electromagnetic FDTD simulations, numerically solving Maxwell's equations by iteration over time. Figure F-4a-c shows FDTD calculations of the change in the normalized absorption, scattering, and extinction cross sections, all plotted as a function of wavelength for the assemblies with a side-by-side NR alignment. The number of NRs in the clusters changed from one to eight NRs.

By comparing the results obtained in experiments and simulations, we observed a small difference in the spectral position and the relative intensity of the transverse SPR of the NRs. The SPR modes are dependent on the direction of propagation of incident radiation. The simulations were carried out for one direction of propagation incident wavevector (k_{inc}), which was perpendicular to the long axis of the NRs. This was not the case for the extinction experiments carried out for the NR solution. To verify the dependence on the

propagation direction, we carried out simulations for two different directions of light propagation, that is, parallel and perpendicular to the long axis of the NRs (Supporting Information). We note that, for the parallel propagation, only the transverse SPR is excited.

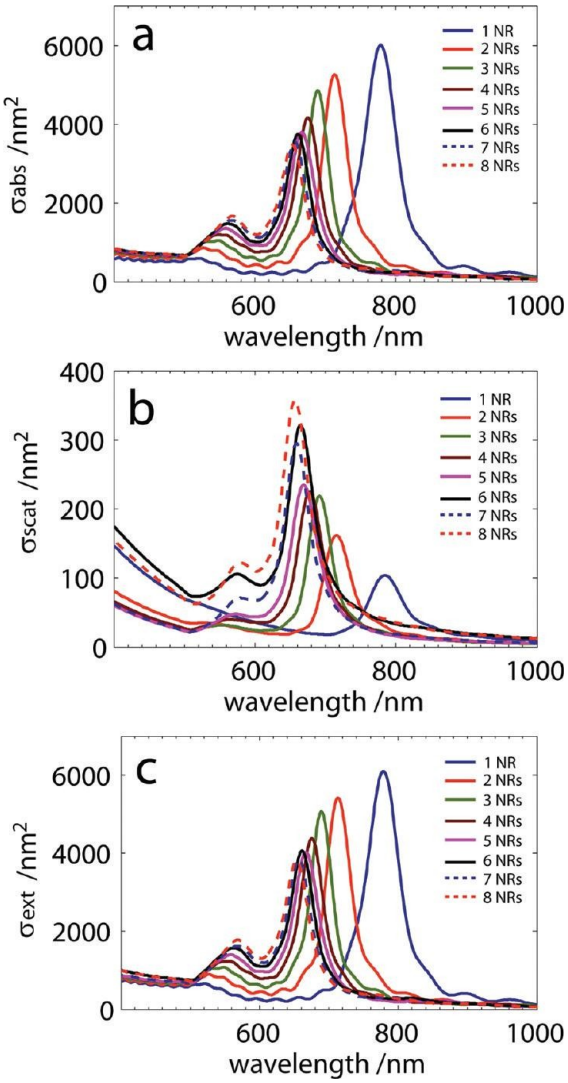

Figure F-4: Calculated normalized absorption (a), scattering (b), and extinction cross section (c), all plotted as a function of wavelength for NR assemblies containing from one to eight NRs. Simulations were carried out using FDTD.

The FDTD simulation showed a blue shift of the resonance wavelength from 779 to 653 nm, as the number of NRs per ensemble increased from one to eight NRs, respectively. The resonance wavelength of a single NR or a stack of NRs arranged in a side-by-side manner is determined by two variables: the propagation constant β of the

radial SP mode and the phase of light reflection from the ends of the NRs. At resonance, the following condition is satisfied [2, 29, 52].

$$\beta L + \phi_{ref} = \pi \tag{F.1}$$

where L is the NR length, ϕ_{ref} is the phase of reflection from the end of the NRs, and β is the propagation constant ($\beta = n_{eff} 2\pi / \lambda$, where n_{eff} is the effective index of the system containing NRs and the surrounding medium). The analytical expression for the phase of reflection from flat-ended NRs has recently been derived [53], whereas only numerical solutions for phase of reflection for NRs with hemispherical ends (common in colloidal systems) are currently available.

The value of β is a geometry-dependent variable, and it can be obtained from the mode shape of the radial SP wave. Figure F-5 shows mode shapes of one NR and side-by-side assemblies of two and three NRs. By using modal solutions, we numerically verified that, as the number of NRs in the ensemble increases, the value of n_{eff} decreases, thereby reducing the value of β. More specifically, for one, two, and three NRs, the resultant value of n_{eff} was 11.81, 9.29, and 8.13, respectively, and the corresponding value of β was 98.9 × 10^6, 77.8 × 10^6, and 68.1 × 10^6 m^{-1}, respectively.

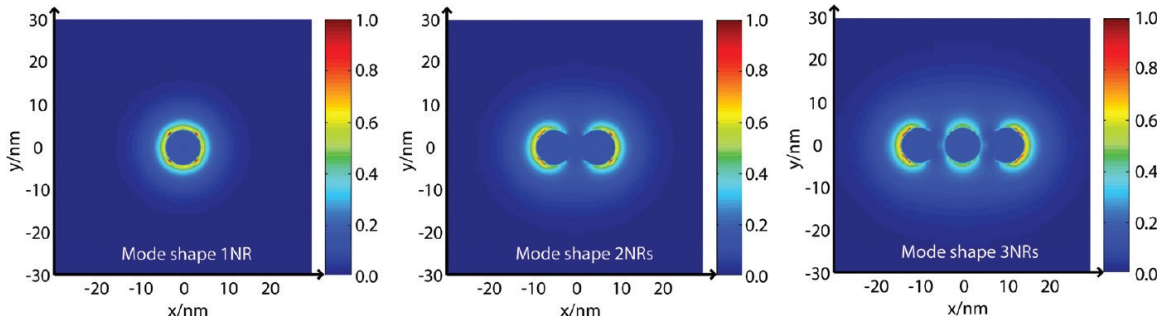

Figure F-5: Modes supported by side-by-side assembly of NRs. Mode shapes of surface plasmons of one to three NRs from left to right (looking down the long axis (z axis) of the NRs). The resulting effective index values are used for the calculation of the propagation constant of surface wave in the different geometries and show that the propagation constant decreases as the number of NRs increase. Fields are normalized to their maximum intensities.

This reduction occurs when the NRs are brought into close proximity to each other in the side-by-side ensembles. Consequently, the mode shape of interacting NRs changed as compared with that of an individual NR. The radial components of the E field of the

neighboring NRs cancel each other, due to destructive interference, resulting in a reduction of the local E field (Figure F-6). To satisfy Eq. 1, the reduction in n_{eff} had to be compensated by a proportional amount of reduction in the resonant wavelength (to first order, ignoring the effects of dispersion in n_{eff}). Therefore, a blue shift occurred as the number of NRs aligned in a side-by-side manner increased (it should be noted that ϕ_{ref} is weakly wavelength-dependent [53], and earlier work [2] suggested that $\phi_{ref} \approx 0$).

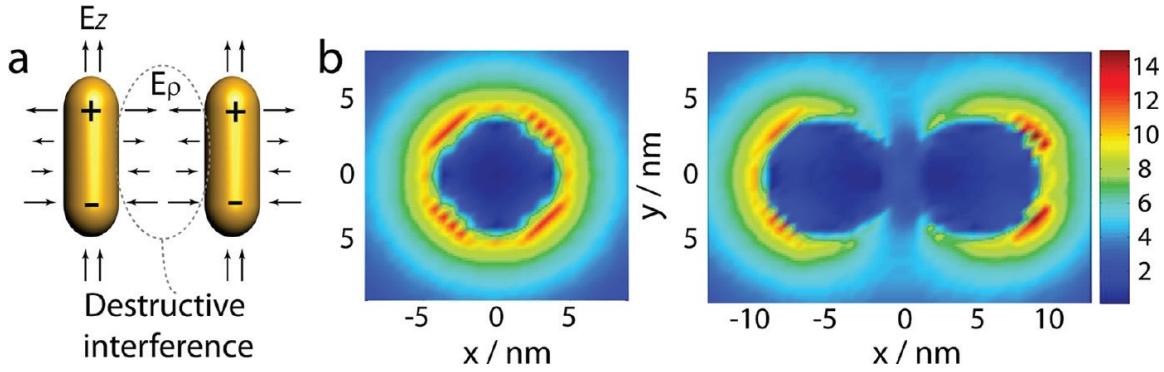

Figure F-6: (a) Schematic illustration of gold NRs assembled in a side-by-side manner showing a reduction of electric field due to destructive interference of the radial component of the E field (E_ρ). (b) Radial E-field profile via FDTD simulations for one and two NRs looking down the long axis (z axis) of the NRs showing the field cancellation in the gap between two NRs.

Figure F-7a-e shows examples of FDTD simulations of E-field intensity profiles of ensembles containing from one to five NRs at their corresponding resonance wavelengths at 780, 713, 690, and 678 nm, respectively (additional simulations are provided in the Supporting Information). We note that the field intensity in the gap between two neighboring NRs is significantly smaller, compared with the field intensity for a single NR. Figure F-7e shows the normalized sum of E-field intensity squared as a function of wavelength. As the number of NRs per stack increased from one to eight, the sum of the intensity squared decreased. Unlike end-to-end NR assembly, which exhibited constructive inference [30], for the side-by-side assembly, the reduction of the field originated from the cancellation of the radial component of the SP mode, thereby leading to destructive interference, as shown in Figure F-6. We note that we examined the E-field intensity of two different geometries of NR assemblies, that is, the 2D "stack" vs a 3D "bundle" [54], and found similar sums of E-field intensities (Supporting Information).

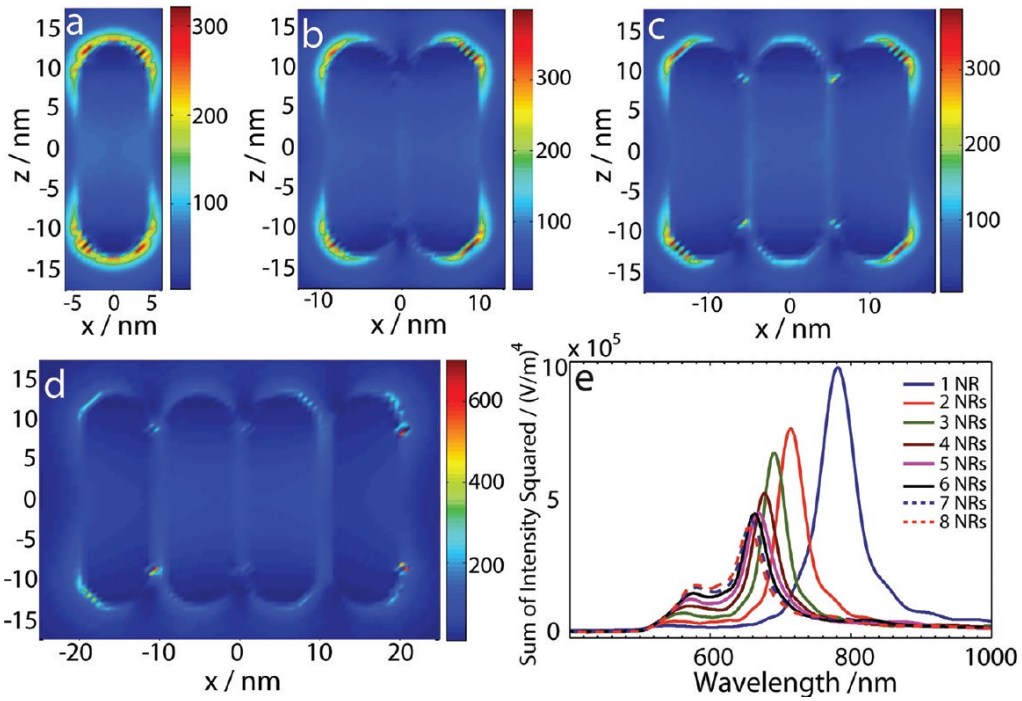

Figure F-7: (a-d) Examples of electric field intensity profiles produced via 3D-FDTD simulation for side-by-side assembled NRs at their resonance wavelengths. Polarization of the incident light is at 45° to the long axis (*z* coordinate) of NRs. (e) Sum of electric field intensity squared of ensembles containing a different number of NRs.

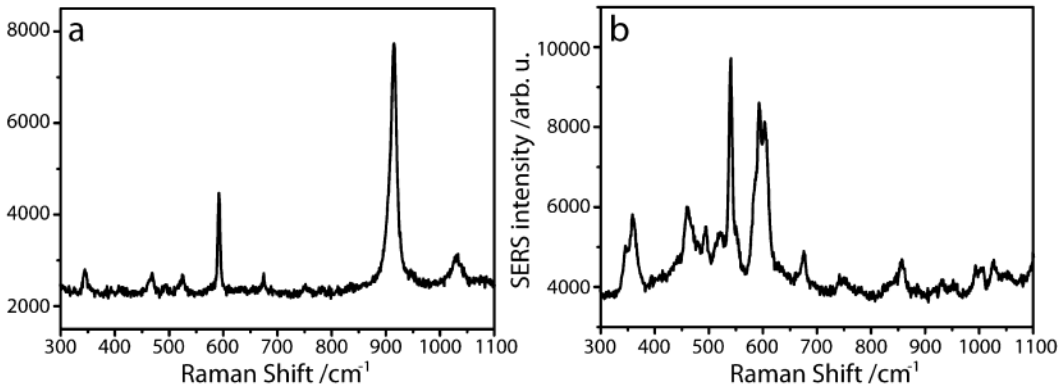

Figure F-8: SERS of CV on a roughened gold substrate in THF (a) and water (b). In THF, the spectral positions of the CV peaks (591 cm^{-1}) were in concordance with those observed for CV coassembled with NRs. A 785 nm laser excitation was used.

The results presented in Figures E5-E7 suggest that, due to destructive interference, the region between the rods is not the "hot spot". To validate this experimentally, we conducted control SERS measurements of CV adsorbed from either THF or water on a roughened gold substrate [55]. Figure F-8 shows that the SERS spectra of CV are

solvent-dependent. In the THF solution, the spectral positions of the CV peaks (591 cm^{-1}) were in concordance with those observed for CV coassembled with NRs (Figure F-3a), whereas in the water environment, CV exhibited a significant shift in the spectral peak positions [52] to 541 and 600 cm^{-1}, in comparison with those measured in the THF solution. The observed changes may be caused by hydrogen bonding between CV and water molecules, which causes the change in the average orientation of the CV molecules with respect to the surface of NRs. On the basis of the similarity of SERS spectra of CV acquired for its THF solution and for the self-assembled NR clusters, we conclude that, in the side-by-side assembled NR experiments, we are probing SERS properties of CV in a THF environment, from which water is largely excluded. Since the SERS signal originates from the "hot-spot" region, this result suggests that the CV species producing most of the Raman scattered signal are located at the ends of NRs (and not between the NR long sides, where destructive interference is dominant), in agreement with numerical calculations presented in Figure F-7. We note that probing of SERS of CV located at the ends of NRs did not exclude the possibility of CV being located on the sides of NRs. Such partition is possible because CV has an amphiphilic nature, due to the presence of an unsaturated ring structure and a cationic imine group. Thus, the hydrophobic moiety of CV can intercalate into the hydrocarbon chains of the CTAB bilayer on the NR long sides. A similar effect was observed for molecules containing both ionic and hydrophobic moieties (e.g., tetraphenylphosphonium) partitioning into a lipid bilayer, when hydrophobic forces dominated over electrostatic repulsion [29].

To further support our finding of the reduction of SERS intensity arising from probing at the ends of NRs, we numerically examined location-specific E-field variation at the ends of NRs (Supporting Information). The normalized sum of E-field intensity squared over volume showed a decrease as a function of the number of NRs. The reduction of E field suggested that SERS of CV should decrease as the number of NRs per ensemble increases, considering only the electromagnetic effect of SERS, which was the predominant factor in our work.

In summary, the present study provides an important insight into the optical properties of side-by-side assembled gold NRs. We showed that the normalized sum of the E-field intensity decreases as the number of NRs in the ensemble increases. The observed

reduction of E-field intensity occurs due to the cancelation of the radial component of SP modes. Calculated and measured extinction spectra show a blue shift of the longitudinal SPR, which is caused by the reduction of effective index, when the number of NRs per ensemble increases. While it is generally expected that aggregates of metal nanoparticles are better SERS platforms than individual nanoparticles, our experimental work showed the reduction in ensemble-averaged SERS intensity, which was in concordance with comprehensive FDTD calculations.

Although there has been significant progress in the organization of NRs in the side-by-side mode, the next challenge is to exploit the functionality of these plasmonic ensembles. While the observed spectral shift in SPR of NRs has found applications in colorimetric sensors, our results suggest that small side-by-side assembled clusters may not be suitable for use as highly sensitive SERS probes. Fundamentally, this study expands our understanding of the interplay between geometry, assembly, and the optical properties of plasmonic nanoparticles.

A.L., A.A., R.G., A.G.B., and E.K. acknowledge financial support of NSERC Canada for the Strategic Network for Bioplasmonic Systems (Biopsys). A.L. thanks Xiaoqiang Zhang for his help. D.P.d.S. acknowledges Inter-American Collaboration in Materials Research (CIAM) grants from NSERC (Canada) and FAPESP (Brazil).

References

[1] A. Ahmed and R. Gordon, "Directivity Enhanced Raman Spectroscopy Using Nanoantennas," *Nano Letters,* vol. 11, pp. 1800-1803, 2011.

[2] L. Novotny, "Effective wavelength scaling for optical antennas," *Physical Review Letters,* vol. 98, p. 4, 2007.

[3] A. G. Curto*, et al.*, "Unidirectional Emission of a Quantum Dot Coupled to a Nanoantenna," *Science,* vol. 329, pp. 930-933, 2010.

[4] T. J. Seok*, et al.*, "Radiation Engineering of Optical Antennas for Maximum Field Enhancement," *Nano Letters,* vol. 11, pp. 2606-2610, 2011.

[5] T. H. Taminiau*, et al.*, "Optical antennas direct single-molecule emission," *Nature Photonics,* vol. 2, pp. 234-237, 2008.

[6] T. W. Ebbesen*, et al.*, "Extraordinary optical transmission through sub-wavelength hole arrays," *Nature,* vol. 391, pp. 667-669, 1998.

[7] L. Martin-Moreno*, et al.*, "Theory of extraordinary optical transmission through subwavelength hole arrays," *Physical Review Letters,* vol. 86, pp. 1114-1117, 2001.

[8] S. Lal*, et al.*, "Nano-optics from sensing to waveguiding," *Nature Photonics,* vol. 1, pp. 641-648, 2007.

[9] S. A. Maier*, et al.*, "Observation of near-field coupling in metal nanoparticle chains using far-field polarization spectroscopy," *Physical Review B,* vol. 65, 2002.

[10] J. Barthes*, et al.*, "Purcell factor for a point-like dipolar emitter coupled to a two-dimensional plasmonic waveguide," *Physical Review B,* vol. 84, 2011.

[11] X. Huang*, et al.*, "Cancer Cells Assemble and Align Gold Nanorods Conjugated to Antibodies to Produce Highly Enhanced, Sharp, and Polarized Surface Raman Spectra: A Potential Cancer Diagnostic Marker," *Nano Letters,* vol. 7, pp. 1591-1597, 2007.

[12] K. S. Lee and M. A. El-Sayed, "Gold and silver nanoparticles in sensing and imaging: Sensitivity of plasmon response to size, shape, and metal composition," *Journal of Physical Chemistry B,* vol. 110, pp. 19220-19225, 2006.

[13] S. Linic, et al., "Plasmonic-metal nanostructures for efficient conversion of solar to chemical energy," Nat Mater, vol. 10, pp. 911-921, 2011.

[14] P. K. Jain, et al., "Noble Metals on the Nanoscale: Optical and Photothermal Properties and Some Applications in Imaging, Sensing, Biology, and Medicine," Accounts of Chemical Research, vol. 41, pp. 1578-1586, 2008.

[15] M. Moskovits, "SURFACE-ENHANCED SPECTROSCOPY," Reviews of Modern Physics, vol. 57, pp. 783-826, 1985.

[16] R. Aroca, "Surface-Enhanced Vibrational Spectroscopy," ed. New York: John Wiley & Sons, 2006.

[17] M. Moskovits and J. S. Suh, "Surface selection-rules for surface-enhanced Raman-spectroscopy - calculations and application to the surface-enhanced Raman-spectrum of phthalazine on silver," Journal of Physical Chemistry, vol. 88, pp. 5526-5530, 1984.

[18] E. C. Le Ru, et al., "A Scheme for Detecting Every Single Target Molecule with Surface-Enhanced Raman Spectroscopy," Nano Letters, vol. 11, pp. 5013-5019, 2011.

[19] S. Shanmukh, et al., "Rapid and sensitive detection of respiratory virus molecular signatures using a silver nanorod array SERS substrate," Nano Letters, vol. 6, pp. 2630-2636, 2006.

[20] K. Kneipp, et al., "Ultrasensitive chemical analysis by Raman spectroscopy," Chemical Reviews, vol. 99, pp. 2957-2975, 1999.

[21] D. A. Weitz, et al., "The enhancement of Raman-scattering, resonance Raman-scattering, and fluorescence from molecules adsorbed on a rough silver surface," Journal of Chemical Physics, vol. 78, pp. 5324-5338, 1983.

[22] N. J. Halas, et al., "Plasmons in Strongly Coupled Metallic Nanostructures," Chemical Reviews, vol. 111, pp. 3913-3961, 2011.

[23] X. Huang, et al., "Gold Nanorods: From Synthesis and Properties to Biological and Biomedical Applications," Advanced Materials, vol. 21, pp. 4880-4910, 2009.

[24] L. S. Slaughter, et al., "Effects of Symmetry Breaking and Conductive Contact on the Plasmon Coupling in Gold Nanorod Dimers," Acs Nano, vol. 4, pp. 4657-4666, 2010.

[25] A. M. Funston, et al., "Plasmon Coupling of Gold Nanorods at Short Distances and in Different Geometries," Nano Letters, vol. 9, pp. 1651-1658, 2009.

[26] P. K. Jain, et al., "Plasmon coupling in nanorod assemblies: Optical absorption, discrete dipole approximation simulation, and exciton-coupling model," Journal of Physical Chemistry B, vol. 110, pp. 18243-18253, 2006.

[27] L. Shao, et al., "Angle- and Energy-Resolved Plasmon Coupling in Gold Nanorod Dimers," Acs Nano, vol. 4, pp. 3053-3062, 2010.

[28] C. Tabor, et al., "Effect of Orientation on Plasmonic Coupling between Gold Nanorods," Acs Nano, vol. 3, pp. 3670-3678, 2009.

[29] R. F. Flewelling and W. L. Hubbell, "Hydrophobic ion interactions with membranes - thermodynamic analysis of tetraphenylphosphonium binding to vesicles," Biophysical Journal, vol. 49, pp. 531-540, 1986.

[30] A. Lee, et al., "Probing Dynamic Generation of Hot-Spots in Self-Assembled Chains of Gold Nanorods by Surface-Enhanced Raman Scattering," Journal of the American Chemical Society, vol. 133, pp. 7563-7570, 2011.

[31] S. J. Lee, et al., "Hot spots in silver nanowire bundles for surface-enhanced Raman spectroscopy," Journal of the American Chemical Society, vol. 128, pp. 2200-2201, 2006.

[32] J. Kumar and K. G. Thomas, "Surface-Enhanced Raman Spectroscopy: Investigations at the Nanorod Edges and Dimer Junctions," Journal of Physical Chemistry Letters, vol. 2, pp. 610-615, 2011.

[33] (a) Z. H. Nie, et al., "Self-assembly of metal-polymer analogues of amphiphilic triblock copolymers," Nature Materials, vol. 6, pp. 609-614, 2007. (b) Z. H. Nie, et al., "Supramolecular" assembly of gold nanorods end-terminated with polymer "Pom-Poms": Effect of pom-pom structure on the association modes," Journal of the American Chemical Society, vol. 130, pp. 3683-3689, 2008. (c) D. Fava, et al., "Evolution of Self-Assembled Structures of Polymer-Terminated Gold Nanorods in Selective Solvents," Advanced Materials, vol. 20, pp. 4318-4322, 2008.

[34] T. S. Sreeprasad and T. Pradeep, "Reversible Assembly and Disassembly of Gold Nanorods Induced by EDTA and Its Application in SERS Tuning," Langmuir, vol. 27, pp. 3381-3390, 2011.

[35] L. Wang, et al., "Side-by-Side and End-to-End Gold Nanorod Assemblies for Environmental Toxin Sensing," Angewandte Chemie-International Edition, vol. 49, pp. 5472-5475, 2009

[36] A. McLintock, et al., "Controlled side-by-side assembly of gold nanorods and dye molecules into polymer-wrapped SERRS-active clusters," Chemical Communications, vol. 47, pp. 3757-3759, 2011.

[37] S. Yun, et al., "Linker-Molecule-Free Gold Nanorod Films: Effect of Nanorod Size on Surface Enhanced Raman Scattering," Journal of Physical Chemistry C, vol. 113, pp. 13551-13557, 2009.

[38] R. A. Alvarez-Puebla, et al., "Gold nanorods 3D-supercrystals as surface enhanced Raman scattering spectroscopy substrates for the rapid detection of scrambled prions," Proceedings of the National Academy of Sciences of the United States of America, vol. 108, pp. 8157-8161, 2011

[39] Taflove A and H. S. C, Computational Electrodynamics: The Finite-Difference Time Domain Method, 2nd ed. Boston: Artech House, 2000.

[40] B. Nikoobakht and M. A. El-Sayed, "Preparation and growth mechanism of gold nanorods (NRs) using seed-mediated growth method," Chemistry of Materials, vol. 15, pp. 1957-1962, 2003.

[41] P. B. Johnson and R. W. Christy, "Optical-constants of noble-metals," Physical Review B, vol. 6, pp. 4370-4379, 1972.

[42] C. J. Murphy, et al., "Gold nanorod crystal growth: From seed-mediated synthesis to nanoscale sculpting," Current Opinion in Colloid & Interface Science, vol. 16, pp. 128-134, 2011.

[43] C. J. Murphy*, et al.*, "The Many Faces of Gold Nanorods," *Journal of Physical Chemistry Letters,* vol. 1, pp. 2867-2875, Oct 7 2010.

[44] K. Liu, et al., "Self-assembly of inorganic nanorods," Chemical Society Reviews, vol. 40, pp. 656-671, 2011.

[45] N. V. Venkataraman and S. Vasudevan, "Hydrocarbon chain conformation in an intercalated surfactant monolayer and bilayer," Proceedings of the Indian Academy of Sciences-Chemical Sciences, vol. 113, pp. 539-558, 2001.

[46] G. G. Warr, et al., "Microemulsion formation and phase-behavior of dialkyldimethylammonium bromide surfactants," Journal of Physical Chemistry, vol. 92, pp. 774-783, 1988.

[47] T. K. Sau and C. J. Murphy, "Self-assembly patterns formed upon solvent evaporation of aqueous cetyltrimethylammonium bromide-coated gold nanoparticles of various shapes," Langmuir, vol. 21, pp. 2923-2929, 2005.

[48] N. V. Venkataraman and S. Vasudevan, "Interdigitation of an intercalated surfactant bilayer," Journal of Physical Chemistry B, vol. 105, pp. 7639-7650, 2001.

[49] K. J. M. Bishop, et al., "Nanoscale Forces and Their Uses in Self-Assembly," Small, vol. 5, pp. 1600-1630, 2009.

[50] E. Vogel, et al., "Vibrational spectroscopic studies on the dyes cresyl violet and coumarin 152," Journal of Molecular Structure, vol. 550, pp. 177-190, 2000.

[51] H. F. Shurvell and M. C. Southby, "Infrared and Raman spectra of tetrahydrofuran hydroperoxide," Vibrational Spectroscopy, vol. 15, pp. 137-146, 1997.

[52] M. Xiao, et al., "Gold nanotags for combined multi-colored Raman spectroscopy and x-ray computed tomography," Nanotechnology, vol. 21, 2010.

[53] R. Gordon, "Reflection of Cylindrical Surface Waves," Optics Express, vol. 17, pp. 18621-18629, 2009.

[54] Side-by-side assembled “bundled” NR structures rather than “stacked” structures can be obtained by the addition of 6 wt % water and 0.2 wt % PS in 10 mL of THF. Nie, Z.; et al. Nat. Mater. 2007, 6, 609-614 . The “bundled” NR ensembles showed a relatively lower sum of E-field intensity squared as compared with the “stacked” configuration.

[55] A. G. Brolo, et al., "The orientation of 2,2′-bipyridine adsorbed at a SERS-active Au electrode surface," Journal of Electroanalytical Chemistry, vol. 547, pp. 163-172, 2003.

Supporting Information for Appendix F

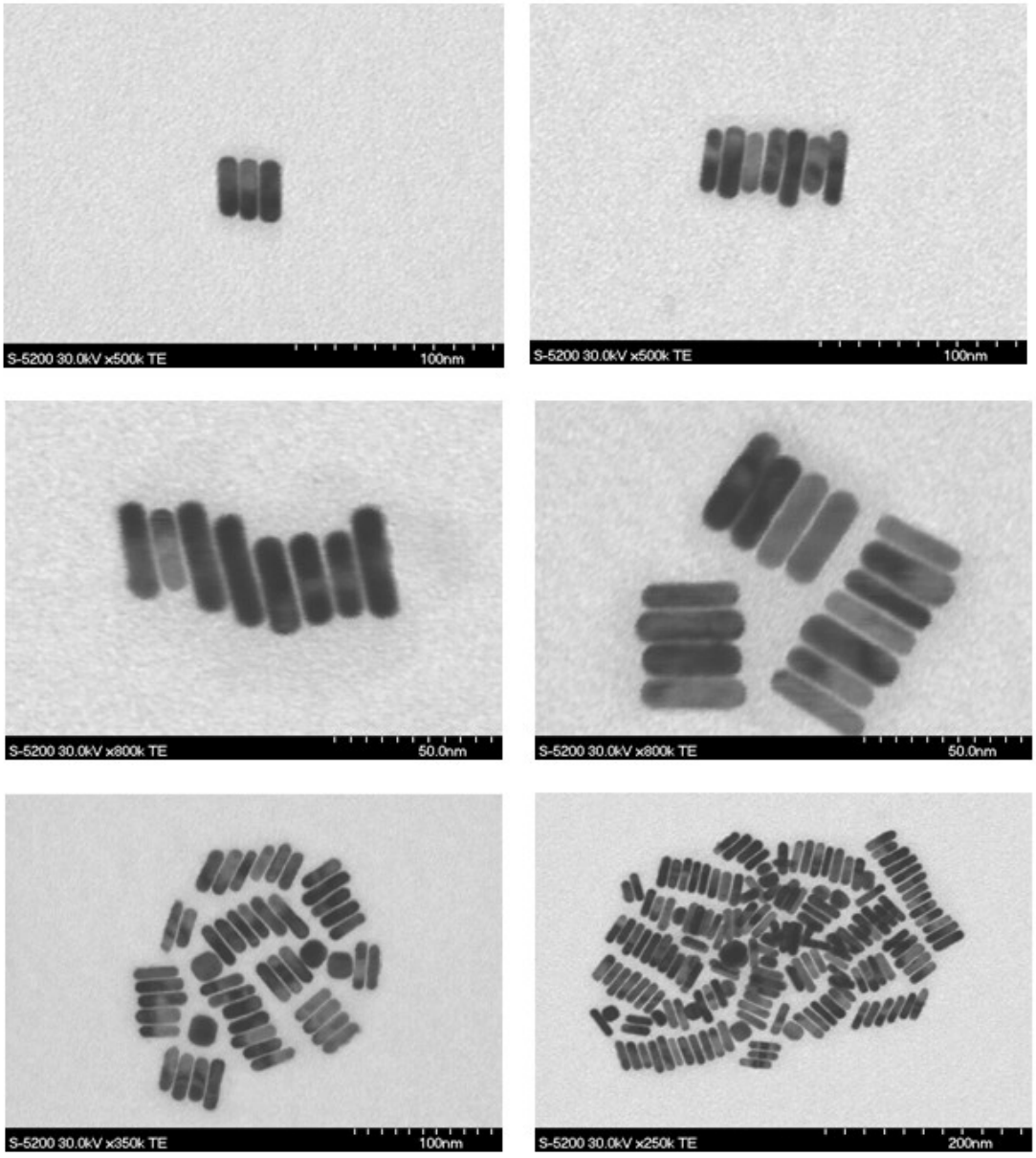

Figure F-S1: Representative scanning transmission electron microscopy (STEM) images of NRs in various stages of side-by-side assembly. Recorded on a Hitachi S-5200 scanning electron microscope operating in STEM mode. Note: as-synthesized NRs contain a small population of spheroids.

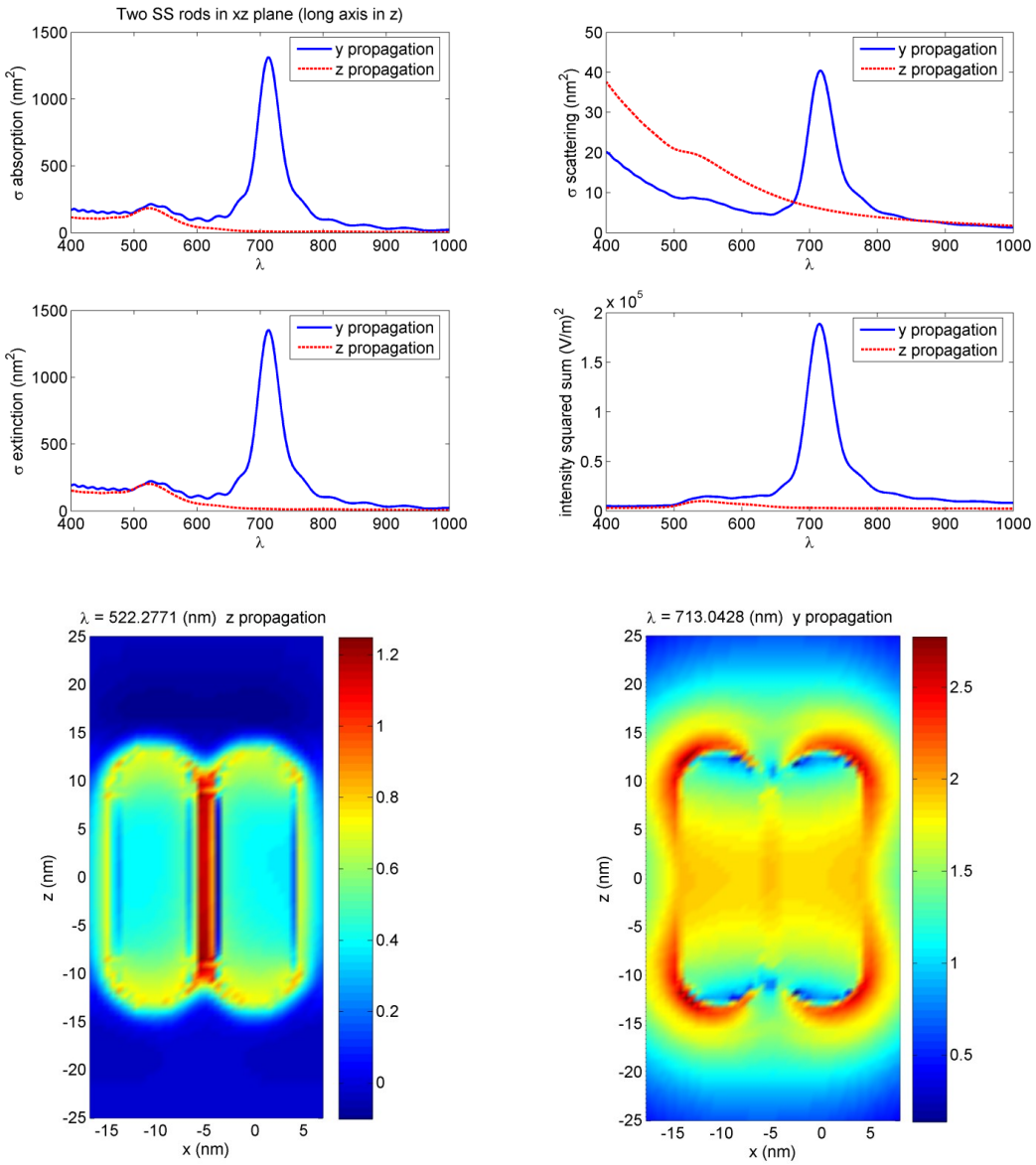

Figure F-S2: FDTD simulations showing absorption, scattering, and extinction of 2 NRs per stack for two different directions of propagation of incident radiation: perpendicular (y-propagation) and parallel (z-propagation) to the long axis of NRs. When wave vector k_{inc} is parallel to the NR axis, a peak at 520 nm is observed corresponding to the transverse SPR. The mode excited by the z-propagation incident light (bottom left) has a very weak response and the field between the NRs does not cancel due to the polarization of the incident light. It should be noted that for this propagation, only the transverse SPR is excited. The color bar represents electric field intensity on $\log_{10}$ scale.

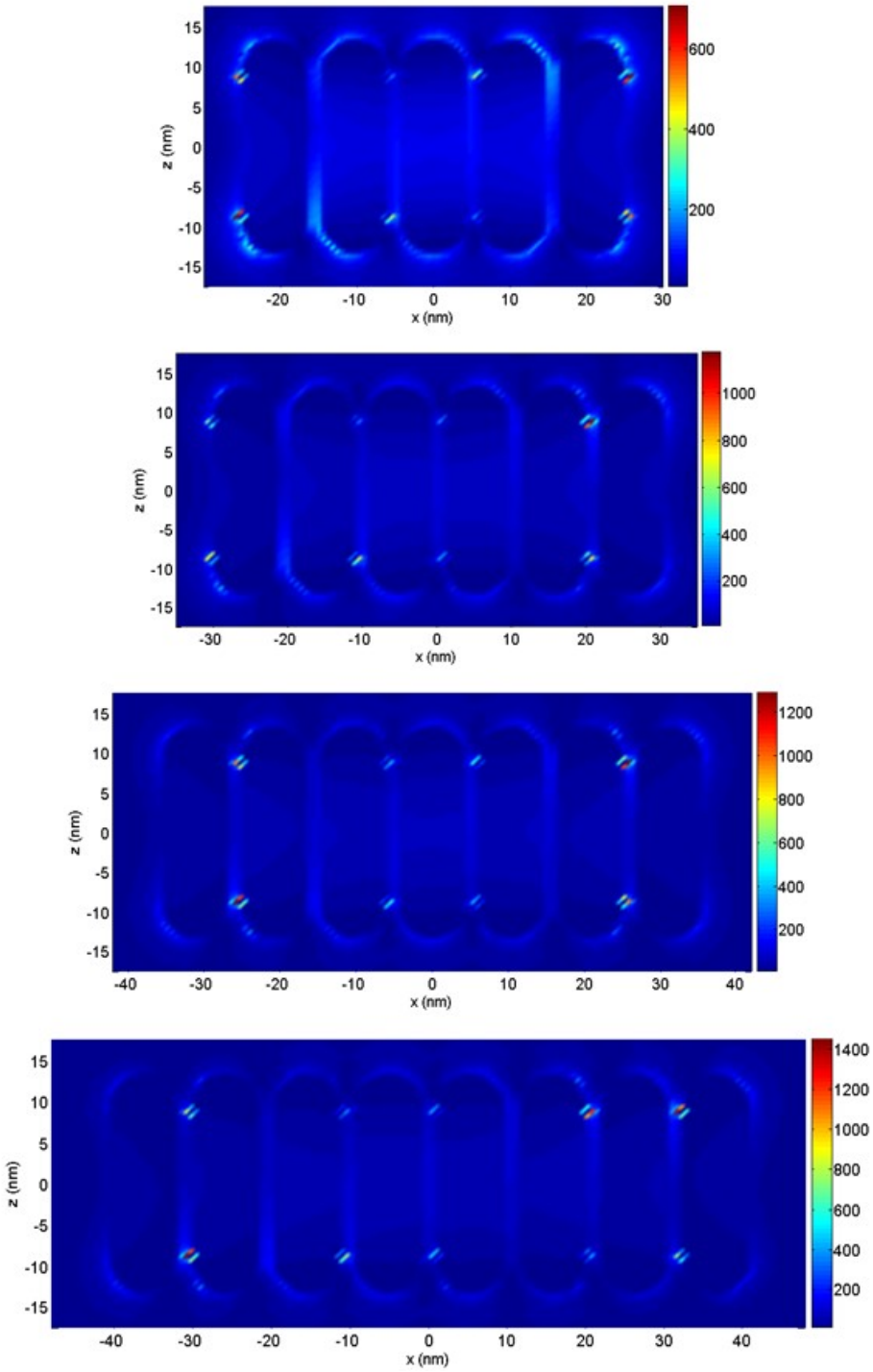

Figure F-S3: Examples of electric field profiles of side-by-side assembled gold NR structures via 3D-Finite Difference Time Domain (FDTD) simulations (for 5 to 8 NRs per stack). Electric field profile was calculated at the resonance wavelength of the NR stack at 669, 663, 659, and 655 nm from top left to the bottom right respectively. Polarization of the incident light is at 45 degrees to the long axis (z-coordinate) of NRs.

a

Bundle of 3 NRs **Bundle of 4 NRs**

b

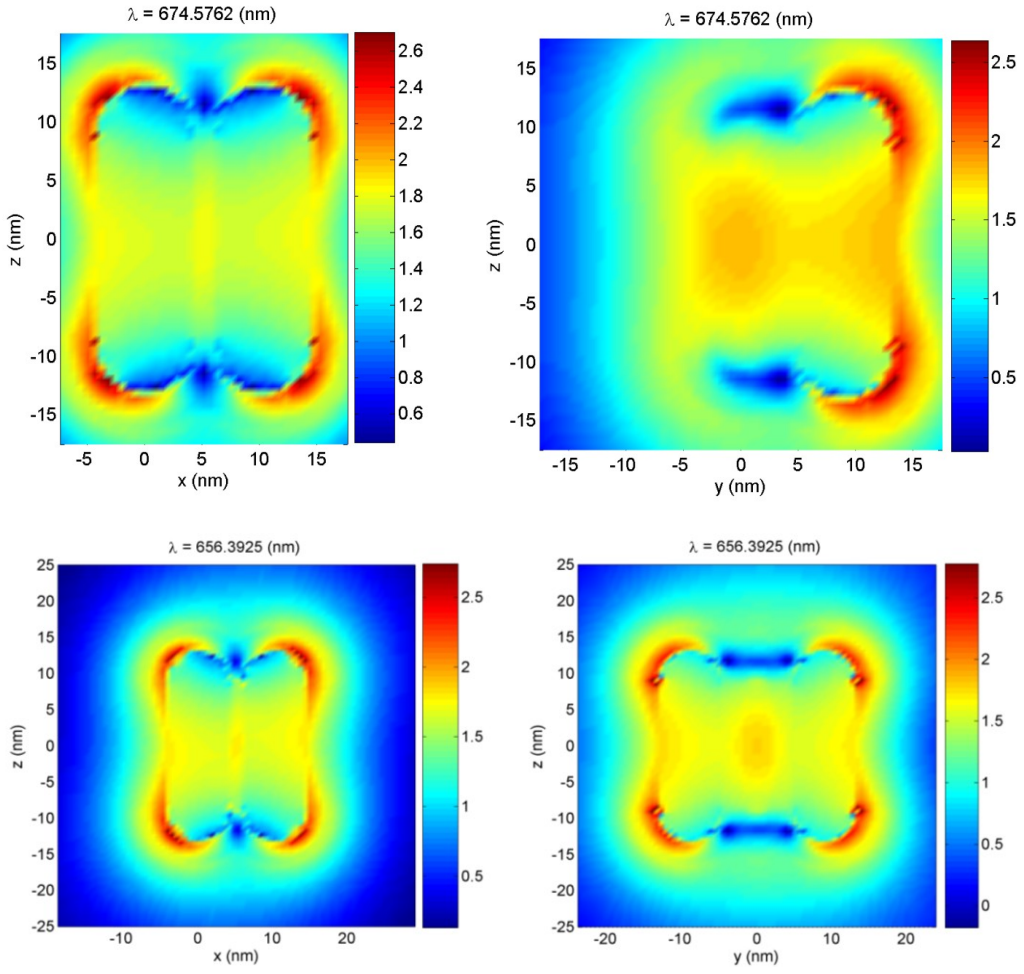

c

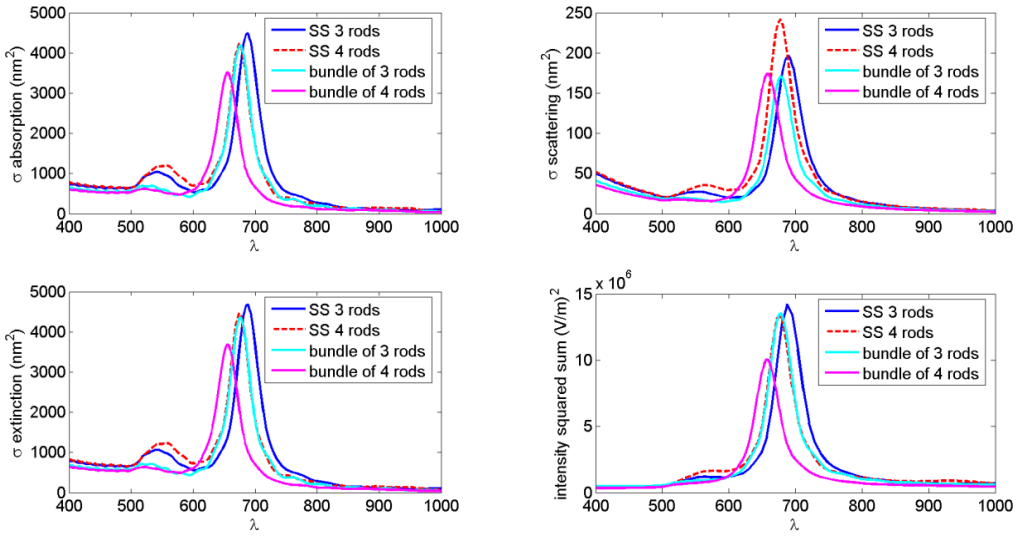

Figure F-S4: (a) Schematic illustration of bundled 3 and 4 NR structures. (b) Electric field profiles of the bundle structures containing 3 and 4 NRs (Log scale) at 674 and 656 nm. (c) Absorption, scattering, extinction and sum over volume of the electric field intensity squared are presented for 3 and 4 NRs in side-by-side (ss) stack and bundle configuration.

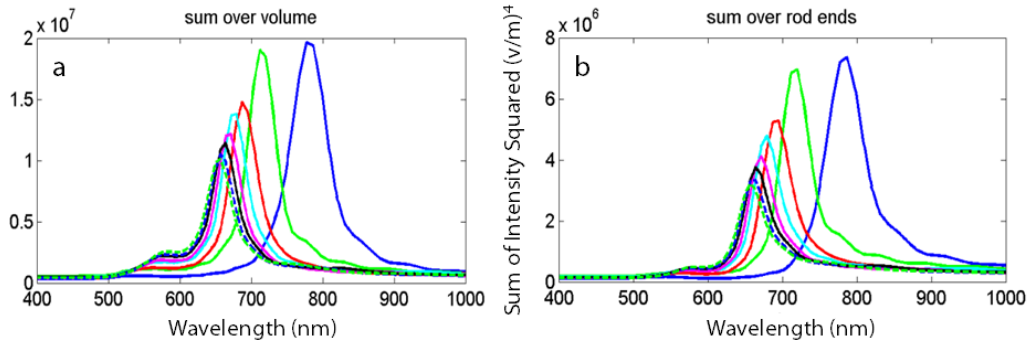

Figure F-S5: A sum over volume of the electric field intensity squared via FDTD simulations for various NR assemblies (number of NRs from 1 to 8) as a function of wave length (nm) (right figure). The total volume of the sum of *E* field intensity squared for the ends of NR ensembles show a decrease with increasing number of NRs. Blue: 1 NR, green: 2 NRs, Red: 3 NRs, light blue: 4 NRs, pink: 5 NRs, black: 6 NRs, dotted blue: 7 NRs, and dotted green: 8 NRs

Appendix G: Optimizing the Resolution of Nanohole Arrays in Metal Films for Refractive Index Sensing

(2012, Submitted to Applied Physics A)

Optimizing the Resolution of Nanohole Arrays in Metal Films for Refractive Index Sensing

*Gabriela Andrea Cervantes Tellez, Aftab Ahmed, Reuven Gordon**

Department of Electrical and Computer Engineering, University of Victoria, Victoria, British Columbia, V8W 3P6, Canada

ABSTRACT: We optimized the resolution of nanohole arrays in metal films for refractive index sensing by increasing the sensitivity with modifications to the hole-array parameters and by reducing the noise of the sensor system. The nanohole array parameters (including film thickness, periodicity and diameter) were first optimized by finite-difference time-domain simulations, and then fabricated and tested, showing good agreement between the two cases (theory and experiment) in terms of optimal parameters. To improve the sensitivity and to reduce the noise, the laser source wavelength was optimized (including the efficiency of the camera for detection) and the intensity was increased to reduce shot noise. A bulk resolution of 6×10-7 RIU was demonstrated. Due to the collinear microscope geometry and potential for multiplexing of nanohole arrays, these results are encouraging for future biosensing applications.

Introduction

Surface plasmon resonance (SPR) sensing is an established technology for monitoring refractive index changes due to mass loading at a surface of a metal film. Since the discovery of extraordinary optical transmission through nanohole arrays in metal films [1], it has been demonstrated that these arrays may be used for sensing applications [2-3]. Compared to Kretschmann-type SPR, sensing using the nanohole arrays is extremely promising for future technologies because it allows for: a small footprint for dense integration, a high degree of multiplexing, collinear optical detection for facile integration and combined optofluidic functionality [4-25].

The optimization of sensors includes sensitivity, resolution, reproducibility and accuracy. Sensitivity depends on the sensor output to the change in refractive index. Resolution is defined as the smallest change in refractive index that the nanohole array sensor can detect and is limited by the noise of the system [26]. Commercial SPR

instruments have a resolution of 10^{-7} refractive index units (RIU) [27]. So far, the resolution of nanohole arrays has been demonstrated to be between 10^{-4}-10^{-6} RIU; however, those works used complicated optical setups [28-30].

In this work, we optimize the resolution of nanohole arrays in metal films for refractive index sensing by increasing the sensitivity with modifications to the hole-array parameters and by reducing the noise of the sensor system. We achieve a bulk resolution of 6×10^{-7} RIU. Due to the collinear microscope geometry and potential for dense multiplexing of nanohole arrays with optofluidic functionality [31-33], the results are encouraging for future biosensing applications.

Simulation Methods and Results

To have an idea of the optimal parameters for nanohole sensors, we performed comprehensive calculations of the transmission spectra of nanohole arrays using the finite-difference time-domain method (FDTD). To model the dispersive gold film a fit to the experimental data of Johnson and Christy was used [34]. The substrate was taken to have refractive index of 1.52 (for glass) and the refractive index of the background was varied to determine the sensitivity. The simulation domain used perfectly matched layer boundaries to prevent reflections and Bloch boundary conditions for the periodic structure. A plane wave source was used normally incident on the nanohole array. A frequency domain profile monitor collected the transmission through the holes in the visible and near infrared wavelength range. A mesh over-ride of 2 nm was used over the metal film, and this was confirmed to capture the surface plasmon dispersion by finite difference mode calculations. The sensitivity was determined by noting the change in the transmission characteristics for varying refractive index of the solution surrounding the holes.

Periodicity of the array, hole-diameter, and metal thickness were varied to obtain the best performance of the nanohole array sensor. FDTD simulations were carried out for hole-diameters from 140 nm to 250 nm, periodicities from 415 nm to 570 nm, and gold film thicknesses from 100 nm to 500 nm.

Figure G-1(a) shows the transmission spectrum of the optimized nanohole arrays for film thickness of 100 nm. The optimization was determined in terms of the resolution, assuming that shot noise is the dominant factor (for which the noise scales as the square

root of the intensity). Considering this, the resolution, when changing the refractive index from $n_1 = 1.330$ to $n_2 = 1.331$ will be proportional to the resolution parameter R:

$$R = \left| \frac{I_{n1} - I_{n2}}{\sqrt{I_{n1}}} \right| \tag{G.1}$$

Using Eq. G.1, we compare the performance between the nanohole arrays, where I_{n1} and I_{n2} are the transmission intensities for the different refractive index values. Figure G-1b shows that the optimal wavelength for operation is at 648 nm for this film thickness, and this occurs for a hole-diameter of 150 nm and a periodicity of 425 nm.

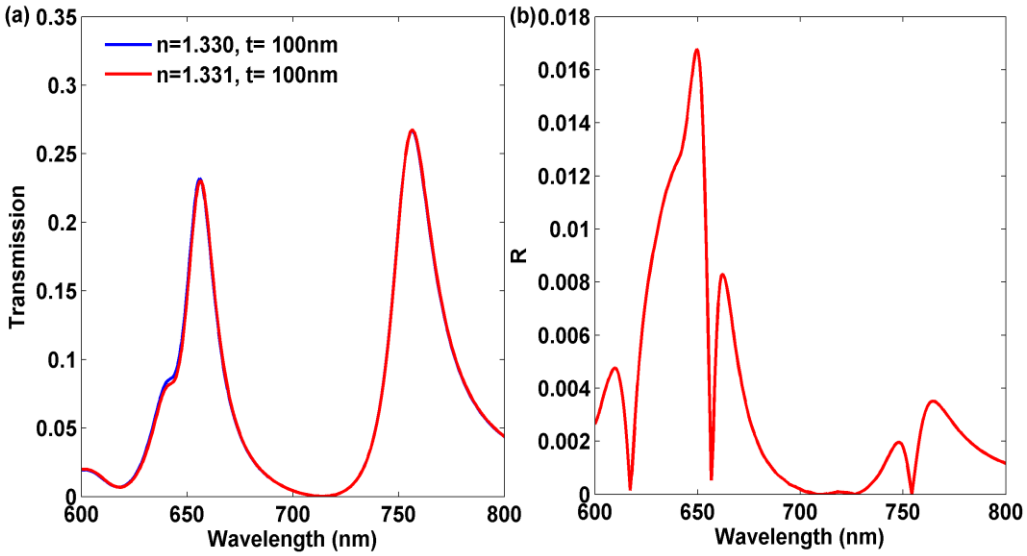

Figure G-1: Results of FDTD simulations. (a) Spectrum of a circular nanohole array of diameter 150 nm and periodicity 425 nm in a gold film of 100 nm thickness. (b) Optimal wavelength for operation is at 648 nm.

It is interesting to note here that the optimal periodicity for the 100 nm film is close to the expected lowest order Bragg resonance of the plasmon dispersion for this wavelength; however, this is not the case for the thicker films. We will discuss this further below in section 6.

Figure G-2 shows equivalent results for a gold film of 300 nm thickness. The optimal parameters found were hole-diameter of 260 nm, periodicity of 570 nm. The wavelength for the best performance was 655 nm.

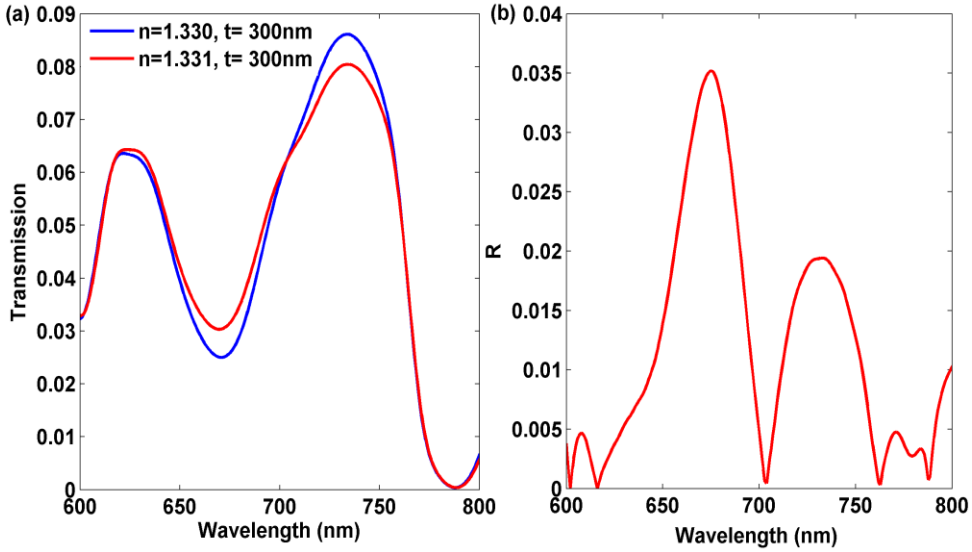

Figure G-2: Results of FDTD simulations. (a) Spectrum of a circular nanohole array of diameter 260 nm and periodicity 570 nm in a gold film of 300 nm thickness. (b) Optimal wavelength for operation 655 nm.

Figure G-3 shows the transmission spectrum and resolution parameter for a 500 nm gold film thickness. The optimal parameters for this thickness were hole-diameter of 260 nm and periodicity of 570 nm. The largest R value change is at the wavelength of 655 nm.

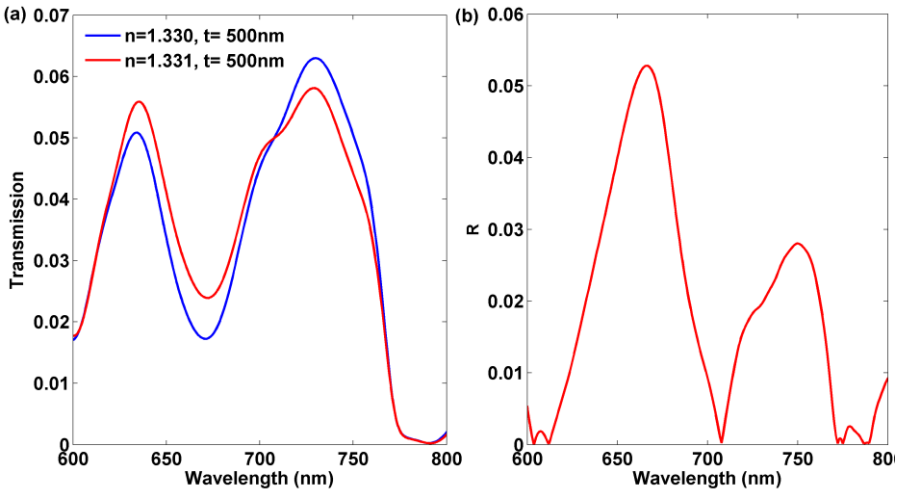

Figure G-3: Results of FDTD simulations. (a) Spectrum of a circular nanohole array of diameter 260 nm and periodicity 570 nm in a gold film of 500 nm thickness. (b) Optimal wavelength for operation is 655 nm.

Comparing Figures G-1 to G-3, it is clear that the thicker films provide better performance. In practice, however, we are limited by the ability to make high-aspect nanoholes in thick films and the duration of milling, and so we do not attempt larger

thicknesses than 500 nm in this work. It is also interesting to note that the optimal wavelength of operation was consistently around 650 nm for all of the film thicknesses, and this has important ramifications for the sensor performance, as discussed further in Section 6.

Fabrication Procedure

The nanohole arrays were fabricated by using a FB-2100 (Hitachi) focused ion beam with a gallium ion source. The ion beam was set to 40 keV for milling, and a beam current of 0.01 nA. Figure G-4 shows a scanning electron microscope image of the circular nanohole array. To match the simulations, the nanohole arrays were milled in film thicknesses of 100 nm, 300 nm and 500 nm. Due to the cost of fabrication, the simulations were used to reduce the range of fabrication parameters. For the 100 nm film thickness, the periodicity was scanned from 415 nm to 435 nm in steps of 5 nm and the diameters used were 150 nm and 160 nm. For the 300 nm and 500 nm film thicknesses, the diameters used were 260 nm and 270 nm and the periodicity was scanned from 550 nm to 575 nm in steps of 5 nm.

Good verticality of the side-walls was confirmed by energy dispersive X-ray spectroscopy studies, which showed that the gold was removed from the region of precisely (to within 5 nm) the specified radius.

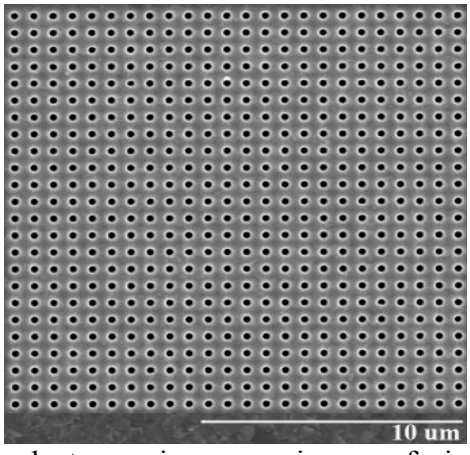

Figure G-4: Scanning electron microscope image of circular apertures with a diameter of 260 nm in a 500 nm thick gold film.

Figure G-5 shows the microfluidic chip. For measuring change in intensity due a change in the index of refraction we use a microfluidic flow channel which consists of a polydimethylsiloxane (PDMS) microchip made by rapid prototyping lithography [35].

The master mold of the channel was patterned on a silicon wafer using SU-8 50 photoresist. For the development of the microchip, a curing agent and PDMS (ratio 10:1) were used. The gold sample with PDMS flow channel was sandwiched between two acrylic layers to seal the flow channel.

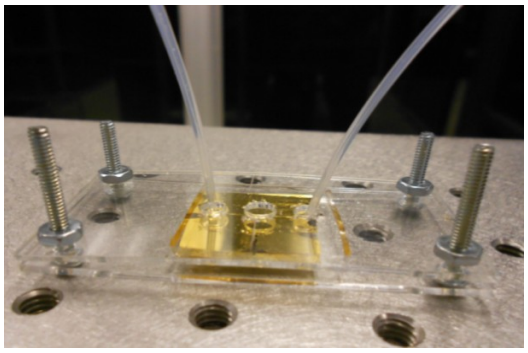

Figure G-5: Microchip of a 500 nm thick gold film sample and with PDMS microfluidic over-channel sandwiched between acrylic layers.

Experimental Setup

Figure G-6 shows the experimental setup for measuring the fabricated gold samples. To enable scanning over a wide range of wavelengths, a supercontinuum light source (Fianium SC400) was used. With the acousto-optic tunable filter (AOTF), any desired wavelength ranging from 400 nm to 1100 nm could be obtained. This source illuminated the top surface of the sub-wavelength apertures. A spatial filter was used to improve the spatial/spectral quality of the laser beam. Two objective lenses had been set up to measure the transmission of the nanohole arrays. First, the laser beam was focused using a microscope objective of 0.1 NA, and then it was collected with a microscope objective of 0.5 NA. We experimented with various objective lens combinations, and we found that this is a good configuration. In particular, the high NA objective below the glass substrate helps to acquire a larger number of photons. By contrast, the low NA objective above the microfluidic channel ensures a low angular deviation in the incident photons, so that the resonances (that are angle-sensitive) are more spectrally pure [36].

A CCD camera (Thorlabs DCU224C) was used to record a video of the sub-wavelength structures while flowing solutions of slightly different refractive index over the sample. Any change in the refractive index of the solution appears as a change in intensity. A syringe pump (Harvard apparatus 11 series) was used for a stable liquid flow rate of 7 μL/min.

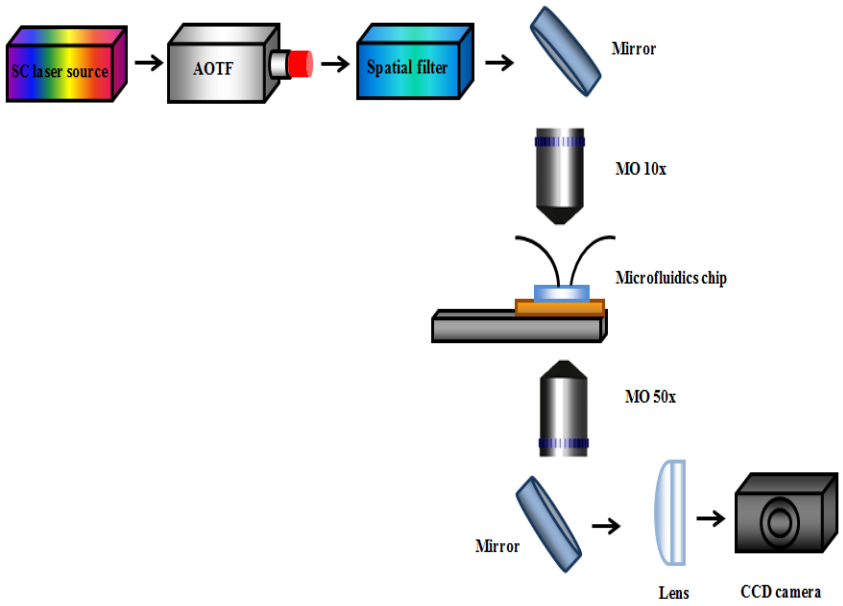

Figure G-6: Schematic of optical setup used for measuring the change in intensity of the fabricated gold samples with a super continuum laser source tunable over the visible near infrared region.

Results

In the experiments, the 100 nm thick gold film showed the largest sensitivity for a hole-diameter of 150 nm and periodicity of 425 nm, with a resolution of 2×10^{-6} RIU. The 300 nm thick film showed largest sensitivity for a hole-diameter of 260 nm and periodicity of 570 nm with a resolution of 8×10^{-7} RIU. The 500 nm thick film showed the largest sensitivity for a hole-diameter of 260 nm and periodicity of 570 nm, with a resolution of 6×10^{-7} RIU. These parameter values are all in close-agreement with the simulation results. It is clear also that the thicker film gives better resolution, as expected from the simulations.

Figure G-7 shows the best result obtained among all the arrays, varying the refractive index to determine the sensitivity. The curve in Figure G-7a has a staircase appearance because it was acquired by scanning the AOTF in 5 nm steps for 5 second duration at each step. For convenience, the figure is plotted versus wavelength instead of time.

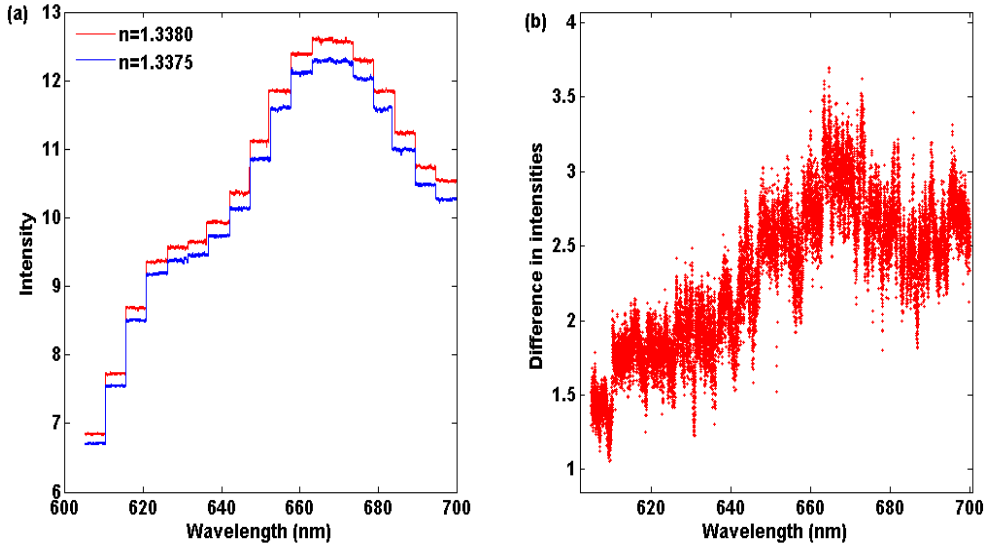

Figure G-7: (a) Representation in time of the spectrum of a nanohole array while flowing two different refractive index solutions. (b) Difference in intensities of two refractive index solutions.

After choosing the optimal wavelength of operation for the nanohole array sensor measurements, by the procedure in Figure G-7, bulk sensitivity measurements were carried out with a higher intensity of 3.6 mW and using a low-pass finite impulse response numerical filter. Figure G-8 shows the intensity change of the circular nanohole arrays subjected to refractive index change of 0.0005 operating at 655 nm. The numerical filtering reduced the time resolution to 0.5 frames per second. The highest resolution that was obtained was 6×10^{-7} RIU.

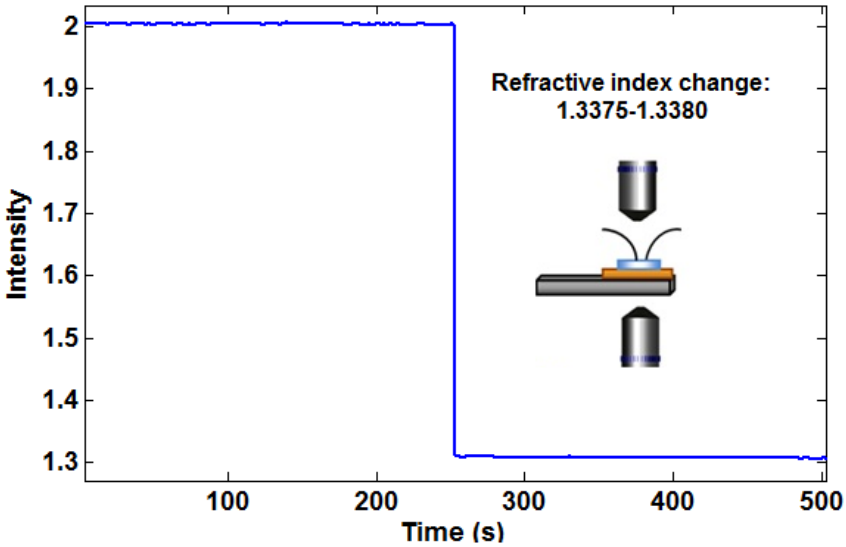

Figure G-8: Experimental results for measuring the change in intensity at 655 nm wavelength for a 500 nm thick gold film. An array of circular holes with diameter of 260 nm and periodicity of 570 nm were used.

Discussion

First we note that good agreement is seen between the simulation and the experiments. The achieved resolution of 6×10^{-7} RIU is a promising step towards competing with existing commercial SPR devices (10^{-7} resolution), while allowing for the integration, multiplexing and optofluidic advantages of nanohole SPR.

It is interesting to note that the optimum resolution found from the simulations was around 655 nm. This is believed to result from the gold dispersion for two reasons. First, gold has a low loss at 655 nm because this wavelength is past the interband absorption peak of gold (around 510 nm). Second, the magnitude of the relative permittivity at 655 nm is not too large (it is closer to the plasma frequency than further in the IR, for example), which allows for significant electromagnetic field penetration into the metal and pronounced plasmonic effects. It is fortuitous that the optimal operation considering the material properties of gold coincides fairly well with the optimal sensitivity of the CCD camera used in this experiment (~600 nm), because this allows for higher photon collection efficiency, and therefore reduced shot-noise signal-to-noise ratio.

It is common to use the SP Bragg relation to determine the optimal periodicity for nanohole array sensing:

$$\lambda_{SP}(i,j) = p\left(i^2 + j^2\right)^{-\frac{1}{2}}\left(\frac{\varepsilon_d \varepsilon_m}{\varepsilon_d + \varepsilon_m}\right)^{1/2} \tag{G.2}$$

where ε_m and ε_d are the permittivities of metal and dielectric material, p is the periodicity, i and j are integers that represent Bragg resonance orders. This gives reasonable results for predicting the resonance wavelength for thinner films for the lowest order resonance. For example, the $i=0$, $j=1$ resonance of the 100 nm film with 425 nm periodicity on the water side is predicted to be 625 nm, and was observed to be 648 nm in the simulations. We see here, however, that larger periodicities are required for thicker films, and these do not seem to match the lowest order resonance. Indeed, they are closer to the $i=1$, $j=1$ resonance. The reason for this effect is still under investigation; however, this shows that future investigations should not simply chose the lowest order resonance wavelength as has been done in the past [37].

Conclusions

We optimized the resolution of circular nanohole arrays in metal films for refractive index sensing by increasing the sensitivity with modifications to the hole-array parameters (film thickness, periodicity and diameter), by determining the optimal wavelength of operation, and by reducing the noise of the sensor system (through increased collection efficiency, increased intensity and numerical filtering). We achieve a bulk resolution of 6×10^{-7} RIU. Due to the collinear microscope geometry, the potential for multiplexing of nanohole arrays and improved optofluidic functionality [32], these results are encouraging for future detection of chemical and biological species.

The authors are grateful for the support of the NSERC Strategic Network for Bioplasmonic Systems (Biopsys).

References

[1] T.W. Ebbesen, H.J. Lezec, H.F. Ghaemi, T. Thio, P.A. Wolff, Extraordinary optical transmission through sub wavelength hole arrays, Nature 391:667-669, 1998.

[2] W.L. Barnes, A. Dereux, T.W. Ebbesen, Surface plasmon subwavelength optics, Nature 424:824-830, 2003.

[3] A.G. Brolo, R. Gordon, B. Leathem, K.L. Kavanagh, Surface plasmon sensor based on the enhanced light transmission through arrays of nanoholes in gold films, Langmuir 20:4813-4815, 2004.

[4] R. Gordon, D. Sinton, K.L. Kavanagh, A.G. Brolo, A new generation of sensors based on extraordinary optical transmission, Acc. Chem. Res. 41:1049-1057, 2008.

[5] A. Lesuffleur, H. Im, N.C. Lindquist, S.H. Oh, Periodic nanohole arrays with shape-enhanced plasmon resonance as real–time biosensors, Appl. Phys. Lett. 90:243110, 2007.

[6] W.L. Barnes, W.A. Murray, J. Dintinger, E. Devaux, T.W. Ebbesen, Surface plasmon polaritons and their role in the enhanced transmission of light through periodic arrays of subwavelength holes in metal film, Phys. Rev. 92:107401, 2004.

[7] A. Lesuffleur, H. Im, N.C. Lindquist, K.S. Lim, S.H. Oh, Laser-illuminated nanohole arrays for multiplex plasmonic microarray sensing, Opt. Express 16:219-224, 2008.

[8] L. Pang, G.M. Hwang, B. Slutsky, Y. Fainman, Spectral sensitivity of two-dimensional nanohole array surface plasmon polariton resonance sensor, Appl. Phys. Lett. 91:123112, 2007.

[9] R. Gordon, A. G. Brolo, D. Sinton, K. L. Kavanagh, Resonant optical transmission through hole-arrays in metal films: Physics and applications, Laser and Photonics Reviews 4:311-335, 2010.

[10] J. Homola, S. Yee, G. Gauglitz, Surface plasmon resonance sensors: Review, Sensor Actuat. B-Chem. 54:3-15, 1999.

[11] A. De Leebeeck, L.K.S. Kumar, V. de Lange, D. Sinton, R. Gordon, A.G. Brolo, On-chip surface-based detection with nanohole arrays, Anal. Chem. 79:4094-4100, 2007.

[12] H. Gao, J. Henzie, T.W. Odom, Direct evidence of surface plasmon-mediated enhanced light transmission through metallic nanohole arrays, Nano Lett. 6:2104-2108, 2006

[13] N.C. Lindquist, A. Lesuffleur, H. Im, S.H. Oh, Sub-micron resolution surface plasmon resonance imaging enable by nano-hole arrays with surrounding Bragg mirrors for enhanced sensitivity and isolation, Lab Chip 9:382-387, 2009.

[14] Y. Liu, S. Blair, Fluorescence enhancement from an array of subwavelength metal apertures, Opt. Express 28:507-509, 2003.

[15] J. Dintinger, S. Klein, T.W. Ebbesen, Molecule-surface plasmon interaction in hole arrays: Enhanced absorption, refractive index changes, and all-optical switching, Adv. Mater 18:1267-1270, 2006.

[16] J.C. Sharpe, J.S. Mitchell, L. Lin, N. Sedoglavich, R.J. Blaikie, Gold nanohole array substrates as immunobiosensors, Anal. Chem. 80:2244-2249, 2008.

[17] T. Allsop, R. Neal, E.M. Davies, C. Mou, P. Bond, S. Rehman, K. Kalli, D.J. Webb, P. Calverhouse, I. Bennion, Low refractive index gas sensing a surface plasmon resonance fibre device, Meas. Sci. Technol. 21:094029, 2010.

[18] J. Ji, J.G. O'Connell, D.J. Carter, D.N. Larson, High-throughput nanohole array based system to monitor binding events in real time, Anal. Chem. 80:491-498, 2008.

[19] X. Shou, A. Agrawal, A. Nahata, Role of metal film thickness on the enhanced transmission properties of a periodic array aperture, Opt. Express 13:9834-9840, 2005.

[20] P.R.H. Stark, A.E. Halleck, D.N. Larson, Short order nanohole arrays in metals for highly sensitive probing of local indices of refraction as the basis for a highly multiplexed biosensor technology, Methods 37:37-47, 2005.

[21] K.L. Lee, S.H. Wu, P.K. Wei, Intensity sensitivity of gold nanostructures and its application for high-throughput biosensing, Opt. Express 17:23104-23113, 2009.

[22] C.J. Alleyne, A.G. Kirk, R.C. McPhedran, N.A.P. Nicorovici, D. Maystre, Enhanced SPR sensitivity using periodic metallic structures, Opt. Express 15:8163-8169, 2007.

[23] J. Homola, Present and future of surface plasmon resonance biosensors, Anal. Bional. Chem. 377:528-539, 2003.

[24] T. Akimoto, S. Sasaki, K. Ikebukuro, I. Karube, Refractive-index and thickness sensitivity in surface plasmon resonance spectroscopy, Appl. Optics 38:4058-4064, 1999.

[25] A. Dhawan, M.D. Gerhold, J.F. Muth, Plasmonic structures based on subwavelength apertures for chemical and biological sensing applications, IEEE Sens. J. 8:942-950, 2008.

[26] J. Homola, Surface plasmon resonace based sensors for detection of chemical and biological species, Chem. Rev. 108:462-493, 2008.

[27] Biacore www.biacore.com

[28] A.K. Tetz, L. Pang, Y. Fainman, High-resolution surface plasmon resonance sensor based on linewidth-optimized nanohole array transmittance, Opt. Express 31:1528-1530, 2006.

[29] A-P. Blanchard-Dionne, L. Guyot, S. Patskovsky, R. Gordon, M. Meunier, Intensity based surface plasmon resonance sensor using a nanohole rectangular array, Opt. Express 19:15041-15046, 2011.

[30] C. Escobedo, S. Vincent, A.I.K. Choudhury, J. Campbell, A.G. Brolo, D. Sinton, R. Gordon, Integrated nanohole array surface plasmon resonance sensing device using a dual-wavelength source, J. Micromech. Michroeng. 21:115001, 2011.

[31] C. Escobedo, A.G. Brolo, R. Gordon, D. Sinton, Optofluidic concentration: Plasmonic nanostructure as concentrator and sensor, Nano Lett. ASAP 2012.

[32] F. Eftekhari, C. Escobedo, J. Ferreira, X. Duan, E.M. Girotto, A.G. Brolo, R. Gordon, D. Sinton, Nanoholes as nanochannels: Flow-through plasmonic sensing, Anal. Chem. 81:4308-4311, 2009.

[33] C. Escobedo, A.G. Brolo, R. Gordon, D. Sinton, Flow-through vs flow over: Analysis of transport and binding in nanohole array plasmonic biosensors, Anal. Chem. 82:10015-10020, 2010.

[34] P.B. Johnson, R.W. Christy, Optical constants of the noble metals, Phys. Rev. B 6:4370, 1972.

[35] D.C. Duffy, J.C. McDonald, O.J.A. Schueller, G.M. Whitesides, Rapid prototyping of microfluidic systems in poly(dimethylsiloxane), Anal. Chem. 70:4974-4984, 1998.

[36] H.F. Ghaemi, T. Thio, D.E. Grupp, T.W. Ebbesen, H.J. Lezec, Surface plasmons enhance optical transmission through subwavelength holes, Phys. Rev. B 58:6779-6782, 1998.

[37] A. Krishnan, T. Thio, T. J. Kim, H. J. Lezec, T. W. Ebbesen, P. A. Wolff, J. Pendry, L. Martin-Moreno, F. J. Garcia-Vidal, Evanescently coupled resonance in surface plasmon enhanced transmission, Opt. Commun. 200:1-7, 2001.

Appendix H: Relating Localized Nanoparticle Resonances to an Associated Antenna Problem

(2011, Physical Review B, volume 84, 195405)

Relating Localized Nanoparticle Resonances to an Associated Antenna Problem

Shakeeb Bin Hasan[1], Robert Filter[1], Aftab Ahmed[2], Ralf Vogelgesang[3], Reuven Gordon[2], Carsten Rockstuhl[1] and Falk Lederer[1]

[1]*Institute for Condensed Matter Theory and Solid State Optics, Friedrich-Schiller-Universit¨at Jena, Max-Wien-Platz 1, D-07743, Jena, Germany*

[2]*Department of Electrical and Computer Engineering, University of Victoria Victoria, British Columbia V8W 3P6, Canada*

[3]*Max Planck Institute for Solid State Research, Heisenbergstr. 1, D-70569, Stuttgart, Germany*

ABSTRACT: On an empirical basis, we indicate the possibility of conceptually unifying the description of resonances existing in some of the analytically studied metallic nanoparticles and optical nanowire antennas. To this end the nanoantenna is treated as a Fabry-Perot-like resonator with arbitrary seminanoparticles forming the terminations. We show that the frequencies of the quasistatic dipolar resonances of the considered nanoparticles coincide with those where the round-trip phase of the complex reflection coefficient of the fundamental propagating plasmon polariton mode at the wire terminations amounts to 2π. The lowest order Fabry-Perot resonance of the optical wire antenna occurs therefore even for a negligible wire length.

Introduction

Small particles are among the earliest cases tackled by light scattering theory. The quasianalytical rigorous solution for spheres dates back to the pioneering work of Mie in 1908 [1]. This approach can be considerably simplified if the size of the spheres is small compared to the illuminating wavelength resulting in the quasistatic approximation [2, 3]. The resulting analytic formulas for the polarizability of the sphere exhibit resonant denominators, such as the well-known expression $\varepsilon_m(\nu) + 2\varepsilon_d(\nu) = 0$ for the dipole resonance of a metallic sphere in a dielectric host medium. In this case and generally, the permittivities of the spheres and their surroundings need to exhibit opposite signs at resonance. The scattered field exhibits strongly enhanced stationary evanescent components at the interface—a phenomenon that is termed localized surface plasmon polariton (LSPP) [4]. Intriguingly, it was shown that in this approximation the quality

factor of the resonance solely depends on the material properties rather than the particle shape [5], which, however, affects the resonance frequency. Only for a few other particle shapes [e.g., ellipsoids and spherical shells or particles with a lower dimensionality (i.e., a cylinder)] the resonance condition can be put in a similar form known from the sphere. The exploitation of these LSPPs at nanoparticles of different shapes has led to various applications and is forming one branch of the prospering field of plasmonics.

If the metal is a perfect conductor, another resonance is supported by metallic wires if their length corresponds to a multiple of half the illumination wavelength. Such metallic wires constitute the basic building blocks of radio-frequency (RF) antennas. Recently, their downscaling into the visible attracted considerable interest and the field of optical antennas is now similarly established. Conceptually, optical antennas differ from RF antennas in that the field propagating along the wire is no more purely photonic but forms another polaritonic excitation [6]. This type of quasiparticle is referred to as a propagating surface plasmon polariton (PSPP) due to its sole energy transport in the propagation direction. As for any guided mode phenomenon, the PSPP dispersion relation may strongly depend on the wire's cross section (see, e.g., Ref. 7).

The origin of resonances in these finite-length nanowires is well understood in terms of Fabry-Perot resonances of the PSPP mode confined between the partially reflecting wire terminations [8-12]. Unlike in antennas at microwave frequencies, here the reflection coefficients are complex valued, providing an additional phase term that mimics an increase of the wire length and depends on the actual shape of the termination. This resembles the situation in a planar Fabry-Perot resonator with Bragg mirrors, where the number of layers also affects the actual phase shift and thus the resonance condition. This is also the reason why multiples of half the resonance wavelength differ from the wire length [8, 10-13]. This peculiarity evoked research interest and both analytical and numerical results on the spectral and geometrical dependence of reflection coefficients were reported for abrupt or flat nanowire terminations [14, 15]. Moreover, associated geometries (e.g., trenches, grooves, or slits on or in flat metal surfaces or metallic thin films) were analyzed with respect to their reflection and transmission properties of PSPP launched along the metal surfaces [16]. It allows for obtaining more insight into the

underlying physics of phenomena observable in such systems. Examples thereof would be the enhanced transmission in subwavelength apertures [17].

To date, aforementioned metallic nanoparticles are largely studied in terms of LSPP resonances whereas wire nanoantennas are commonly analyzed in terms of PSPP standing wave phenomena and these seemingly disparate approaches have not been systematically integrated. A few reports on variable length nanoantennas [13, 18] consider spherical particles as the limiting case of cylindrical wires. Nevertheless, it is challenging to disclose the mechanism behind this convergence of resonances in analytically understood geometries at a physical level. Here we attempt to provide a unifying view on some of the analytically understood nanoparticles in research. It turns out that the LSPP resonances of all of them follow straightforwardly from solving the reflection problem at the nanowire termination.

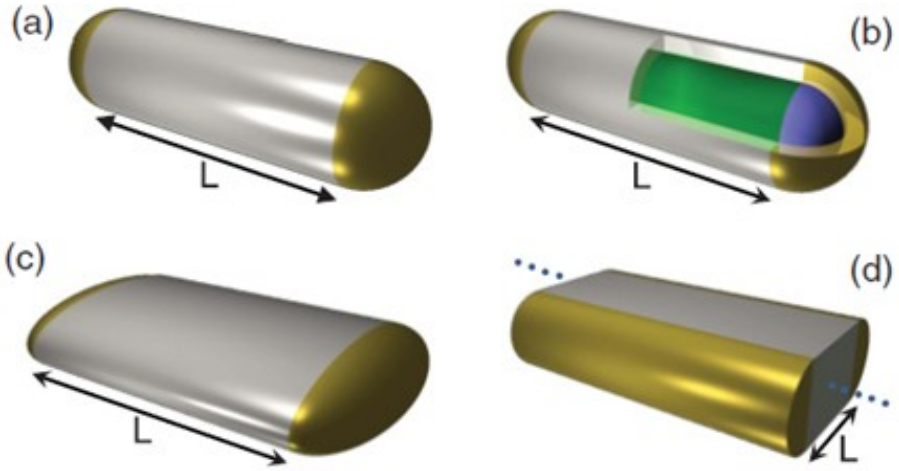

Figure H-1: (Color online) Sketch of considered metallic nanoantenna geometries. (a) Circular cylinder and (b) cylindrical shell with a hemispherical termination; (c) elliptical cylinder with a semielliptical termination; (d) one-dimensional (1D) nanoantenna with a semicylindrical termination. All nanoantennas are composed of a nanowire (metallic color) and a termination (golden) while *L* is the nanowire's length

Modelling Sphere as an Antenna

Beginning with the simplest case, we take nanowires of circular cross section with hemispherical terminations at both ends [Figure H-1(a)]. This nanoantenna becomes a sphere for vanishing wire length *L*. We hypothesize that the dipolar resonance of a sphere that is observable in the far field (e.g., as a peak in the scattering cross section is caused by the constructive interference of the forward and backward propagating fundamental

(m = 0) PSPP mode of the nanowire) [19-21]. Then, the necessary condition for a Fabry-Perot resonance—that is, the round trip reproduction of the phase factor—is a total phase accumulation of an integer multiple of 2π. This condition can already be met for a wire with negligible length (i.e., the sphere). It implies a phase shift of π upon reflection at each termination. In general, higher order PSPP modes do not need to be considered since all modes with $|m| \geq 2$ cut-off below a threshold wire radius [22]. Moreover, the PSPP mode with $|m| = 1$ diverges for a vanishing radius, thereby suffering from increasing radiation losses. Therefore, it cannot be excited anymore[23] and the system becomes simple enough to be understood in terms of a fundamental (m = 0) PSPP mode. In the limit when the radius becomes comparable to the incident wavelength, our model requires further substantiation owing to additional dynamics brought in by the higher order modes.

We use the COMSOL MULTIPHYSICS simulation platform to numerically solve the reflection problem at the wire termination. The metallic nanowire is assumed to be semi-infinite and it is surrounded by a dielectric medium with a permittivity ε_d. The computational cell is enclosed by perfectly matched layers to mimic an open space. Silver (Ag) is used as the metal, with its dispersive permittivity fully considered [24]. The cylindrical wire has a radius of 10 nm. The exact value of the radius is not important provided it is much less than the wavelength.

First we calculate the dispersion relation of the fundamental wire eigenmode and subsequently use this mode as illumination of the termination of the semi-infinite wire. Then the total (incident and scattered) field is calculated in a plane normal to the wire axis and located at z = 0. The complex reflection coefficient of this mode at the termination is extracted by employing the orthogonality relations obtained through unconjugated reciprocity theorem [25], which yields an expression for reflection coefficient as

$$r = -\exp^{-i\beta L} \frac{\int_0^\infty E_{\rho,0}(\rho,0)\left[H_{\phi,tot}(\rho,0) - H_{\phi,0}(\rho,0)\right]\rho d\rho}{\int_0^\infty E_{\rho,0}(\rho,0)H_{\phi,0}(\rho,0)\rho d\rho} \tag{H.1}$$

where $H_{\varphi,0}(\rho,0)$ being the azimuthal magnetic field and $E_{\rho,0}(\rho,0)$ the radial electric field components of the incident PSPP mode ($m = 0$) at $z = 0$, β is the associated propagation constant and L is the distance between origin ($z = 0$) and the initial plane of the antenna termination. All quantities, except the wire geometry, depend on frequency. In passing we note that the distinction of what belongs to the wire and what belongs to the termination is arbitrary to a certain extent. The phase accumulated due to propagation and the phase accumulation due to reflection can easily be merged. However, since we wish to discuss solely the properties of the termination, the length L is understood as the length of the nanoantenna along which no change of the cross-sectional profile occurs.

In Figure H-2 the complex-valued propagation constant β of the lowest order PSPP mode is displayed as a function of the frequency and the permittivity of the surrounding medium. The real part exhibits the usual dispersion characteristic where the propagation constant increases with frequency until back bending sets in. This back bending is associated with a strongly increasing damping (imaginary part). In the succeeding spectral domain, any analysis of the reflection coefficient tends to be cumbersome since dissipation entirely dominates the system.

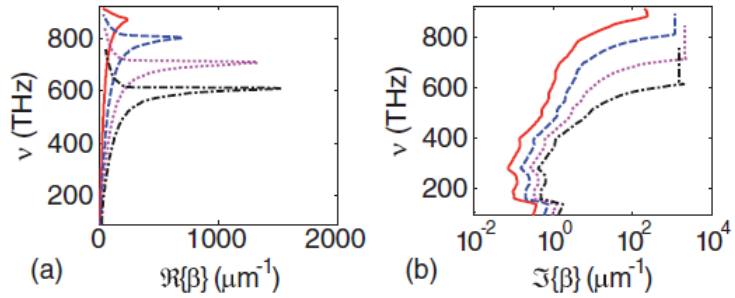

Figure H-2: (Color online) (a) Real and (b) imaginary part of the propagation constant β of the lowest order PSPP mode as a function of frequency ν for selected values of ε_d; $\varepsilon_d = 1$ (solid red), $\varepsilon_d = 2.8$ (dashed blue), $\varepsilon_d = 5.4$ (dotted magenta), $\varepsilon_d = 9$ (dotted-dashed black).

Figure H-3 shows the complex reflection coefficient as a function of frequency for different ε_d extracted from the simulation of a semi-infinite wire for the respective lowest order PSPP mode. It can be seen that at low frequencies the modulus is constant and large with a phase shift around zero, suggesting a perfect metal-like behavior. The phase increases with frequency and undergoes an abrupt change at a critical frequency. This jump is associated with the decrease in the reflected amplitude and it appears in the

frequency interval where back bending occurs. Now it is easy to extract the frequency where a phase jump of π occurs and to compare it to the resonance frequency predicted by the quasistatic theory for a small sphere. Additionally, it can be seen that the phase surpasses even values corresponding to multiples of π. As the scope of this work is restricted only to resonances visible in the analytical formulation of quasistatic limit, we will not attempt to disclose any possible relation of these higher order Fabry-Perot resonances to the ones accessible in rigorous Mie theory. But it suffices to say that for isolated particles such resonances are not observed because they are dipole forbidden and suffer from excessive damping.

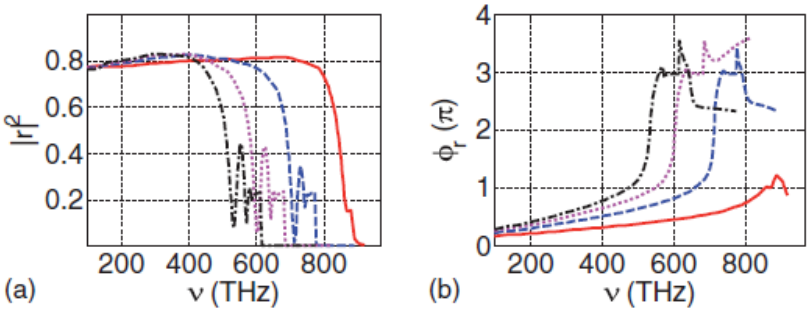

Figure H-3: (Color online) (a) Amplitude and (b) phase of the reflection coefficient of the nanowire for selected values of ε_d; ε_d = 1 (solid red), ε_d = 2.8 (dashed blue), ε_d = 5.4 (dottedmagenta), ε_d = 9 (dotted-dashed black).

Figure H-4a shows a comparison of the resonance frequencies predicted by the quasistatic theory as well as the PSPP reflection calculation for different surrounding media. The excellent agreement between both approaches demonstrates that the resonances of a sphere in the quasistatic limit are directly related to the corresponding limit of the nanoantenna problem.

Additional Examples

Nanoshell

To further investigate the applicability of this conclusion, we briefly analyze other well-known particle geometries in the following. Another special case of a spherical nanoparticle is one with a dielectric core and a metallic shell. It is of appreciable practical relevance since its resonance frequency can be tuned across the entire visible spectral region by varying the metallic shell thickness [26]. Such particles exhibit lower and higher energy LSPP resonances, which appear as a result of the hybridization of

individual resonances of the constituting metallic sphere and dielectric void [27]. We approximate the structure similarly as before by a nanowire made of a dielectric core surrounded by a metallic shell terminated with a hemispherical shell of the same construction [Figure H-1b]. Guided by intuition, we regard the lower (upper) branch of the fundamental PSPP mode of the cylindrical metallic shell wire [28] as responsible for the lower (higher) resonance frequency of these particles. We repeat the aforementioned analysis for the lower branch PSPP mode and show a similar comparison between resonance frequencies predicted by quasistatic approximation and the reflected field where $\varphi_r = \pi$ in Figure H-4b as a function of the ratio b/a between shell and core radii, respectively. An analysis of the highly dissipative upper branch was not attempted due to the conceptual difficulties associated with overdamped PSPPs (see also Figure H-2).

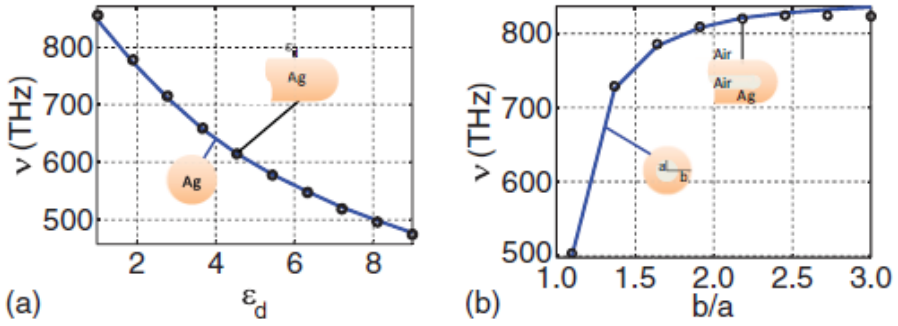

Figure H-4: (Color online) Resonance frequency of a sphere (a) with a radius of 10 nm as a function of permittivity of surrounding medium and of a spherical core shell particle (b) as a function of the ratio between shell and core radii b/a. The core radius $a = 10$ nm is fixed. The permittivity of both the core and the surrounding medium is $\varepsilon_d = 1$. Dots correspond to resonance frequencies as extracted from the phase of the reflection coefficients and the solid lines correspond to the predictions from quasistatic theory.

Ellipsoid

We extend the scope of our study toward ellipsoids which have a non-spherical geometry except in specific cases. First we consider an elliptical wire cross section [see Figure H-1c]. These particles can be envisioned straightforwardly to be composed of an elliptical nanowire (radii a and b) of negligible length and terminations consisting of rotational symmetric semi-ellipsoids [Figure H-1c]. Note that the resonance frequencies of ellipsoids depend upon the illuminating polarization [29]. We set the semi-axis a to be the symmetry axis and present the results for the electric field polarized both

perpendicular and parallel to it. Figure H-5a shows the resonance frequency as calculated from the phase of the reflected field at the wire termination compared to the predictions from quasistatic theory. In the antenna simulation the polarization is chosen by selecting the eigenmode corresponding to the nanowire under respective illumination. Overall we find good agreement in the predicted resonance frequencies by both methods.

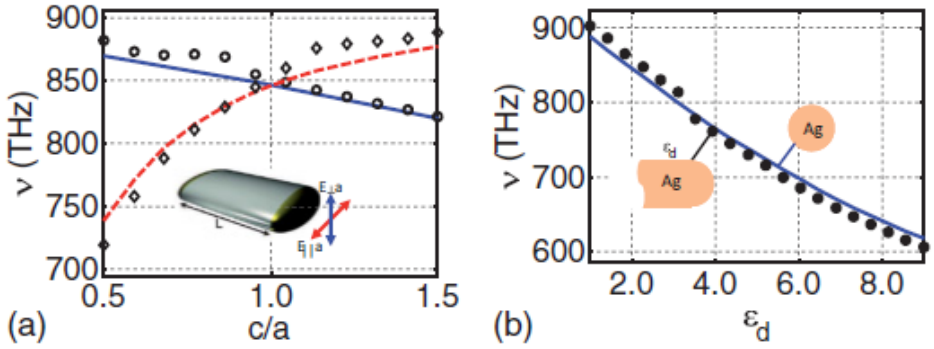

Figure H-5: (Color online) Resonance frequency in (a) of an ellipsoid with $b = c = 20$ nm surrounded by $\varepsilon_d = 1$ as a function of the ratio c/a between semi-axes and in (b) of a cylinder with a radius of 10 nm as a function of ε_d. In (a), solid blue (dashed red) curve corresponds to quasistatic resonance of the spheroid under illuminating polarization perpendicular (parallel) to semi-axis a. Circular (diamond) marks indicate frequencies at $\varphi_r = \pi$ for polarization perpendicular (parallel) to semi-axis a. The polarization in the antenna simulation is selected by choosing respective wire mode as the illuminating field. In (b), the solid blue curve corresponds to quasistatic resonance while circular marks denote the frequencies at which $\varphi_r = \pi$.

2D Cylinder

The foregoing examples treated the case of 3D nanoparticles. Now we move on to a (quasi-) 2D object in the form of a cylinder extending to infinity along its axis. Such cylinders exhibit a dipolar resonance in the quasistatic limit under illumination with a plane wave having a magnetic field polarized along the cylinder's axis if $[\varepsilon_m(\nu) + \varepsilon_d(\nu) = 0]$. Technically, this is dealt with by considering a 2D insulator-metal-insulator (IMI) strip or nanowire having semicircular terminations [Figure H-1d]. The whole geometry then extends invariably out of the plane. The IMI strip waveguide is well known to support hybridized symmetric and antisymmetric PSPPs [4], with the latter being strongly delocalized in the limit of a vanishing thickness (long-range surface plasmon polariton). The symmetric mode, on the contrary, localizes increasingly with decreasing thickness thereby standing out as the plausible source of LSPP resonance of cylinders in the

quasistatic limit. Therefore, taking a 20-nm thick IMI strip terminated with semicircular caps of 20 nm diameter, we obtain the reflection coefficient for the symmetric plasmonic mode. Figure H-5b shows the comparison of the theoretically predicted resonance frequencies with the standing wave resonance. Again, good agreement between the two approaches can be recognized.

Composite Particle

In the end, we present a practical application of the ideas established above by considering an asymmetric particle that cannot be divided into symmetric halves. Such a nanoparticle can be formed straightforwardly in Figure H-1a by replacing one of the two terminal caps by a half-spheroid whose semi-axes (*a,b*) perpendicular to the nanowire's axis are equal and the same as the nanowire's radius (inset of Figure H-6).

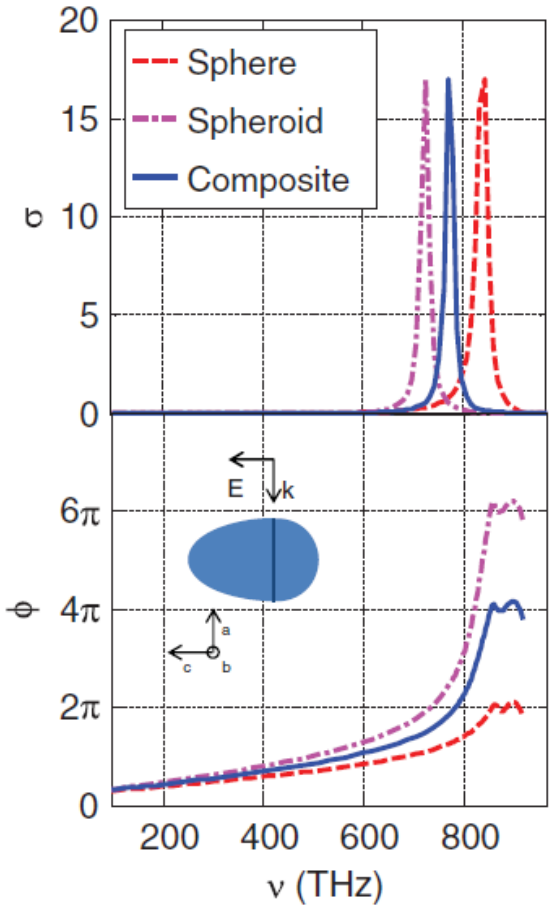

Figure H-6: (Color online) Normalized scattering cross section σ (top) and total phase jump φ (bottom) for an asymmetric composite particle (inset) made up of a hemisphere (radius = 10 nm) and a half prolate spheroid (a = b = 10 nm, c = 20

nm). Inset shows the 2D perspective of the proposed asymmetric composite particle.

The semi-axis (c) of the spheroid parallel to the axis of the nanowire is made different in length than the other two semi-axes to introduce asymmetry in the entire particle. In our simulation, we set the radius of the hemisphere as well as the semi-axes $a = b$ of the half-spheroid equal to 10 nm. The semi-axis c is finally set to 20 nm to form an egg-shaped particle. As there is no analytical formulation to predict a resonance in these particles, we rigorously compute the far-field scattering cross section by illuminating the particle with a plane wave having the E field polarized parallel to the c axis of the semispheroid (inset of Figure H-6). A first-order Fabry-Perot resonance is obtained when the round-trip phase jump φ upon reflection from both hemispherical and semispheroidal ends becomes equal to 2π. As it is evident from Figure H-6, both methods are in excellent agreement.

Conclusion

In conclusion, we have proposed an alternate perspective for looking at the LSPP resonances of specific metallic nanoparticles and relate them to resonances of corresponding optical nanoantennas. We show that the LSPP resonances appear at frequencies where the total phase jump upon reflection of PSPPs from both terminals amounts to 2π. Numerical studies show that the resonance frequencies coincide with those obtained for LSPPs in the quasistatic approximation provided that this approximation is valid. Moreover, we foresee that further research devoted to the question of how to relate the reflection phase to measurable scattering quantities will be a fruitful direction.

Support by the German Federal Ministry of Education and Research (PhoNa), by the Thuringian State Government (MeMa), and the German Science Foundation (SPP 1391 Ultrafast Nano-optics) is acknowledged. We would like to thank S. Fahr for assistance in preparing some figures.

References

[1] G. Mie, "Articles on the optical characteristics of turbid tubes, especially colloidal metal solutions.," Annalen Der Physik, vol. 25, pp. 377-445, 1908.

[2] C. F. Bohren andD. R.Huffman, Absorption and Scattering of Light by Small Particles Wiley-Interscience, New York, 1983.

[3] D. R. Fredkin and I. D. Mayergoyz, "Resonant behavior of dielectric objects (electrostatic resonances)," Physical Review Letters, vol. 91, 2003

[4] S. A. Maier, Plasmonics: Fundamentals and Applications Springer, New York, 2007.

[5] F. Wang and Y. R. Shen, "General properties of local plasmons in metal nanostructures," Physical Review Letters, vol. 97, 2006.

[6] J. J. Hopfield, "Theory of the Contribution of Excitons to the Complex Dielectic Constant of Crystals," Physical Review, vol. 112, pp. 1555-1567, 1958.

[7] E. Feigenbaum and M. Orenstein, "Nano plasmon polariton modes of a wedge cross section metal waveguide," Optics Express, vol. 14, pp. 8779-8784, 2006.

[8] L. Novotny, "Effective wavelength scaling for optical antennas," Physical Review Letters, vol. 98, 2007.

[9] E. S. Barnard, et al., "Spectral properties of plasmonic resonator antennas," Optics Express, vol. 16, pp. 16529-16537, 2008.

[10] T. Sondergaard, et al., "Slow-plasmon resonant-nanostrip antennas: Analysis and demonstration," Physical Review B, vol. 77, 2008.

[11] J. Dorfmuller, et al., "Fabry-Perot Resonances in One-Dimensional Plasmonic Nanostructures," Nano Letters, vol. 9, pp. 2372-2377, 2009.

[12] J. Dorfmuller, et al., "Plasmonic Nanowire Antennas: Experiment, Simulation, and Theory," Nano Letters, vol. 10, pp. 3596-3603, 2010.

[13] G. W. Bryant, et al., "Mapping the plasmon resonances of metallic nanoantennas," Nano Letters, vol. 8, pp. 631-636, 2008.

[14] S. J. Al-Bader and H. A. Jamid, "Diffraction of surface plasmon modes on abruptly terminated metallic nanowires," Physical Review B, vol. 76, 2007.

[15] R. Gordon, "Reflection of Cylindrical Surface Waves," Optics Express, vol. 17, pp. 18621-18629, 2009.

[16] P. Lalanne, et al., "A microscopic view of the electromagnetic properties of sub-lambda metallic surfaces," Surface Science Reports, vol. 64, pp. 453-469, 2009.

[17] H. T. Liu and P. Lalanne, "Microscopic theory of the extraordinary optical transmission," Nature, vol. 452, pp. 728-731, 2008.

[18] J. Aizpurua, et al., "Optical properties of coupled metallic nanorods for field-enhanced spectroscopy," Physical Review B, vol. 71, 2005.

[19] J. C. Ashley and L. C. Emerson, "Dispersion-Relations for Non-Radiative Surface Plasmons on Cylinders," Surface Science, vol. 41, pp. 615-618, 1974.

[20] C. A. Pfeiffer, et al., "Surface Polaritons in a Circularly Cylindrical Interface - Surface Plasmons," Physical Review B, vol. 10, pp. 3038-3051, 1974.

[21] H. Khosravi, et al., "Surface-Polaritons in Cylindrical Optical Fibers," Journal of the Optical Society of America a-Optics Image Science and Vision, vol. 8, pp. 112-122, 1991.

[22] D. E. Chang, et al., "Strong coupling of single emitters to surface plasmons," Physical Review B, vol. 76, 2007.

[23] Z. P. Li, et al., "Correlation between Incident and Emission Polarization in Nanowire Surface Plasmon Waveguides," Nano Letters, vol. 10, pp. 1831-1835, 2010.

[24] P. B. Johnson and R. W. Christy, "Optical-Constants of Noble-Metals," Physical Review B, vol. 6, pp. 4370-4379, 1972.

[25] A. W. Snyder and J. Love, Optical Waveguide Theory Springer, New York, 1983.

[26] S. J. Oldenburg, et al., "Nanoengineering of optical resonances," Chemical Physics Letters, vol. 288, pp. 243-247, 1998.

[27] E. Prodan, et al., "A hybridization model for the plasmon response of complex nanostructures," Science, vol. 302, pp. 419-422, 2003.

[28] S. J. Albader and M. Imtaar, "Optical Fiber Hybrid-Surface Plasmon Polaritons," Journal of the Optical Society of America B-Optical Physics, vol. 10, pp. 83-88, 1993.

[29] T. Okamoto, in Near-Field Optics and Surface Plasmon Polaritons Springer, Berlin, 2001.